# Scalable, Gravure-Printed Transparent Electronics: Materials and Process Design for Metal Oxide Thin-Film Transistors

*Will Scheideler*

Electrical Engineering and Computer Sciences
University of California at Berkeley

Technical Report No. UCB/EECS-2017-147
http://www2.eecs.berkeley.edu/Pubs/TechRpts/2017/EECS-2017-147.html

August 11, 2017

Acknowledgement

I was fortunate to work with many amazing people during my PhD. I appreciate all of their support, and I wish only that I had space to acknowledge here all of the kind things that they have done to help me along my way. I would like to express my gratitude to Professor Vivek Subramanian, for giving me every opportunity a PhD student could ask for. I appreciate the doors you opened for me and the freedom that you give to all your students. Thank you for letting me explore my interests and have a fulfilling PhD.

# Scalable, Gravure-Printed Transparent Electronics: Materials and Process Design for Metal Oxide Thin-Film Transistors

By

William Joseph Scheideler

A dissertation submitted in partial satisfaction of the

requirements for the degree of

Doctor of Philosophy

in

Engineering – Electrical Engineering and Computer Sciences

in the

Graduate Division

of the

University of California, Berkeley

Committee in charge:

Professor Vivek Subramanian, Chair

Associate Professor Ana Claudia Arias

Assistant Professor Hayden Taylor

Summer 2017

Abstract

Scalable, Gravure-Printed Transparent Electronics: Materials and Process Design for Metal Oxide Thin-Film Transistors

by

William Joseph Scheideler

Doctor of Philosophy in Engineering – Electrical Engineering and Computer Sciences

University of California, Berkeley

Professor Vivek Subramanian, Chair

Transparent metal oxides are one of the most promising material systems for thin film flexible electronics due to their unique balance of optical transparency and high electron mobility. Rapid progress in the field of solution-processed metal oxides in the last decade has established them as the leading material system for thin film transistors. Fully-integrating metal oxide materials with printing technologies could enable a wide range of applications such as flexible displays, imaging systems, resorbable bioelectronics, and low-power sensors that remain uneconomical or unmanufacturable with incumbent technologies. This thesis contributes materials and methods that can advance the scalable fabrication of transparent thin film transistors by high-speed gravure printing. Through these studies, an understanding of the interactions between ink chemistry, fluid parameters, printed feature formation, and electronic properties is presented.

In the past, gravure-printed electronics has been limited to printing organic inks and metal nanoparticles. Here we couple an understanding of the physics of gravure printing on glass with strategies for inorganic sol-gel ink design to extend the scope of high-speed printing to new high-performance inorganic materials including transparent conductive oxides (TCOs). We explore the impact that ink design has on material properties such as crystallinity, conductivity, transparency, and performance under mechanical bending stress, leading to effective co-optimization of patterning and TCO performance. Furthermore, these ink design principles are applied to silver nanowire hybrid sol-gel inks which allow gravure printing of high figure of merit mechanically robust, transparent conducting films using low processing temperatures.

Additionally, this thesis will discuss the design and construction of a custom gravure printer for high-speed patterning and accurate registration of printed layers. The novel design allows the decoupling of the individual subprocesses of gravure to allow mechanistic studies of major printing artifacts and improved areal uniformity. A new understanding of the role of gravure contact mechanics in ink transfer and doctoring is presented.

This work also develops high-performance materials for scaling down the process temperatures of printed metal oxide devices. Aqueous ink formulations are explored for inkjet printing transparent electrodes and channel materials in transparent thin film transistors. The unique printing physics, electrical contact properties to aqueous semiconductors, and low-temperature processability of

these inks are studied to achieve high-resolution printed TCOs at plastic compatible temperatures below 220 °C. Additionally, low-temperature, UV-annealed high-k dielectrics are presented for processing printed metal oxide transistors. High-performance printed transistors are achieved with high operational stability and connections between bias-stress stability and low-temperature processing are studied.

Acknowledgements

I was fortunate to work with a great number of amazing people during my PhD. I appreciate all of their support, and I wish only that I had space to acknowledge here all of the kind things that they have done to help me along my way.

I would like to express my gratitude to Professor Vivek Subramanian, for giving me every possible opportunity a PhD student could ask for. I appreciate the doors you opened for me and the freedom that you give to all of your students. Thank you for letting me explore my interests and have a fulfilling PhD.

I would also like to thank Professor Hayden Taylor and Professor Ana Arias– I am grateful for your insightful input. Thank you for being a part of my thesis and qualifying committees.

To my lab group – mentors, friends and ping pong foes, thank you for all of your support and clever banter. Rungrot Kitsomboonloha, Gerd Grau, Jaewon Jang, and Seungjun Cheung – you were my mentors and my role models when I joined the group; thank you for being so encouraging, inspiring, and positive. To the new group: Raj Kumar, Matt McPhail, Carlos Biaou, Yasuhiro Kobyashi, Lance O'Hari P. Go, Nishita Deka, Alvin Li, Thomas Rembert, and Jacob Sporrer – thank you for your love of puns, basketball, and all things ridiculous. Your humor has always been a welcome reprieve from the doctoral grind. To my friends Rumi Karim, Jeremy Smith, Andre Zeumault, Sarah Swisher, Jake Sadie, and Steve Volkman, I enjoyed working with all of you and had a lot of fun at football and group barbecues.

To my research collaborators at BASF, University of New Mexico, TU Darmstadt, Ataneo, and Hochschule Mannheim, I really appreciate the chance that I had to work with you and learn from you.

I want to thank the many undergraduates that I worked with here at Berkeley. I always appreciated your enthusiasm and fresh ideas. Saavan, Eli, Riad, Ava, Derek, Alex, Aldrich, Brandon, Eric, Nick, Xingchen, and Paul, working with you all made me a better mentor and helped me get excited about the work I was doing. I am especially grateful to all of you who worked with me on the design and construction of the new gravure tool.

To my wife, Olivia, I thank you for your daily support and inspiration. I am the luckiest PhD student to be able to have you right here next to me through the hardest moments and the best times of graduate school. Finally, I want to give special thanks to my family for always supporting me and helping me to keep things in perspective.

# Table of Contents

# Chapter 1: Introduction

## 1.1 Ubiquitous Transparent Electronics

The next generation of ubiquitous electronics, known as the Internet of Things (IoT) or Internet of Everything (IoE), calls for new thinking about the way computing devices interface with our physical world via sensing, information display, communication, etc. Visions of these pervasive computing devices include electronics which are flexible or transparent, as well as biocompatible and wearable. The hope is that these new form-factors will expand the scope of microelectronics and lead to further innovation. However, materials, packaging, and manufacturing must evolve alongside these devices to make these concepts economical and environmentally sustainable.

This future calls for devices and systems that connect traditional, power-efficient, high-speed CMOS electronics with the physical world. Large area systems based on thin film transistors (TFTs) are poised to satisfy this need for interfaces between computing, sensing, and information display. A variety of material systems have been explored for fabricating active thin film devices, including amorphous silicon, organic semiconductors, carbon-nanotubes,[1] and inorganic transparent metal oxides. Though metal oxides were once used primarily as transparent conductors for devices such as solar cells, new processing methods and control over their stoichiometry [2] have led to exciting discoveries that reveal its potential as material set for fabricating active switching devices. In fact, inorganic metal oxides have emerged as leading materials to drive thin film transistors because they offer significantly higher performance than competing active materials such as amorphous silicon[3] and organic semiconductors[4], as evidenced by the recent shift to oxide TFTs for use in commercial flat panel display backplanes[5].

The fascinating properties of transparent metal oxides facilitate applications which are unachievable with other thin film materials. A few representative examples of the wide range of thin film systems which have been demonstrated with metal oxide transistors are illustrated below in Figure 1.1. These applications can roughly be sorted into three main areas: display, imaging, and sensing. Because of their high electrical performance and excellent visible range transparency, metal oxides are excellent candidate materials for various optoelectronic devices such as flexible displays, which can use their low-temperature processing capability in pixel switching TFTs[6]. Historically, transparent conductive oxides have also had a significant role as window electrodes for solar cells[7]–[9], lasers, and LEDs[10], [11] due to their wide electronic bandgap (typically 2.5 eV – 4.1 eV). Analogously, the wide bandgap absorption of high energy radiation has enabled applications such as UV and visible light[12] imaging based on metal oxide active matrix sensors. Because of their extreme radiation hardness[13] and compatibility with large area flat panel manufacturing[14], metal oxide devices have also become interesting candidates for large area x-ray detectors[15], an essential instrument for biomedical imaging and industrial inspection of additively manufactured parts[16]. Medical applications requiring implantable, flexible electronics can take advantage of the biocompatibility and resorbability of metal oxide TFTs[17]. Finally, the inherent sensitivity of metal oxide thin films to ambient conditions and gas adsorption can also enable room-temperature, low-power gas sensing[18].

Collectively, these potential applications of metal oxide transistors share a common thread, which is that they are either inherently large area (displays, solar cells, imaging systems, etc.) or they require the unique form-factors offered by flexible substrates. Printing technologies are particularly well-suited to address these requirements and enable the commercial viability of these new thin film systems. Printed electronics can leverage the high-throughput, additive manufacturing demonstrated at extremely low cost in the graphic arts industry. Applying printing to metal oxide materials could open new application spaces that cannot be addressed by more expensive incumbent technologies such as vacuum-deposition, which typically utilize rigid substrates.

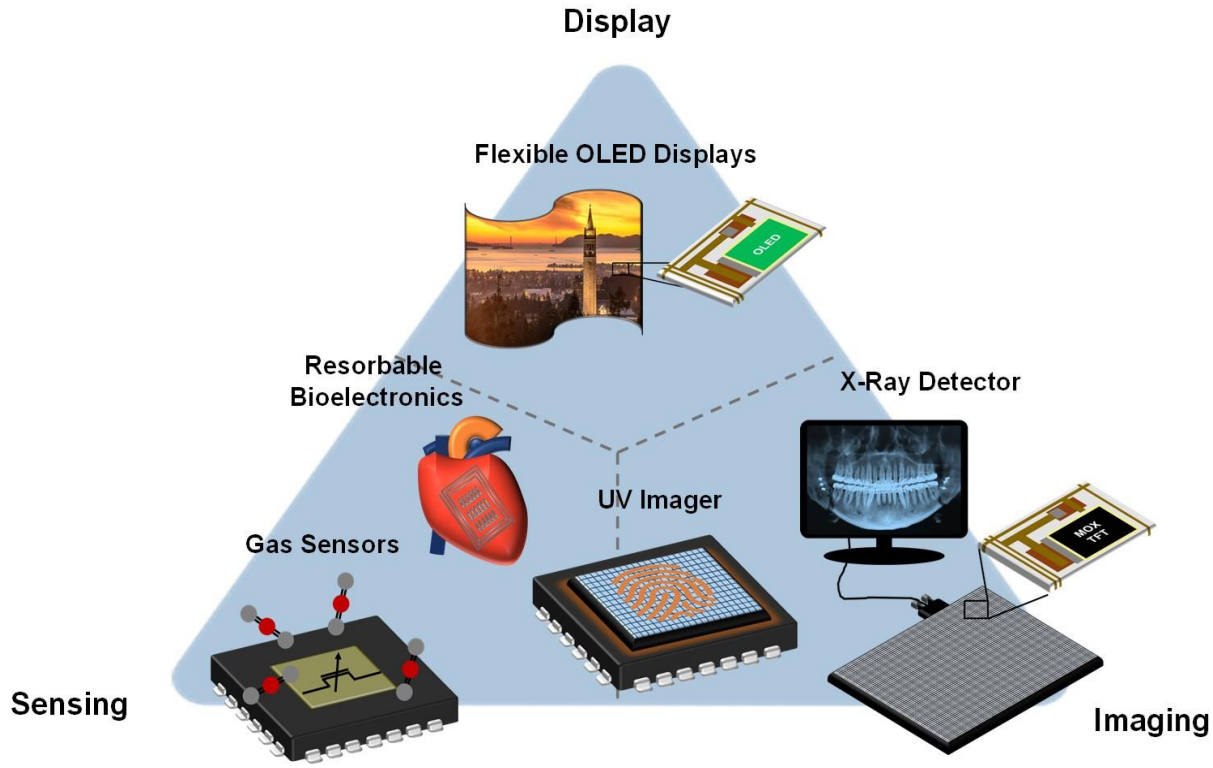


Figure 1.1 Application space of metal oxide transistors, encompassing sensing, display, and imaging.

However, realizing large area flexible electronics consisting of printed metal oxide transistors will require overcoming several challenges in materials design, ink formulation, processing, and integration. A large driving force behind current trends in the metal oxide literature is the incentive to use low-cost plastic substrates that can be conformable and economical for a variety of applications such as wearable medical devices[19]. However, this goal conflicts with the current constraint that high-temperature annealing be employed to achieve high device performance[20] and good reliability. Translating low-temperature annealing strategies to *printed* metal oxide transistors and then exploring the performance of printed transistors under flexion are two critical steps in advancing this field. This thesis will address these issues by developing low-temperature

ink chemistries, low-temperature annealing strategies, and scalable printing on flexible thin glass substrates.

Further integration of high-resolution and high-throughput printing methods will also be essential to advance the state of oxide transistor manufacturing. Developing inks, surface treatments, and device designs for roll-based printing methods can ensure that short channel lengths and high-frequency operation are achievable with metal oxide transistors. Likewise, advances in material integration is needed since the printability of the dielectric and conductor layers lags behind that of the semiconductors, requiring vacuum-processed films which are not comparably scalable. *This thesis will address the materials, printing, and device-level codesign which can deliver high performance reliable metal oxide transistors which are ultimately, fully-printed on flexible substrates.*

### 1.2 Printing Methods for Transparent Electronics

A range of established printing techniques are available for fabricating metal oxide thin films. The choice of printing method has a critical impact on the resolution and performance of printed transistors, as well as the requirements for functional ink design. These tradeoffs require a codesign of materials, devices, and printing. The printing techniques used for metal oxides can be roughly categorized as nozzle-based, serial printing methods, or roller-based, parallel methods. The most common printing methods in both of these categories are summarized in Table 1.1, along with their patterning performance and the requirements for ink formulation.

Table 1.1: Printing Method Characteristics.

| **Method** | **Throughput ($m^2/s$)** | **Resolution (µm)** | **Viscosity (cP)** | **Contact** | **Pattern Carrier Cost** |
|---|---|---|---|---|---|
| Gravure | 1 – 50 | < 5 | $10\text{-}10^3$ | CONTACT | High |
| Screen | 0.1 – 1 | 30 | $500\text{-}10^5$ | CONTACT | Medium |
| Flexography | 1 – 30 | 20 | 50 – 500 | CONTACT | Low |
| Offset | 1-20 | 10 | $100 – 10^5$ | CONTACT | Medium |
| Inkjet | 0.1 – 1 | 20 | $1\text{-}10^2$ | NON-CONTACT | Free (Digital) |
| EHD Jet | < .01 | < 1 | $1\text{-}10^4$ | NON-CONTACT | Free (Digital) |
| Aerosol Jet | < 0.1 | 10 | $1\text{-}10^2$ | NON-CONTACT | Free (Digital) |

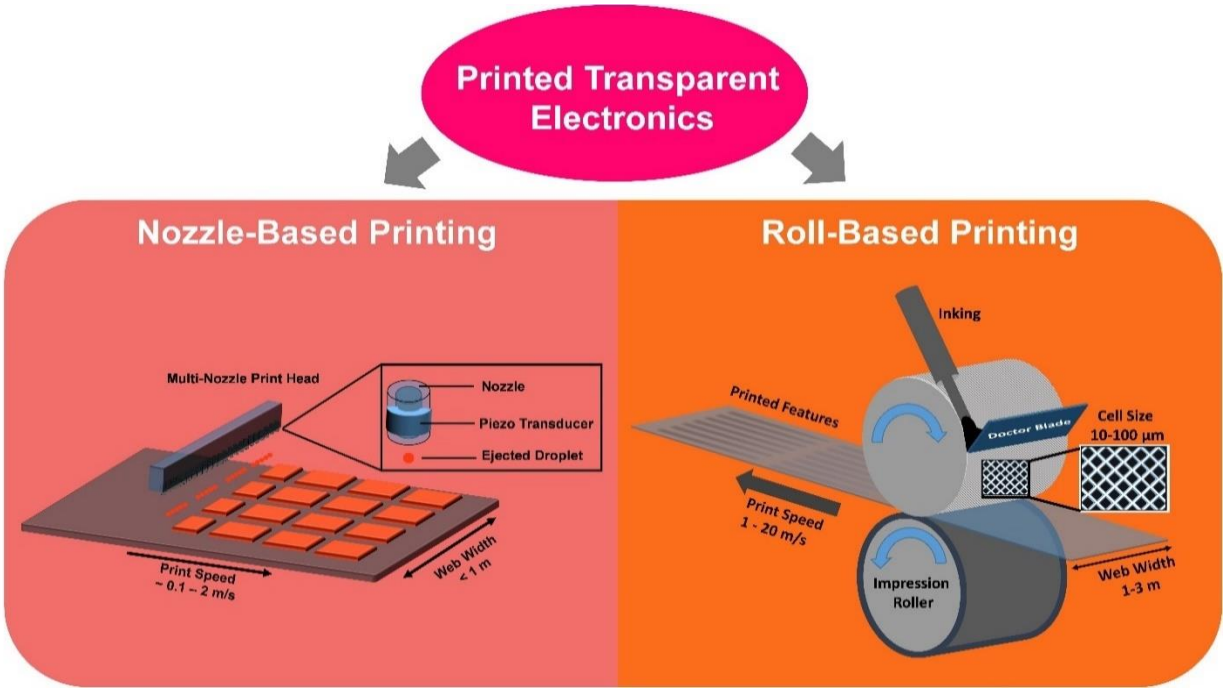


Figure 1.1 Schematic of representative nozzle and roll-based printing processes (left – inkjet, right-gravure) available for printing transparent electronics.

The fundamental difference that separates these categories is that nozzle-based methods dispense material serially in droplets whose size generally scales with the dimension of the nozzle. Scaling the resolution of these printing techniques requires utilizing smaller nozzles and trading off overall throughput, which becomes limited by the need to mechanically raster a print head across large substrates. Roll-based techniques on the other hand, do not experience an intrinsic tradeoff between resolution and throughput because deposition and ink transfer occurs in a parallel fashion. For this reason, roll-based techniques can print on wider webs (> 3m in some cases) and at faster speeds (> 10 m/s) than nozzle-based methods. Figure 1.2 illustrates inkjet printing and gravure printing, two representative examples of these categories. As shown in the schematic, the caveat of the parallel printing methods is that their patterns are physically encoded in rollers or plates, meaning that they cannot typically accommodate the rapid design changes that nozzle based methods (e.g. drop-on-demand inkjet printing) allow. For this reason, parallel-based methods are attractive for high-volume manufacturing of identical components whereas on-demand patterning methods are often well suited for customized production and short print-runs. Additionally, most roll-based patterning methods require contact based ink transfer in contrast to nozzle-based printing which is contactless. This difference has major implications for integrating printed materials and devices on top of variable 3D surface topologies.

Printing processes designed for metal oxide transistors must weigh the throughput and resolution with electronic, system level requirements. High resolution printing is advantageous for scaling down the channel length, as well as enhancing the DPI of active matrix based-displays. However, the resolution requirements are also a function of the individual printed layer. For example, the electrodes of printed transistors have more stringent resolution requirements to give high performance devices. The semiconductor and dielectric, on the other hand, have relaxed resolution

requirements. Printing artifacts such as corner rounding and edge roughness are less impactful for these layers because the feature edges are outside the channel area and contribute only via fringing fields and gate leakage current to the overall operation of the device. One implication of different resolution and thickness requirements for the electrodes, semiconductor, and dielectric layers is that a process consisting of mixed printing techniques could become viable. Lower resolution techniques which excel at highly uniform and reliable film deposition could be attractive options for printing the semiconductors and dielectrics while high resolution techniques would be necessary for the source, drain, and gate layers. Process design tradeoffs such as these require that we develop a more detailed understanding of the thin film transistor structures and ink design.

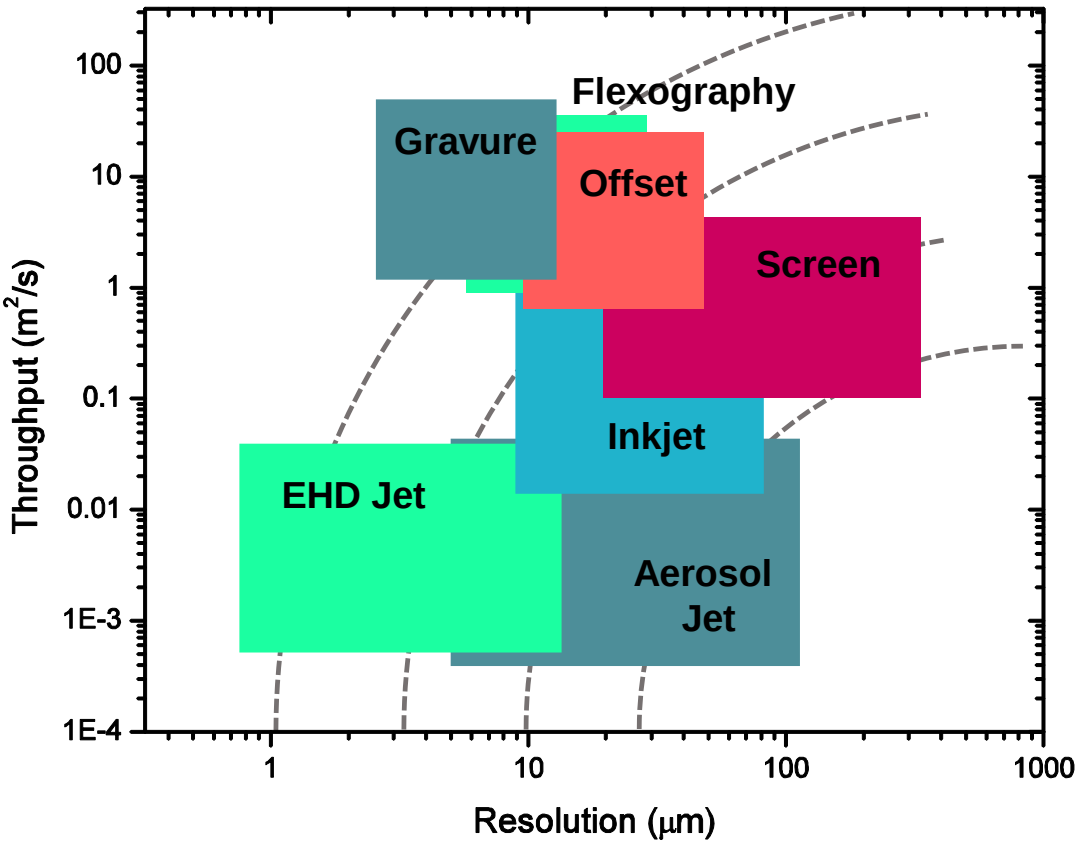


Figure 1.3 Throughput vs resolution for various printing methods. Dashed lines indicate contours qualitatively representing the tradeoff between resolution and throughput.

Previous research on printed metal oxide TFTs has largely focused on inkjet printing, which utilizes piezoelectric drop-on-demand jetting of pL-scale droplets. Inkjet offers a useful platform for material and device development of metal oxide transistors due to its on-the-fly pattern design and accurate layer-to-layer registration. However, scaling printed metal oxides to smaller device dimensions and higher print speeds will require transitioning to high-throughput methods such as gravure, flexography, and reverse offset printing, particularly for the critical dimension conductive layers such as the source / drain electrodes. Figure 1.3 displays these various printing methods in a comparison between manufacturing throughput and resolution. This plot shows the advantages that gravure has over competing methods, since it can print at high resolution *and* high speed. While other printing methods such as aerosol jet and EHD jet can approach the resolution of

gravure printing, they are at least four to five orders of magnitude slower. Low-cost manufacturing and R2R processing will require the exceptional throughput of the roll-based patterning methods which occupy the upper quadrant of the plot. This thesis focuses primarily on the printing physics and materials for gravure-printed transistors to leverage these advantages of gravure.

### 1.2.1 Gravure Printing Process Overview

Gravure printing is a complex process which can be understood as a sequence of fluid mechanical subprocesses: ink filling, doctoring, transfer, and spreading[21]. A diagram of these subprocesses is show below in Figure 1.4 for a R2R implementation of gravure printing. This diagram highlights the major components of gravure printing including the engraved roller which carries the pixelated pattern, the doctor blade which performs the wiping step, and the impression roller which meets the printing cylinder at the *printing nip*. We may consider ink *filling* to be the first step in this process. After ink is deposited on the roller, the ink wets the roller surface and capillary action helps to draw it into the engraved or etched cells that form the pattern on the surface[22]. The excess ink is then wiped from the roller by a stationary doctor blade in close contact with the roller surface. Pressure is applied to the doctor blade to minimize the volume of ink left after *wiping*. Ink *transfer* occurs at the nip as a capillary bridge is formed and then subsequently broken during the separation of the roller from the substrate, leaving one printed droplet per cell on the substrate. Finally, these individual droplets spread to merge and form the desired features. Because gravure is a continuous printing method, the cycle repeats with each subsequent rotation, as additional substrate fed into the system. Each of these subprocesses will be discussed in greater detail in Chapter 4.

The efficiency of each of these steps can be expressed as a fraction, $\varphi$, of the ideal value. The overall printed volume fraction is then expressed as a function of the cell volume and the product of these subprocesses, as shown in Figure 1.4. Previous research on microscale gravure printing has shown that these subprocesses can be modeled as a function of the Capillary Number, *Ca*. *Ca* is a dimensionless constant in fluid mechanics which represents the balance of viscous and surface tension forces. When applied to gravure printing, the Capillary Number summarizes the most important printing (speed) and ink parameters (viscosity, surface tension). Ideal gravure printing occurs when these forces are well balanced, typically in the range of $Ca \sim 1$[21]. Similarly, gravure printing artifacts can be mapped as a function of *Ca*, showing how the print parameters and ink design can optimize feature formation, uniformity, and resolution. Chapters 2-4 of this thesis will leverage this understanding of gravure printing, designing inks and processes to control the *Ca* for individual subprocesses. Additional control parameters such as the surface properties of the substrate and the contact mechanics will be investigated to amend this idealized model of gravure printing and address the specific physics of industrially viable R2R gravure systems.

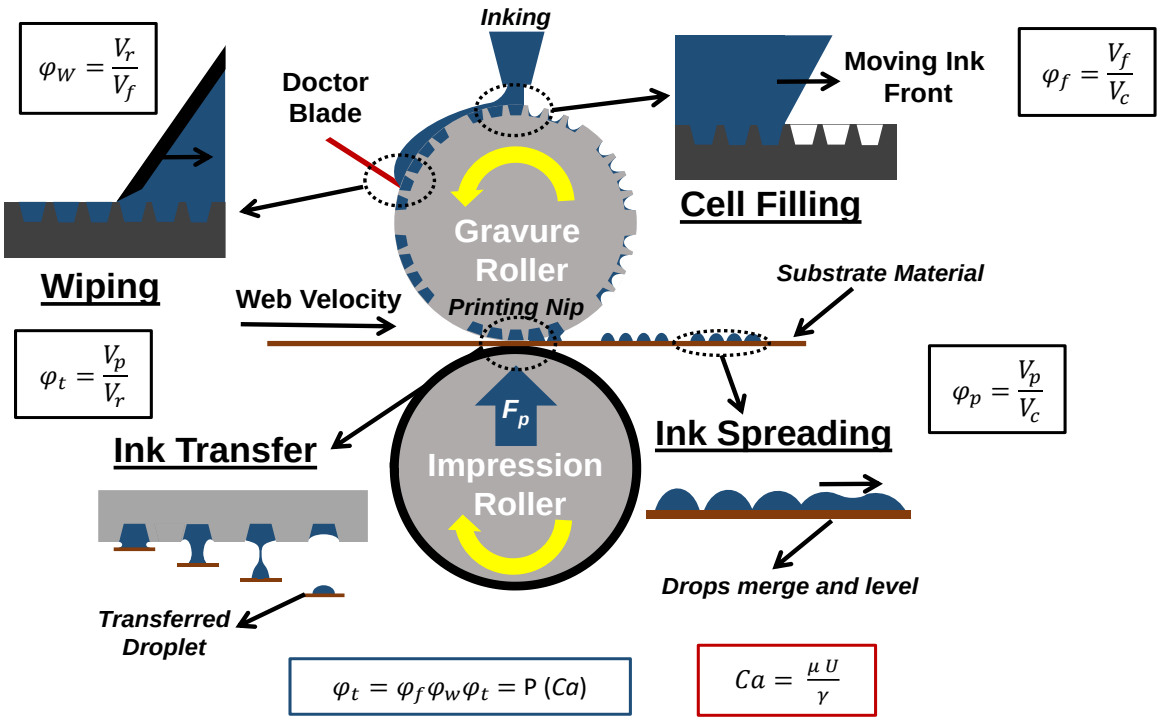


Figure 1.4 Summary of gravure printing subprocesses with overall printing process expressed in terms of the Capillary Number (*Ca*).

### 1.3 Fundamental Fluid Properties of Printed Inks

Intuition into the basic fluid mechanics of printed inks can be developed from a few representative problems in fluid statics and dynamics. These problems represent a variety of the subprocesses which occur during complex, multi-step printing processes. For this reason, fluid characterization begins with understanding how formulations impact fluid behavior in each of these cases. Figures 1.5-1.7 illustrate these three basic problems in fluid mechanics. The first problem (Figure 1.5), known as the *sessile drop*, defines the behavior of the 3-phase contact line between a liquid, solid, and a gas for the case of a drop resting in equilibrium. This problem illustrates the role of surface energies and surface tension. The balance of interfacial forces at the contact line can be expressed in Young's equation, as shown below in Figure 1.5, in terms of the surface energy ($\gamma$) of the respective interfaces ($\gamma_{SL}$: Solid – Liquid, $\gamma_{LV}$ : Liquid – Vapor, $\gamma_{SV}$: Solid – Vapor). This relation predicts that for a given surface, high surface tension liquids ($\gamma_{LV}$) will display higher contact angles. The diagram also illustrates the role of surface tension of a fluid ($\gamma_{LV}$ ) as a force per unit length which drives surface area minimization of fluid. Finally, Young's equation also predicts that a given liquid will have a lower contact angle for higher substrate surface energy. Liquids which have $\theta_c < 90°$ are said to *wet* these substrates. Because water contact angles are often used as a reference point, surfaces which are wetted by water are referred to as *hydrophilic* and surfaces not wetted are *hydrophobic*.

However, this representation of Young's relation describes only the static version of this problem in fluid mechanics. An important distinction must be made between the equilibrium shape of a drop and the dynamic shape of a droplet with a moving contact line. The processes of building and withdrawing a contact line are generally not energetically equivalent. The difference between these two processes results in a different contact angle for advancing contact lines (*spreading out*) vs receding (*contracting*) contact lines. The value of this difference, known as contact angle hysteresis, is a critical parameter for understanding various printing processes such as inkjet and gravure. As Chapter 2 will discuss, there are ways to engineer the contact angle hysteresis of a given ink on a surface to optimize ink transfer and printed film morphology.

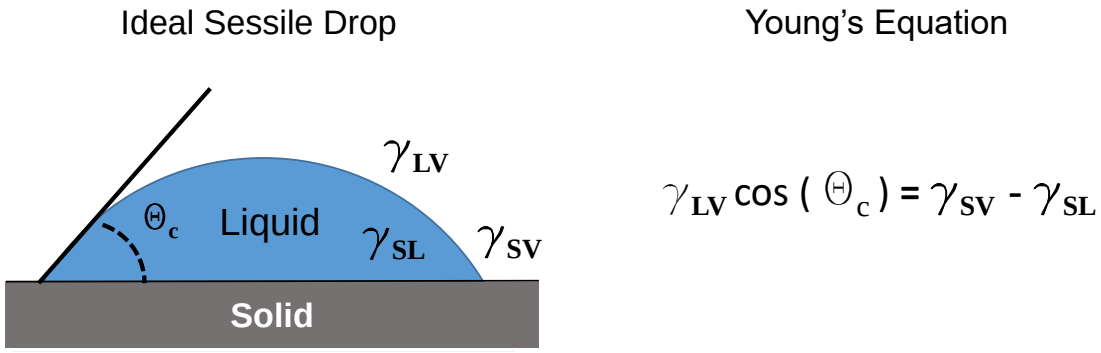


Figure 1.5 Sessile drop diagram with contact angle and Young's equation components defined.

A similar case to the basic sessile drop is that of a capillary bridge between two planar, wetting surfaces. The capillary bridge depicted in Figure 1.6 illustrates the contact lines formed at each surface and the concave shape of the bridging filament which results from the action of the surface tension of a liquid. In most cases, $\theta_1 \neq \theta_2$, for the two surfaces, for example, a printing cylinder and a plastic substrate. Separation of the liquid bridge results in a thinning of the bridge, necessary to conserve the total volume of liquid. In addition to this thinning, the separation of the plates can often cause the motion of the contact lines on either surface. Eventually, the bridge thins to a diameter at which it breaks and each surface is left with a portion of the initial volume. Modeling this behavior is critical to understanding contact-based printing technologies such as gravure printing, which depend on liquid transfer from one solid surface to another. The influence of the individual planar surface energies and the separation speeds on this transfer process will be discussed in Chapter 5.

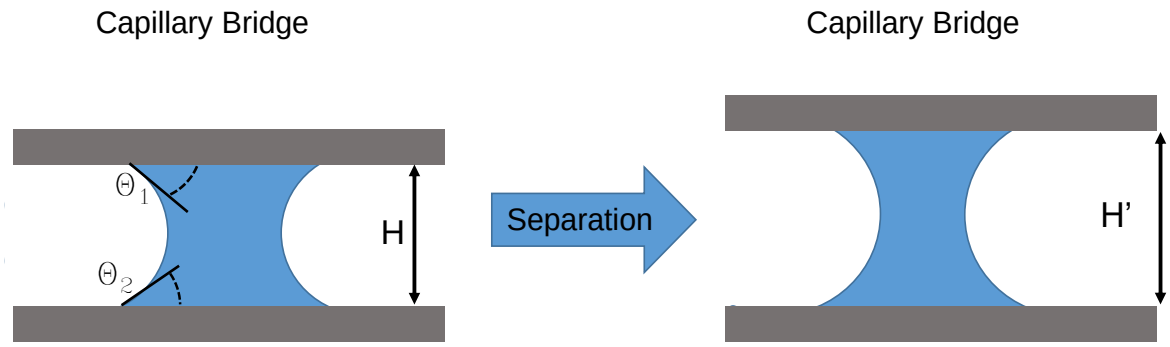


Figure 1.6 Capillary bridge between two planar wetting surfaces undergoing separation.

The second fundamental parameter of printed inks is the viscosity. Viscosity describes the response of the fluid to an applied shear stress. Viscous fluids resist shear stress while inviscid fluids do not. Processes which shear fluids occur frequently in printing technologies which depend on the action of cylinders or blades in contact with a liquid film. Figure 1.7 illustrates planar Couette flow, a third key problem in fluid mechanics. This problem describes the shearing action of a moving solid planar boundary relative to a stationary boundary. The fluid velocity has a linear profile, matching the speed of the respective boundary at each surface. The shear rate ( $\frac{\partial u}{\partial y}$ ) for this case of shear flow is determined by dividing the speed of the moving boundary, *U*, by the thickness of the fluid film, *H*. For *Newtonian* fluids, the viscosity remains constant, giving a linear relationship between shear rate and shear stress. However, many fluids, including some electronic inks, have varying viscosity as a function of the applied shear rate. For example, many inks exhibit shear thinning behavior due to the breakdown of cohesive forces within the fluid at higher shear rates. The shear stress vs shear rate relationship for these inks is depicted in Figure 1.7b, below, alongside a Newtonian fluid with a similar high shear rate viscosity. This rheological

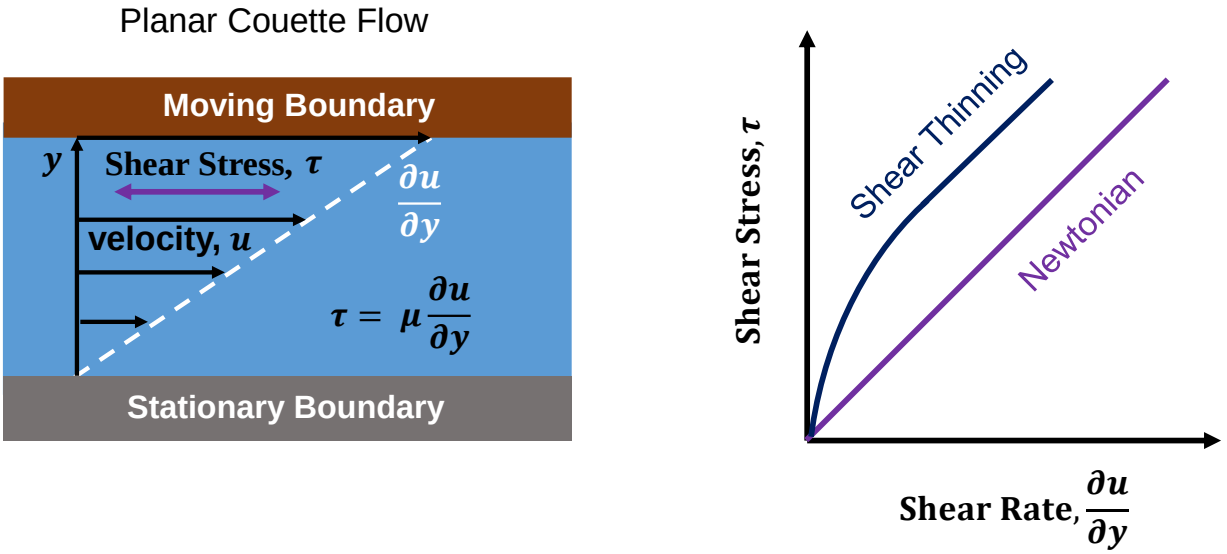


Figure 1.7 Planar Couette flow defining relationship between shear rate, viscosity, and shear stress.

characterization of the viscous response of a fluid to varying rates and patterns of shear stress will be used throughout this thesis to understand various printing processes including gravure and inkjet printing.

### 1.4 Material Design for Printing Metal Oxides

The route to solution-processed metal oxide devices such as thin film transistors includes sequential deposition and conversion of various liquid precursor inks. These precursor inks can be formulated as nanoparticle dispersions or as solutions of metal halide and metal organic sol-gel precursors. In most cases, these chemistries require careful post-treatment annealing steps after deposition to become electronically functional films (conductors, semiconductors, dielectrics, etc). The design of materials for printed metal oxide transistors therefore involves a consideration of the tradeoffs between the electronic performance of the final thin films the required annealing processes, and the printed feature morphology. This thesis will focus primarily on sol-gel-based routes to metal oxide devices, whose potential has been demonstrated extensively in spin-coated systems [27].

Translating ink chemistries to high-resolution printed devices requires an understanding of the relevant printing physics of metal oxide inks. The fluid parameters of inks such as the viscosity and surface tension ensure that the inks can be printed reliably by nozzle or roll-based methods. The main factors in formulation which can control the fluid mechanics are the ink concentration and the solvent composition. High concentration inks also facilitate scalable printing by allowing printing of thick features in a single-pass or using smaller droplet sizes. Similarly, in gravure printing, concentrated, viscous inks reduce spreading and allow the use of smaller cell sizes[25], [26]. Both these cases illustrate the critical link between ink formulation, printing resolution, and, ultimately, printed transistor device performance.

Sol-gel metal oxides are traditionally formed by two step processes involving low-temperature drying followed by high-temperature annealing. At low temperatures, the sol-gel wet film is dried as solvents are removed and the film volume shrinks considerably. This step typically occurs soon after, or during the deposition process, depending on the temperature and atmospheric conditions during printing. The second step of the process occurs at higher temperatures, designed to drive forward the condensation reactions which form the M-O-M network structure of the sol-gel film. These condensation reactions illustrated in Figure 1.8 produce byproducts of water as well as solvent molecules, both of which must be expelled to completely convert and densify the film. Extended high-temperature treatment of the film then results in densification and continued removal of impurities, which is typically associated with a higher dielectric constant and a higher index of refraction, reflections of the higher physical density of the films[27]. Finally, at sufficiently high temperatures, crystallization may also occur by similar mechanisms, driven by the condensation of the M-O-M network[27]. The combination of these different subprocesses is

responsible for transforming a printed film to a functional thin film in a TFT, and optimization of the individual steps is often necessary for each particular sol-gel ink.

With a few notable exceptions, printed metal oxide transistors have been fabricated using sol-gel-based metal oxides rather than metal oxide nanoparticles. In some cases, nanoparticle systems offer significant advantages in terms of their low-temperature processability and crystallinity because their synthesis step is decoupled from film deposition[28]. However, the resulting performance of nanoparticle-based metal oxide devices has remained lower than sol-gel systems, even at low processing temperatures around 200 °C[29]. Figure 1.9 shows these two classes of materials, highlighting the crystallinity of metal oxide nanoparticles, the porous structure of printed nanoparticle films, and dense structure of sol-gel films. For ceramic nanoparticles composed of metal oxides, interparticle sintering and coalescence is not observed at such low-

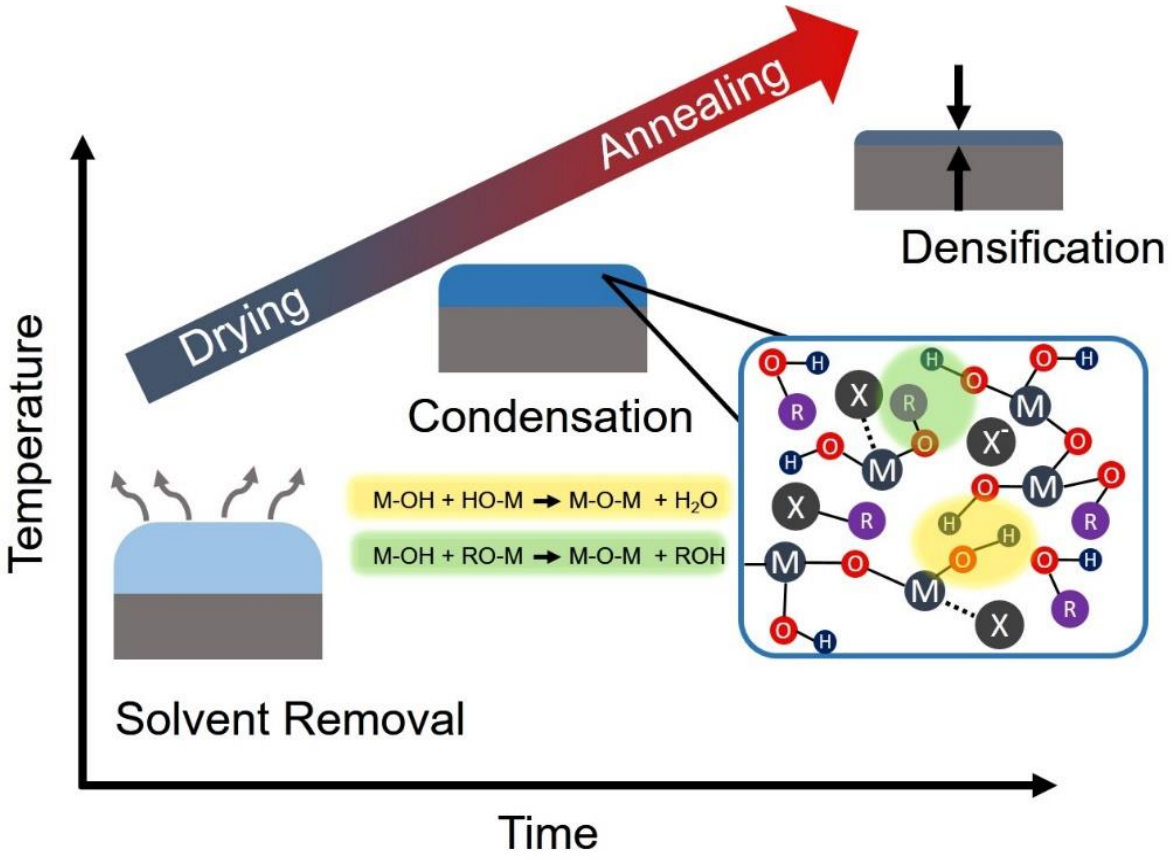


Figure 1.8 Sol-gel film formation process, including film drying, condensation reactions, and film densification.

temperatures, resulting in poor percolative transport[30], [31]. Another critical issue is the relative lack of printed rather than printable formulations of metal oxide nanoparticles. At this time, there have been only a limited number of demonstrations of metal oxide devices which, in fact, printed the metal oxide nanoparticle layers[29], [32], [33] rather than spin-coating them. Further development and optimization of metal oxide nanoparticles aimed at transistor applications must address the material and device integration issues which are unique to multilayer printed devices, such as enhancing the adhesion and mechanical stability of metal oxide nanoparticle thin films.

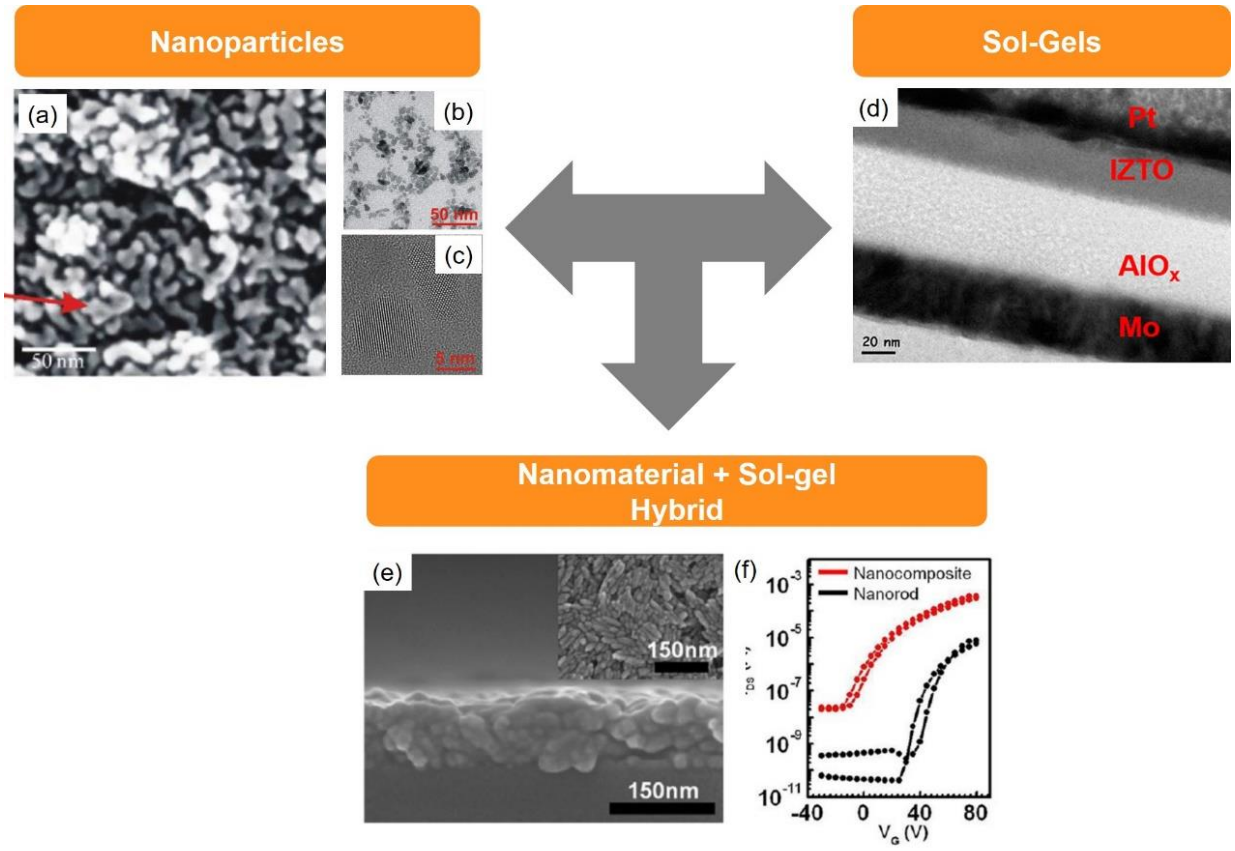


Figure 1.9: Illustration of metal oxide ink precursors such as nanoparticles (a,b,c) [32,33], sol-gels (d) [30], and nanomaterial sol-gel hybrids (e,f) [30].

A promising alternative to the sole use of sol-gel or nanoparticle inks is a hybrid approach which utilizes the strengths of both material systems. A hybrid ink consisting of nanomaterials and sol-gels has the potential to achieve high performance semiconductors and conductors at low-temperatures (< 150 °C), using the sol-gel as a functional binder which improves the film density and enhances transport [30]. The result of using this strategy are shown above in Figure 1.9, for a zinc oxide nanocomposite spin-coated film processed at 150 °C[30]. Application of hybrid inks to printed metal oxide transistors could be an important step in fabricating conductors and channel materials at plastic-compatible temperatures without sacrificing performance. An important step in enabling this will be advancing ink chemistries which allow one-step deposition of hybrid films rather than sequential coating and alignment of nanomaterial and sol-gel layers[34]. Chapter 3 will leverage these principles of hybrid ink design to develop high performance printed transparent conductors which are processed at low temperatures and printed on plastic substrates.

### 1.5 Printed Film Morphology Control

Printed film morphology control is essential for achieving high device yield and optimal TFT performance. The final film morphology is controlled by physicochemical properties of the ink and substrate, as well as the printing physics associated with the particular deposition process.

From a device physics perspective, thickness uniformity is the primary concern, since layer thicknesses of the semiconductor and dielectric determine nearly all of the critical electrostatics in a thin film transistor. Because of this, the uniformity of printed layers across an entire substrate is essential for controlling the variability of printed device parameters, such as threshold voltage, off-state current, and mobility. Active matrix arrays of TFTs require a high-degree of uniformity in these various performance parameters to deliver applications such as displays and imaging systems in which the human eye can perceive differences in brightness below 2% contrast[35]. Thus, the study of the printing physics which govern film morphology is critical. This thesis will demonstrate methods for controlling the film morphology which are compatible with printed transistor architectures and enhance the uniformity of gravure and inkjet-printed features.

### 1.6 Thin Film Transistor Structure & Integration

Metal oxide TFTs are four layer devices which are comprised of conductors, dielectrics, and semiconductors. As shown in Figure 1.10, the variants of the thin film transistor structure include top-gate and bottom-gate varieties with staggered or coplanar contacts. The choice of a particular TFT structure is informed by the material and printing requirements, as well as compatibility with other components, such as sensors or light emitting devices (OLEDS, photodiodes, etc). TFT structures which are customarily used for sputtered and lithographically patterned thin film transistors may not necessarily be optimal, let alone viable for printed transistors because of the need for chemical compatibility during wet-processing steps and the limitations to printed materials' electronic properties. A prime example which illustrates the material compatibility constraint is the case of printed ZnO. Nearly all printed transistors incorporating Zn precursors into the channel material have used InZnO or ZnSnOx alloys rather than pure ZnO because ZnO has extremely weak etch resistance. The consequence of weak etch resistance is that ZnO channels usually cannot be used in any configuration *except* the coplanar top gate structure, because printed source/drain material or dielectrics on top of the ZnO cause etching and degradation. Many works avoid this issue by depositing contacts using thermal evaporation, but this nullifies the benefits of using high-throughput printing processes to achieve cost reduction and large area scaling.

In many ways, the process design challenge of printed metal oxide TFTs resembles that of organic transistors, which must be designed with overlapping layers deposited via orthogonal solvents. However, in the case of metal oxides, underlying films must resist etching by acidic sol-gel inks throughout printing and ink drying processes. This etch resistance is found in some, but not all metal oxide semiconductors, conductors, and dielectrics. Without the etch resistance, the deposited film stoichiometry and the underlying films can undergo intermixing, which may be worsened by diffusion during extended high temperature annealing. For example, depositing a dielectric on a slightly soluble gate electrode could result in the presence of high concentrations (> 1 %) of the solubilized impurity (Sn, In, etc). In some cases, metal oxide films are relatively unaffected by these extrinsic impurities due to their extremely high intrinsic defect concentrations[36], but in other cases the impurities can be detrimental to electrical performance or stability. Thus, these features of printed TFTs suggest that significant material, printing, and device-level codesign are necessary to achieve high performance reliable devices which are ultimately, fully-printed.

## 1.7 Scaling Printed Oxide TFT Dimensions

High-resolution, high-throughput roll-based printing methods can allow scaling of critical device dimensions in printed transistors while improving manufacturing throughput. As discussed in

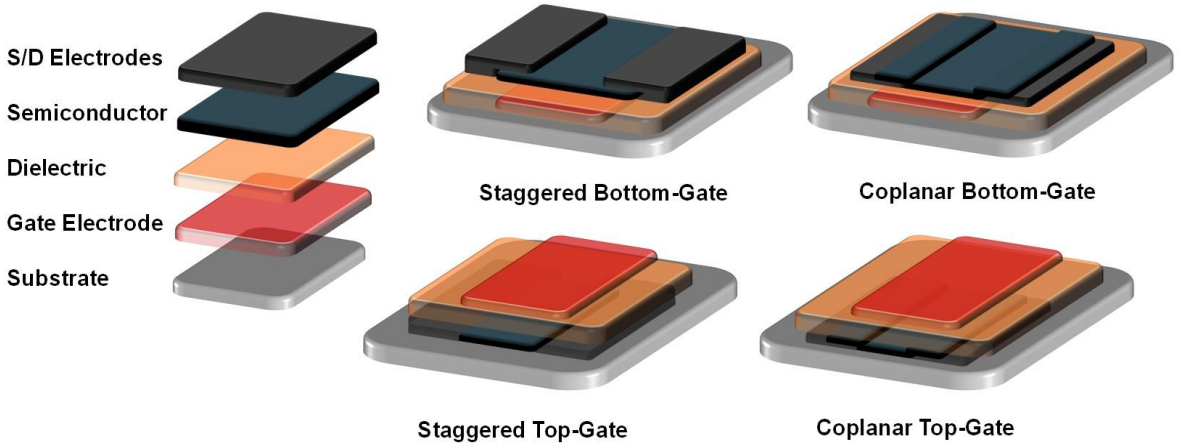


Figure 1.10 Printed transistor layer structures for bottom gate and top-gate devices with staggered and coplanar configurations, as indicated.

Section 2.1 above, method such as gravure printing and flexography are well-suited to printing fine features at high speeds. This capability can be a powerful tool in improving the switching performance of printed transistors, which benefits from scaling down the channel length, reducing parasitic overlap capacitance[25], and increasing the device density. These advances will ensure that printed oxide transistors can satisfy even demanding thin film applications such as high end displays with high numbers of pixels-per-inch (PPI) and increased brightness. Additionally, applications such as radio-frequency identification (RFID) tags which require high AC-switching performance at MHz frequencies will necessitate high-resolution patterning to improve transconductance and reduce the parasitic capacitances of printed devices.

The electrode layers including the gate and source-drain stand to benefit the most from the use of high-resolution printing technologies because the electrode patterns determine the critical lateral dimensions of thin film transistors, as well as the overlap areas. Methods such as gravure and reverse-offset printing have been used quite successfully in the printing of organic transistors with short channel lengths below 5 μm[26], [37], but these methods have seen limited application in printing metal oxides[24], [38]. The development of high concentration precursor inks which allow precise spreading control and mitigate low-viscosity printing artifacts will be a first step towards developing gravure and offset-printed metal oxide electronics. High-concentration inks are also needed in order to print high-resolution features while maintaining a suitable film thickness, because the deposited ink thickness typically scales down with the feature size in roller-based techniques. These demands may call for new ink chemistries and precursors which differ from inkjet printed or spin-coated formulations.

Self-alignment strategies offer an alternative route to fabricating short channel length devices, as recently demonstrated by Li, et al[39]. These processes use dewetting processes to align printed electrodes to a fluoropolymer template consisting of pairs of fine lines formed by the coffee-ring effect. Controlling the coffee-ring defined template led to printed $InO_x$ transistors with printed ITO electrodes and channel lengths below 5 µm, the lowest to-date for printed metal oxide transistors. However, these positive results also illustrated a key challenge, which is achieving short channel devices which are not limited by contact effects.

Finally, a key challenge specific to this material system is adapting roll-based printing techniques to print on rigid substrates such as glass which can accommodate the higher temperatures (400 – 600 °C) typically used to process printed metal oxides. Flexible glass substrates[24] or flexible high-temperature-compatible polyimide substrates can solve the issue by conforming to roller imperfections and accommodating the bending stresses inherent to R2R processing, but low-temperature-processable materials which are compatible with transparent plastics such as polyethylene naphthalate are favored due to their lower cost and extensive use in the packaging industry. However, as discussed below in section 1.8.1, the use of lower-process temperatures often involves an inevitable tradeoff with device performance and reliability. Thus, again we see that the printing process depends closely on a codesign with the precursor materials and annealing post-processes.

## 1.8 Developing Materials for Transparent Transistors

### 1.8.1 Printed Metal Oxide Semiconductors

A principle goal for the work in this thesis, as well as the field of printed metal oxides in general, has been to scale down processing temperatures to become compatible with various flexible polyester substrates such as polyethylene naphthalate (PEN) and polyethylene terephthalate (PET). The low-cost and high transparency of these plastic substrates make them well-suited to many large scale applications of printed electronics. However, the thermal budget required to utilize these substrates is in the range of 100 °C – 200 °C, well below the temperatures used to process the various conductors, semiconductors, and dielectrics that are necessary for printing thin film metal oxide transistors. Printed metal oxide transistors have typically been fabricated using high temperature annealing in the range of 300 °C – 500 °C, which has required the use of rigid substrates such as display glass or silicon wafers. As Figure 1.11 illustrates below, there is a clear tradeoff between the performance of printed semiconductor channel materials and the maximum processing temperature that is used. Most of the highest performance devices which report mobility over 5 $cm^2/Vs$ have utilized temperatures above 300 °C. As several authors have shown, the thermal budget chosen for these processes is closely connected to the need to decompose and volatilize[40], [41] precursor species and induce the condensation reactions[42], [43] which form a network of M-O-M bonds within the film.

Incomplete conversion at low-temperatures (below 250 °C) on the other hand, results in low electrical performance[41] as well as large fractions of M-OH signal in XPS and FTIR measurements[41], [44], [45] and poor long-term operational device stability[36]. As a result of these issues, there have been very few demonstrations of printed metal oxide transistors at PEN or PET compatible temperatures, as highlighted in Figure 1.11 below.

The significant effects of channel layer composition are also highlighted in Figure 1.11. Indium-containing compounds make up a large fraction of the low-temperature processed, printed semiconductors with high-mobility, particularly for low-temperature processed devices. Indium Gallium Zinc Oxide (IGZO), in particular, is a popular channel material due to its amorphous

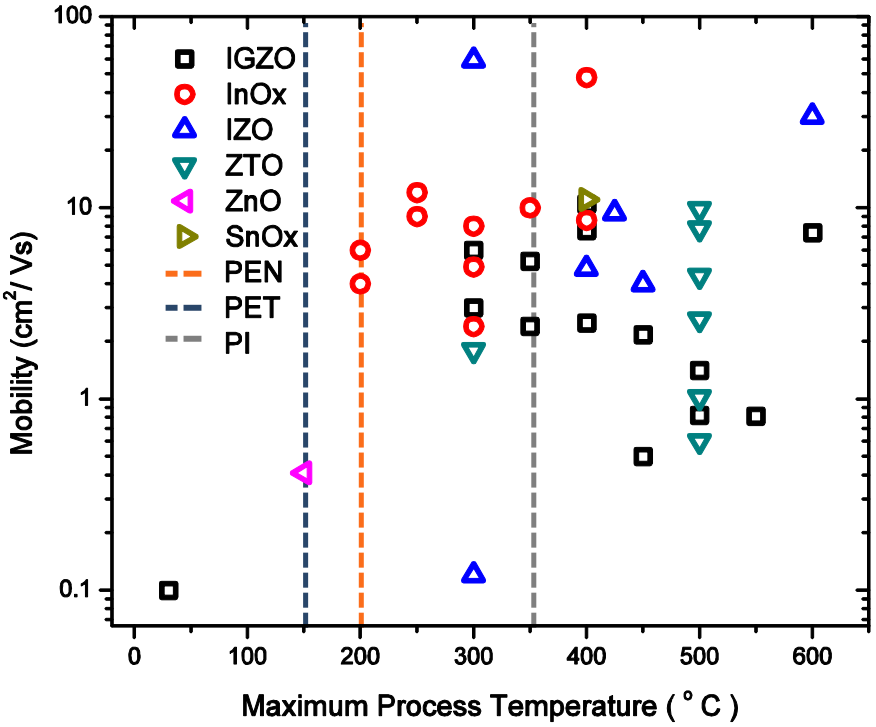


Figure 1.11 Field-effect mobility vs maximum process temperature for printed transistors of various channel materials. Processing window for flexible plastic substrates is indicated with dotted vertical lines.

nature and high operational stability, but there remains a lack of low-temperature processed printed IGZO devices. Tin and zinc-based channel compositions which exclude indium generally require higher temperatures (400 - 500 °C) to achieve good performance. While spin-coated ZnO based devices have shown higher performance at low temperatures[46], these methods have not yet been translated to printed inks and TFTs with multiple printed layers. Processing methods and ink design which can boost the performance of indium-free semiconductors will be important if the field looks to address the high cost and scarcity of indium for long-term scalability. This will also have to include solutions to the weak chemical stability and solubility of ZnO films which preclude their use in many multilayer transistor structures.

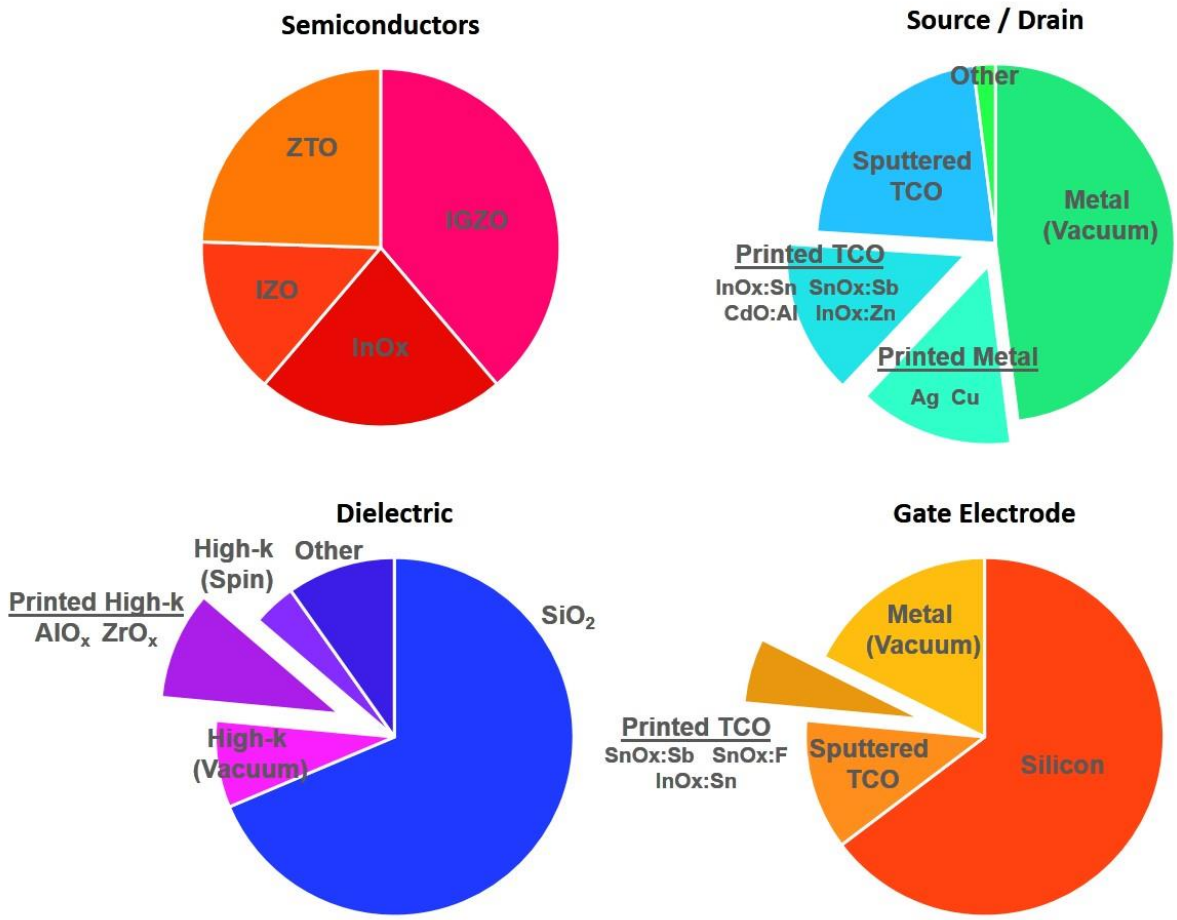


Figure 1.12 Material composition of each layer in various printed transistors demonstrated in literature, to-date. Separated slices in the source / drain, dielectric, and gate charts indicate that these demonstrations were printed.

### 1.8.2 Printed Electrodes for Metal Oxide TFTs

Important progress has also been made in addressing the need for printed electrodes suitable for printed metal oxide transistors. As shown in Figure 1.12, the vast majority of printed metal oxide transistors reported in the literature have utilized vacuum-deposited source and drain electrodes composed of metals such as aluminum or sputtered TCOs such as ITO. R2R scalable processing of these devices requires electrode materials which can be printed by comparable techniques to the semiconductor layers, otherwise the benefits of printing are sharply reduced or eliminated. While there have been a few successful demonstrations of printed Ag or Cu electrodes for metal oxide transistors[38], [47], [48], these works highlight device-stability related issues[49] associated with the rapid diffusion of Ag and Cu metal into the oxide thin films. Because this diffusion is accelerated by the applied electric field as well as any subsequent thermal annealing, the integration of Cu and Ag into any structure but staggered bottom-gate devices has been unsuccessful. The alternative materials which have been pursued include graphene-based conductors[50] and TCO contacts[39], [51], [52], which show improved thermal and chemical

stability during device annealing steps, as well as higher transparency. Printed transparent conductors offer the possibility of fully-transparent devices[52] which can be used advantageously in various optoelectronic applications, for example, to improve the pixel aperture ratio in emissive display technologies[53]. However, developing low-temperature compatible inks for printed electrode deposition remains a challenge and most demonstrations[50] have required high temperature (> 300 °C) annealing to ensure adequate conductivity and low contact-resistance. Indeed, the process temperatures used for TCO metal oxide contact materials have lagged further behind the temperatures used for semiconductors and dielectrics, suggesting that these components may be the limiting factor in whether printed metal oxide devices can be integrated on flexible plastic substrates. Chapter 5 will address this need for printed metal oxide conductors that are suitable as printed transistor electrodes.

### 1.8.3 Printed Dielectrics for Metal Oxide TFTs

The gate dielectric is a critical element of all thin film transistors. The performance of solution-processed metal oxide transistors is particularly sensitive to the choice of dielectric material, the processing conditions, and the film morphology. Devices with solution-processed high-k dielectrics show significant enhancements in mobility and peak transconductance, particularly for low-temperature processed systems[54]. However, as shown above in Figure 1.12, most of the work on printed oxide transistors has utilized vacuum deposited silicon dioxide gate dielectrics or spin coated high-k dielectrics. Of the few successful demonstrations of oxide transistors with printed dielectrics, nearly all have utilized printed $ZrO_x$ films[52], [55], [56]. In these cases, the high dielectric constant of $ZrO_x$ ($\varepsilon_r \sim 15 - 23$) allowed low-voltage operation even for moderately thick dielectrics (45-60nm) with leakage currents below $10^{-6}$ A/cm$^2$. These methods used annealing at temperatures from 300 °C – 500 °C to convert the dielectric films and reduce low-frequency dispersion. Alternative dielectric inks have utilized chemistries based on silicon sol-gels (polymethylsilsequioxane) or on hybrids of dielectric nanosheets ($Ca_2Nb_3O_{10}$) mixed with polymethylmethacrylate (PMMA) to form insulating layers at plastic compatible temperatures below 150 °C. However, the performance of transistors fabricated using these low-temperature dielectrics has remained lower than control devices constructed on $SiO_2$ dielectrics, and considerable hysteresis was observed in the transfer characteristics[57]. The formulation and printing of high-quality dielectrics at low processing temperatures remains an important challenge in this field which must be overcome to accomplish full printing integration of flexible transparent electronics. This motivates the work presented in Chapter 6 of this thesis, which will develop printed high-k dielectrics which are processable at low-temperatures using UV-annealing.

### 1.8.4 Printing Metal Oxide Transistors on Flexible Substrates

Various strategies are available to reduce the processing temperatures used in solution-processed metal oxide transistors to achieve compatibility with flexible plastic substrates. Modifications to the ink design and use of alternative annealing methods have been successfully used lowered the processing temperature of some spin-coated metal oxides to below the threshold for plastics including PEN[58], polyarylite[42] and Polyimide[59]. Low-temperature ink design for spin-coated transistors has utilized two primary strategies: self-combustion ink chemistries[40] and aqueous inks[60]. Combustion inks incorporate an oxidizer (e.g. the nitrate sol-gel precursor anion) and a fuel (e.g. acetylacetone, urea, etc) which display abrupt decomposition exotherms once ignited at low temperatures in the range of 150 °C – 250 °C, facilitating the formation of

high-mobility thin films which exceed the performance of inks processed in organic solvents without combustion precursor chemistries[30]. The approach has successfully been applied to various metal oxide semiconductors (IGZO[61], IZO[40], ZnO[30], ZTO, InOx[40], etc), as well as conductors (ITO[30]) and dielectrics. Alternately, aqueous, carbon-free ink chemistries based on metal nitrate precursors also display low-temperature decomposition and few residual impurities when processed at 150 - 250 °C. Pushing process temperatures even lower can also be achieved with alternative annealing strategies such as ultraviolet annealing or intense pulsed white light (IPWL) annealing. These photochemical strategies[42] use light to enable conversion of sol-gel precursors to metal oxide films at low temperatures (often below 150 °C). Complexes formed between sol-gel precursors and organic solvents absorb high energy UV photons, promoting densification and polycondensation reactions.

However, these novel ink designs and annealing strategies have for the most part not yet been extended to printed systems. Adapting low-temperature materials and processing for printing which were originally developed for spin-coating will require greater knowledge of critical impact of factors such as precursor concentration, drying rate, and solvent composition. The additional layer of requirements for printability, pattern fidelity, coffee-ring control, and film uniformity offer a challenging set of constraints which will need to be investigated for these low-temperature systems. Solving these issues will ensure that the success demonstrated with printing devices on high-temperature rigid substrates can be extended to low-temperature processed flexible systems. This thesis aims to answer questions about these tradeoffs between the performance, processing temperatures, and the amenability of these materials to high-resolution additive patterning by R2R-compatible methods.

### 1.9 Thesis Organization

This thesis develops materials and methods for printing metal oxide thin film transistors. The overarching goals of this work are to enable scalable fabrication by developing gravure printing and low-temperature processing of these devices. The approach taken in this work is to start by understanding the cooperative design of materials, devices, and printing processes, as illustrated below in Figure 1.13. By mapping out the physical links between ink design and functional material properties, high-performing printed metal oxide are fabricated.

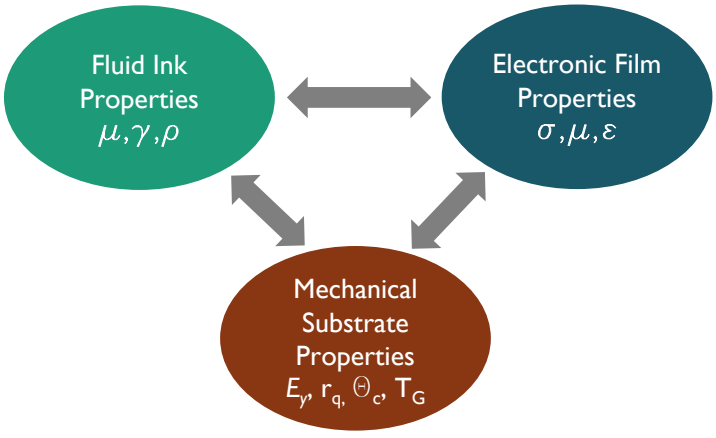


Figure 1.13 Diagram of the codesign of ink fluid properties, functional electronic properties, and thermomechanical substrate limitations.

Chapter 2 explores the design of metal oxide inks for patterning high-resolution transparent electrodes suitable for printed metal oxide TFTs. The contact mechanics of printing on flexible glass substrates and the influence of ink design on feature formation are investigated, as well as the tradeoffs between printability and material properties such as conductivity, crystallinity, and transparency. Chapter 3 addresses these limitations of gravure-printed transparent conductors by developing hybrid materials consisting of metal oxides and 1D silver nanowires. The integration of these materials results in enhancements to the electronic properties and thermomechanical stability, as well as advantages in low-temperature processing of transparent electrodes.

Chapter 4 presents the design and testing of a new laboratory scale tool for the experimental investigation of gravure printing physics at a subprocess level. This tool allows the study of the influence of transfer contact mechanics on the formation of mesoscale dragout printing artifacts.

In Chapter 5, aqueous ink chemistries are developed to address the limitations of conventional sol-gel metal oxide inks revealed in Chapter 2 and Chapter 3. The intrinsic aqueous fluid properties lead to enhanced printing fidelity, high electrical performance, and better ambient stability than the conventional organic-solvent-based sol-gel inks. Degenerately-doped transparent conductors (CdO:Al) are developed as a low contact-resistance inkjet-printed electrode for high-performance printed $InO_x$ thin film transistors processed at low temperatures. Chapter 6 builds on this low-temperature-processable material set by developing R2R-compatible ultraviolet (UV)-annealing methods and printed high-k dielectrics for fully-printed metal oxide transistors. The impact of UV-annealing on printed device performance and long-term bias-stress stability are investigated to understand links between ink chemistry, annealing, and device design.

Finally, Chapter 7 offers future research directions to address the key remaining challenges for scalable printed metal oxide transistors. New tooling and printing methods are suggested to address the manufacturing issues that limit the viability of high-speed gravure printing of inorganic printed electronics. Finally, promising system-level integration of these devices is considered and routes to these applications are discussed.

## 1.10 References


[1] K. Chen *et al.*, "Printed Carbon Nanotube Electronics and Sensor Systems," *Adv. Mater.*, vol. 28, no. 22, pp. 4397–4414, Jun. 2016.

[2] R. A. Street, "Thin-Film Transistors," *Adv. Mater.*, vol. 21, no. 20, pp. 2007–2022, May 2009.

[3] J. F. Wager, B. Yeh, R. L. Hoffman, and D. A. Keszler, "An amorphous oxide semiconductor thin-film transistor route to oxide electronics," *Curr. Opin. Solid State Mater. Sci.*, vol. 18, no. 2, pp. 53–61, Apr. 2014.

[4] K. Fukuda and T. Someya, "Recent Progress in the Development of Printed Thin-Film Transistors and Circuits with High-Resolution Printing Technology," *Adv. Mater.*, p. n/a-n/a, Nov. 2016.

[5] H. Kumomi, T. Kamiya, and H. Hosono, "(Invited) Advances in Oxide Thin-Film Transistors in Recent Decade and Their Future," *ECS Trans.*, vol. 67, no. 1, pp. 3–8, May 2015.

[6] "Flexible full color organic light-emitting diode display on polyimide plastic substrate driven by amorphous indium gallium zinc oxide thin-film transistors," *Appl. Phys. Lett.*, vol. 95, no. 1, p. 013503, Jul. 2009.
[7] E. Fortunato, D. Ginley, H. Hosono, and D. C. Paine, "Transparent Conducting Oxides for Photovoltaics," *MRS Bull.*, vol. 32, no. 03, pp. 242–247, Mar. 2007.
[8] K.-H. Choi *et al.*, "Characteristics of flexible indium tin oxide electrode grown by continuous roll-to-roll sputtering process for flexible organic solar cells," *Sol. Energy Mater. Sol. Cells*, vol. 93, no. 8, pp. 1248–1255, Aug. 2009.
[9] K. Zilberberg, J. Meyer, and T. Riedl, "Solution processed metal-oxides for organic electronic devices," *J. Mater. Chem. C*, vol. 1, no. 32, pp. 4796–4815, Jul. 2013.
[10] S. J. Chang *et al.*, "Highly reliable nitride-based LEDs with SPS+ITO upper contacts," *IEEE J. Quantum Electron.*, vol. 39, no. 11, pp. 1439–1443, Nov. 2003.
[11] "Nitride-based light emitting diodes with indium tin oxide electrode patterned by imprint lithography," *Appl. Phys. Lett.*, vol. 91, no. 1, p. 013504, Jul. 2007.
[12] J. Kim *et al.*, "Ultrahigh Detective Heterogeneous Photosensor Arrays with In-Pixel Signal Boosting Capability for Large-Area and Skin-Compatible Electronics," *Adv. Mater.*, vol. 28, no. 16, pp. 3078–3086, Apr. 2016.
[13] J. I. Ramirez *et al.*, "Radiation-Hard ZnO Thin Film Transistors," *IEEE Trans. Nucl. Sci.*, vol. 62, no. 3, pp. 1399–1404, Jun. 2015.
[14] R. Latz, K. Michael, and M. Scherer, "High Conducting Large Area Indium Tin Oxide Electrodes for Displays Prepared by DC Magnetron Sputtering," *Jpn. J. Appl. Phys.*, vol. 30, no. 2A, p. L149, Feb. 1991.
[15] R. A. Lujan and R. A. Street, "Flexible X-Ray Detector Array Fabricated With Oxide Thin-Film Transistors," *IEEE Electron Device Lett.*, vol. 33, no. 5, pp. 688–690, May 2012.
[16] H. E. Martz, C. M. Logan, D. J. Schneberk, and P. J. Shull, *X-Ray Imaging: Fundamentals, Industrial Techniques and Applications*. CRC Press, 2016.
[17] S. H. Jin *et al.*, "Water-Soluble Thin Film Transistors and Circuits Based on Amorphous Indium–Gallium–Zinc Oxide," *ACS Appl. Mater. Interfaces*, vol. 7, no. 15, pp. 8268–8274, Apr. 2015.
[18] "Room-temperature-operated sensitive hybrid gas sensor based on amorphous indium gallium zinc oxide thin-film transistors," *Appl. Phys. Lett.*, vol. 98, no. 25, p. 253503, Jun. 2011.
[19] Y. Khan, A. E. Ostfeld, C. M. Lochner, A. Pierre, and A. C. Arias, "Monitoring of Vital Signs with Flexible and Wearable Medical Devices," *Adv. Mater.*, vol. 28, no. 22, pp. 4373–4395, Jun. 2016.
[20] C.-H. Choi, L.-Y. Lin, C.-C. Cheng, and C. Chang, "Printed Oxide Thin Film Transistors: A Mini Review," *ECS J. Solid State Sci. Technol.*, vol. 4, no. 4, pp. P3044–P3051, Jan. 2015.
[21] R. Kitsomboonloha, S. J. S. Morris, X. Rong, and V. Subramanian, "Femtoliter-Scale Patterning by High-Speed, Highly Scaled Inverse Gravure Printing," *Langmuir*, vol. 28, no. 48, pp. 16711–16723, Dec. 2012.
[22] J. Cen, R. Kitsomboonloha, and V. Subramanian, "Cell Filling in Gravure Printing for Printed Electronics," *Langmuir*, vol. 30, no. 45, pp. 13716–13726, Nov. 2014.
[23] J. Leppäniemi, K. Eiroma, H. Majumdar, and A. Alastalo, "Far-UV Annealed Inkjet-Printed In2O3 Semiconductor Layers for Thin-Film Transistors on a Flexible Polyethylene Naphthalate Substrate," *ACS Appl. Mater. Interfaces*, vol. 9, no. 10, pp. 8774–8782, Mar. 2017.
[24] W. J. Scheideler, J. Jang, M. A. U. Karim, R. Kitsomboonloha, A. Zeumault, and V. Subramanian, "Gravure-Printed Sol–Gels on Flexible Glass: A Scalable Route to Additively

Patterned Transparent Conductors," *ACS Appl. Mater. Interfaces*, vol. 7, no. 23, pp. 12679–12687, Jun. 2015.
[25] R. Kitsomboonloha, H. Kang, G. Grau, W. Scheideler, and V. Subramanian, "MHz-Range Fully Printed High-Performance Thin-Film Transistors by Using High-Resolution Gravure-Printed Lines," *Adv. Electron. Mater.*, vol. 1, no. 12, p. n/a-n/a, Dec. 2015.
[26] H. Kang, R. Kitsomboonloha, J. Jang, and V. Subramanian, "High-Performance Printed Transistors Realized Using Femtoliter Gravure-Printed Sub-10 μm Metallic Nanoparticle Patterns and Highly Uniform Polymer Dielectric and Semiconductor Layers," *Adv. Mater.*, vol. 24, no. 22, pp. 3065–3069, Jun. 2012.
[27] J. H. Park *et al.*, "Low-Temperature, High-Performance Solution-Processed Thin-Film Transistors with Peroxo-Zirconium Oxide Dielectric," *ACS Appl. Mater. Interfaces*, vol. 5, no. 2, pp. 410–417, Jan. 2013.
[28] S. L. Swisher, S. K. Volkman, and V. Subramanian, "Tailoring Indium Oxide Nanocrystal Synthesis Conditions for Air-Stable High-Performance Solution-Processed Thin-Film Transistors," *ACS Appl. Mater. Interfaces*, vol. 7, no. 19, pp. 10069–10075, May 2015.
[29] Y.-Y. Noh, X. Cheng, H. Sirringhaus, J. I. Sohn, M. E. Welland, and D. J. Kang, "Ink-jet printed ZnO nanowire field effect transistors," *Appl. Phys. Lett.*, vol. 91, no. 4, p. 043109, Jul. 2007.
[30] M.-G. Kim, J. W. Hennek, H. S. Kim, M. G. Kanatzidis, A. Facchetti, and T. J. Marks, "Delayed Ignition of Autocatalytic Combustion Precursors: Low-Temperature Nanomaterial Binder Approach to Electronically Functional Oxide Films," *J. Am. Chem. Soc.*, vol. 134, no. 28, pp. 11583–11593, Jul. 2012.
[31] N.-R. Kim *et al.*, "Enhanced conductivity of solution-processed indium tin oxide nanoparticle films by oxygen partial pressure controlled annealing," *J. Mater. Chem. C*, vol. 1, no. 37, pp. 5953–5959, 2013.
[32] S. Dasgupta, R. Kruk, N. Mechau, and H. Hahn, "Inkjet Printed, High Mobility Inorganic-Oxide Field Effect Transistors Processed at Room Temperature," *ACS Nano*, vol. 5, no. 12, pp. 9628–9638, Dec. 2011.
[33] S. Dasgupta *et al.*, "Printed and Electrochemically Gated, High-Mobility, Inorganic Oxide Nanoparticle FETs and Their Suitability for High-Frequency Applications," *Adv. Funct. Mater.*, vol. 22, no. 23, pp. 4909–4919, Dec. 2012.
[34] W. J. Scheideler, J. Smith, I. Deckman, S. Chung, A. C. Arias, and V. Subramanian, "A robust, gravure-printed, silver nanowire/metal oxide hybrid electrode for high-throughput patterned transparent conductors," *J Mater Chem C*, vol. 4, no. 15, pp. 3248–3255, 2016.
[35] J. Wang and S. Langer, "A brief review of human perception factors in digital displays for picture archiving and communications systems," *J. Digit. Imaging*, vol. 10, no. 4, pp. 158–168, Nov. 1997.
[36] J. Socratous *et al.*, "Electronic Structure of Low-Temperature Solution-Processed Amorphous Metal Oxide Semiconductors for Thin-Film Transistor Applications," *Adv. Funct. Mater.*, vol. 25, no. 12, pp. 1873–1885, Mar. 2015.
[37] K. Fukuda *et al.*, "Reverse-Offset Printing Optimized for Scalable Organic Thin-Film Transistors with Submicrometer Channel Lengths," *Adv. Electron. Mater.*, vol. 1, no. 8, p. n/a-n/a, Aug. 2015.
[38] Y. H. Han, J.-Y. Won, H.-S. Yoo, J.-H. Kim, R. Choi, and J. K. Jeong, "High Performance Metal Oxide Field-Effect Transistors with a Reverse Offset Printed Cu Source/Drain Electrode," *Acs Appl. Mater. Interfaces*, vol. 8, no. 2, pp. 1156–1163, Jan. 2016.

[39] Y. Li *et al.*, "Coffee-Ring Defined Short Channels for Inkjet-Printed Metal Oxide Thin-Film Transistors," *ACS Appl. Mater. Interfaces*, vol. 8, no. 30, pp. 19643–19648, Aug. 2016.
[40] M.-G. Kim, M. G. Kanatzidis, A. Facchetti, and T. J. Marks, "Low-temperature fabrication of high-performance metal oxide thin-film electronics via combustion processing," *Nat. Mater.*, vol. 10, no. 5, pp. 382–388, May 2011.
[41] S. Jeong, J.-Y. Lee, S. S. Lee, Y. Choi, and B.-H. Ryu, "Impact of Metal Salt Precursor on Low-Temperature Annealed Solution-Derived Ga-doped In2O3 Semiconductor for Thin-Film Transistors," *J. Phys. Chem. C*, vol. 115, no. 23, pp. 11773–11780, Jun. 2011.
[42] Y.-H. Kim *et al.*, "Flexible metal-oxide devices made by room-temperature photochemical activation of sol-gel films," *Nature*, vol. 489, no. 7414, pp. 128–132, Sep. 2012.
[43] S. Park *et al.*, "In-Depth Studies on Rapid Photochemical Activation of Various Sol–Gel Metal Oxide Films for Flexible Transparent Electronics," *Adv. Funct. Mater.*, vol. 25, no. 19, pp. 2807–2815, May 2015.
[44] P. K. Nayak, J. A. Caraveo-Frescas, Z. Wang, M. N. Hedhili, and H. N. Alshareef, "Six-Fold Mobility Improvement of Indium-Zinc Oxide Thin-Film Transistors Using a Simple Water Treatment," *Adv. Electron. Mater.*, vol. 1, no. 6, p. n/a-n/a, Jun. 2015.
[45] Y. Meng *et al.*, "Low-temperature fabrication of high performance indium oxide thin film transistors," *RSC Adv.*, vol. 5, no. 47, pp. 37807–37813, Apr. 2015.
[46] Y.-H. Lin *et al.*, "High-Performance ZnO Transistors Processed Via an Aqueous Carbon-Free Metal Oxide Precursor Route at Temperatures Between 80–180 °C," *Adv. Mater.*, vol. 25, no. 31, pp. 4340–4346, Aug. 2013.
[47] H. Ning *et al.*, "Direct Inkjet Printing of Silver Source/Drain Electrodes on an Amorphous InGaZnO Layer for Thin-Film Transistors," *Materials*, vol. 10, no. 1, p. 51, Jan. 2017.
[48] S. K. Park, Y.-H. Kim, and J.-I. Han, "All solution-processed high-resolution bottom-contact transparent metal-oxide thin film transistors," *J. Phys. Appl. Phys.*, vol. 42, no. 12, p. 125102, 2009.
[49] G. R. Hong *et al.*, "Unraveling the Issue of Ag Migration in Printable Source/Drain Electrodes Compatible with Versatile Solution-Processed Oxide Semiconductors for Printed Thin-Film Transistor Applications," *ACS Appl. Mater. Interfaces*, vol. 9, no. 16, pp. 14058–14066, Apr. 2017.
[50] E. B. Secor, J. Smith, T. J. Marks, and M. C. Hersam, "High-Performance Inkjet-Printed Indium-Gallium-Zinc-Oxide Transistors Enabled by Embedded, Chemically Stable Graphene Electrodes," *ACS Appl. Mater. Interfaces*, vol. 8, no. 27, pp. 17428–17434, Jul. 2016.
[51] W. J. Scheideler, R. Kumar, A. R. Zeumault, and V. Subramanian, "Low-Temperature-Processed Printed Metal Oxide Transistors Based on Pure Aqueous Inks," *Adv. Funct. Mater.*, p. n/a-n/a, Mar. 2017.
[52] J. Jang, H. Kang, H. C. N. Chakravarthula, and V. Subramanian, "Fully Inkjet-Printed Transparent Oxide Thin Film Transistors Using a Fugitive Wettability Switch," *Adv. Electron. Mater.*, vol. 1, no. 7, p. n/a-n/a, Jul. 2015.
[53] S.-H. K. Park *et al.*, "42.3: Transparent ZnO Thin Film Transistor for the Application of High Aperture Ratio Bottom Emission AM-OLED Display," *SID Symp. Dig. Tech. Pap.*, vol. 39, no. 1, pp. 629–632, May 2008.
[54] A. Zeumault and V. Subramanian, "Mobility Enhancement in Solution-Processed Transparent Conductive Oxide TFTs due to Electron Donation from Traps in High-k Gate Dielectrics," *Adv. Funct. Mater.*, vol. 26, no. 6, pp. 955–963, Feb. 2016.

[55] A. Zeumault, S. Ma, and J. Holbery, “Fully inkjet-printed metal-oxide thin-film transistors on plastic,” *Phys. Status Solidi -Appl. Mater. Sci.*, vol. 213, no. 8, pp. 2189–2195, Aug. 2016.
[56] Y. Li *et al.*, “All Inkjet-Printed Metal-Oxide Thin-Film Transistor Array with Good Stability and Uniformity Using Surface-Energy Patterns,” *ACS Appl. Mater. Interfaces*, vol. 9, no. 9, pp. 8194–8200, Mar. 2017.
[57] X. Wu, F. Fei, Z. Chen, W. Su, and Z. Cui, “A new nanocomposite dielectric ink and its application in printed thin-film transistors,” *Compos. Sci. Technol.*, vol. 94, pp. 117–122, Apr. 2014.
[58] J.-S. Seo *et al.*, “Solution-Processed Flexible Fluorine-doped Indium Zinc Oxide Thin-Film Transistors Fabricated on Plastic Film at Low Temperature,” *Sci. Rep.*, vol. 3, p. 2085, Jun. 2013.
[59] Y. S. Rim, H. Chen, Y. Liu, S.-H. Bae, H. J. Kim, and Y. Yang, “Direct Light Pattern Integration of Low-Temperature Solution-Processed All-Oxide Flexible Electronics,” *ACS Nano*, vol. 8, no. 9, pp. 9680–9686, Sep. 2014.
[60] Y. S. Rim, H. Chen, T.-B. Song, S.-H. Bae, and Y. Yang, “Hexaaqua Metal Complexes for Low-Temperature Formation of Fully Metal Oxide Thin-Film Transistors,” *Chem. Mater.*, vol. 27, no. 16, pp. 5808–5812, Aug. 2015.
[61] X. Yu *et al.*, “Spray-combustion synthesis: Efficient solution route to high-performance oxide transistors,” *Proc. Natl. Acad. Sci.*, vol. 112, no. 11, pp. 3217–3222, Mar. 2015.

# Chapter 2: Ink Design for Gravure-Printing Transparent Conductors on Flexible Glass

## 2.1 Introduction

Transparent conducting oxide (TCO) electrodes are essential components in ubiquitous thin film devices including solar cells[1], [2], LEDs[3], touch screens[4], displays[5]–[7], and transparent thin film transistors (TFTs)[8], the main focus of this thesis. Conventional fabrication approaches for patterning TCOs require vacuum technologies and subtractive processing, which result in low material utilization and limit the viable material set to TCOs with suitable etch selectivity. Solution-processed TCO electrodes can potentially leverage the advantages of additive processing techniques, such as printing technologies, to greatly improve material utilization and enhance throughput for patterned TCO films at a reduced cost[9]. These benefits are particularly relevant to leading transparent conductors based on indium and silver which [10] exist in limited earth abundance, but have rapidly growing applications in photovoltaics and display technology. In this chapter, we address the technological need for high-resolution additively patterned TCOs by developing gravure-printed sol-gel transparent conductors for printed metal oxide transistors.

Gravure printing is a competitive technique for patterning high-resolution (<5 μm) features at high speeds (≥ 1 m/s)[16]. However, the scope of gravure-printed electronic materials has previously been limited to polymeric organic inks and nanoparticle inks. A principle reason for this has been the limited thermal capability of transparent plastic substrates, which have poor dimensional stability above 200 °C. However, thin glass substrates offer a favorable combination of excellent thermal stability ($T_g$ ~ 600 °C), ultra-smooth surface quality ($R_a$ < 0.5 nm) for device fabrication, and reasonable flexibility[17], enabling many new applications and scalable R2R manufacturing methods for high performance materials requiring processing temperatures in the range of 400° - 600° C. In addition to thermal stability, thin glass substrates provide mechanical flexibility, which is essential for facilitating R2R contact printing such as gravure[18]. This flexibility allows substrates to conform to roll runout, forming an intimate contact for printing high-resolution lines and films at a high speed, as illustrated in Figure 2.1. Because of its higher Young's modulus (E = 70 GPa[18]), glass also limits substrate deformation during printing and thermal processing to enhance registration. Therefore, thin glass substrates are promising candidates for flexible, printed electronics technologies that need high process temperatures.

Here, we utilize flexible glass substrates to realize high-resolution conductive (500 S / cm) printed TCO electrodes with line widths as small as 35 μm via highly concentrated sol-gel precursor inks. The rheology of sol-gel precursors is studied and controlled via precursor concentration and cosolvent addition to guide the development of printable gravure inks and fabricate uniform, smooth electrodes. The line morphology, optical transparency, crystallinity, and electrical performance of tin-doped indium oxide (ITO) electrodes and antimony-doped tin oxide (ATO) electrodes are studied as a function of the ink formulation. Finally, the electrical performance under flexion fatigue is examined to understand the mechanical reliability of printed sol-gel conductors.

## 2.2 Gravure Ink Design

The sol-gel process (Section 1.4) is a well-known strategy for forming TCO films directly from liquid phase precursors. However, formulating sol-gel inks that exhibit both optimal material

properties and suitable rheology for roll-based printing is a challenge. Solution-processed TCOs formed by spin-coating have recently reached record conductivities[19] that approach the performance of sputtered ITO while utilizing metal salts.[20] While these sol-gel chemistries yield high performance TCOs, the spin-coated precursors' rheology is unsuitable for gravure printing.

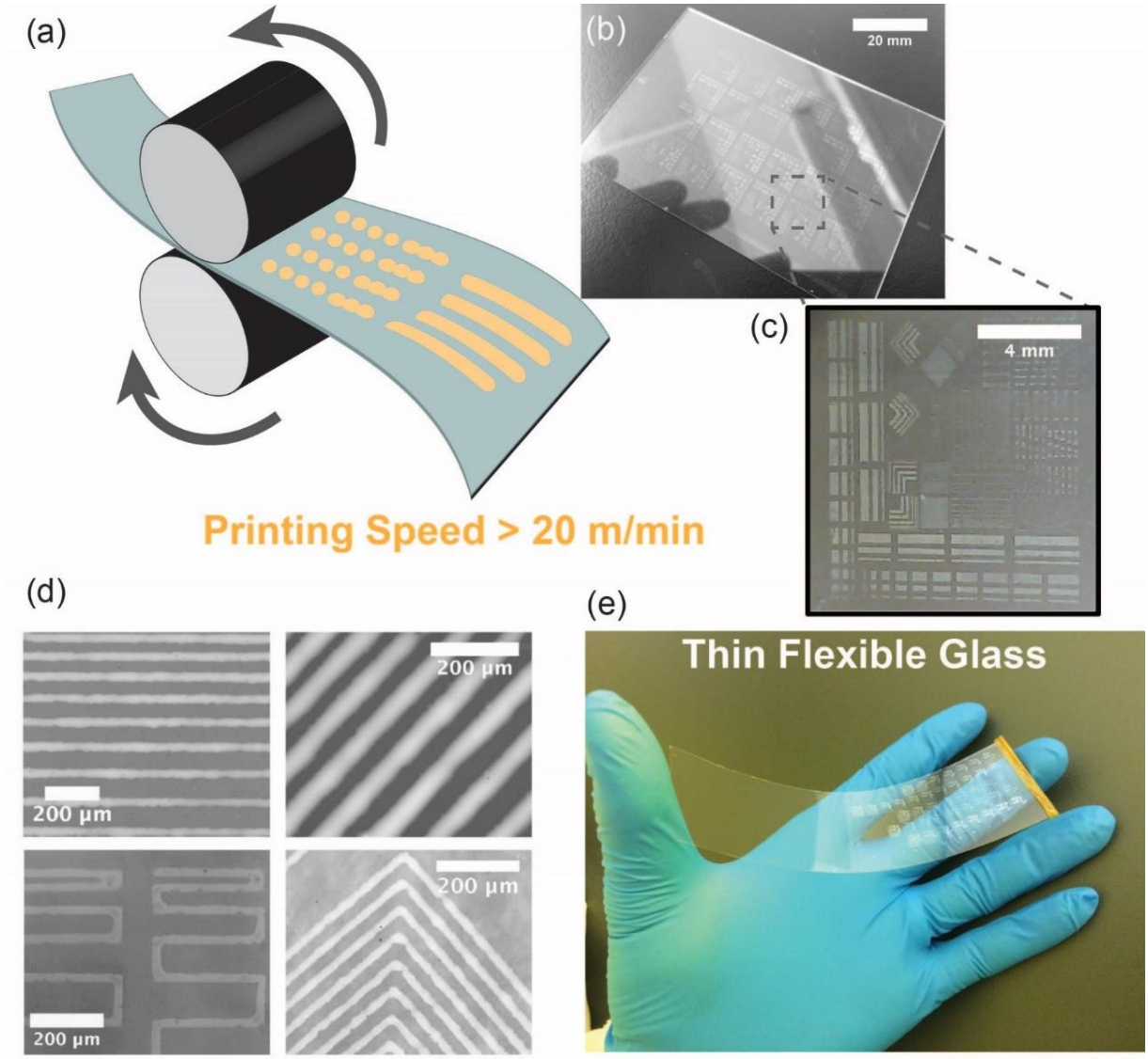


Figure 2.1 Schematic of gravure printing process on thin flexible glass with metal gravure cylinders (a). Glass substrate with patterned ATO (2M) printed at 0.4 m/s (24 m / min). Printed ATO features on glass (c). Fine lines (35um) printed with ITO (top-left, bottom-left) and ATO (top-right, bottom-right) on flexible glass substrates (e).

Common metal salt sol-gel schemes using aging[21] or stabilizer addition[22] have also been used to increase viscosity slightly from 1 cP to about 10 cP[23], but these viscosities remain too low for gravure printing. Formulating an ink for high-resolution gravure printing requires viscosities near

100 cP to produce fine lines with smooth edges, few pinholes, and controllable width[24]. Furthermore, as discussed in Section 1.3, the surface tension ( $\gamma$ ) of an ink plays an important role in high-resolution patterning, as it balances viscous forces during ink transfer and pattern formation. This balance of viscous forces and surface tension forces can be represented at a particular printing speed as the non-dimensional Capillary Number, Ca, offering a useful metric for predicting printability of an ink, as detailed in [17]. At very low Capillary Number, ($Ca << 1$) pattern fidelity is deteriorated by ink drag-out from the cells and at very high Capillary Number ($Ca >> 1$) inefficient doctoring leaves ink in non-patterned areas. Optimal printing can be achieved by adjusting printing speed and ink parameters to make $Ca \sim 1$[16]. Therefore, to achieve optimal pattern formation at a particular printing speed (limited by printing machine capabilities) requires appropriate tuning of the fluid viscosity and surface tension of an ink.

### 2.2.1 Ink Preparation & Characterization

Sol-gel inks were mixed at room temperature in air using hydrated metal salts obtained from Strem Chemicals ($Sn(IV)Cl4 \cdot H_2O$ 98%, $In(NO_3)_3 \cdot xH_2O$ 99.99%), or Sigma Aldrich ($Sn(II)Cl_2 \cdot x(H_2O)$ 99.995%, $SbCl3 \cdot x(H_2O)$ 99.99%). Precursors were dissolved in EG (99.8%, Fisher Scientific), ethanol (anhydrous, 99.5%, Sigma-Aldrich), or AcAc (99.5%, Sigma-Aldrich) and sonicated for 1 hour until complete dissolution occurred, leaving a clear solution. ITO inks were dissolved in pure AcAc or pure EG and were doped with 10% at. Sn(IV). ATO inks were dissolved in a binary solvent of EG and ETOH and were doped with 8% at. EG content above 20% by volume was required to keep ATO inks stable over long periods of time (more than two months). Ink viscosities were extracted from shear stress during an ascending sweep of shear rates obtained at 30 s intervals measured using a Brookfield Cone/Plate Viscometer (DV-III +) for freshly mixed solutions. Pendant drops of various inks were captured at room temperature and surface tension was calculated using the measured inks density and drop geometry extracted in ImageJ. Inks with high concentrations (> 30%) of the stabilizing solvent (i.e. Ethylene Glycol) exhibited excellent stability, with viscosity and electrical performance changing by less than 10% after 1-month storage in air. However, inks which did not contain the stabilizer began to precipitate out of solution after approximately 1 day of storage.

### 2.2.2 Sol-gel Ink Rheology

In this work, we explore methods for controlling viscosity and surface tension of metal salt-based sol-gel inks to effectively access optimal printing conditions. In the first method, varying the concentration of the precursor tunes the sol-gel ink viscosity, similar to methods used for nanoparticle dispersions and polymer solutions. This principle is illustrated in Figure 2.1a for two electronically functional sol-gel inks, including indium tin oxide (ITO) and antimony-doped tin oxide (ATO), each of which is enhanced to gravure-printable viscosities (20-100 cP). Viscosity depends exponentially on precursor concentration in the case of the ITO and ATO dissolved in a strongly complexing solvent such as pure acetylacetone (AcAc) or pure ethylene glycol (EG). In contrast, sols dissolved in a mixture of EG and ethanol (ETOH) show a weaker dependence of viscosity on concentration, increasing less relative to the neat viscosity. Observations of thixotropic behavior such as counter-clockwise hysteresis loops in measurements of shear stress may also reflect the formation of a solvated network in concentrated inks.[26] The range of viscosities accessed by this method is highlighted in Figure 2.2a, showing how concentrated metal salt sol-gels can reach viscosities near 100 cP to allow high resolution printing. While it is true that alkoxide chemistries can give similar tunability in fluid properties, their high cost relative to metal

salts could inhibit large scale printed electronics applications. Although this method effectively tuned the viscosity over two orders of magnitude, the surface tension of inks remained nearly constant over a wide range of metal concentrations. This property is attractive for facilitating the use of similar surface treatments for different ink concentrations.

### 2.2.3 Printing Process & Annealing

All printing studies were conducted on a sheet fed commercial IGT G1-5 gravure printer. Custom gravure cylinders from Rotadyne Corp were used to pattern arrays of fine lines with 20 μm square shaped wet etched gravure cells (400 lines/cm, depth 8 μm, theoretical transfer volume 4.0 $mL/m^2$). An IGT gravure roller (402.150.433) with 150 μm cells (70 lines/cm, depth 50 μm, theoretical transfer volume 13.5 $mL/m^2$, screen 53°, stylus 120°) was used to deposit blanket films. A printing speed of 0.4 m/s and a printing force of 100N were used unless otherwise indicated. Glass substrates (100 μm thick Corning Willow glass or .5mm thick Eagle XG glass) were sonicated in acetone, IPA, and DI water before spin-coating a thin layer of PMMA (0.6% in anisole) to adjust the wetting properties; this layer burns off during subsequent thermal processing, and has not been found to impact TCO performance[25]. The PMMA layer (~10 - 15nm thick) was cured at 200 °C for 10 minutes on a hot plate and treated with a UV-Ozone cleaner (Jelight Model 42) for 10 minutes prior to printing to improve ink transfer from the roller to the substrate. Printed films were dried immediately following printing at 125 °C (ITO) or 225 °C (ATO) for 10 minutes, then transferred to a tube furnace for annealing at 400 °C (ITO) or 500 °C (ATO) for 15 minutes in clean dry air; this high temperature anneal also functions to decompose the sacrificial PMMA surface treatment layer. ITO films were post-annealed at 300 °C in a reducing atmosphere of $N_2/H_2$ gas for 20 minutes to optimize conductivity and induce higher oxygen vacancy concentrations. Extended forming gas annealing at higher temperatures (400 °C – 500 °C) was observed to cause further improvement in the conductivity, but significant decreases in optical transmittance and the appearance of metallic streaks in the film.

(a)

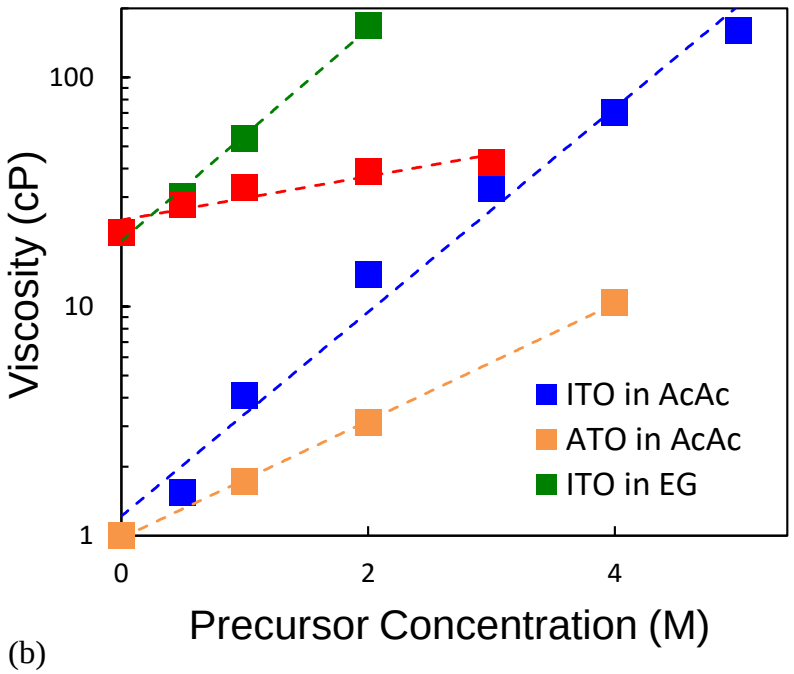


(b)

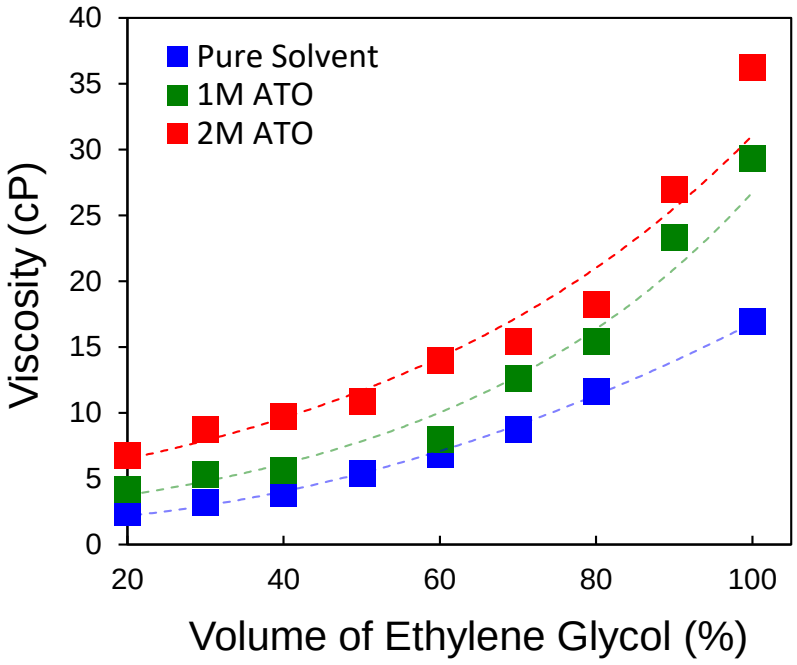


Figure 2.2 Measured viscosity vs precursor concentration of ITO and ATO inks dissolved in the indicated solvents (a). Viscosity (shear rate = 15 s-1) of ATO inks vs solvent composition, plotted as a function of the volumetric fraction of EG in an ethanol / EG mixture (b).

### 2.2.4 Ink Transfer on Rigid Glass Substrates

Gravure printing on glass involves several unique physical phenomena which distinguish it from printing on flexible plastic substrates. Glass substrates designed for use in electronics have uniquely smooth and homogeneous surfaces for allowing the successful manufacturing of thin film devices[18]. These smooth surfaces are essential for depositing uniform thin films by vacuum processing and other coating technologies, but they can make ink transfer challenging in gravure printing. Gravure printing relies on a contact based ink transfer process illustrated below in Figure 2.3. During roller to substrate contact, a liquid bridge is formed linking residual ink in the engraved cell to the deposited drop on the substrate. As the roller recedes during the printing action, the bridge is broken, leaving the droplet in the desired position on the substrate. The volume of ink transferred to the roller is sensitive to the fluid mechanics of this breakup process. One of the important features of the transferred drop is the contact line at which it meets the substrate. Pinned contact lines often form on plastic substrates which have some degree of chemical or physical heterogeneity, often from surface roughness. This 'pinning' prevents the retreat of the contact line which would otherwise facilitate flow back up the liquid bridge to the engraved cell.

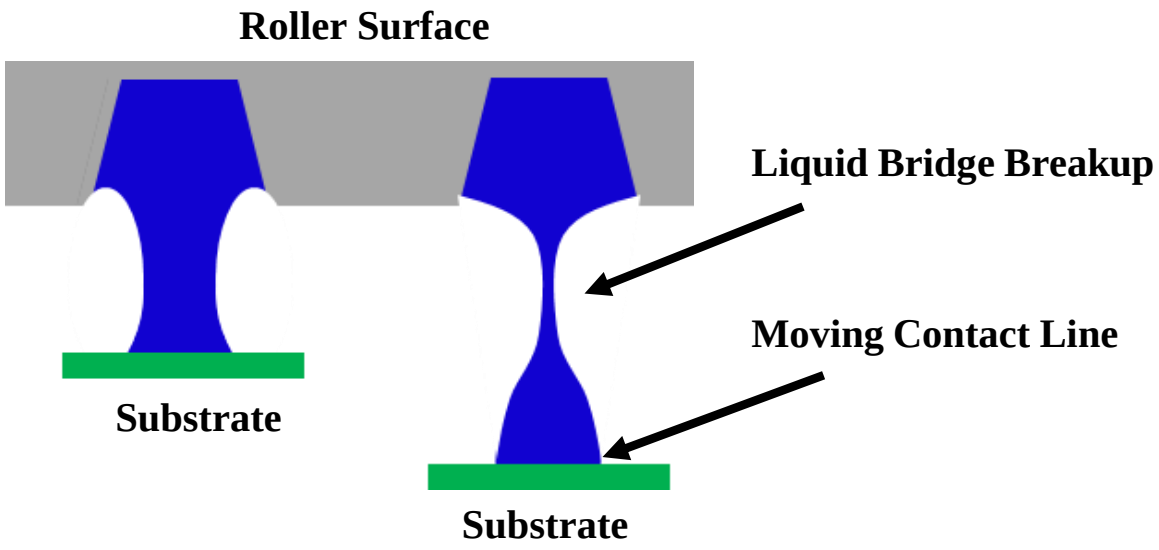


Figure 2.3 Schematic of gravure ink transfer process highlighting the role of the moving contact line and liquid bridge during the separation of the roller and the substrate.

A measure of the tendency of inks to form pinned contact lines is the contact angle hysteresis observed on a surface. To investigate the interactions between these surface properties and the gravure-printed feature formation, we engineered the substrate to have different degrees of contact angle hysteresis (measured using $H_2O$). Using an ultrathin layer of PMMA which was subsequently partially etched in a UV ozone chamber to form a rougher, more heterogeneous surface, contact angle hysteresis was induced. The degree of hysteresis as a function of the treatment conditions is shown below in Figure 2.4a. The contact angle hysteresis window opens after several minutes of UV ozone treatment, before closing after a longer treatment when both the receding and advancing contact angles are quite low. The normalized transferred ink volume of sol-gel inks increases and peaks for intermediate treatment times when the hysteresis is maximized. This suggests that the contact line pinning is essential to enhancing the volume fraction

of ink which remains on the substrate during transfer. Although this study did not directly investigate high printing speeds due to tool limitations, the fluid mechanics of the bridge breakup can also be optimized by varying the print speeds. At high speeds the breakup process occurs very quickly and there is minimal time available for the meniscus to recede on the substrate. In some cases this appears to correlate with higher transferred volume fraction[16].

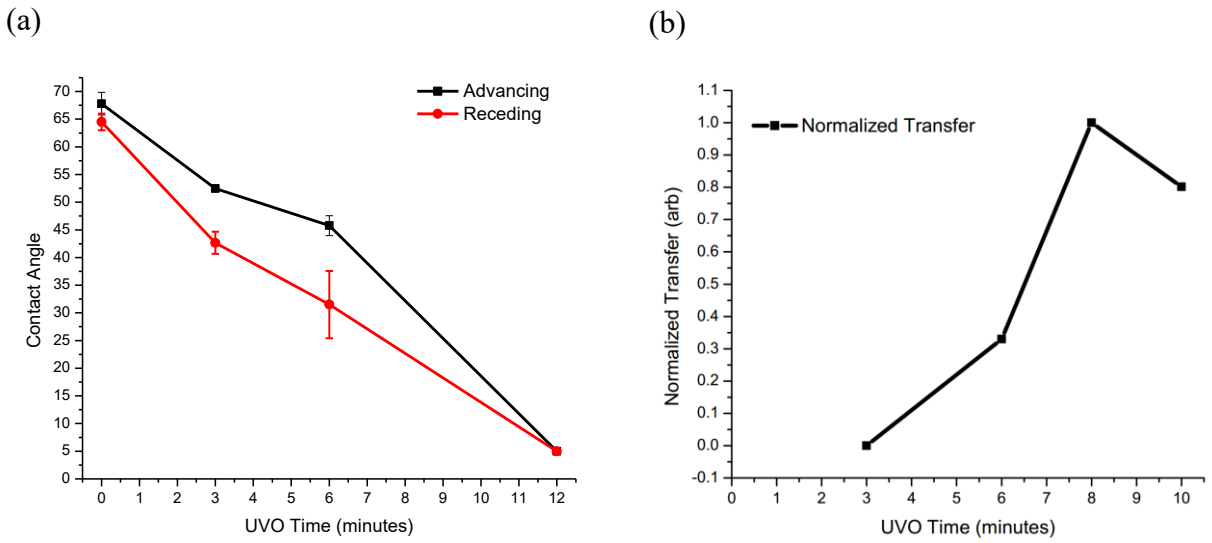


Figure 2.4 Water contact angle on glass substrates treated with PMMA surface layer as a function of UV ozone treatment time (a). Normalized transferred volume of sol-gel ink as a function of the UV ozone treatment time (b).

### 2.2.5 Printed TCO Line Morphology

Sol-gel inks formulated by this method were gravure printed at similar speeds and contact pressure, with equivalent surface treatments and drying conditions. The three dimensional line morphology of these prints was studied to understand the effect of increasing *Ca* through viscosity tuning. Figure 2.5 illustrates the profiles of gravure-printed lines as a function of the metal concentration of ITO sol-gels in pure AcAc. Line morphology was measured with a 3D Laser Measuring Microscope (Olympus OLS4000) and a stylus profilometer (Veeco Dektak 6M) after the final annealing step was completed. Line width and edge morphology were automatically extracted using a commercial software package (SuMMIT) for off-line analysis of optical microscope images.

The observed line profiles suggest that more viscous, high concentration inks lead to a reduction in the spreading rate and a suppression of the coffee ring effect, forming thicker dome-shaped or parabolic lines. Another appropriate explanation is that higher concentration inks have a smaller volumetric percentage of solvents, which evaporate during drying, elevating the viscosity so that the 2D pattern is frozen into its final geometry by a sol-gel transition[26], [27]. The line widths (Figure 2.4) of gravure-printed ITO sol-gels shows that significant spreading occurs after ink is transferred to the substrate for low precursor concentrations (< 3M). In comparison, concentrated inks give better control over the line width and show significantly lower line-edge-roughness and

line-width-roughness (Figure 2.6), a reflection of stable line formation. These trends reflect the enhanced printability of concentrated inks, as predicted by the longer relaxation times following application of shear stress as shown in creep-recovery tests.

Controlling the solvent composition of sol-gel precursors is a complementary method to enhance the *Ca* and span the ink design space for optimizing printability. This second method is demonstrated here for ATO sol-gel inks with a binary solvent of EG and ethanol. Figure 2.2b illustrates the increase in viscosity obtained by adding EG to ATO sol-gels in ethanol. Sol-gel inks with different precursor concentrations show similar enhancements in viscosity, reaching a suitable range for gravure printing at concentrations between 1M and 2M. Although the viscosity of the binary solvent ATO inks does not increase exponentially with this mechanism, this cosolvent system has the added benefit of reducing coffee-ring effects, which typically result in sharply peaked line edges and non-uniform deposition.

Cosolvent based systems are a well-known method for managing the coffee-ring effect in printed inks. Cosolvents can induce recirculating flows, which homogenize particle concentrations to yield uniform films and smooth line profiles [28]. In the case of the ATO inks utilized in this study, ink wetting on the substrate significantly changes with respect to the EG content, as expected from the higher surface tension of EG (48.6 mN/m) vs. ethanol (21.8 mN/m) [29]. The increased contact angle, originating from the higher surface tension of EG, may slow preferential evaporation at the edges due to the increased volume of ink per unit area. The reduced evaporation rate at the edges also decreases potential spreading originating from the outward liquid flow to replace evaporated solvent. As a result, coffee-ring-less uniform ATO electrodes were successfully printed with inks of 50% - 70% EG in ethanol (Figure 2.5b) by using this method to access the optimal range of *Ca* shown in Figure 2.4. These results indicate that this second method of ink formulation consisting of a cosolvent system is a viable technique to obtain favorable line morphologies at lower precursor concentrations (1M - 2M) than are required for single solvent concentrated inks (3M – 5M).

(a)

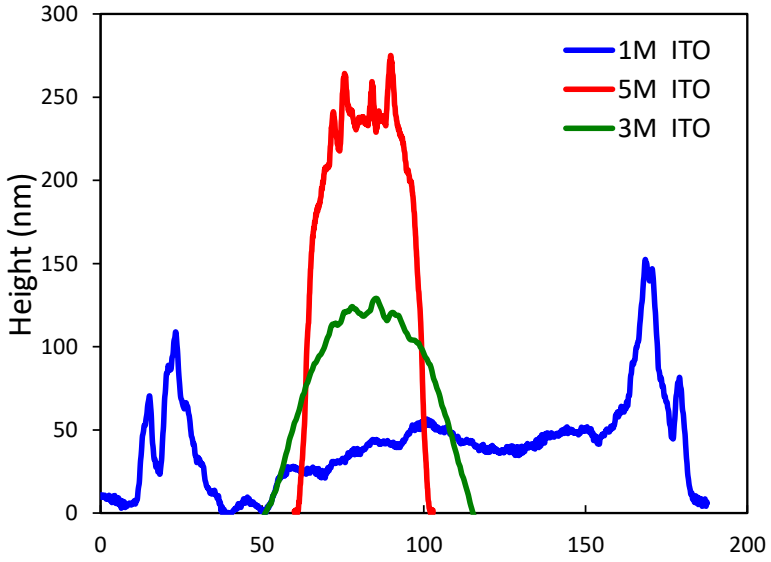


(b)

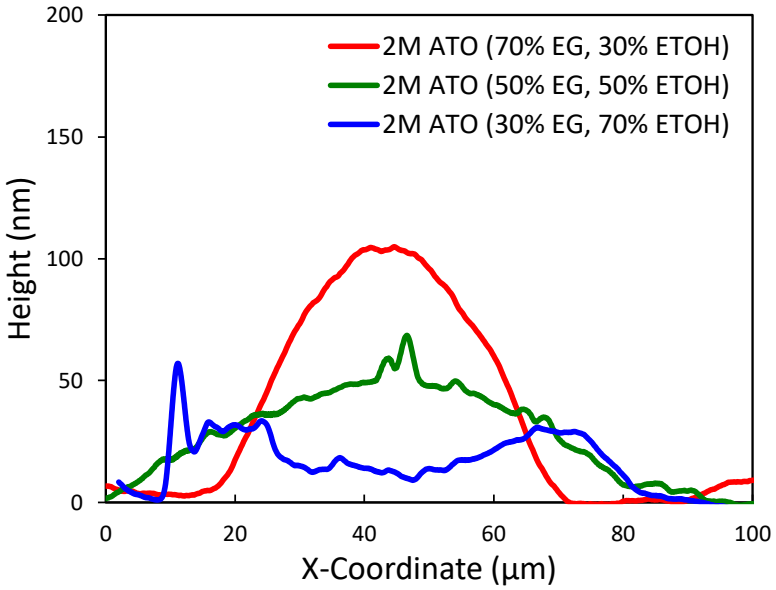


Figure 2.5 Line profiles for 1, 3, and 5 M ITO inks in AcAc printed with 20 um cells at 0.4 m / s and 100 N printing force. (a) Line profiles for 2 M ATO inks with various solvent compositions. (b)

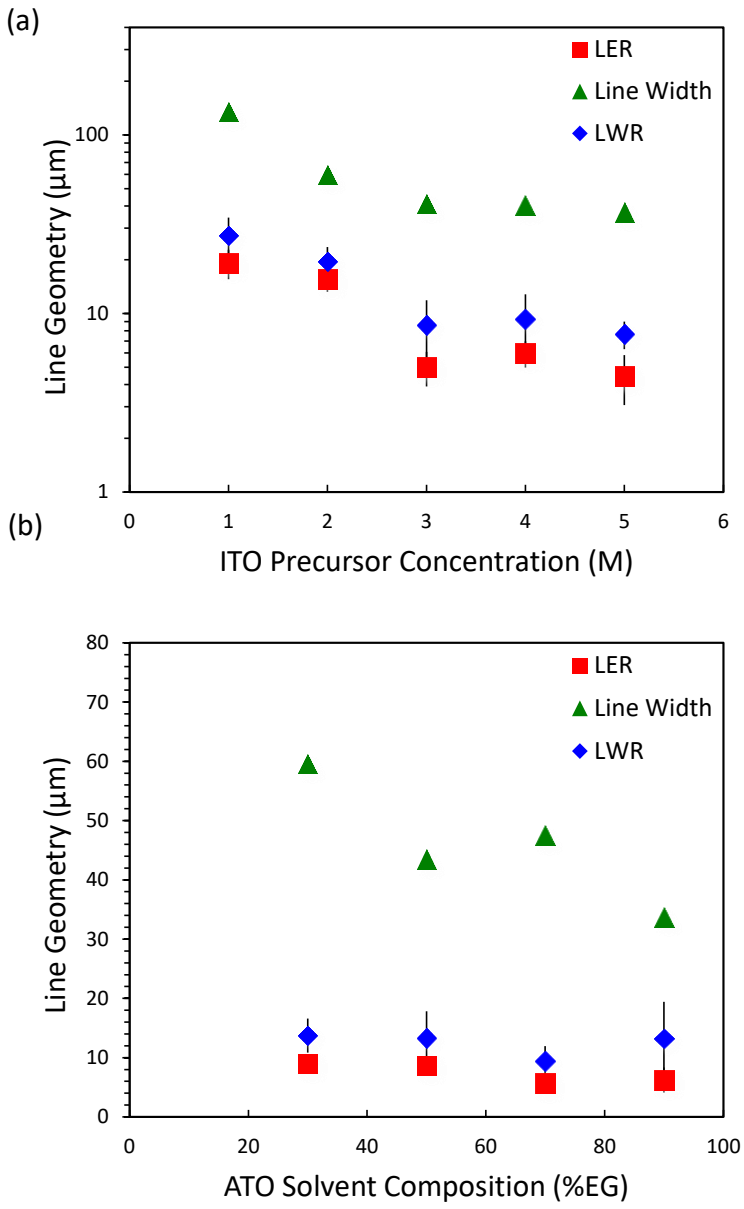


Figure 2.6 Line-width, line-edge-roughness (LER), and line-width-roughness (LWR) for ITO inks of varying concentration in acetylacetone. (a) Line width, line-edge-roughness (LER), and line-width-roughness (LWR) for 2 M ATO inks of varying solvent composition (EG %)

Collectively these two methods offer useful tools to span the parametric space of fluid parameters that guide gravure ink design. This capability allows one to optimize printable sol-gel inks for arbitrary printing speeds and surfaces. However, for these functional inks it is also important to consider the impact of ink design on material performance.

## 2.3 Electrical Performance of Sol-gel Inks

The electrical performance of the printed sol-gels was characterized as a function of ink formulation to understand the impact of rheological ink optimization on the functional material properties such as sheet resistance and conductivity. The sheet resistance and thickness were directly measured for printed inks formulated from concentrated precursor method and cosolvent method. The sheet resistance of printed blanket films was measured using a 4-point probe system (Agilent 34401A). Printed lines were characterized by a precision semiconductor parameter analyzer (HP 4155A) using two point and four point configurations. Figure 2.7 and Figure 2.8 illustrate the sheet resistance and resistivity of ITO and ATO sol-gels as a function of the sol-gel precursor concentration for different gravure cell sizes. In both cases, sheet resistance is improved at higher precursor concentrations as thicker solid films are deposited. ITO features with optimized annealing conditions are highly conductive, with sheet resistance ($R_S$) as low as 100 Ω/□ for single-layer blanket films and 200 Ω/□ for lines. ATO sol-gels formed from Sn(II) and Sb(III) salts have slightly lower performance, but still allow printing of conductive lines with $R_S$ as low as 700 Ω/□.

The resistivity of these single layer gravure-printed features in this study compares favorably to sol-gel-derived films formed by other coating method such as dip-coating and spin-coating despite the fact that these methods use multilayer films of 5-10 layers that effectively fill cracks and pinholes to ensure film continuity. Resistivity as low as $2 \cdot 10^{-3}$ Ω-cm ($\sigma \sim 500$ S / cm) is achieved for single-layer printed ITO. To our knowledge, this is the best conductivity achieved for solution-processed TCO features patterned by roll-based techniques. The gravure-printed ATO lines have a resistivity of $7 \cdot 10^{-3}$ Ω-cm (143 S/cm), which is comparable to other reports of solution-processed ATO[21] by methods such as spin coating and spray deposition. In both cases, these results demonstrate that high performance transparent conductors may be formulated as highly concentrated inks while retaining the high performance of more dilute sol-gel inks used in spin coating. This suggest that similar ink chemistries to those presented would be viable for printing techniques such as flexography or offset printing. These alternative techniques have their own set of advantages for printing on fragile thin rigid substrates like Willow glass, since they can utilize softer mechanical contact via an intermediate roller.

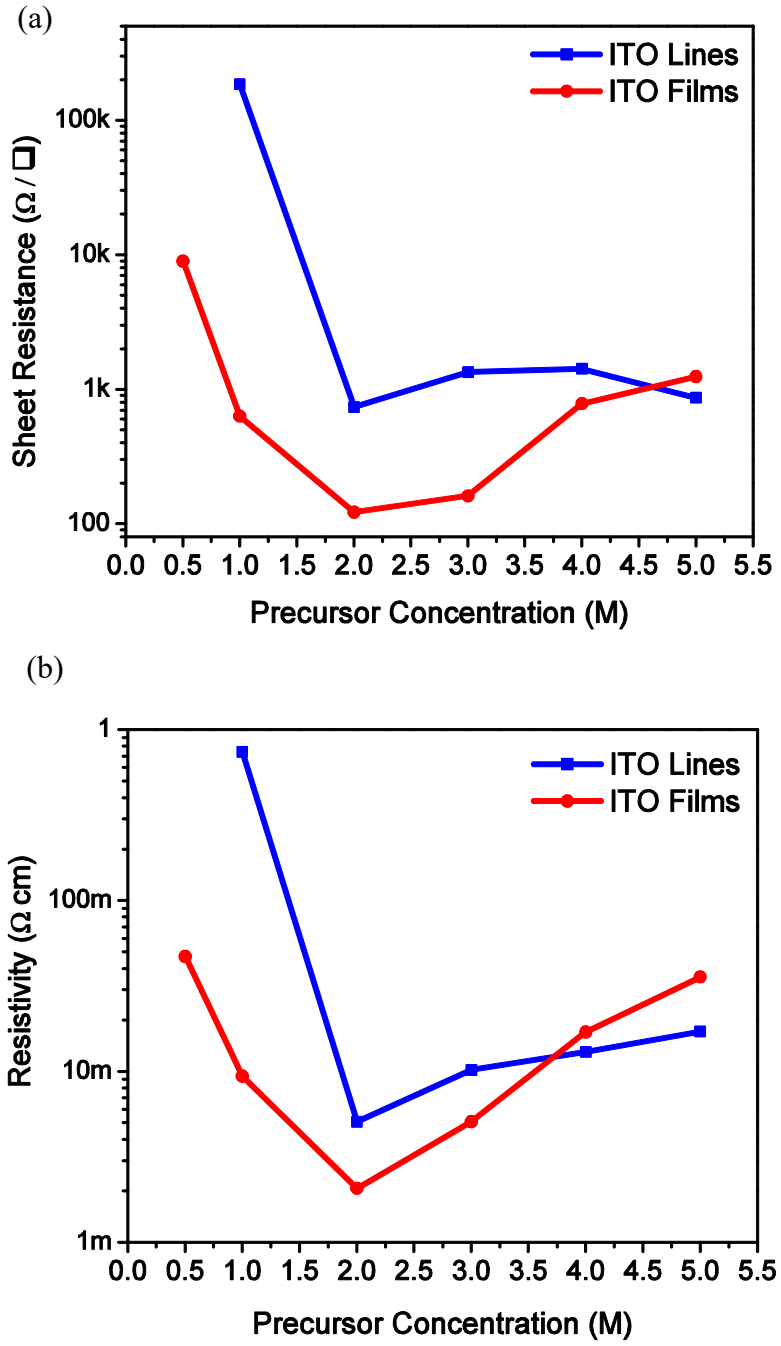


Figure 2.7 Sheet resistance (a) and resistivity (b) of printed ITO lines and films as a function of precursor ink concentration.

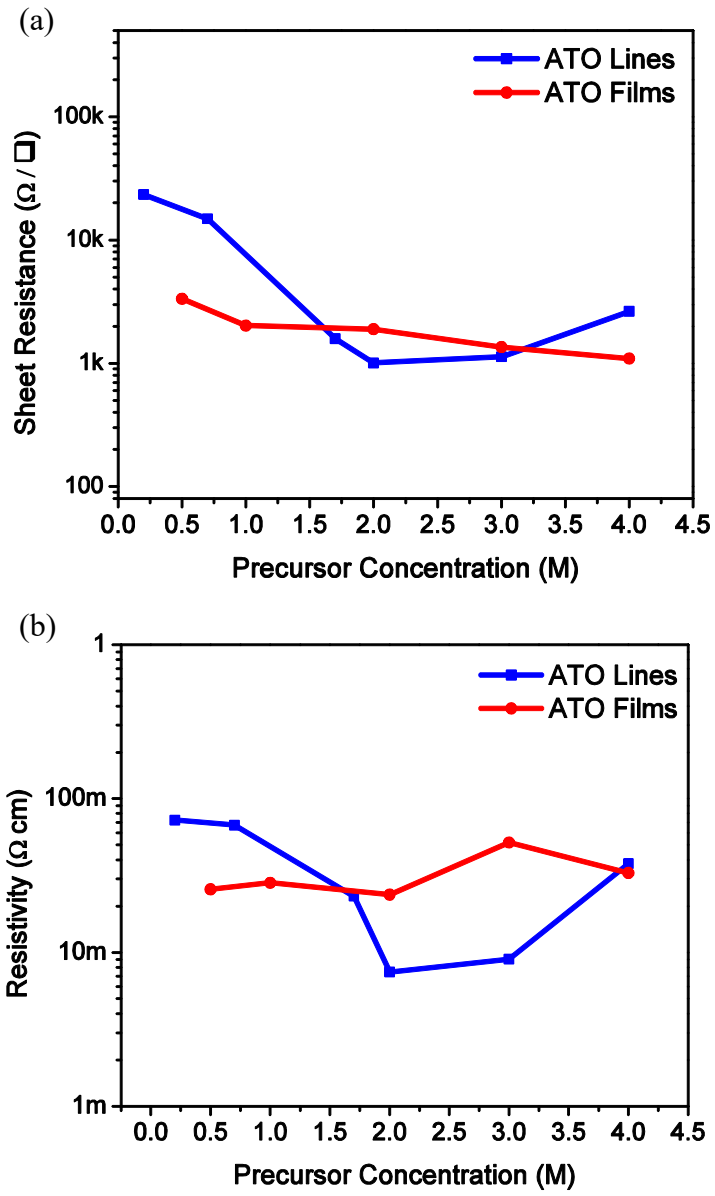


Figure 2.8 Sheet resistance (a) and resistivity (b) of printed ITO lines and films as a function of precursor ink concentration.

## 2.4 Morphology and Crystallinity of Printed TCO Films

As shown above in Figure 2.7 and Figure 2.8, the measured resistivity of the printed features is observed to be a function of the ink concentration. One explanation for this may related to the variation in film thickness. Film thickness should affect the morphology of the sol-gel-derived film in multiple ways. In the case of polycrystalline TCO films such as ITO and ATO, it has been reported that crystallite size increases with film thickness for a given composition and annealing

process, leading to improved conductivity[30], [31]. These factors were explored for the printed TCO films used in this study by performing grazing-incidence x-ray diffraction measurements. XRD spectra were measured using an X-Pert Analytical system with 0.43° incidence angle. The spectra recorded for ATO and ITO films with varying precursor concentration are shown below in Figure 2.9, alongside the primary reference peaks for each material[32], [33]. In the case of gravure-printed ITO, the conductivity of the films improves with precursor concentration and is optimized at approximately 2M. An analysis of the primary (222) peak FWHM in the XRD spectra (Figure 2.9b) of the ITO films indicates that the crystallite size is largest at 2M and decreases with increasing precursor concentration. AFM imaging (Figure 2.10) also shows larger crystallites in 2M ITO films than in thicker 4M films. ATO resistivity does not show a strong optimum at intermediate concentrations, but does demonstrate slight degradation at very high concentrations. In the XRD spectra (Figure 2.9a) of ATO films, no significant variation is observed in the primary (110) peaks. However, by AFM it is possible to observed that the aggregates in ATO printed films grow larger for higher concentration precursors, leading to an increase in surface roughness and the development of microcracks or voids which could give rise to the increased resistivity [34].

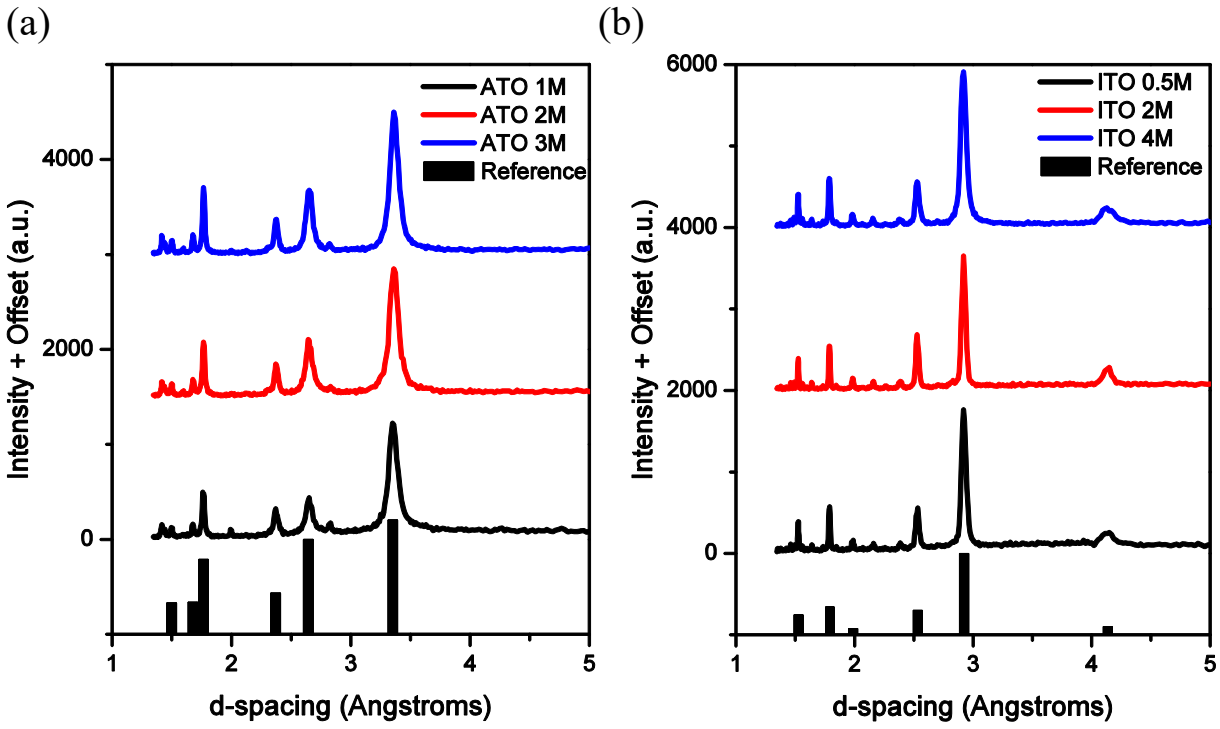


Figure 2.9 GIXD spectra of printed ATO (a) and ITO (b) films plotted with reference signal primary peaks indicated below in black (ICSD no. 154961, LPF no. 1216580).

Table 2.2 Scherrer-Debye equation estimated representative crystallite sizes for primary XRD peaks of ITO and ATO gravure-printed films.

| Ink | Concentration | Scherrer Crystallite Size | |
|---|---|---|---|
| **ITO** | | | |
| | 0.5 M | 3.65 nm | (222) |
| | 2 M | 4.38 nm | (222) |
| **ATO** | | | |
| | 1 M | 1.60 nm | (110) |
| | 2 M | 1.79 nm | (110) |
| | 3 M | 1.92 nm | (110) |

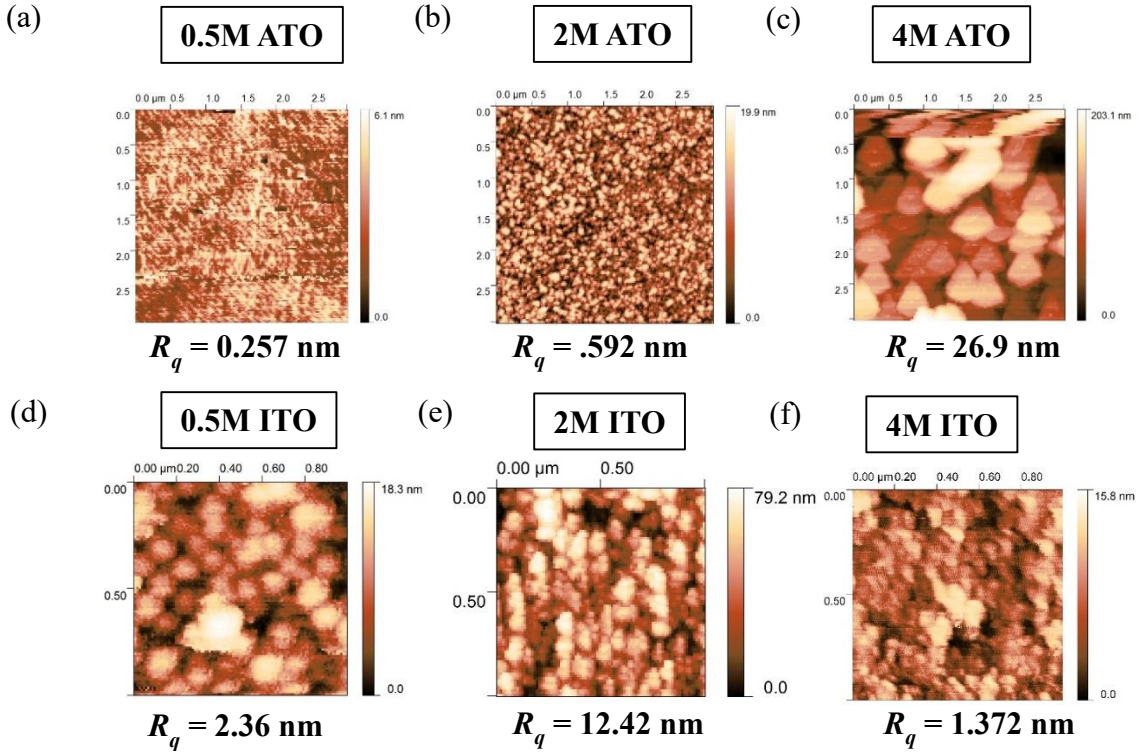


Figure 2.10 Printed film microscale surface morphology as measured by atomic force microscopy for ATO films (a,b,c) of varying precursor concentration and ITO films of varying precursor concentration (d,e,f).

## 2.5 Transparency of Printed TCOs

The effects of the sol-gel ink formulation on the quality of deposited films can similarly be observed by studying the transparency of the printed features. The sol-gel ink concentration

strongly determines the transparency of the gravure-printed sol-gel films. Optical transmittance was measured with a UV-visible spectrometer for normal incidence at wavelengths between 240nm and 1040nm with a spot size of diameter approximately 1mm. The measured transmittance in the visible range for ATO and ITO films follows similar trends to the conductivity of the material, degrading slightly as the film thickness increases. As illustrated in Figure 2.11a, the average optical transmittance over the visible spectrum (400 nm – 800 nm) decreases with increasing concentration of the ITO precursor. For films of optimal conductivity (*t ~ 100-150 nm*), the average transmittance is above 88% for both ITO and ATO. In the case of the highest concentration ink, the films (*t >300 nm*) have transmittance above 84%. ATO films formed by printing are also highly transparent, with transmittance above 88% for dilute precursors (0.5 M – 1.0 M). Concentrated ATO films are less transparent in the visible range and demonstrate a broader UV absorption edge. The printed films microstructure, as shown in Figure 2.10, suggests that in high concentration films, large aggregates and microcracks may scatter incident light, reducing transmittance.

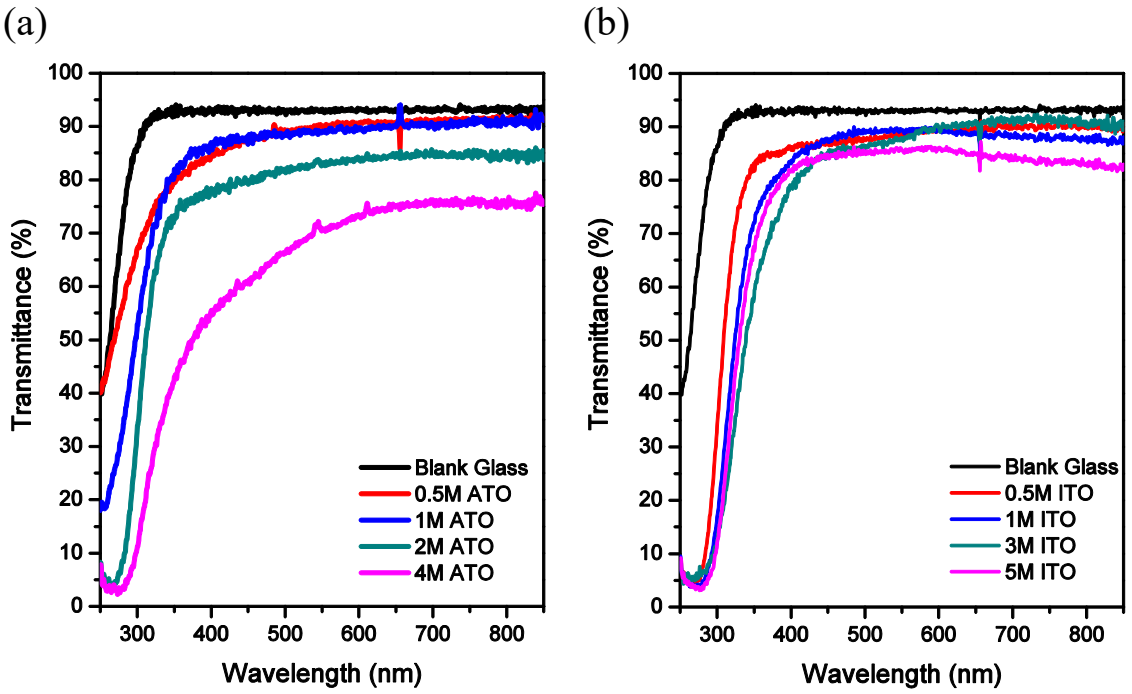


Figure 2.11 Transmittance of printed ATO films with bare glass substrate transmittance shown in black. (a) Transmittance of ITO film printed from inks of varying concentration. (b)

The mesoscale uniformity is another important parameter for transparent electrode applications. Uniformity was examined by optical microscopy and SEM, showing that low viscosity inks (1 M-2 M) give visually uniform films with high uniformity and fewer defects. High viscosity inks (4 M – 5 M) yield films with non-uniformities consisting of spinodal variations in thickness on lateral length scales of 1 – 5 mm, and, in the thickest films, cracking. While these results do show a limitation to printing thicker TCO layers, they may suggest that alternative annealing strategies (i.e. UV photo-annealing) could be employed to improve film quality and manage film stress.

Indeed, Chapter 6 in this thesis will utilize these strategies to develop low-temperature annealed sol-gel metal oxides.

### 2.6 Mechanical Flexibility of Sol-gel Inks

To understand the mechanical properties of TCO lines printed with the chosen ink formulations, bending tests were performed using TCO patterns and films on flexible willow glass substrates. Uniaxial bending stress tests and fatigue tests were performed on printed lines and films using an automated setup consisting of a 3-axis linear stage. The thin glass substrate was clamped on one end with two flat aluminum plates while the free end was deflected. The radius of curvature was extracted using curve fitting features in ImageJ. Figure 2.12 shows the variation of the sheet resistance of gravure-printed ATO with the measured bending radius. There is no detectable change in the electrical performance of the film during flexion after consecutive tests at various bending radii. As plotted in Figure 2.10a, the film strain is lower than 0.1% in all cases, since the flexible glass substrate consistently failed at a strain of approximately 0.12% - 0.15%. The glass substrate is visibly *flexible and bendable* in this application because it is thin. Likewise, the film sees low bending strains because the substrate is thin. Thinner flexible glasses which have been produced at thicknesses down to 50 μm can allow even greater bending, albeit at the expense of increased fragility.

The sheet resistance was also measured as a function of the number of bending cycles (Figure 2.12b) for compressive and tensile strain to study the fatigue properties of the ATO blanket film under flexion. There is negligible change in the sheet resistance of the ATO film under low strains (0.050% - 0.083%) for up to 10,000 cycles. Compared to the spatial variation in the sheet resistance, the small changes observed in resistance are not considered significant evidence for material degradation. Similar results have been reported for sputtered ITO on 50 μm thick glass substrates for tensile and compressive strain up to 0.21% [35]. Indeed, it is unsurprising that the ATO film is not degraded by moderate bending, considering that the onset of cracking and film degradation is typically above 1% strain in sputtered films on plastic foils[36]. This indicates that thermally capable substrate materials with greater flexibility than glass could extend the bendability and available form factors for metal oxide thin film electronics even further.

There are two important implications of the mechanical reliability of the printed ATO films. The first is the viability of R2R processing of flexible glass substrates. The finding that film stress in the ATO layer is low enough to avoid cracking or degradation in sheet resistance is important for allowing extensive web-based processing during which the film and substrate would sustain many cycles of moderate tensile and compressive stress during spooling operations. Indeed, the flexibility characteristics are vital for taking full advantage of the scalability of gravure printing for forming high quality TCO electrodes and films in a high-throughput roll-to-roll process. Secondly, we expect that these materials and methods provide an effective route to enabling large area applications that require the flexibility, transparency, and light weight substrates. The light weight aspect of these substrates could potentially contribute to lowering the overall balance of systems cost for energy technologies.

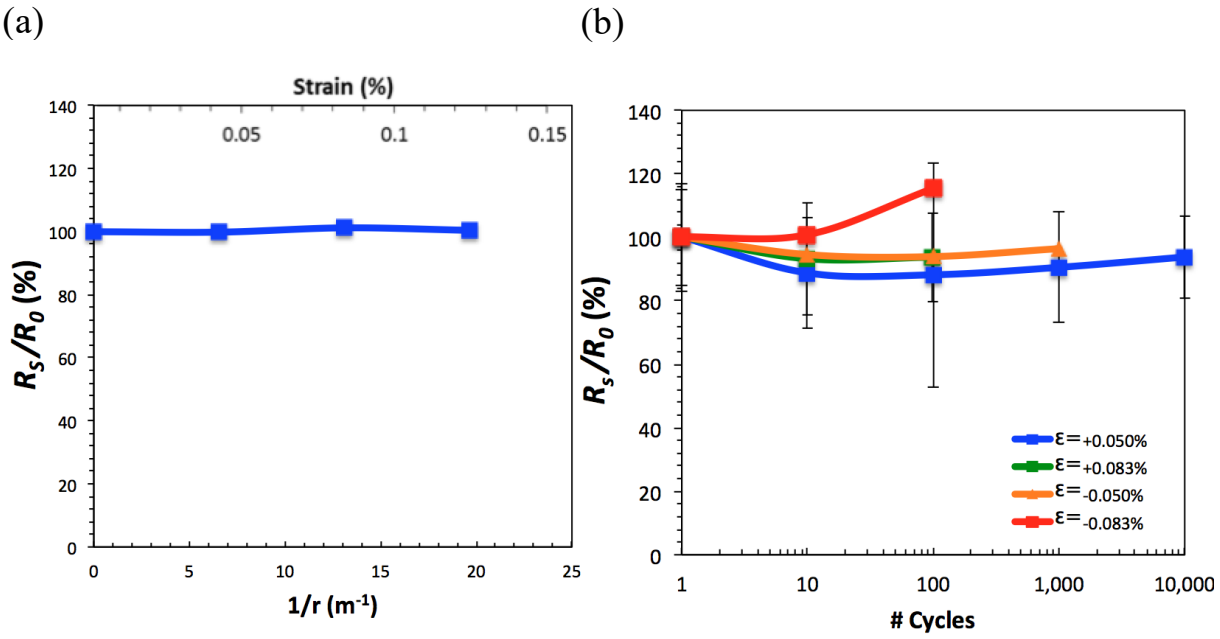


Figure 2.12 Normalized sheet resistance of printed ATO lines (40 µm width) as a function of inverse bending radius and strain for uniaxial bending applied along the axis of the printed lines. (a) Normalized sheet resistance of printed ATO films vs number of cycles for compressive (+) and tensile ( - ) strain. (b)

## 2.7 Summary

TCO sol-gel inks for gravure printing have been developed for patterning fine features (line widths ~ 35-50 µm) and the properties of printed conductors have been investigated as a function of the ink formulation. Ink formulations methodologies based on concentrated sol-gel precursors and cosolvent systems are demonstrated as methods for designing gravure inks with the proper fluid properties to achieve optimal patterning. Sol-gel inks including ITO and ATO prepared with high precursor concentration show improved printing performance due to their increased viscosity (over 100 cP). Patterning metrics such as line-edge roughness and line-width roughness are improved and the 3D morphology is enhanced, producing lines free of coffee-ring features. The electrical performance of printed lines and films also improves with increasing precursor concentration, resulting in single layers with $R_S$ as low as 100 Ω / ☐ with average (400 nm ≤ λ ≤ 800 nm) visible transmittance of 85-88 %. Finally, the flexibility of printed ATO electrodes on Corning Willow glass (100 µm thick) was investigated, showing negligible variation in $R_s$ with bending stress and bending fatigue up to $10^4$ cycles. Collectively, these results illustrate the tradeoffs between fluid ink design and electronic material properties a theme which will be addressed throughout this thesis. Later chapters will show how this tradeoff can be mitigated by using alternative ink designs and annealing methods which allow low temperature conversion. These strategies enhance electrical performance and lower the thermal budget to make these gravure-printed inorganic electronics more technologically viable.

## 2.8 References


[1] F. C. Krebs, S. A. Gevorgyan, and J. Alstrup, "A roll-to-roll process to flexible polymer solar cells: model studies, manufacture and operational stability studies," *J. Mater. Chem.*, vol. 19, no. 30, pp. 5442–5451, 2009.

[2] E. Fortunato, D. Ginley, H. Hosono, and D. C. Paine, "Transparent Conducting Oxides for Photovoltaics," *MRS Bull.*, vol. 32, no. 03, pp. 242–247, Mar. 2007.

[3] A. Andersson, N. Johansson, P. Bröms, N. Yu, D. Lupo, and W. R. Salaneck, "Fluorine Tin Oxide as an Alternative to Indium Tin Oxide in Polymer LEDs," *Adv. Mater.*, vol. 10, no. 11, pp. 859–863, Aug. 1998.

[4] K. A. Sierros and S. N. Kukureka, "Mechanical integrity of touch-screen components," *J. Soc. Inf. Disp.*, vol. 17, no. 11, pp. 947–952, Nov. 2009.

[5] M. Eritt, C. May, K. Leo, M. Toerker, and C. Radehaus, "OLED manufacturing for large area lighting applications," *Thin Solid Films*, vol. 518, no. 11, pp. 3042–3045, Mar. 2010.

[6] M. Katayama, "TFT-LCD technology," *Thin Solid Films*, vol. 341, no. 1, pp. 140–147, Mar. 1999.

[7] U. Betz, M. Kharrazi Olsson, J. Marthy, M. F. Escolá, and F. Atamny, "Thin films engineering of indium tin oxide: Large area flat panel displays application," *Surf. Coat. Technol.*, vol. 200, no. 20, pp. 5751–5759, May 2006.

[8] S. Ju et al., "Fabrication of fully transparent nanowire transistors for transparent and flexible electronics," *Nat. Nanotechnol.*, vol. 2, no. 6, pp. 378–384, Jun. 2007.

[9] S. E. Habas, H. A. S. Platt, M. F. A. M. van Hest, and D. S. Ginley, "Low-Cost Inorganic Solar Cells: From Ink To Printed Device," *Chem. Rev.*, vol. 110, no. 11, pp. 6571–6594, Nov. 2010.

[10] A. C. Arias, J. D. MacKenzie, I. McCulloch, J. Rivnay, and A. Salleo, "Materials and Applications for Large Area Electronics: Solution-Based Approaches," *Chem. Rev.*, vol. 110, no. 1, pp. 3–24, Jan. 2010.

[11] D.-H. Lee, Y.-J. Chang, G. S. Herman, and C.-H. Chang, "A General Route to Printable High-Mobility Transparent Amorphous Oxide Semiconductors," *Adv. Mater.*, vol. 19, no. 6, pp. 843–847, Mar. 2007.

[12] J. Puetz and M. A. Aegerter, "Direct gravure printing of indium tin oxide nanoparticle patterns on polymer foils," *Thin Solid Films*, vol. 516, no. 14, pp. 4495–4501, May 2008.

[13] J. Puetz, S. Heusing, M. de Haro Moro, C. M. Ahlstedt, and M. A. Aegerter, "Gravure printing of transparent conducting ITO coatings for display applications," *Proc. SPIE* 2005, vol. 5963, p. 59631E–59631E–8.

[14] M. Jørgensen, K. Norrman, and F. C. Krebs, "Stability/degradation of polymer solar cells," *Sol. Energy Mater. Sol. Cells*, vol. 92, no. 7, pp. 686–714, Jul. 2008.

[15] Y. Zhou et al., "A Universal Method to Produce Low–Work Function Electrodes for Organic Electronics," *Science*, vol. 336, no. 6079, pp. 327–332, Apr. 2012.

[16] R. Kitsomboonloha, S. J. S. Morris, X. Rong, and V. Subramanian, "Femtoliter-Scale Patterning by High-Speed, Highly Scaled Inverse Gravure Printing," *Langmuir*, vol. 28, no. 48, pp. 16711–16723, Dec. 2012.

[17] S. M. Garner et al., "Cholesteric Liquid Crystal Display With Flexible Glass Substrates," *J. Disp. Technol.*, vol. 9, no. 8, pp. 644–650, Aug. 2013.

[18] S. Garner, S. Glaesemann, and X. Li, "Ultra-slim flexible glass for roll-to-roll electronic device fabrication," *Appl. Phys. A*, vol. 116, no. 2, pp. 403–407, Aug. 2014.

[19] Z. Chen, W. Li, R. Li, Y. Zhang, G. Xu, and H. Cheng, "Fabrication of Highly Transparent and Conductive Indium–Tin Oxide Thin Films with a High Figure of Merit via Solution Processing," *Langmuir*, vol. 29, no. 45, pp. 13836–13842, Nov. 2013.
[20] K. Ellmer, "Past achievements and future challenges in the development of optically transparent electrodes," *Nat. Photonics*, vol. 6, no. 12, pp. 809–817, Dec. 2012.
[21] T. D. Senguttuvan and L. K. Malhotra, "Sol gel deposition of pure and antimony doped tin dioxide thin films by non alkoxide precursors," *Thin Solid Films*, vol. 289, no. 1, pp. 22–28, Nov. 1996.
[22] C. Avis, H. R. Hwang, and J. Jang, "Effect Of Channel Layer Thickness On The Performance Of Indium–Zinc–Tin Oxide Thin Film Transistors Manufactured By Inkjet Printing," *ACS Appl. Mater. Interfaces*, vol. 6, no. 14, pp. 10941–10945, Jul. 2014.
[23] D. Kim, Y. Jeong, K. Song, S.-K. Park, G. Cao, and J. Moon, "Inkjet-Printed Zinc Tin Oxide Thin-Film Transistor," *Langmuir*, vol. 25, no. 18, pp. 11149–11154, Sep. 2009.
[24] H. Kang, R. Kitsomboonloha, J. Jang, and V. Subramanian, "High-Performance Printed Transistors Realized Using Femtoliter Gravure-Printed Sub-10 μm Metallic Nanoparticle Patterns and Highly Uniform Polymer Dielectric and Semiconductor Layers," *Adv. Mater.*, vol. 24, no. 22, pp. 3065–3069, Jun. 2012.
[25] J. Jang, H. Kang, H. C. N. Chakravarthula, and V. Subramanian, "Fully Inkjet-Printed Transparent Oxide Thin Film Transistors Using a Fugitive Wettability Switch," *Adv. Electron. Mater.*, vol. 1, no. 7, p. 1500086, Jul. 2015.
[26] C. J. Brinker and G. W. Scherer, "Sol → gel → glass: I. Gelation and gel structure," *J. Non-Cryst. Solids*, vol. 70, no. 3, pp. 301–322, Apr. 1985.
[27] C. J. Brinker and G. W. Scherer, Sol-Gel Science: The Physics and Chemistry of Sol-Gel Processing. Academic Press, 2013.
[28] M. Majumder et al., "Overcoming the 'Coffee-Stain' Effect by Compositional Marangoni-Flow-Assisted Drop-Drying," *J. Phys. Chem. B*, vol. 116, no. 22, pp. 6536–6542, Jun. 2012.
[29] S. Azizian and M. Hemmati, "Surface Tension of Binary Mixtures of Ethanol + Ethylene Glycol from 20 to 50 °C," *J. Chem. Eng. Data*, vol. 48, no. 3, pp. 662–663, Mar. 2003.
[30] S. R. Ramanan, "Dip coated ITO thin-films through sol–gel process using metal salts," *Thin Solid Films*, vol. 389, no. 1, pp. 207–212, Jun. 2001.
[31] M. M. Koebel, D. Y. Nadargi, G. Jimenez-Cadena, and Y. E. Romanyuk, "Transparent, Conducting ATO Thin Films by Epoxide-Initiated Sol–Gel Chemistry: A Highly Versatile Route to Mixed-Metal Oxide Films," *ACS Appl. Mater. Interfaces*, vol. 4, no. 5, pp. 2464–2473, May 2012.
[32] B. Gržeta et al., "Structural studies of nanocrystalline SnO2 doped with antimony: XRD and Mössbauer spectroscopy," *J. Phys. Chem. Solids*, vol. 63, no. 5, pp. 765–772, May 2002.
[33] J. Popović, E. Tkalčec, B. Gržeta, C. Goebbert, V. Ksenofontov, and M. Takeda, "Defect structure examination of Sn-doped indium oxide (ITO)," *Z. Krist. Suppl.*, vol. 2007, pp. 489–494, Nov. 2007.
[34] G. Zhang and M. Liu, "Preparation of nanostructured tin oxide using a sol-gel process based on tin tetrachloride and ethylene glycol," *J. Mater. Sci.*, vol. 34, no. 13, pp. 3213–3219, Jul. 1999.
[35] K. Alzoubi, M. M. Hamasha, S. Lu, and B. Sammakia, "Bending Fatigue Study of Sputtered ITO on Flexible Substrate," *J. Disp. Technol.*, vol. 7, no. 11, pp. 593–600, Nov. 2011.
[36] M. D. J. Auch, O. K. Soo, G. Ewald, and C. Soo-Jin, "Ultrathin glass for flexible OLED application," *Thin Solid Films*, vol. 417, no. 1, pp. 47–50, Sep. 2002.

# Chapter 3: Gravure-Printed Nanowire Hybrid Transparent Conductors

## 3.1 Introduction

Active and passive transparent electronics depend on the use of transparent conductive electrodes for current injection and collection. In Chapter 2 of this thesis, methods were developed for printing sol-gel based transparent conductors on glass substrates. These studies revealed a few of the limitations of sol-gel based transparent conductors, including the lower conductivity relative to vacuum deposited films and the requirement of high-temperature annealing steps in a furnace which precludes the use of plastic substrates. High performance thin film solar cells, sensors, and OLEDs, will require transparent conductors which have comparable performance and high uniformity. This chapter will show how to solve these issues by using a hybrid ink that achieves high performance using 1D nanomaterials and enhances printability and mechanical robustness using sol-gel conductors.

Nanomaterials including metal nanowire meshes, graphene, and composites of both these materials have recently demonstrated high DC to optical conductivity ratios on par or better than sputtered transparent conducting oxides such as ITO, while retaining excellent performance under high bending strain[1]. Importantly, these nanomaterial-based flexible TCE's have each been processed from liquid precursors by techniques such as spin-coating[1], spray deposition[2], inkjet printing[3], and blade coating[4], which theoretically can allow for vacuum-free processing over large areas and the use of low-cost transparent polymer substrates.

The development of large-scale applications of these flexible solution-processed TCEs depends on continued advances in two areas. First, the development of mechanically robust and chemically stable materials is needed to allow TCE integration in multilayer devices that have ubiquitous applications. Wearable devices, for example, will require greater stability under tactile stresses and moist or wet conditions. Composite materials formed from metallic nanowires and polymers[5], [6], graphene[7], or metal oxides[8], [9] are strong candidates to address this mechanical and chemical robustness, respectively, of TCE's. To date, however, composite Ag NW films have utilized multi-step deposition processes which add considerable process complexity and cost and required vacuum-processing [10]. The second area in which TCEs must advance is in the development of deposition techniques that are high-throughput and roll-to-roll (R2R) compatible. There is significant economic motivation for additive patterning of relatively expensive TCE materials, such as silver nanowires and graphene, which may initially have a high cost driven by expensive synthesis procedures and bulk material prices. Techniques such as spin-coating, with low material utilization, may be unsuitable for these reasons. Thus, leveraging the full benefits of solution-processing will be essential for these alternative TCEs to be competitive in transparent thin film device applications over incumbent technologies.

High-throughput, additive printing processes, such as gravure printing, can offer a route to more sustainable TCE production for a range of applications requiring patterned or blanket films. As discussed in Section 1.2, gravure is a widespread, industrially proven technique that is among the highest resolution[11] and highest speed methods in R2R printing. The advantages of gravure stem from its use of microscale cells engraved in the polished surface of a rigid metallic cylinder to

directly deposit metered ink volumes. The use of cell-based engraving can allow formation of an extensive variety of microscale patterns (< 20 μm)[12], and the use of a wide range of ink viscosities (10 cP - 200 cP)[13]. In the past, the use of gravure printing for depositing TCEs has primarily been limited to depositing polymeric materials such as PEDOT:PSS[14], which can easily be formulated into inks with suitable rheology. However, compared to leading materials, such as metal nanowire meshes (Ag, Cu, Au), polymeric conductors have lower performance and limited environmental and chemical stability due to water absorption[15], [16]. New ink design strategies for high-throughput printing of metal nanowire conductors that give good printability *and* high performance are, therefore, of critical interest.

In the past, however, the printing and patterning of metal nanowires has been limited by their high-aspect ratio geometry (lengths > 10μm), which typically causes clogging for nozzle based printing techniques. High aspect ratios are needed to ensure the high conductivity and high transparency of the nanowire mesh network[17]. Recently, the unfavorable geometry of metal nanowires was overcome using inverse gravure to pattern silver nanowires utilizing rigid copper plates with etched trenches resembling intaglio print forms.[18] Additionally, inkjet printing has been used to print lines of silver nanowires, using dilute solutions and more than 50 printing passes[19]. However, the use of high-speed roll-based gravure printing has not been investigated for depositing and patterning silver nanowire composite films. Thus, there is a strong need for developing robust TCE materials that are amenable to high-throughput printing, particularly for allowing integration with other printed materials and devices.

In this chapter, we develop R2R-compatible printed composite TCE materials based on a highly conductive silver nanowire (Ag NW) mesh embedded in a mechanically robust sol-gel metal oxide matrix of Indium Zinc Oxide (IZO). Air stable hybrid ink formulations are presented, which allow rapid deposition of IZO/Ag NW composite films from a *single* liquid precursor ink by gravure printing on both glass and plastic substrates. Gravure printing methods are presented for high-speed (1 m/s) additive patterning of transparent conductive films. These composite inks show improved printing performance relative to inks formulated from pure nanowire dispersions with higher uniformity and significantly lower sheet resistance. The hybrid printed films also exhibit adhesion, planarity, and thermal stability which are significantly improved during the densification of the encapsulating sol-gel metal oxide matrix. Thus, this study introduces a class of composite materials that simultaneously leverage the properties of 1D conductive nanomaterials and sol-gel metal oxides to address the current limitations of flexible TCE materials and manufacturing.

### 3.2 Nanowire Hybrid Ink Design

Sol-gel metal oxides are a class of well-studied solution-processed materials with excellent mechanical and chemical stability. But while these materials offer suitable ink rheology for R2R compatible printing, they have limited transparency and relatively low conductivity compared to metallic nanowire mesh systems[13]. Bare metallic nanowire meshes alone have excellent conductivity and transparency but suffer from low environmental stability and poor adhesion[6]. To capture the key benefits of these two classes of materials, hybrid IZO/Ag NW composite liquid precursor inks were formulated from organic sol-gel precursors and silver nanowires dispersed in ethanol. IZO was used as the sol-gel metal oxide matrix rather than tin-containing indium tin oxide (ITO) or zinc tin oxide (ZTO), first because of the improved solubility of indium and zinc acetate precursors in stable Ag NW dispersions relative to tin-based precursors. IZO also offers a

combination of high conductivity[20] and good resistance to crystallization[21] during thermal annealing, which have important implications for use in applications requiring stable performance under bending stress[22].

The nanowire hybrid inks were prepared from a mixture of Ag NWs dispersed in ethanol (Blue Nano Inc., average diameter 33nm, average length 14um) and IZO sol-gel precursors (Indium Acetate, 99.99%, Zinc Acetate dehydrate, 99.99%) dissolved in a 2:1 mixture (volume ratio) of 2-methoxyethanol and monoethanolamine. The sol-gel precursor ink was sonicated for 1 hour until complete dissolution occurred, and the solution was subsequently filtered through a 0.2 μm PTFE filter before mixing with the Ag NW dispersion. During storage in a dry environment, the ink remained stably dispersed for more than three months without showing signs of flocculation. In contrast, the addition of inorganic sol-gel precursors composed of chloride or nitrate anions caused immediate flocculation of silver nanowires and could not form stable inks. This prevented the extension of these ink formulation methods to the precursor set used for previous studies of gravure-printed TCO materials, which primarily utilized nitrate and chloride based chemistries. Two step depositions were performed, however, using nitrate and chloride based ITO and ATO sol-gels in separate inks from the Ag NWs.

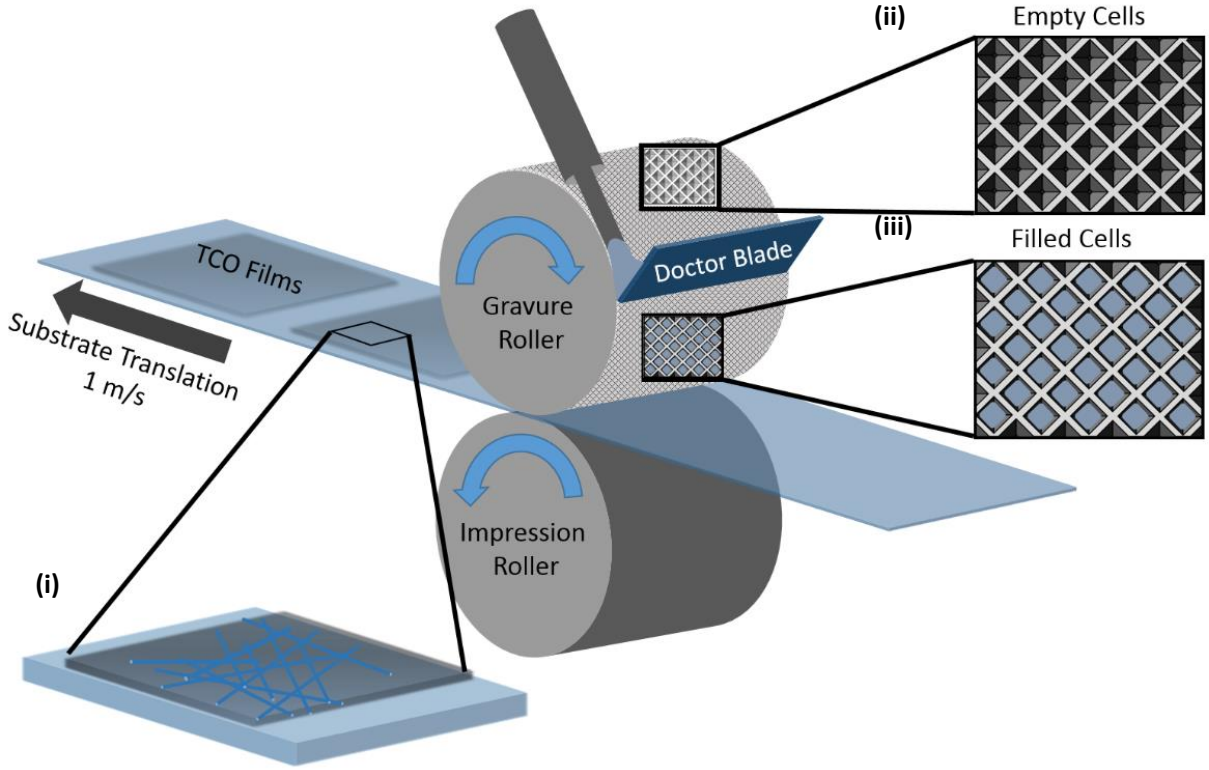


Figure 3.1. Schematic of the high-speed roll-based process used to print nanowire conductive hybrid films (inset i) with metal rollers engraved with gravure cells (ii, iii).

The rheology of these functional hybrid inks was first investigated to determine formulations appropriate for gravure printing. The gravure printing process (Figure 3.1) is known to be highly sensitive to the ink viscosity over a range of shear rates and typically requires viscosities in the range of 5 - 500 cP for effective ink transfer and pattern formation[11]. To achieve a target viscosity in this range, the hybrid inks were enhanced by the inclusion of the metal oxide sol-gel precursors. A rotational viscometer (Brookfield DV-III) was used to measure the viscosity of the printed inks. As shown in Figure 3.2, the viscosity of Ag NW inks can be increased significantly by using such a hybrid ink formulation. For the highest concentrations of Ag NWs, viscosities above 20 cP were obtainable with the hybrid inks (Figure 3.2c) whereas Ag NW inks without IZO precursors (Figure 3.2a) did not exceed 6 cP. Raising the concentration of Ag NW's resulted in a

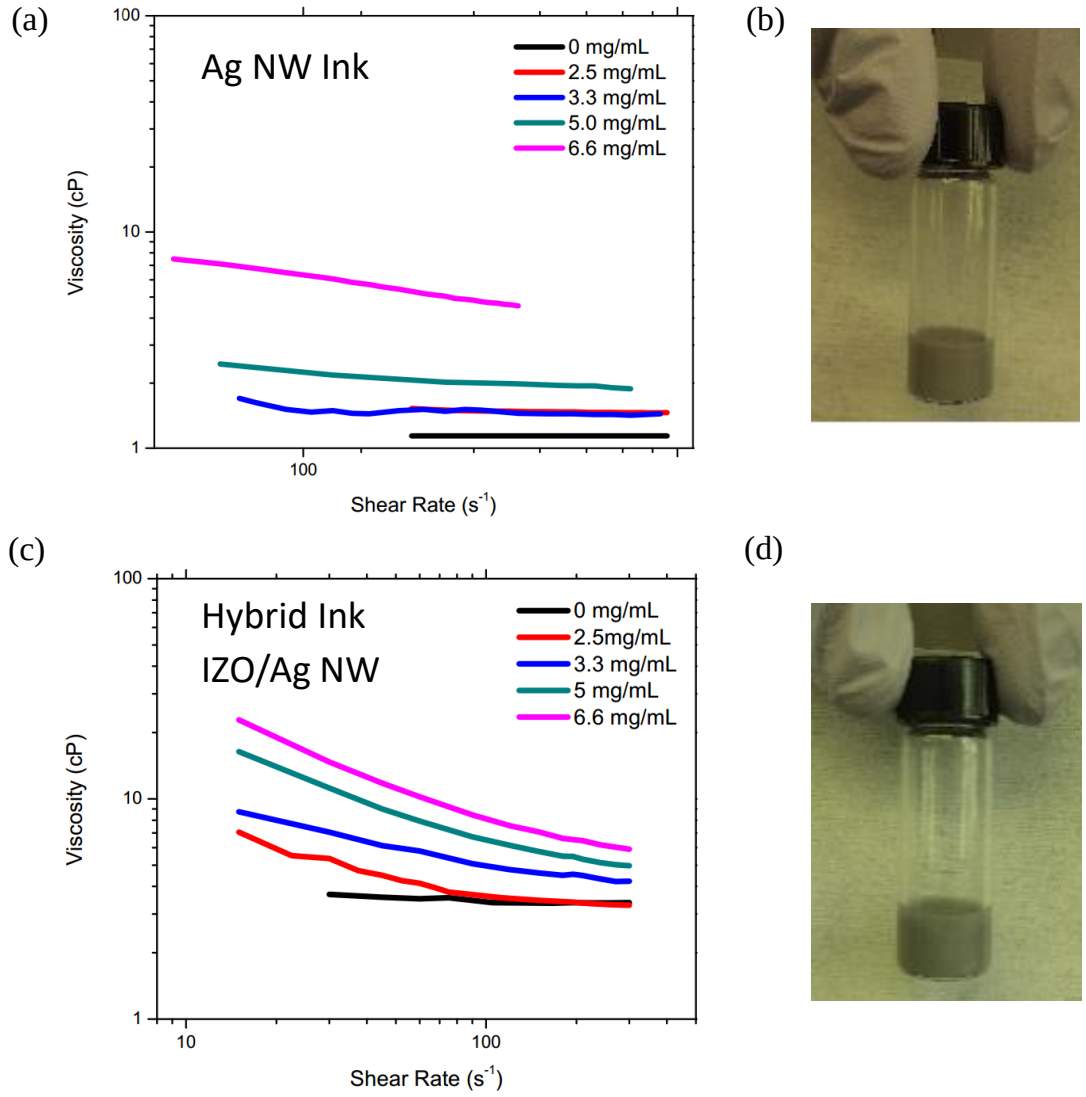


Figure 3.2 Viscosity of (a) pure Ag NW gravure inks and (c) hybrid IZO/Ag NW gravure inks vs shear rate for varying Ag NW concentrations. Pictures illustrate air-stable formulated inks consisting of 3.3 mg/mL Ag NW without (b) and with (d) IZO sol-gel precursors.

roughly linear increase in the viscosity of both types of inks. In the case of the hybrid IZO/Ag ink, stronger shear-thinning behavior appeared at higher Ag NW concentrations (5 mg/mL and 6.6 mg/mL). This trend of shear thinning at higher concentrations is also commonly observed for silver nanoparticle inks[23] and is suggestive of stronger interactions between dispersed particles, which may result from the ionic strength of the sol-gel precursors. Thus, by including sol-gel precursors, a stable ink with suitable rheology was formulated for gravure printing blanket films.

The solvent composition of the hybrid inks (Figure 3.3a) was designed to allow sufficient time for ink spreading and leveling for the formation of uniform films. This was accomplished with a mixture of low boiling point solvents (ethanol and 2-methoxyethanol) and a higher boiling point solvent (monoethanolamine). Monoethanolamine also served as the stabilizer for the sol-gel components of the hybrid ink to limit aging that would otherwise cause precursors to form precipitates that crash out of solution. The solid composition of the ink, as shown in Figure 3.3b, primarily consisted of indium and zinc acetate metal salt sol-gel precursors. This is to be expected since the bulk of the film is still composed of the sol-gels rather than the silver wires. Inks mixed with higher concentrations of sol-gel precursors and silver nanowires were also formulated, resulting in higher ink viscosity. These concentrated inks may be more suitable for printing patterned features rather than blanket films because their high viscosity may reduce spreading, as demonstrated for sol-gel inks in Chapter 2.

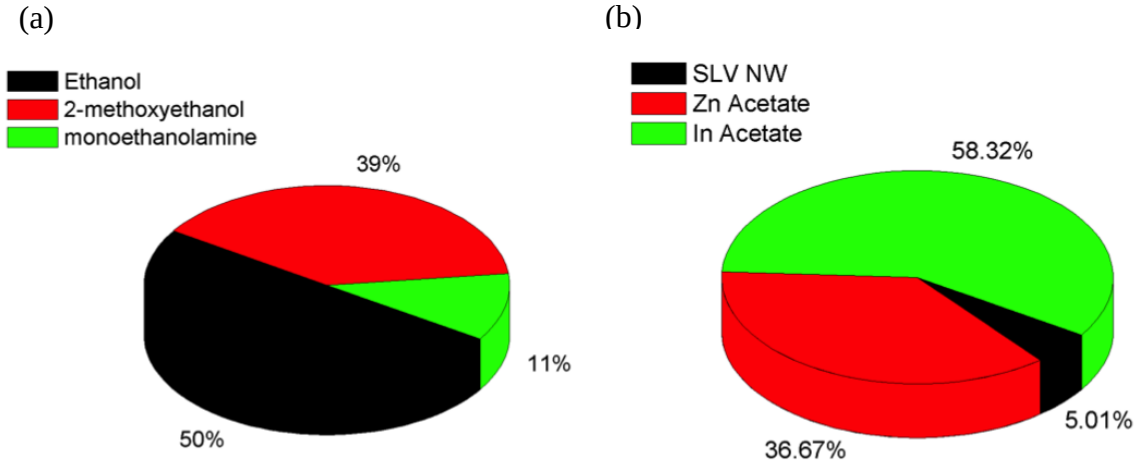


Figure 3.3 Solvent composition (a) and dissolved solid mass-loading composition of printed hybrid inks.

### 3.3 Gravure Printing Conductive Silver Nanowire Films

The nanowire-containing inks were gravure printed on glass and plastic substrates as shown in the schematic of Figure 3.1. Gravure cylinders with cells (Figure 3.1a-ii) larger than 60 μm in width were utilized to facilitate effective cell filling (Figure 3.1a-iii) of inks containing nanowires approximately 10 - 20 μm in length. Gravure cell sizes below 35 μm (depth 20 - 25 μm) showed

limited printing of nanowire inks. Instead, ink was captured by the doctor blade wiping process and only fragments of wires and residue filled the cells and transferred to the substrate.

Gravure printing of blanket films was performed with a blanket coating cylinder (Figure 3.4a)

(a) (b)

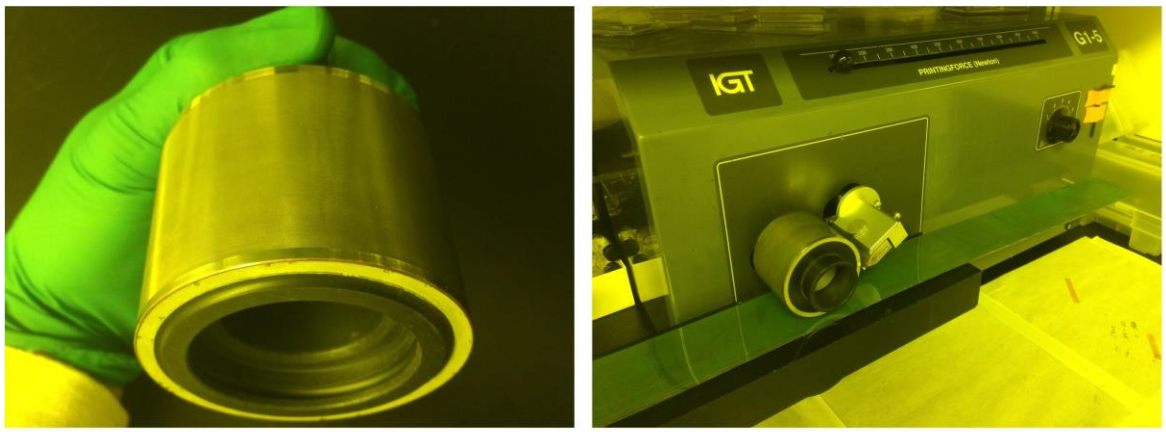


Figure 3.4 Chrome-coated blanket coating gravure roller (a) and IGT G1-5 benchtop gravure printer with speed and printing contact force control (b).

from IGT Systems (402.450.133) with a theoretical coating volume of 13.5 mL/m$^3$, a cell density of 300 lines/cm, and a stylus angle of 54°,. Printing was performed on an IGT G1-5 proofer (Figure 3.4b) at 1.0 m/s with a printing force of 200 N/500 N for glass and PEN substrates, respectively. To investigate the printing physics of 1D nanostructures, rectangular films of silver nanowires were printed on both plastic and glass substrates using 60 µm gravure cells, resulting in features with dimensions on the order of 500 µm – 2 mm. The printed films were observed to be electrically isolated from one another, but some residual nanowires remained in the field regions between the patterns. These deposits are consistent with a form of *residue* or lubrication film as has been discussed in Section 1.2.1 for other gravure-printed inks. Besides these regions of residual nanowires, the films exhibited relative uniform densities of deposited ink. The angular distribution of the silver nanowires was analyzed to determine whether any significant alignment occurred during deposition. A 2D fourier transform of microscope images of the printed films (Figure 3.5a-i) shows a slight weighting in the ± 30° direction, which roughly corresponds to the orientation of the array of diamond shaped cells on the gravure roller. This degree of alignment was not found to considerably influence transport in the printed nanowire films, as electrical measurements in the orthogonal and parallel directions were roughly equivalent.

The uniformity and ink transfer also appear to improve with print speed. As shown below in Figure 3.6, the sheet resistance of printed films of pure Ag NW improves by approximately 50 % as the print speed is increased from 200 mm/s to 1000 mm/s. At high print speeds, more uniform films are observed with fewer clumps of nanowires. The variation in the sheet resistance across the substrate reflects these changes in the film, with high print speeds resulting in tighter distributions of film conductivity across a single printed substrate.

(a)

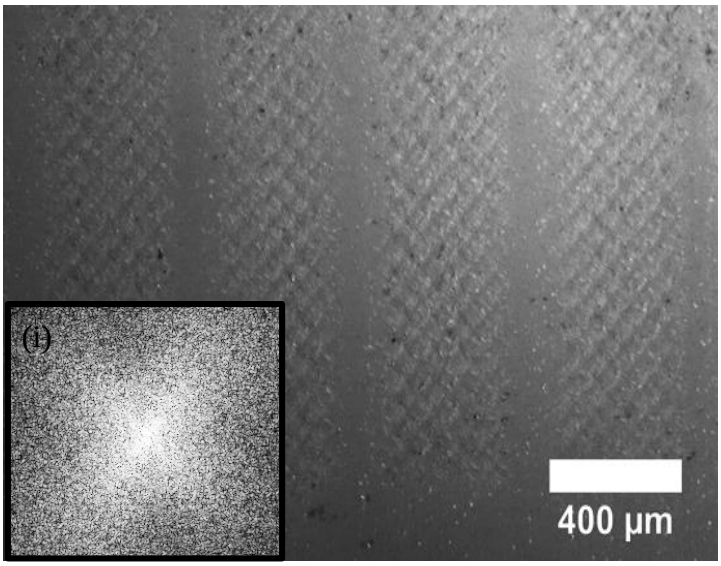


(b)

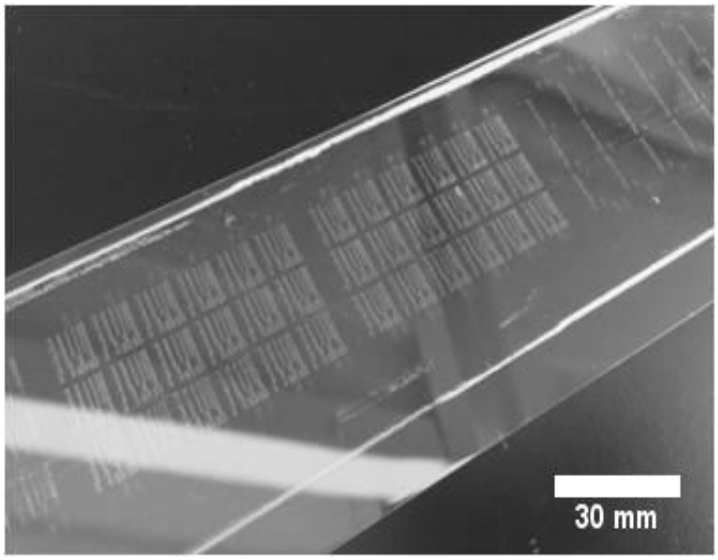


Figure 3.5 Patterned films of Ag NW printed with 60 µm gravure cells (a) with inset (i) showing 2D Fourier transform of printed films. Plastic substrate with patterned silver nanowire regions (b).

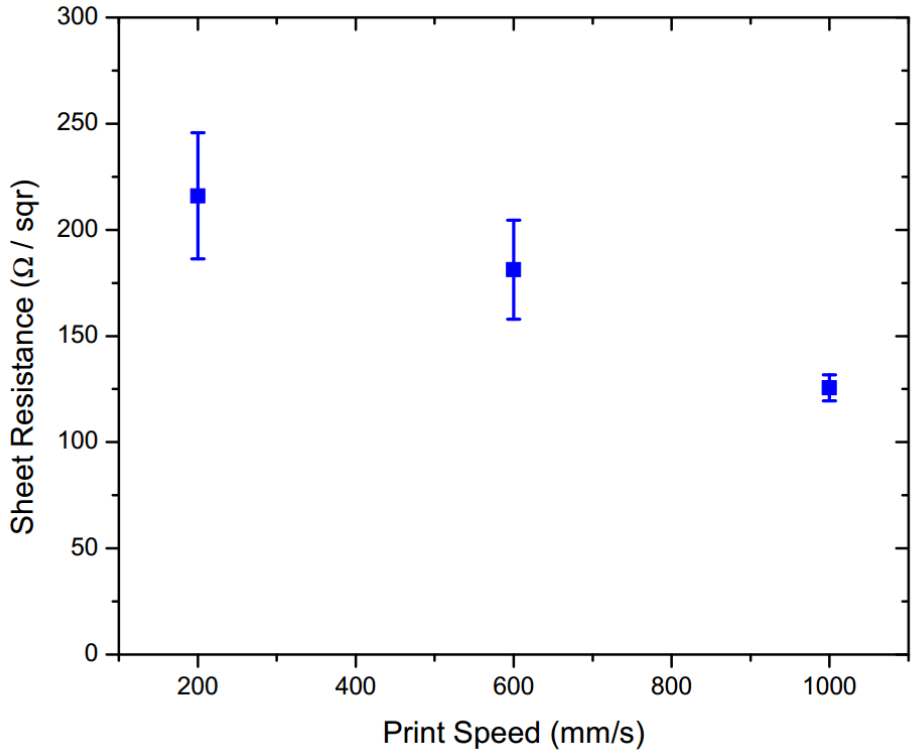


Figure 3.6 Sheet resistance vs print speed for 10 mg/mL pure Ag NW inks annealed at 125 °C in air for 10 minutes.

### 3.4 Conductivity of Printed TCO Films

Thermal annealing of glass substrates was performed in air on a hot plate (100 °C – 300 °C) with an aluminum vacuum chuck or in a tube furnace under clean dry air flow (10 scfh) for higher temperature anneals (325 °C). PEN substrates were annealed at 175 °C on a vacuum hotplate to maintain intimate contact despite thermal expansion. The duration of each anneal was 10 minutes. Substrates were prepared for gravure printing by sonication in soapy water, acetone, and isopropanol. Substrates were treated with ultraviolet ozone for 5 minutes to improve ink transfer and enhance ink spreading. Printing on untreated substrates resulted in poor uniformity and visible pinholes.

The printed nanowire inks were annealed on a hot plate to produce transparent conductive thin films. The effects of increasing the inks' silver nanowire mass-loading on conductivity were examined for a given printing condition (1.0 m/s, 100 N) and annealing temperature (175°C), as shown in Figure 3.7. Conductivity measurements were performed both with a semiconductor parameter analyzer (HP 4155) and a four-point probe (Agilent 5400) in ambient conditions. Two point measurements were achieved by pre-patterning 2mm wide silver contact pads by inkjet printing a low temperature sintering silver ink (ANP DGP-0LT40) and mechanically isolating measurement regions to avoid current spreading. Similar four point measurements indicated that the contact resistance between silver contact pads and the nanowire films was negligible. Sheet resistances were calculated after measuring a set of 15 devices distributed across a total area of

approximately 35 $cm^2$. The sheet resistance of the resulting films decreases strongly for higher Ag NW mass-loading as a denser network of wires is formed. The comparison between hybrid inks and pure Ag NW inks indicates that the sol-gel hybrid ink results in more conductive and uniform films, with sheet resistance as low as 9.3 Ω/□ at the highest mass-loading of 6.6 mg/mL. For lower mass-loading cases, the difference between hybrid inks and pure Ag inks is also significant, showing nearly an order of magnitude of improvement at 2 mg/mL Ag mass loading.

The use of a hybrid ink also influences the uniformity of the printed films electrical properties. The relative variance of the sheet resistance, computed after sampling approximately 15 locations across a 35 $cm^2$ area, is generally improved for films fabricated from high mass-loading inks. Particularly for the hybrid inks, the higher mass-loading cases result in more uniform values of sheet resistance with a low coefficient of variation ($\sigma / \mu < 5\%$). These results suggest that a more even areal distribution of Ag NW is obtained in films printed from the hybrid inks, which favors their lower sheet resistance at a given nanowire mass-loading. This enhanced homogeneity and low sheet resistance is critical for optoelectronic applications such as OLEDs, which must achieve highly uniform luminous intensity across a large area for applications such as indoor lighting[24]. It also could be essential for thin film solar cells which require highly conductive window electrodes.

### 3.5 Nanowire network modelling

The nanowire composites were modelled as 2-D random resistor networks embedded in a matrix of constant sheet resistance $R_{matrix}$. The resistance per unit length of the nanowires was based on the bulk conductivity of silver and a junction resistance, $R_{int}$, was included at each intersection of two nanowires. Solving the Laplacian matrix of the network permitted the calculation of two-point resistances between nodes and thus an estimation of the sheet resistance of the composite. To explore the influence of the hybrid ink on charge transport, simulation-based transport analysis was performed. To achieve this, the film was modeled as a randomly generated network of Ag nanowires embedded in a homogeneous conductive matrix. Nanowire networks with various areal densities were randomly generated by this method (Figure 3.8) with material and geometric properties matching those of the films fabricated herein (Table 3.1). The resulting sheet resistances were obtained by solving a matrix representation of the resistive network for different values of the junction resistance ($R_{int}$) between nanowires. Finally, the simulated networks were plotted against experimental results by calibrating to areal densities of printed films as measured by top view HRSEM imaging.

As shown in Figure 3.7b, these network simulations capture the critical behavior of the films' sheet resistance with respect to the ink design and annealing conditions. For example, the dramatic decrease in sheet resistance at relatively low areal densities could represent the onset of effective percolation conduction, indicating that small increases in Ag NW mass-loading result in large improvements in film conductivity. The strong influence of the nanowire junction resistance at high mass-loadings predicted by simulation matches previous reports [25], and indicates the important role of generating low-resistance nanowire to nanowire contacts by various means to improve network conductivity.

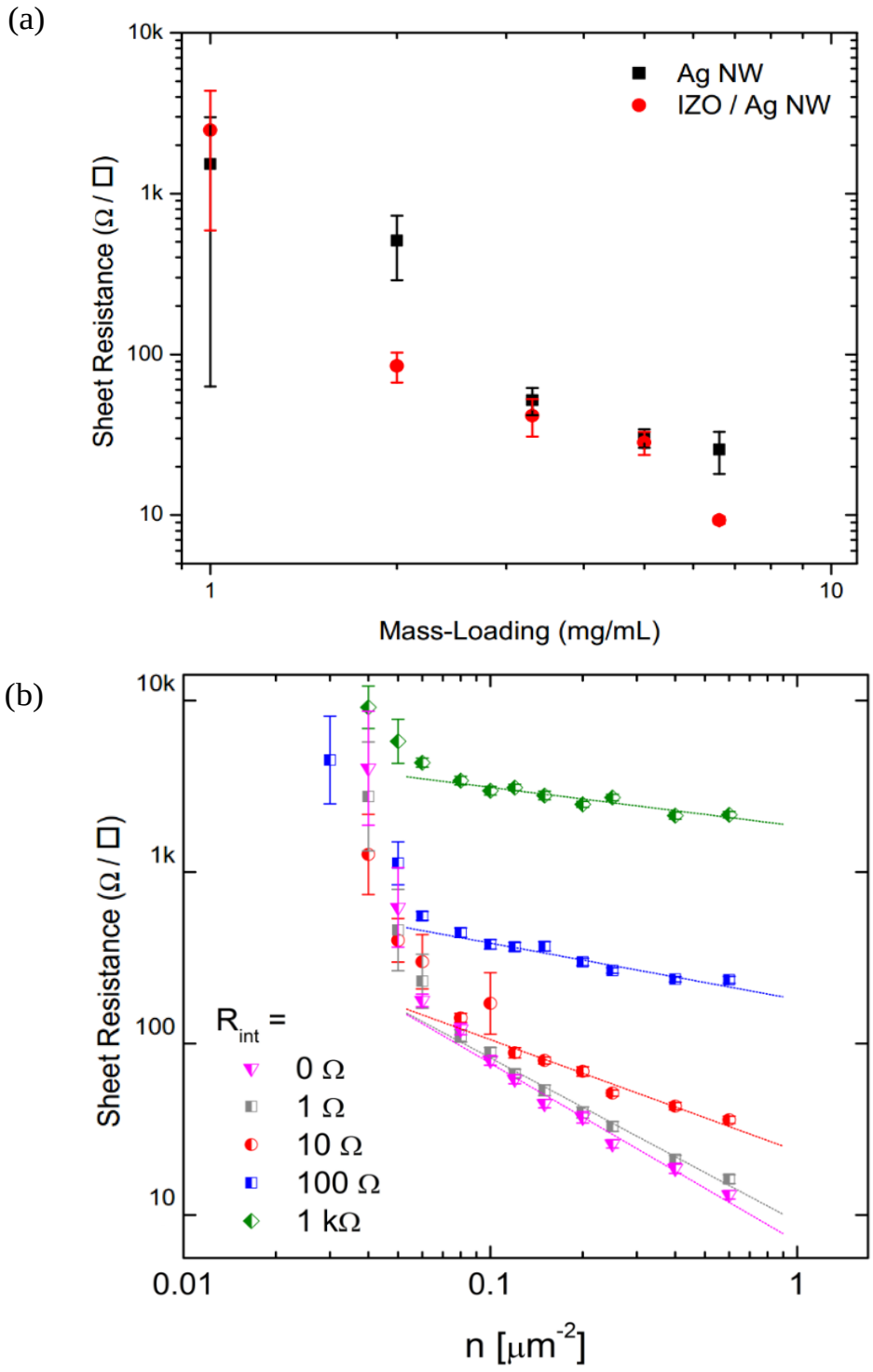


Figure 3.7 Sheet resistance of pure Ag NW and hybrid films printed on glass substrates vs. mass-loading of Ag NW in the ink (a) and simulated sheet resistances of hybrid films vs. areal density for films with varying nanowire junction resistance (b).

Table 3.1 Parameters used in nanowire network model

| Parameter | Value | Unit |
|---|---|---|
| $\rho_{Ag}$ | 0.0159 | Ω.µm |
| $D$ | 0.033 | µm |
| Average NW length | 14 | µm |
| Standard deviation of NW lengths | 4 | µm |

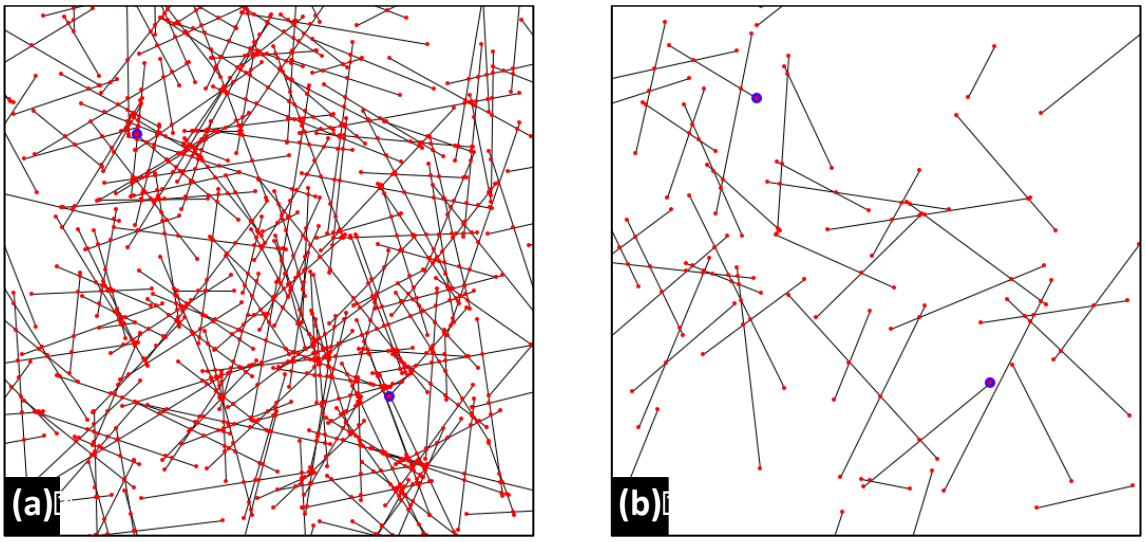


Figure 3.8 Examples of nanowire networks generated using the described model. $n$ = 0.1 µm$^{-2}$, (a) $n$ = 0.02 µm$^{-2}$ (b). Substrate areas are 50×50 µm$^2$ in both cases. Every node in the model is marked by a red dot; example 2-point resistance test nodes are also marked with blue dots.

### 3.6 Thermal Stability of Printed Hybrid TCO Films

To achieve low resistance nanowire – nanowire contacts, the thermal annealing process was studied for both hybrid films and pure Ag NW films. Films were annealed at temperatures from 125°C - 325°C to determine the impact of using the hybrid IZO/Ag NW ink in which the silver nanowires are embedded in a sol-gel matrix during the film conversion process. As shown in Figure 3.10, hybrid IZO/Ag NW films and pure Ag NW films demonstrate distinctly different behavior with respect to thermal annealing. At lower annealing temperatures, conductivity improved dramatically for hybrid IZO / Ag films, with sheet resistance decreasing from above 1 kΩ/□ at 125°C to below 10 Ω/□ at 175°C. At these temperatures, the sol-gel undergoes drying and densification, compressing the composite film. The IZO film's thickness steeply decreases from 160 nm to 40 nm as solvent vapor and organic precursors are liberated during heating from 125°C to 200°C. The thickness of the sol-gel films was measured by stylus profilometry (Dektak Veeco

6M), showing a large reduction with low-temperature annealing within plastic compatible thermal budgets.

In contrast, films composed only of Ag NWs show only minor improvement with additional thermal annealing, reaching an optimal conductivity at 175°C annealing. In both hybrid and pure Ag NW films, conductivity is degraded at temperatures above 225°C. But while pure Ag NW films become entirely non-conductive in this temperature range, hybrid films remain functional (17 Ω/□ at 275°C).

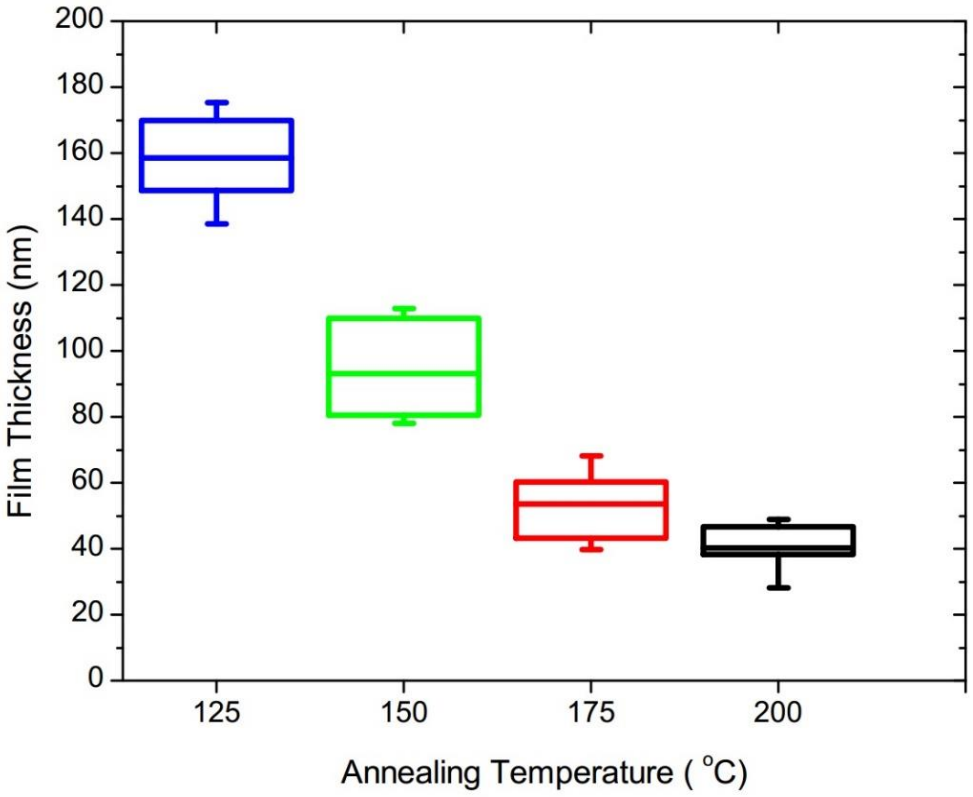


Figure 3.9 Thickness of hybrid TCO films after annealing at 125 °C – 200 °C.

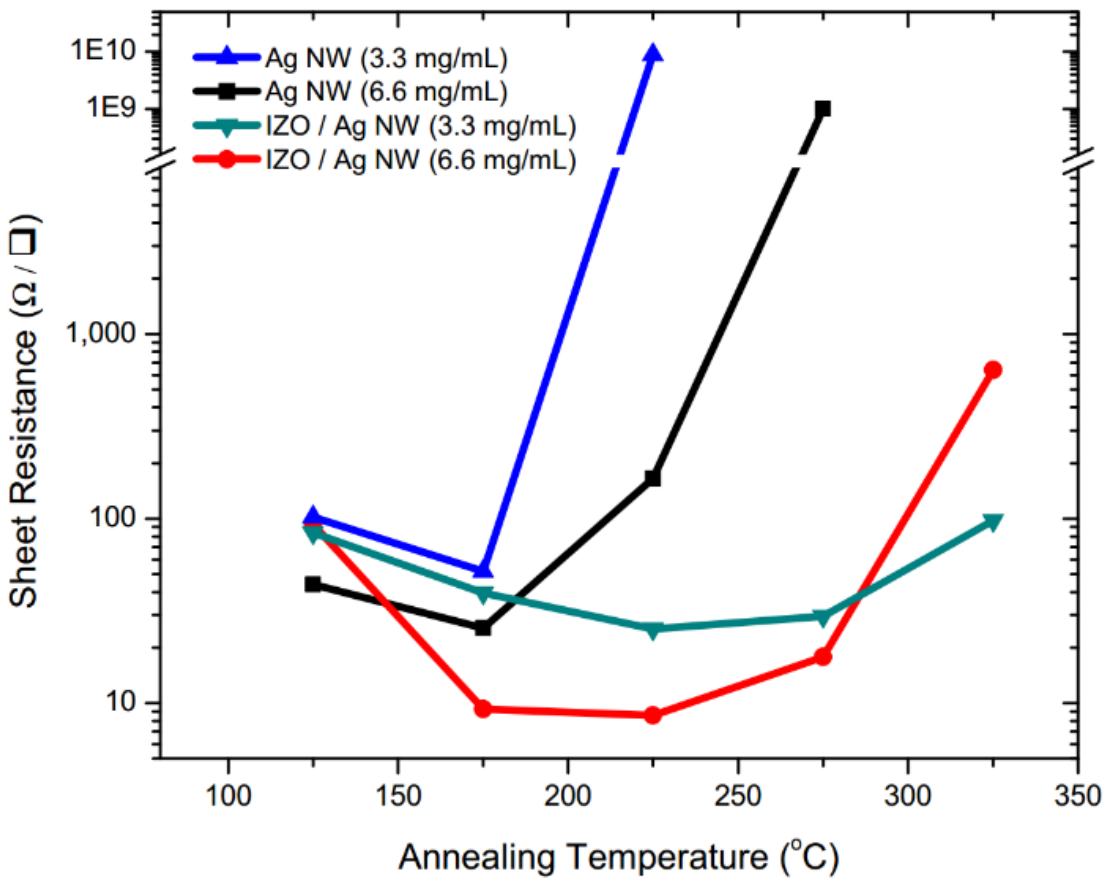


Figure 3.10 Sheet resistance of IZO/Ag NW hybrid films and pure Ag NW films printed on glass vs. annealing temperature.

The excellent stability of the hybrid films at elevated annealing temperatures suggests that the sol-gel matrix is encapsulating the silver nanowire network, preventing the degradation in connectivity that should otherwise occur at temperatures well above the melting point of silver nanowires (M.P. ~200°C)[25], [26]. Scanning electron microscopy (SEM) was performed to examine the morphology of the nanowire films annealed at different temperatures and investigate the encapsulating properties of the IZO matrix. SEM micrographs of glass samples were obtained using a Zeiss Ultra Plus high-resolution scanning electron microscope equipped with a Schottky field emission electron source. The images were acquired using secondary electrons (in-lens detector) at a relatively low accelerating voltage of 1.5 - 2 kV and at working distances of 3 mm.

As shown in Figure 3.11a and 3.11d, low temperature films annealed at 125°C show no evidence of welding at nanowire junctions, in both the case of bare Ag NWs and hybrid IZO/Ag NW inks.

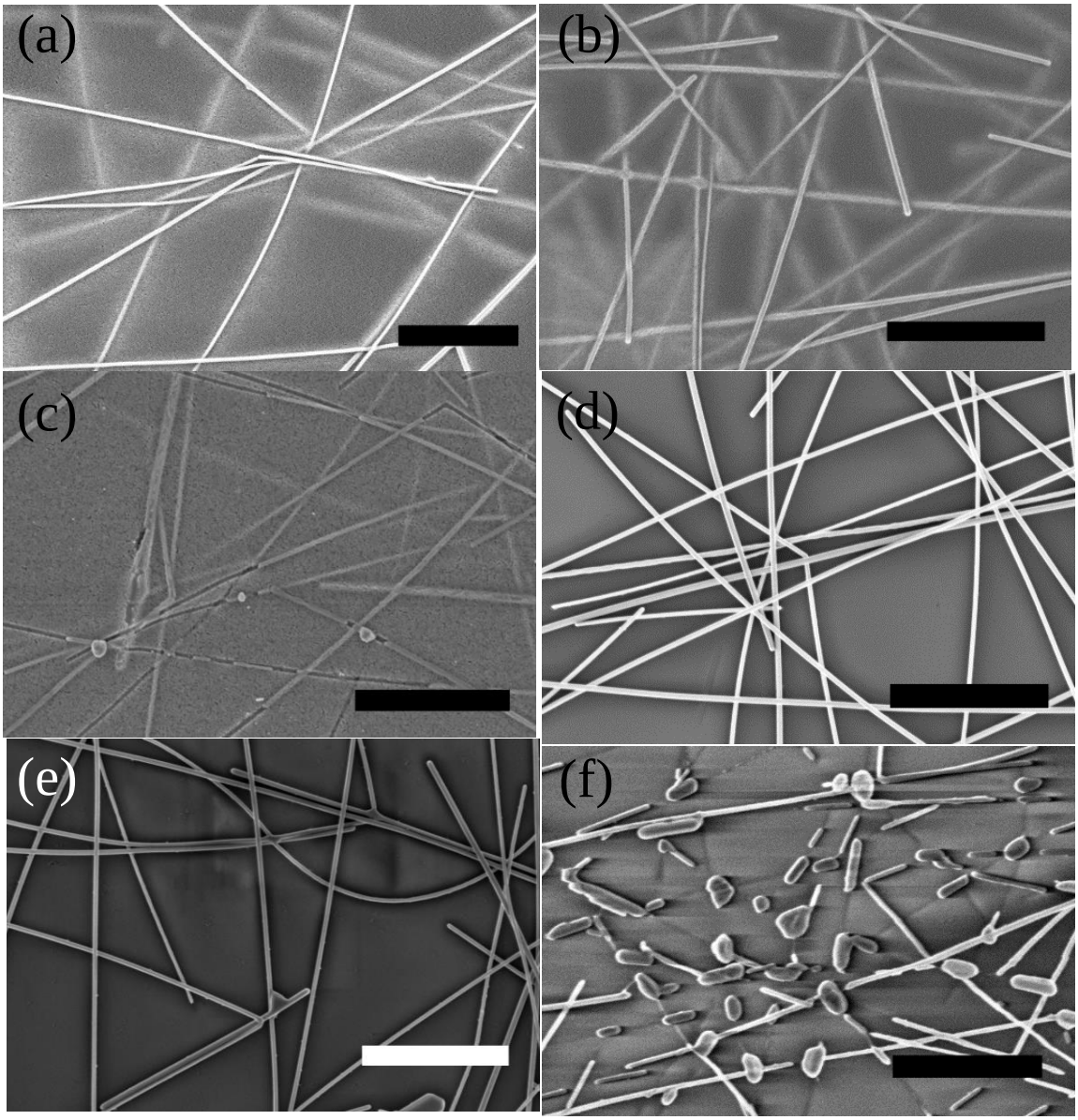


Figure 3.11 HRSEM images of (a,b,c) gravure-printed hybrid IZO/Ag NW films and (d,e,f) bare Ag NW films (3.3 mg/mL Ag NW mass-loading) on glass substrates annealed at (a,d) 125°C, (b,e) 175°C, and (c,f) 275°C. Scale bars are 1 μm in length.

In contrast, Figure 3.11b and 3.11e show morphological changes in the films, with a substantial number of welded junctions forming at a moderate annealing temperature of 175°C, which may result in lower contact resistance between individual wires[27]. Finally, in Figure 3.11f, we see that at high annealing temperatures (275°C) there is disintegration of the conductive network in the case of the bare Ag NW films, consistent with Rayleigh-instability-driven fragmentation[28]. However, in the case of the hybrid IZO/Ag NW films (Figure 3.11c), the conductive network is largely preserved as wires submerged in the IZO matrix are not fragmented. This shows the advantage of using a matrix material such as IZO, which is sufficiently stiff to encapsulate and

protect the nanowires, while remaining stable at high annealing temperatures. This is an important result because it can facilitate the use of silver nanowires in a range of printed electronic devices with inorganic layers requiring[10] thermal annealing above 200°C, such as metal oxide resistive memories, thin film transistors, and mesoporous perovskite solar cells.[29] [30]

The differences in conductivity and uniformity of the hybrid vs. pure Ag NW films can be further understood by considering the contact mechanics of the gravure printing process. In general, films formed from pure Ag NW appear textured in a diamond pattern (Figure 3.12a) matching the impression of the chrome gravure roller surface, suggesting the embossing action of the high contact pressure between the roller and the glass substrate. Indeed, Hertzian non-adhesive elastic contact theory predicts a contact pressure of 30 - 50 MPa (4 - 7 ksi) at the printing nip for a uniform line contact between the chrome coated gravure roller and the glass substrate, given the printing forces used in this study. This pressure is even higher than those used in calendaring and hot pressing of nanowire films[31]. The advantage of utilizing gravure printing in this case is that deposition and calendaring are performed simultaneously without additional post-processing. In contrast to pure Ag NW inks, the films formed from hybrid inks show a more uniform density of NWs and lack the diamond patterned texture. These observations appear to be consistent with the higher viscosity and longer drying time observed in the hybrid inks, which facilitate greater ink transfer and reflow of printed ink, respectively. Both of these factors lead to the printing of more conductive and homogeneous TCEs.

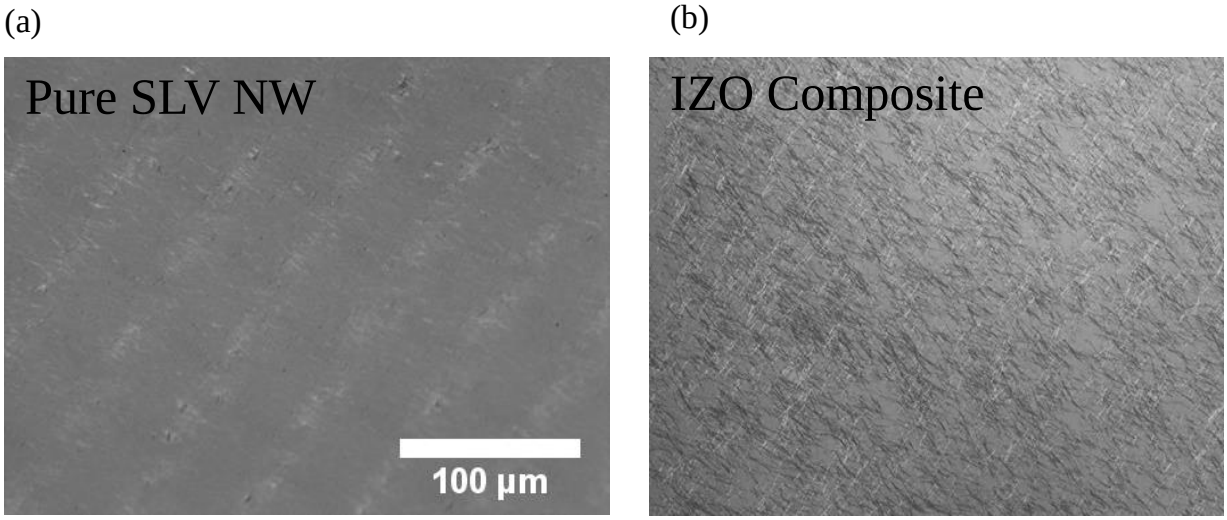


Figure 3.12 – Textured nanowire film printed from pure Ag NW ink (a). Hybrid film printed from IZO / Ag NW ink (b).

### 3.7 Optical Transparency of Printed Hybrid TCO Films

These improvements in the uniformity of the hybrid films are achieved while simultaneously increasing the visible range transparency of the films. Transmittance spectra were measured at normal incidence with a Shimadzu UV-2600 spectrometer. Transmittance spectra shown in Figure 3.13 were obtained for bare nanowire and hybrid films with similar mass-loadings (6.6 mg/mL). A comparison of the transparency between 400 nm and 800 nm shows that the IZO/Ag NW hybrid

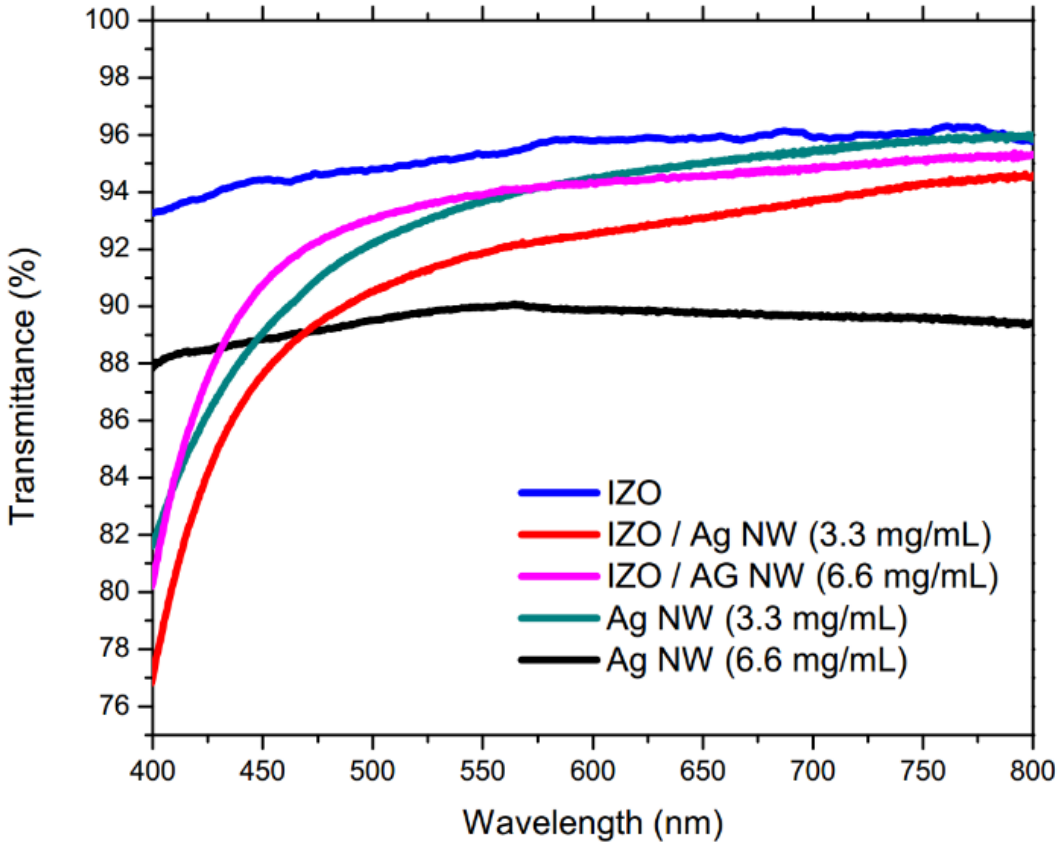


Figure 3.13 Transmittance spectra of hybrid IZO/Ag NW films (red) and pure Ag NW electrodes (black) printed on glass, with IZO film transmittance (blue) shown for reference.

films ($T_{550nm}$ ~ 91%) have similar, but slight improved transmittance relative to bare nanowire films ($T_{550nm}$ ~ 89%). One possible explanation for the small increase in transparency is that the areal uniformity of the hybrid films is improved as they lack the textured characteristics of the pure silver nanowire films. The observed texturing appears to produce nodes with high densities of Ag NW's, which could reduce transmittance in the films printed from pure Ag NW inks. This is consistent with prior observations that high areal densities of silver nanowires lead to significantly enhanced forward scattering and absorption[32]. Further characterization of the optical haze would reveal whether these nanowire-dependent phenomena can explain these observations. Alternatively, it is possible that the sol-gel metal oxide coating is also acting as an antireflection coating for the glass and silver nanowires.

To evaluate the suitability of these films as ideal transparent conductors, it is useful to compare their Haacke figure of merit. The Haacke figure of merit ($\Phi_{TCO} = T^{10} / R_{\square}$) is an often cited metric for the performance of transparent conductive films[33],[34] which incorporates the two most important parameters, sheet resistance and visual range transparency. The result of the improvements to the transparency and conductivity of the hybrid films is that the Haacke figure of merit for the optimal IZO hybrid film ($4.3 \cdot 10^{-2}\ \Omega^{-1}$ on glass) is approximately three times higher than that of pure silver nanowire films ($1.35 \cdot 10^{-2}\ \Omega^{-1}$). To demonstrate the versatility of the

methods shown herein, we have also gravure printed the hybrid IZO / Ag NW inks onto flexible PEN plastic substrates. Similar ink transfer and film uniformity are achieved for prints on plastic substrates as well as outstanding conductivity and transparency, giving a figure of merit as high as $3.2 \cdot 10^{-2}\ \Omega^{-1}$. This FOM is approximately 25 % lower than that of glass substrates, which may result from the lower annealing temperature used for the PEN samples (175 °C) in order to maintain dimensional stability (shrinkage increases significantly for T > 180 °C)[35]. These low temperatures allow for roll-to-roll fabrication of nanowire TCEs on a range of flexible or, even, stretchable substrates, which can facilitate devices that leverage the performance and versatility of these materials. [36]–[40]

Table 3.2 Properties of Leading Composite Ag NW Transparent Conducting Films

| **Substrate** | **Composite** | $R_s$ **( Ω / □)** | $T_{550nm}$ **(%)** | $\Phi_{TCO}$ **$(10^{-2}\ \Omega^{-1})$** | **Process** | **Ref** |
|---|---|---|---|---|---|---|
| Glass | IZO + Ag NW | 9.30 | 91 | 4.28 | One-Step Gravure Printing | This Work |
| Plastic | IZO + Ag NW | 10.9 | 90 | 3.20 | One-Step Gravure Printing | This Work |
| Glass | ZnO + Ag NW | 10.0 | 91 | 3.89 | ALD + Rod-Coating | Ref. 19 |
| Glass | $TiO_2$ + Ag NW | 13.2 | 86 | 1.60 | Two-Step Spin-coating | Ref. 20 |
| Glass | ZnO + Ag NW | 8.00 | 91 | 4.86 | Sputtering & Spin-Coating | Ref. 21 |

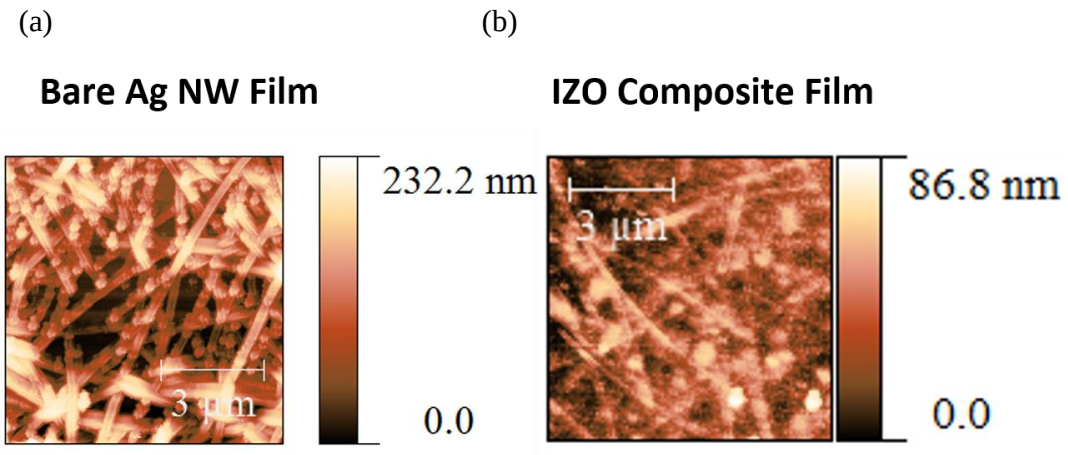


Figure 3.14 Semi-contact AFM scans of bare Ag NW gravure-printed film (a) and hybrid IZO sol-gel / Ag NW composite film (b).

Table 3.2 compares the figure of merit for these printed electrodes on glass and plastic to leading examples of composite nanowire films. Previous reports of metal oxide/Ag NW composites have utilized multistep coating processes to generate the films, whereas here a comparable figure of merit is achieved by high-speed gravure printing in a single coating step. It is worth noting that

these solution-processed films approach the theoretical maximum Haacke figure of merit for ITO films of comparable thickness[34] but are deposited at a high-speed speed of 1 m/s by a roll-to-roll scalable technique. Furthermore, improvements are potentially within reach since the methods shown here should be extensible to silver wires with higher aspect ratios[17] and could be used with advanced annealing methods, such as photonic sintering[25].

### 3.8 Mechanical Stability of Printed Hybrid TCOs

There are several mechanical properties of nanowire-based TCE's that are often insufficiently considered when discussing their performance. Of foremost concern for transparent electrodes are their mechanical properties, such as smoothness and adhesion. These properties dictate available applications and the allowable post-processing to fabricate various devices. The smoothness of the hybrid electrodes and pure silver nanowire films were investigated with atomic force microscopy (AFM). The pure silver nanowire film shows a high surface roughness ($R_q$ ~ 34 nm), whereas the hybrid films have a significantly reduced surface roughness ($R_q$ ~ 4.8 nm) due to the encapsulation provided by the IZO matrix. The IZO matrix gives a smoother surface to the film that is more

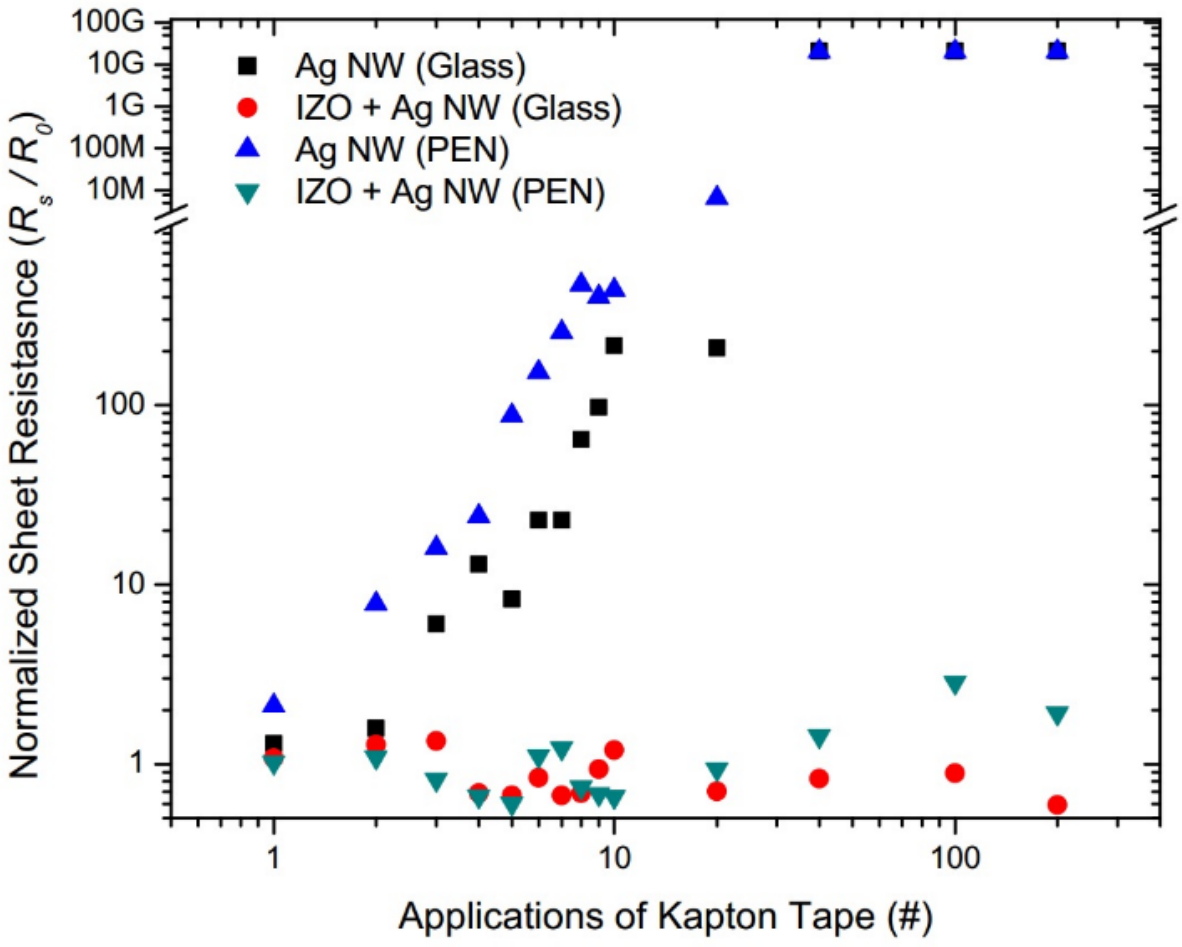


Figure 3.15 Normalized sheet resistance of Ag NW films and hybrid IZO/Ag NW films vs. number of applications of Kapton© tape on glass (red) and plastic (blue) substrates.

suitable for devices, such as OLEDs and organic photovoltaics that have thin active layers. Rougher pure nanowire layers would be likely to cause issues with the continuity of overlying films.

A tape test consisting of the application and removal of adhesive Kapton© tape on the film shows the differences in adhesion between the hybrid and pure Ag NW films. In this test, the sheet resistance was measured after each application of Kapton© tape (Figure 3.15). While the conductivity of the bare nanowire film is reduced by nearly three orders of magnitude within ten applications of tape, the hybrid films' conductivity remains relatively constant after 200 applications of tape, even improving slightly. This matches observations made on the microscope, of the visibly sparser films in the case of the pure silver nanowire films. The nanowires appear to be rapidly peeled away from the glass and plastic substrates, but the hybrid film remains intact due to the encapsulation provided by the IZO matrix. This property is highly desirable as it allows these electrodes to endure stresses during fabrication or to be used in wearable devices in which tactile stresses could abrade the film.

## 3.9 Summary

In this chapter, hybrid nanowire / sol-gel TCO inks were developed to resolve the limitations of high-temperature processed pure sol-gel inks. High-performance TCO films are prepared by high-throughput gravure printing from a single, air stable, printable ink consisting of metal oxide sol-gel precursors and silver nanowires. The electrical, optical, and mechanical properties of these films are enhanced relative to bare Ag NW films due to the densification of a rigid metal oxide matrix material, IZO. To understand the influence of hybrid ink design on film conductivity, transport simulations were performed to analyze randomly generated nanowire networks in an IZO matrix. Additionally, surface roughness, adhesion, and thermal stability of the conducting films improve dramatically as the nanowire network is encapsulated by the IZO film. Thus, this study explores a composite material that simultaneously leverages the properties of 1D conductive nanomaterials and sol-gel metal oxides to address current limitations of flexible TCEs and allow new applications in transparent, printed electronics. The principles introduced here for improved mechanical film stability via hybrid inks could also be extended to other materials and ink designs.

## 3.10 References

[1] J. Han et al., "Fully indium-free flexible Ag nanowires/ZnO:F composite transparent conductive electrodes with high haze," *J. Mater. Chem.* A, vol. 3, no. 10, pp. 5375–5384, Mar. 2015.

[2] G. Y. Margulis et al., "Spray Deposition of Silver Nanowire Electrodes for Semitransparent Solid-State Dye-Sensitized Solar Cells," *Adv. Energy Mater.*, vol. 3, no. 12, pp. 1657–1663, Dec. 2013.

[3] D. J. Finn, M. Lotya, and J. N. Coleman, "Inkjet Printing of Silver Nanowire Networks," *ACS Appl. Mater. Interfaces*, vol. 7, no. 17, pp. 9254–9261, May 2015.

[4] F. Guo et al., "Nanowire Interconnects for Printed Large-Area Semitransparent Organic Photovoltaic Modules," *Adv. Energy Mater.*, p. n/a-n/a, Apr. 2015.

[5] Q. Zhang, Y. Di, C. M. Huard, L. J. Guo, J. Wei, and J. Guo, "Highly stable and stretchable graphene–polymer processed silver nanowires hybrid electrodes for flexible displays," *J Mater Chem C*, vol. 3, no. 7, pp. 1528–1536, 2015.

[6] Y. Jin, L. Li, Y. Cheng, L. Kong, Q. Pei, and F. Xiao, “Cohesively Enhanced Conductivity and Adhesion of Flexible Silver Nanowire Networks by Biocompatible Polymer Sol–Gel Transition,” *Adv. Funct. Mater.*, vol. 25, no. 10, pp. 1581–1587, Mar. 2015.
[7] S.-T. Hsiao et al., “A highly electrically conductive graphene–silver nanowire hybrid nanomaterial for transparent conductive films,” *J. Mater. Chem. C*, vol. 2, no. 35, p. 7284, Jun. 2014.
[8] Q. Huang et al., “Highly Thermostable, Flexible, Transparent, and Conductive Films on Polyimide Substrate with an AZO/AgNW/AZO Structure,” *ACS Appl. Mater. Interfaces*, vol. 7, no. 7, pp. 4299–4305, Feb. 2015.
[9] K.-H. Choi, J. Kim, Y.-J. Noh, S.-I. Na, and H.-K. Kim, “Ag nanowire-embedded ITO films as a near-infrared transparent and flexible anode for flexible organic solar cells,” *Sol. Energy Mater. Sol. Cells*, vol. 110, pp. 147–153, Mar. 2013.
[10] D. Chen et al., “Thermally Stable Silver Nanowire–Polyimide Transparent Electrode Based on Atomic Layer Deposition of Zinc Oxide on Silver Nanowires,” *Adv. Funct. Mater.*, p. n/a-n/a, Nov. 2015.
[11] H. Kang, R. Kitsomboonloha, J. Jang, and V. Subramanian, “High-Performance Printed Transistors Realized Using Femtoliter Gravure-Printed Sub-10 μm Metallic Nanoparticle Patterns and Highly Uniform Polymer Dielectric and Semiconductor Layers,” *Adv. Mater.*, vol. 24, no. 22, pp. 3065–3069, Jun. 2012.
[12] S. G. Higgins, F. L. Boughey, R. Hills, J. H. G. Steinke, B. V. O. Muir, and A. J. Campbell, “Quantitative Analysis and Optimization of Gravure Printed Metal Ink, Dielectric, and Organic Semiconductor Films,” *ACS Appl. Mater. Interfaces*, vol. 7, no. 9, pp. 5045–5050, Mar. 2015.
[13] W. J. Scheideler, J. Jang, M. A. U. Karim, R. Kitsomboonloha, A. Zeumault, and V. Subramanian, “Gravure-Printed Sol–Gels on Flexible Glass: A Scalable Route to Additively Patterned Transparent Conductors,” *ACS Appl. Mater. Interfaces*, vol. 7, no. 23, pp. 12679–12687, Jun. 2015.
[14] J. M. Ding, A. de la Fuente Vornbrock, C. Ting, and V. Subramanian, “Patternable polymer bulk heterojunction photovoltaic cells on plastic by rotogravure printing,” *Sol. Energy Mater. Sol. Cells*, vol. 93, no. 4, pp. 459–464, Apr. 2009.
[15] D. Alemu, H.-Y. Wei, K.-C. Ho, and C.-W. Chu, “Highly conductive PEDOT:PSS electrode by simple film treatment with methanol for ITO-free polymer solar cells,” *Energy Environ. Sci.*, vol. 5, no. 11, p. 9662, 2012.
[16] Y. H. Kim, C. Sachse, M. L. Machala, C. May, L. Müller-Meskamp, and K. Leo, “Highly Conductive PEDOT:PSS Electrode with Optimized Solvent and Thermal Post-Treatment for ITO-Free Organic Solar Cells,” *Adv. Funct. Mater.*, vol. 21, no. 6, pp. 1076–1081, Mar. 2011.
[17] S. Ye, A. R. Rathmell, Z. Chen, I. E. Stewart, and B. J. Wiley, “Metal Nanowire Networks: The Next Generation of Transparent Conductors,” *Adv. Mater.*, vol. 26, no. 39, pp. 6670–6687, Oct. 2014.
[18] J. D. Park, S. Lim, and H. Kim, “Patterned silver nanowires using the gravure printing process for flexible applications,” *Thin Solid Films*, vol. 586, pp. 70–75, Jul. 2015.
[19] P.-H. Wang, S.-P. Chen, C.-H. Su, and Y.-C. Liao, “Direct printed silver nanowire thin film patterns for flexible transparent heaters with temperature gradients,” *RSC Adv.*, vol. 5, no. 119, pp. 98412–98418, Nov. 2015.
[20] E. Fortunato, D. Ginley, H. Hosono, and D. C. Paine, “Transparent Conducting Oxides for Photovoltaics,” *MRS Bull.*, vol. 32, no. 03, pp. 242–247, Mar. 2007.

[21] K. K. Banger et al., “Low-temperature, high-performance solution-processed metal oxide thin-film transistors formed by a ‘sol–gel on chip’ process,” *Nat. Mater.*, vol. 10, no. 1, pp. 45–50, Jan. 2011.
[22] P. Heremans et al., “Mechanical and Electronic Properties of Thin-Film Transistors on Plastic, and Their Integration in Flexible Electronic Applications,” *Adv. Mater.*, p. n/a-n/a, Dec. 2015.
[23] K. Ankireddy, S. Vunnam, J. Kellar, and W. Cross, “Highly conductive short chain carboxylic acid encapsulated silver nanoparticle based inks for direct write technology applications,” *J Mater Chem C*, vol. 1, no. 3, pp. 572–579, 2013.
[24] E. Jung, C. Kim, M. Kim, H. Chae, J. H. Cho, and S. M. Cho, “Roll-to-roll preparation of silver-nanowire transparent electrode and its application to large-area organic light-emitting diodes,” *Org. Electron.*, vol. 41, pp. 190–197, Feb. 2017.
[25] E. C. Garnett et al., “Self-limited plasmonic welding of silver nanowire junctions,” *Nat. Mater.*, vol. 11, no. 3, pp. 241–249, Mar. 2012.
[26] Jung-Yong Lee, Stephen T. Connor, Yi Cui, and Peter Peumans, “Solution-Processed Metal Nanowire Mesh Transparent Electrodes,” *Nano Lett.*, vol. 8, no. 2, pp. 689–692, 2008.
[27] T. Tokuno et al., “Fabrication of silver nanowire transparent electrodes at room temperature,” *Nano Res.*, vol. 4, no. 12, pp. 1215–1222, Oct. 2011.
[28] S. Karim et al., “Morphological evolution of Au nanowires controlled by Rayleigh instability,” *Nanotechnology*, vol. 17, no. 24, p. 5954, 2006.
[29] T.-B. Song et al., “Highly Robust Silver Nanowire Network for Transparent Electrode,” *ACS Appl. Mater. Interfaces*, Oct. 2015.
[30] A. Kim, Yulim Won, Kyoohee Woo, Chul-Hong Kim, and Jooho Moon, “Highly Transparent Low Resistance ZnO/Ag Nanowire/ZnO Composite Electrode for Thin Film Solar Cells,” *ACS Nano*, vol. 7, no. 2, pp. 1081–1091, 2013.
[31] T. L. Chen, D. S. Ghosh, V. Mkhitaryan, and V. Pruneri, “Hybrid Transparent Conductive Film on Flexible Glass Formed by Hot-Pressing Graphene on a Silver Nanowire Mesh,” *ACS Appl. Mater. Interfaces*, vol. 5, no. 22, pp. 11756–11761, Nov. 2013.
[32] J. van de Groep, D. Gupta, M. A. Verschuuren, M. M. Wienk, R. A. J. Janssen, and A. Polman, “Large-area soft-imprinted nanowire networks as light trapping transparent conductors,” *Sci. Rep.*, vol. 5, p. 11414, Jun. 2015.
[33] G. Haacke, “New figure of merit for transparent conductors,” *J. Appl. Phys.*, vol. 47, no. 9, pp. 4086–4089, Sep. 1976.
[34] K. Ellmer, “Past achievements and future challenges in the development of optically transparent electrodes,” *Nat. Photonics*, vol. 6, no. 12, pp. 809–817, Dec. 2012.
[35] W. A. MacDonald et al., “Latest advances in substrates for flexible electronics,” *J. Soc. Inf. Disp.*, vol. 15, no. 12, pp. 1075–1083, Dec. 2007.
[36] W. Hu, X. Niu, L. Li, S. Yun, Z. Yu, and Q. Pei, “Intrinsically stretchable transparent electrodes based on silver-nanowire–crosslinked-polyacrylate composites,” *Nanotechnology*, vol. 23, no. 34, p. 344002, 2012.
[37] T. Sekitani et al., “Stretchable active-matrix organic light-emitting diode display using printable elastic conductors,” *Nat. Mater.*, vol. 8, no. 6, pp. 494–499, Jun. 2009.
[38] T. Kim et al., “Inkjet-printed stretchable single-walled carbon nanotube electrodes with excellent mechanical properties,” *Appl. Phys. Lett.*, vol. 104, no. 11, p. 113103, Mar. 2014.

[39] J. Liang et al., “Silver Nanowire Percolation Network Soldered with Graphene Oxide at Room Temperature and Its Application for Fully Stretchable Polymer Light-Emitting Diodes,” *ACS Nano*, vol. 8, no. 2, pp. 1590–1600, Feb. 2014.
[40] B. S. Kim et al., “Reversibly Stretchable, Optically Transparent Radio-Frequency Antennas Based on Wavy Ag Nanowire Networks,” *ACS Appl. Mater. Interfaces*, Jan. 2016.

# Chapter 4: Custom Gravure Printer Design for Process-Decoupled Investigation of Dragout Artifacts

## 4.1 Introduction

Printed electronics leverages the high speed and low cost of technologies used in graphic arts printing to fabricate thin film electronics such as organic transistors[1], solar cells[2], transparent conductors[3], and wearable bio sensors[4]. The graphic arts industry routinely patterns a large variety of inks on flexible substrates such as plastic and paper at resolutions below 50 μm and at very low overall cost. However, extending these methods to manufacturing a new generation of smart packaging[5] and flexible thin film electronics will require greater knowledge of printing physics of gravure as well as new tools and processes for developing printed devices. This is primarily because, unlike graphic arts prints which must only satisfy visual inspection, nanomaterial-based printed electronic components have high sensitivity to nanometer scale thickness variations[6] or micron-scale area variations invisible to the naked eye[7]. Thus, realizing printed electronic systems will require nanomaterial printing processes that push the limits of resolution and uniformity[8]. However, large-scale deployment of printed wireless sensors, flexible displays, and wearable electronics, will require greater understanding of the printing physics of nanomaterial-based inks in order to improve the resolution, reliability, and uniformity of printed systems.

This chapter presents the design, construction, and testing of a custom sheet-fed gravure printer which features multilayer printing for nanomaterial exploration and thin film device development. The design allows precise, independent control of the speeds and forces of each of the subprocesses of gravure (ink filling, wiping, and transfer), enabling novel experimental controls for dissecting the printing process fluid mechanics. We use these new capabilities to investigate the primary artifacts which distort printed nanomaterial patterns, such as *dragout* tails, edge roughness, and pinholes. These artifacts are studied as a function of print parameters such as contact pressure, wiping speed, and transfer speed, by printing silver nanoparticle ink to form features in the range 100 μm to 10 mm. The results of these studies indicate that the contact mechanics of the ink transfer process have a strong influence on the formation of dragout artifacts, indicating the presence of a transfer-driven squeezing flow which distorts the trailing edges of features. By engineering the transfer contact mechanics with varying rubber substrate backing stiffness, we found it is also possible to suppress this artifact formation for a particular nanomaterial ink. The improved areal uniformity and print quality achieved using these methods highlight the potential for gravure printing to be a versatile nano-manufacturing tool for patterning a variety of thin film smart materials. We also hope that the open-source printer designs presented here can serve to accelerate the development of high-speed nanomaterial printing.

Detailed studies of the fluid mechanics of gravure printing of nanomaterials have been performed for small-scale plate-based *inverse* gravure printing[9] to reveal the trends of how print fidelity scales with speed and ink viscosity, summarized as a dimensionless Capillary Number defined as follows

$$\text{Capillary Number } (Ca) = \frac{\eta U}{\gamma}$$

By optimizing ink viscosity ($\eta$) and print speed ($U$), features as small as 2 µm were successfully printed and utilized for thin film transistors [1]. But while this guiding work showed several important aspects of highly-scaled gravure printing physics, important questions remain about how these phenomena apply to industrially viable roll-based printing systems and more complex mesoscale patterns printed from arrays of cells.

Further understanding of gravure printing of nanomaterials requires experimental tools which elucidate new printing physics. Gravure printing is a complex process which can be understood as a sequence of fluid mechanical subprocesses: ink filling, doctoring, transfer, and spreading[6]. A diagram of these subprocesses is show below in Figure 4.1 for the traditional R2R implementation of gravure printing.

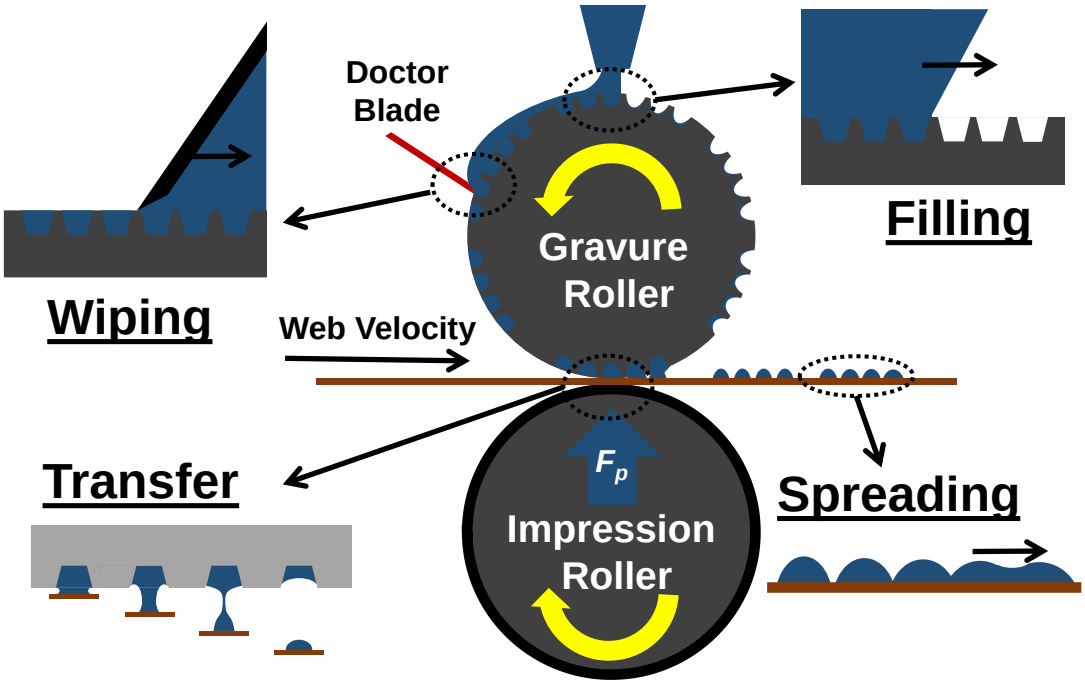


Figure 4.2 Roll-to-roll gravure printing process schematic.

These subprocesses happen continuously and simultaneously in conventional R2R printing, making their individual effects difficult to separate. As a result, diagnosing printing artifacts and optimizing the ink composition of printed inks is often performed by proprietary heuristics or trial and error. However, if the subprocesses of gravure can be separated, then empirical models for printing artifact formation can be developed to guide ink formulation and process optimization. Conventional printing presses cannot allow this due to the direct mechanical coupling of substrate motion and printing cylinder motion. As a result, the speeds and timing of ink filling, wiping, and transfer may not be decoupled. Here we present a laboratory scale sheet-fed gravure printer design which decouples the major printing subprocesses and allows precise control of the contact mechanics of ink transfer. We utilize this printer to investigate the most prominent printing

artifacts in mesoscale nanomaterial features, leading to a new understanding of the impact of contact mechanics on ink transfer and film formation.

### 4.2 Process-Decoupled Gravure Printer Design

The gravure printer designed and constructed in this study is shown below in Figure 2. The design was intended to be a suitable laboratory-scale model for studying high-speed gravure printing of nanomaterial inks. As a result, the forces and print speeds, as well as the roller dimensions used here are more comparable to printing presses used in industrial gravure, ensuring that results from this model system are extensible to wide web, R2R processing. The dimensions, speeds, forces, and accuracy of the gravure printer are reported below in Table 4.1.

Table 4.2 Gravure Printer Specifications

| **Print Parameter** | **Specified Range** |
|---|---|
| Print Speed | 1 mm/s – 2000 mm/s |
| Wiping Speed | 1 mm/s – 4000 mm/s |
| Wiping Pressure | 1.0 - 12.5 N / cm |
| Print Force | 50-1000 N |
| Roller Line Pressure | 4 – 80 N/cm |
| Roller Diameter | 125 ± 0.025 mm |
| Roller Width | 125 mm |
| Linear Stage Accuracy | ≤ 2 μm |
| Print Area | 120 mm x 300 mm |

Process decoupling was achieved in this design by utilizing a sheet-fed printing process with the substrate mounted on a high precision linear stage and the gravure roller mounted to a spindle block on vertical rails. Using dual-acting pneumatic actuators, the roller can be landed on the traveling substrate with a particular printing force to control the contact mechanics. Similarly, the doctor blade can be independently, pneumatically actuated to control doctoring force. The free rotation of the roller prior to printing has important implications for modeling R2R processing on a laboratory scale, because it allows steady state printing physics to be achieved without using excessive ink volumes and consuming many meters of substrate material. Smart materials development requires tools with this capability, since custom inks are often available in limited quantities.

(a)

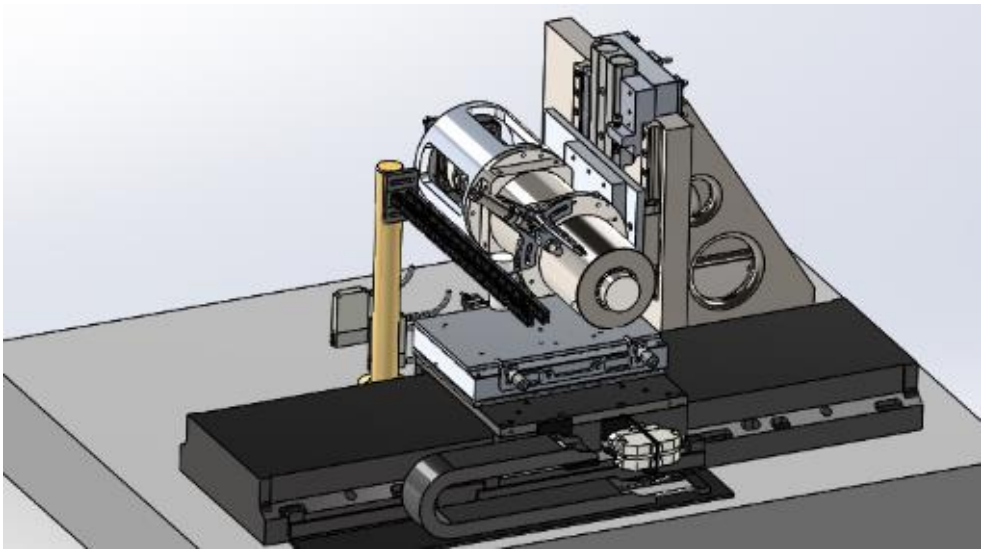

(b)

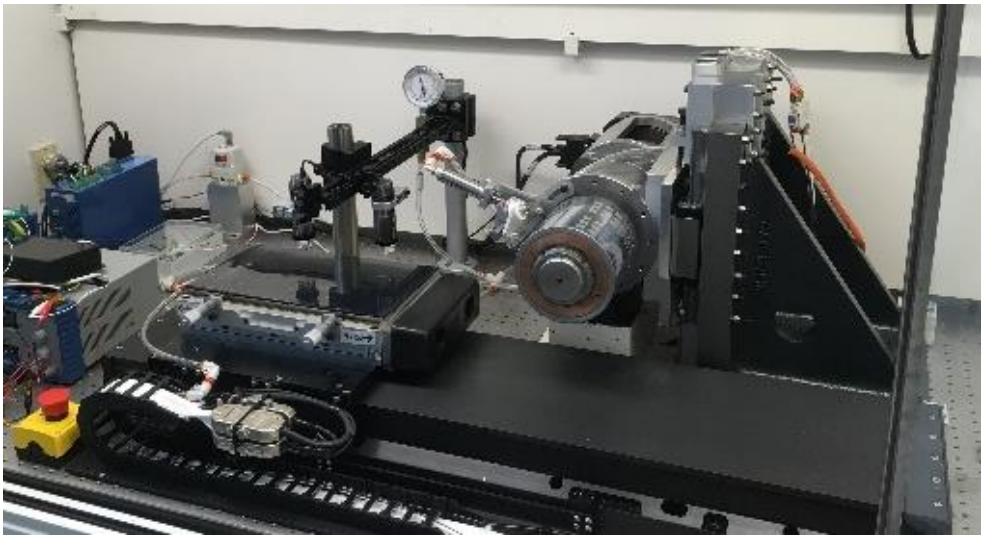

Figure 4.2 Process-decoupled gravure printer CAD (a). Picture of operational printer (b).

Additionally, because the roller can be freely rotated, doctoring and ink filling processes are decoupled from the ink transfer process. R2R printing is a typically a continuous process during which ink transfer is immediately followed by successive filling and wiping. This is also due to the fact that the speeds of the impression rollers and printing rollers are often driven and mechanically synchronized by interconnecting gears[10]. The continuous free rotation allowed in this design facilitates filling and wiping cycles of arbitrary length and speed. This aspect of the design also leads to an important experimental control. Multiple cycles of rotation can ensure that the cylinder has fully-filled cells, an important assumption in quantitative evaluation of the volume of ink that transfer to the substrate.

The design also features a cantilevered roller and spindle block containing a highly rigid *zero-runout* bearing assembly specifically designed for printing systems (GT+W Gmbh). The goal of minimizing the roller runout is to improve the uniformity of printed patterns and enhance the accuracy of registration to underlying patterns for multilayer printing. Runout is a particularly detrimental issue for contact printing systems such as gravure, which depend on uniform, non-slip contact between the engraved roller and the substrate[10]. In this case, the cantilevered design of the roller assembly was utilized to allow ease of roll-mounting as well as facilitate imaging of the printing process and allow space for post-processing tools for ink drying / curing. Pneumatic actuators and rigid linear slides (*Bosch R180525932*) were used to control the vertical motion of the spindle block assembly. Runner blocks (*Bosch RWA-025-SLH-C3-U-2*) with high moment-load capacity were used to support the cantilevered spindle block and the opposing pneumatic cylinders (*SMC CXSJL32-75*) provided the force to actuate the entire assembly. This configuration is displayed in Figure 4.4a below, with a force sensor secured inline (*Transducer Techniques MLP-300*). The two axes of motion (x and ⊖) were controlled with a direct-drive linear stage (*Aerotech PRO280LM*) and a direct-drive brushless motor (*Aerotech ADRS150*). The roller-driving motor was coupled to the spindle via a flex-coupler to account for axis misalignment and runout. The two axes of motion were then position synchronized over a high-speed ethernet connection between the two controllers (*Aerotech Ensemble HPe30*).

The ink doctoring process was controlled using a pneumatically actuated doctor blade assembly. The assembly was designed to clamp a 150 µm, 125 mm wide thick carbon-steel doctor blade against a 200 µm thick steel backing shim, which limited deflection of the blade under high wiping pressure. The blade assembly was mounted in a cantilevered fashion to a base attached to a linear slide. The linear slide and blade assembly was designed to use the spring-return feature in the pneumatic cylinder to retract the blade when not in use. Similar to the system for controlling the large pneumatic cylinders providing the forces for printing, an electronic regulator was used to control the pressure delivered to the pneumatic cylinder for the doctor blade.

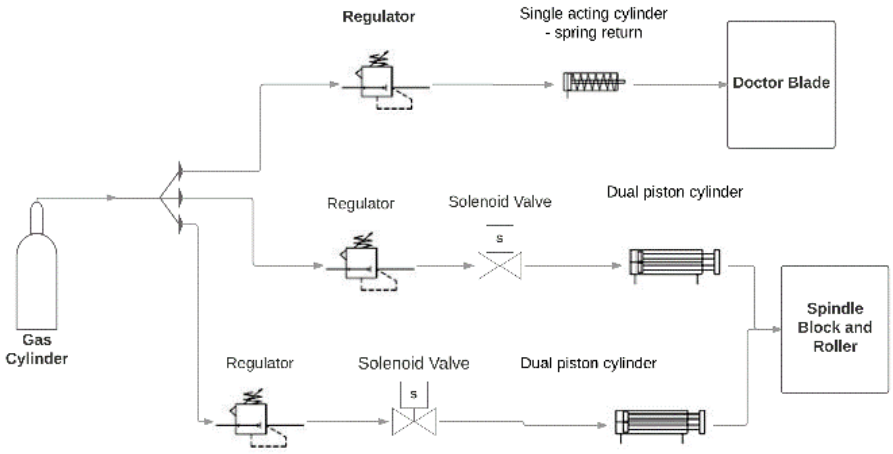


Figure 4.3 Diagram of the pneumatic subsystem driving the roller and doctor blade pneumatic actuators.

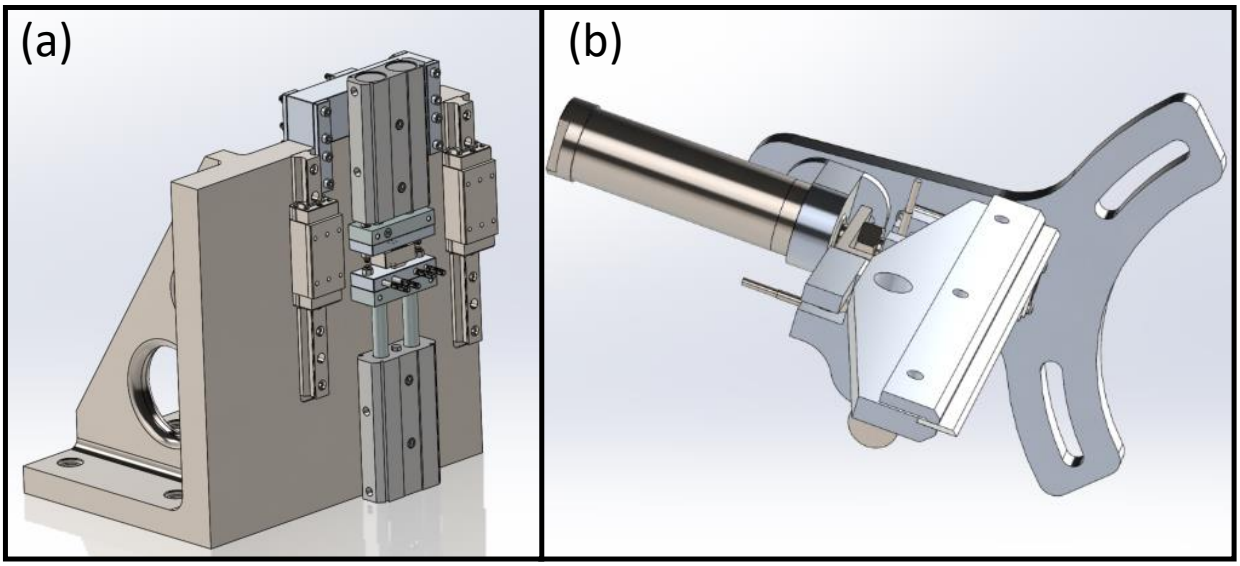


Figure 4.4 Angle plate with vertical rails, pneumatic actuators for spindle block lowering, and load cell for printing force measurement (a). Cantilevered doctor blade assembly actuated by compact pneumatic cylinder (b).

### 4.3 Shuttle-Based Sheet-Fed Printing

The gravure printer was designed for sheet-fed processing to accommodate integration with laboratory scale pre and post-processing tools. Sheet fed processing is a practical requirement for designing complex experiments within the constraints of material cost and availability. Additionally, sheet-fed processing facilitates a modular design in which the printing function can be paired with a variety of processing and inline characterization tools which utilize the linear stage motion control capabilities and vacuum chuck substrate mounting. To accomplish these design requirements, substrates (150 µm, *Dupont Teijin PQA1*) were mounted on a lightweight aluminum shuttle, as depicted in Figure 4.5. The shuttle is composed of a butyl rubber sheet adhered to an aluminum plate. Substrates are mounted to the shuttle, which is kinematically aligned by a central, spring-loaded locating pin and a pair of precision micrometers. Following optomechanical alignment, the substrate plate is fixed by the application of vacuum to the shuttle. The shuttle-style substrate mounting ensures that the substrate can be easily post-processed (i.e. cured in an oven) and returned to the printer without repeated mounting. Additionally, the shuttles can be adapted with variable rubber backings to engineering the contact mechanics to the substrate. These features are expected to facilitate multilayer printing of electronic devices such as printed transistors, organic light emitting diodes (OLEDs), or organic photodetectors (OPDs).

Registration of the printed layers was achieved using semiautomatic optomechanical alignment methods. Alignment was characterized using printed alignment markers designed into the engraved patterns on the rollers. The alignment features consisted of regularly spaced cross-shaped alignment markers approximately 0.5 mm x 0.5 mm in size along the periphery of the patterns on the roller. A string of approximately 25 alignment markers, with one distinct origin marker shaped like an ‘X,’ was used so that semi-automatic methods of scanning and image processing the various

markers would allow a least-squares fitting of the positions of the roller and the substrate. This is important for ensuring good alignment across the entire width of the print rather than in a single area. It is also a design requirement because of the manufacturing tolerances of the engraved rollers, which have variability in their diameter of approximately 25 micron. This tolerance translates to variability in the printed feature location which must be accommodated via test prints and pre-printing calibration steps. An example of the image processing used to calculate positions from images of the alignment marks is shown below in Figure 4.6. After applying thresholds and creating a binary image, an object detection algorithm finds the marks and calculates a centroid position for each. A linear fit of the centroid positions provides the overall x, y, and $\theta$ positions, from which the offset values are calculated. Similar techniques were used for adjusting the $\theta$ position of the pattern on the roller. Because the roller is not *keyed* to the spindle, the position can vary from day to day when the roller is removed for cleaning or is replaced by a different roller. The position must therefore be calculated relative to an absolute reference position provided by a camera mounted above the roller, attached directly to the spindle block. This roller camera, in combination with the high precision rotary stage, allows calibration of the theta position of the roller by scanning the pixelated version of the alignment marks on the roller.

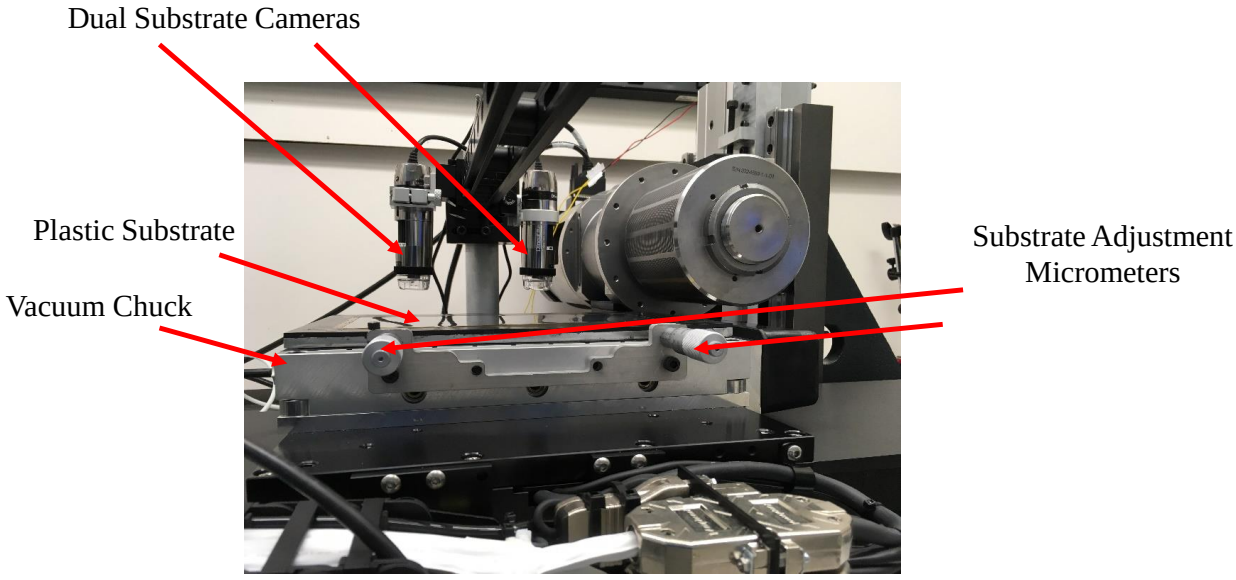


Figure 4.5 Substrate mounting assembly including vacuum chuck, substrate cameras, and micrometers for substrate position adjustment.

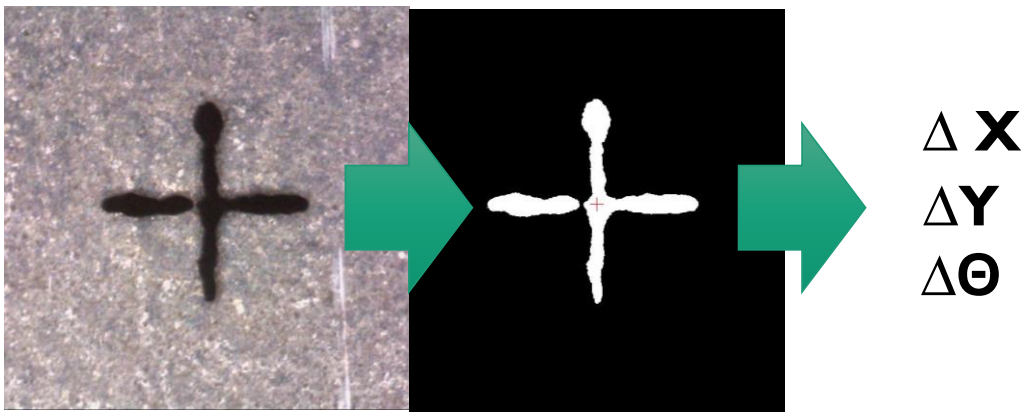


Figure 4.6 Cross-shaped alignment marks are used with automatic and semiautomatic optomechanical alignment to calculate the offsets in the x, y, and Θ positions.

### 4.4 Mechanisms of Mesoscale Dragout Artifact Formation

Gravure printing experiments were conducted with the new process-decoupled tool to better understand prominent mesoscale printing artifacts. Nanomaterial-based printed electronics is particularly sensitive to printing artifacts because of the stringent requirements for continuity and uniformity of films. Electronic devices such as printed transistors and organic light-emitting diodes require precise feature dimensions, areas, and thicknesses for reliable operation. This requires mitigating artifacts which degrade pattern fidelity and impact electrical performance. The most important artifacts for mesoscale (e.g. 100 µm – 10 mm) features include edge roughness, pinholes, and ink dragout, as illustrated below in Figure 4.7.

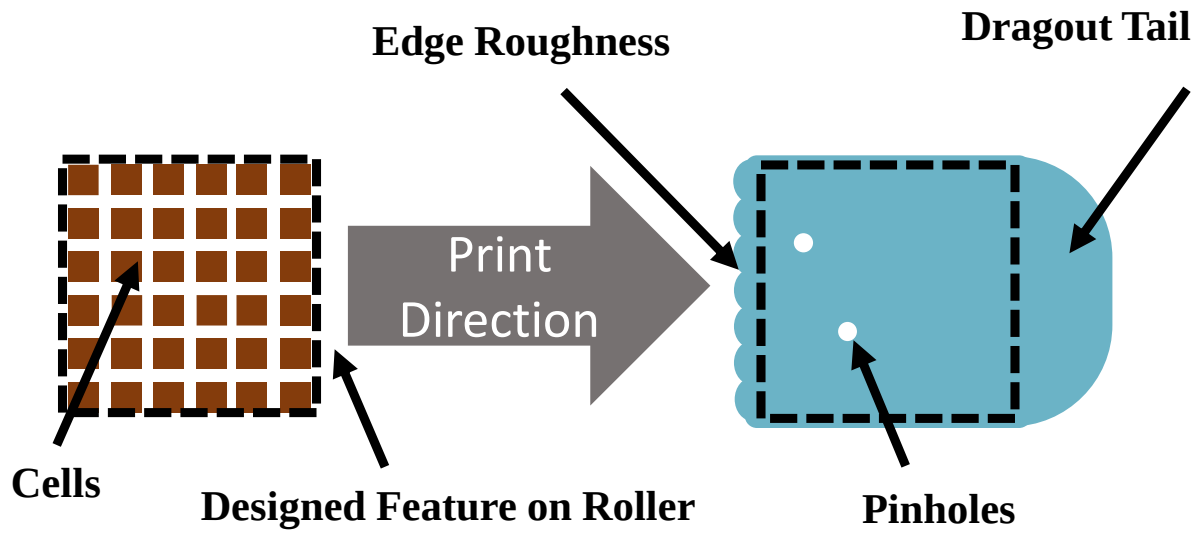


Figure 4.7 Gravure-printed feature formation with prominent artifacts highlighted (dragout, edge roughness, and pinholes).

Square test features were printed from silver nanoparticle inks (*Advanced Nanoproducts DGP 15-LT*) using arrays of 85 µm square gravure cells (24 µm depth, 15 $cm^3/m^2$ ~ 10 BCM). Upon transfer to PEN plastic substrates, the individual ink droplets coalesced to form continuous, square films

with nominal dimensions of 200 µm – 10mm. Figure 4.7 shows this process for a single square feature made up of an array of smaller square cells. Using this pixelated representation, gravure rollers can be designed to have a large variety of shapes and patterns. For this particular ink and for features of this size, the print fidelity is mainly limited by the dragout-related artifacts. The presence of pinholes, leading edge roughness, and the dragout tails are often correlated, suggesting that they can arise from common mechanisms. An example of a printed feature showing some of these artifacts is shown below in Figure 4.8.

To investigate the mechanisms that create these printing artifacts, doctoring speed, print speed, and transfer force were varied independently. The resulting printed features demonstrated significant differences in their shape and size as a function of each of these physical parameters. Doctoring speed was varied from 100 mm/s to 800 mm/s, while maintaining a constant, independent print speed of 1000 mm/s. The shapes of the printed features showed larger *dragout tails* for low doctoring speeds. Figure 4.9 displays the length of the tails (total length minus width) expressed as a ratio of the total length at varying print speeds. At high speeds, the tail artifact is minimized and the feature approaches a more ideal square shape.

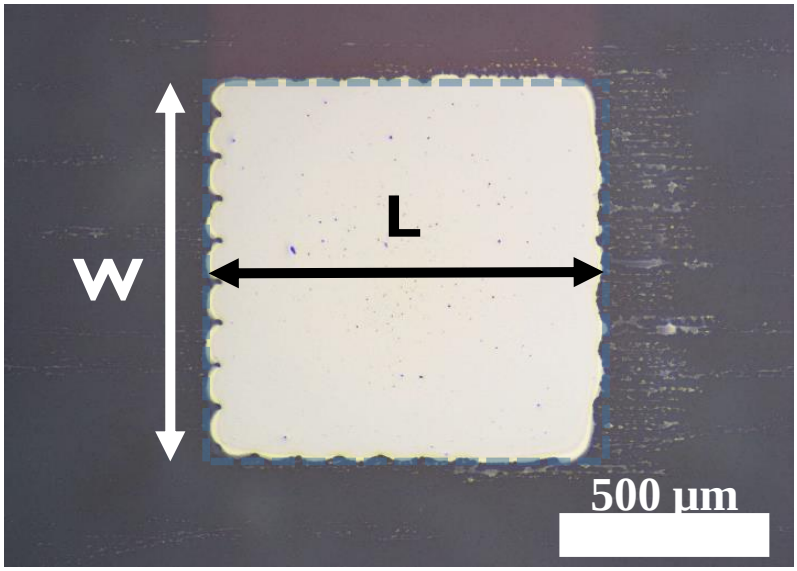


Figure 4.8 Example square feature printed with ANP silver ink at 1000 mm/s and 700 N printing force, showing leading edge artifacts and extraction of width and length measurements.

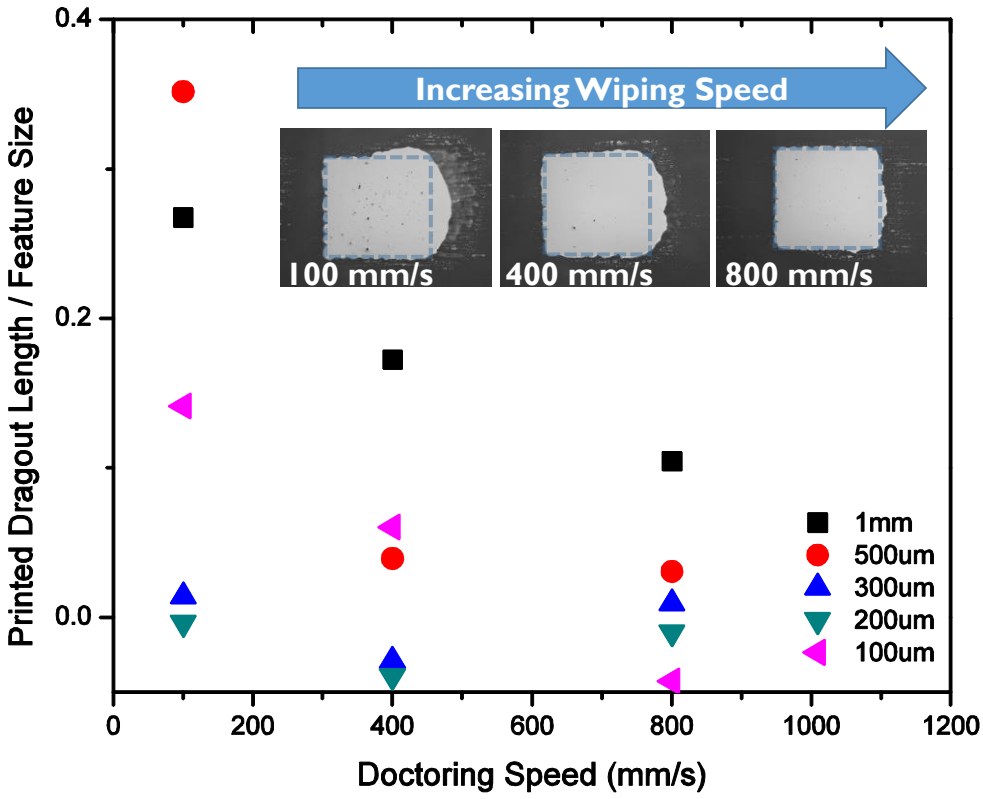


Figure 4.9 Normalized dragout tail length vs doctoring speed for silver inks transferred at 1000 mm/s. Inset shows 1 mm x 1 mm printed squares.

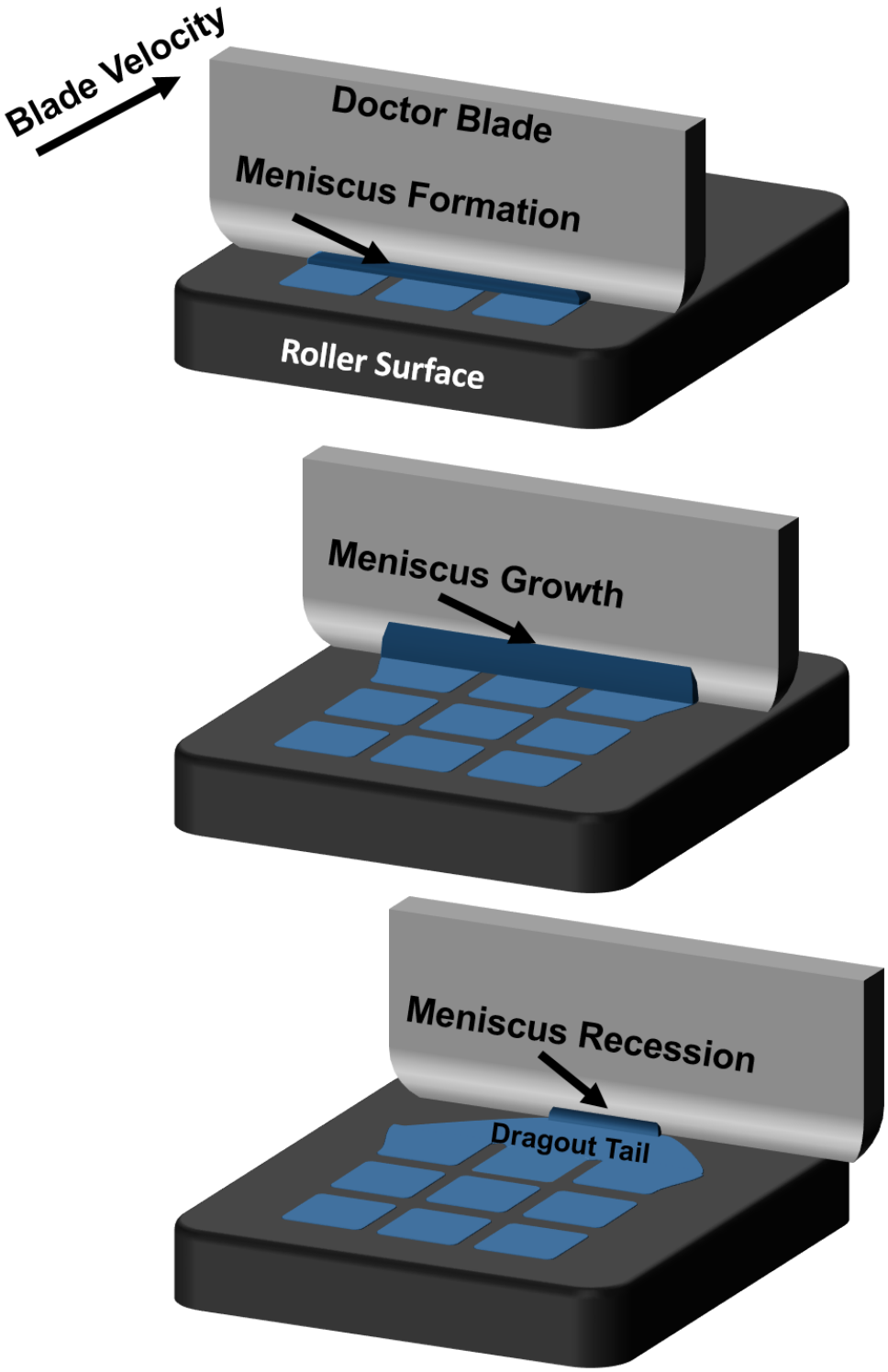


Figure 4.10 Illustration of the sequence of dragout tail formation, including meniscus formation, meniscus growth, and meniscus recession from the blade edge.

Previous studies on highly-scaled inverse gravure printing proposed that the dragout tail deposit could be caused by the wetting of ink on the backside of the doctor blade. The capillary effect on the backside adds volume to the growing meniscus which would then be redeposited as a trailing tail behind the cell [9], [11]. This mechanism is consistent with our two key observations of reduced dragout tail lengths at higher doctoring speeds and increased tail lengths for larger features (even after normalizing by feature size). This process is illustrated below in Figure 4.10 for a square array of cells, showing the proposed process occurring on the engraved roller surface.

While this model can account for the tail formation on the roller, there has been little study to date on the influence of the transfer process on these artifacts. To study this aspect, we utilized the process-decoupled nature of the system to independently control the transfer conditions. In the first case, we printed the same ink and features using different transfer speeds, while maintaining a constant doctoring speed. Interestingly, the dragout tails have a strong inverse dependence on print speed. At low print speeds, the features have trailing edges with *tail*-like deposits whereas at high speeds the trailing edges of the printed features are relatively flat and uniform. These results suggest that the print speed has an important role in extending and spreading tails during the contact-based transfer process. Because contact-based printing processes can be highly dependent on the contact mechanics, the printing force was varied while maintaining constant doctoring and print speed conditions. The printed features show enhanced tail lengths for high print force and line pressure.

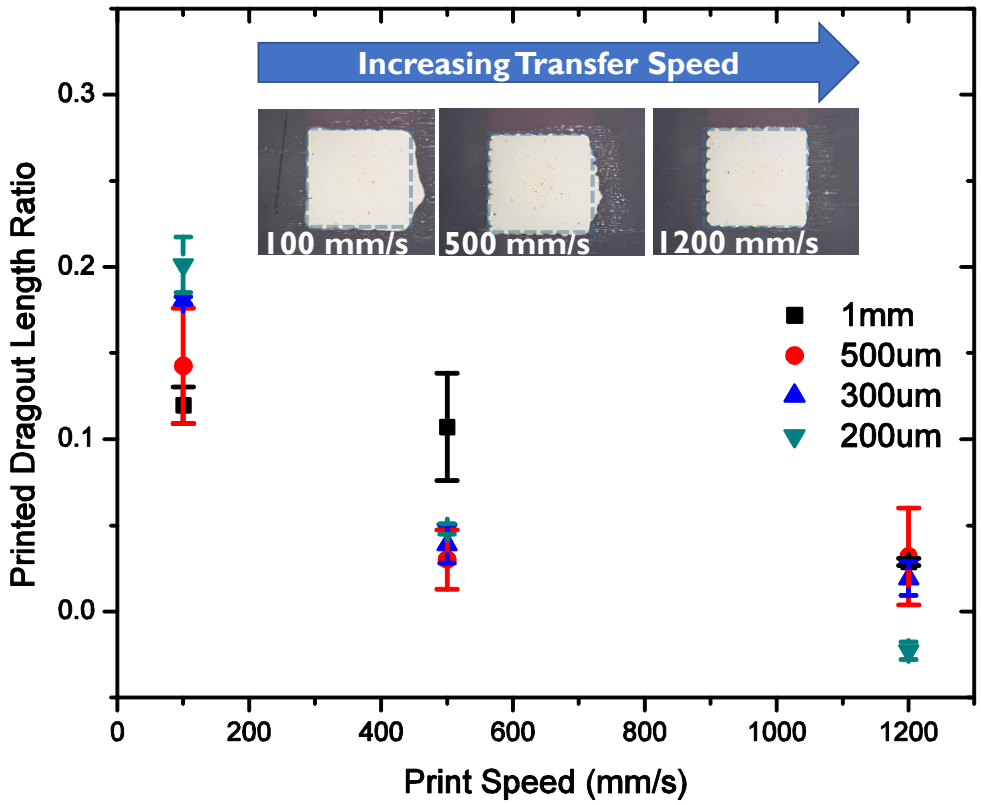


Figure 4.11 Normalized dragout tail length vs print speed for nanoparticle silver inks doctored at 1000 mm/s. Inset shows 1 mm x 1 mm printed square features.

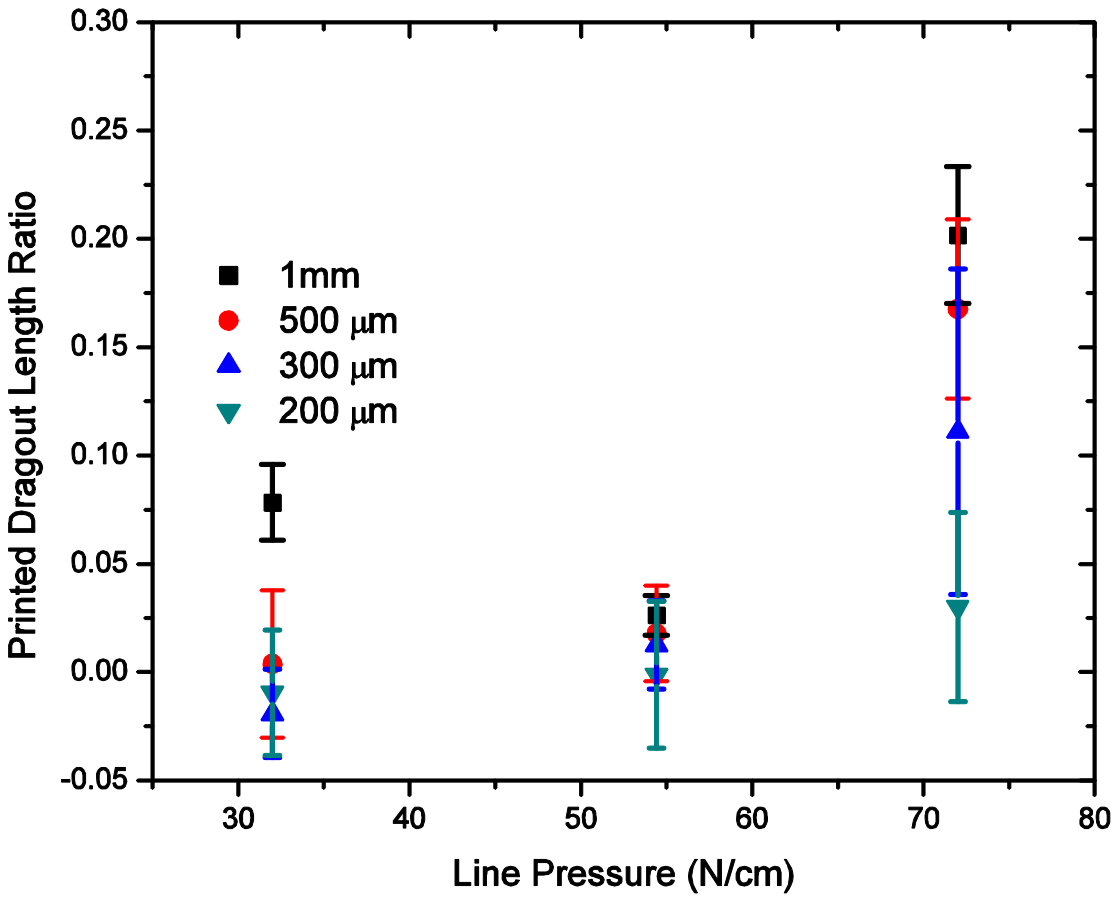


Figure 4.12 Normalized dragout tail length vs print pressure for nanoparticle silver inks doctored at 1000 mm/s and printed at 500 mm/s. Inset schematic illustrates application of printing force to form line contact with substrate.

### 4.5 Ink Transfer Contact Mechanics

The results of the process-decoupled printing experiments reveal an interesting dependence of gravure-printed feature fidelity on the transfer contact mechanics. This allows us to amend the previous understanding of dragout tails as artifacts dominantly controlled by the doctoring conditions. Instead, the feature tails appear to be created and enhanced during conditions of low speed or high pressure transfer. This could suggest the presence of squeezing flows induced by the line contact transfer pressure distribution. In this scenario, ink which remains deposited outside the gravure cells after doctoring could be squeezed by the rolling contact line. The time allowed for this squeezing flow to occur would be determined by a combination of the print speed and the contact area between the roller and the substrate. Hertzian contact theory predicts that this contact area should also scale roughly with $F_p^{0.5}$, and, indeed, measurements of the contact area stamped by ink at varying print forces display this trend (Figure 4.13). The contact area was measured by using an inked roller and a stationary substrate with variable backing material. The printing force was varied to observe the changes in the contact width. A visualization of the deformation in the backing material and substrate is shown in Figure 4.12. The compliance of the backing rubber results in the enlarged contact area.

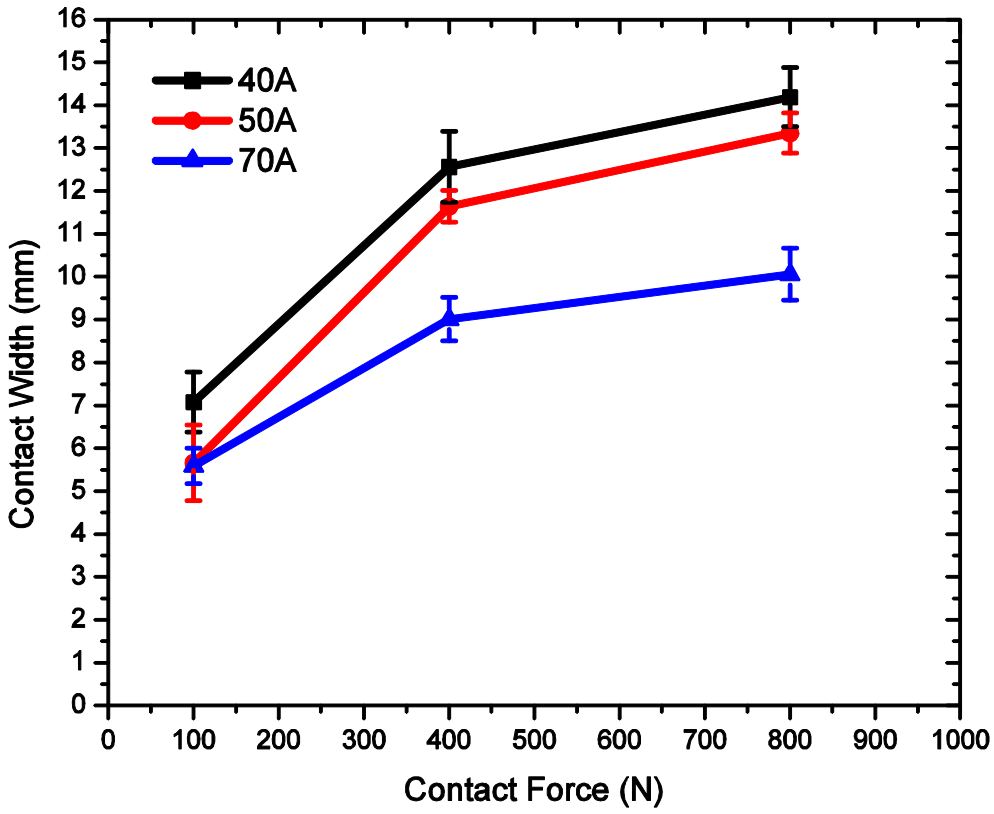


Figure 4.13 Measured contact width vs total contact force for rubber substrate backing of varying Shore A scale hardness.

Table 4.2 Hardness of butyl rubber substrate backing materials

| **Durometer Hardness** | **Young's Modulus (MPa)** |
|---|---|
| 40A | 1.7 |
| 50A | 3.0 |
| 70A | 8.0 |

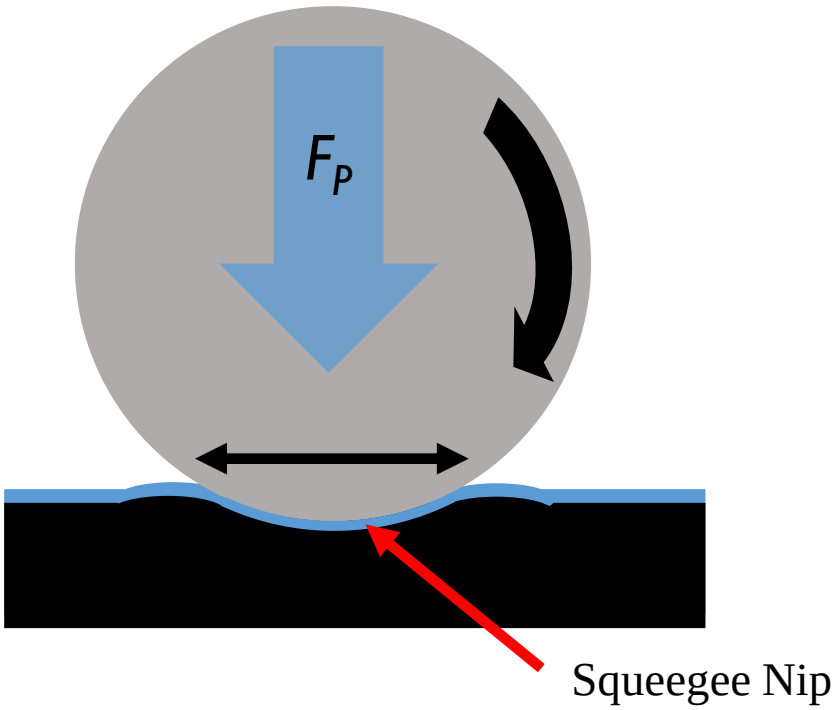


Figure 4.14 Contact diagram between gravure roller and substrate, highlighting the squeegee nip at which ink transfer and squeezing flows can occur.

To test the mechanism behind the squeezing flow and control the contact mechanics, similar prints were performed using rubber sheets of varying hardness for substrate backing. Softer, more compliant rubber (Shore A 40 vs Shore A 65) sheets resulted in enhanced ink spreading in both the width and length direction of the sample, as shown below in Figure 4.15. As expected, this isotropic spreading also resulted in corners of larger radii and rounded dragout tails. A positive consequence of the compliant substrate, however, is that the contact pressure uniformity across the width of the substrate was improved due to the larger deformation of the rubber backing. The result of this is that large area prints (120 mm x 300 mm) can be achieved with higher yield and uniformity (Figure 4.16). Stiffer substrate backing materials, on the other hand, require extremely flat shuttle surfaces and rubber with highly uniform thickness to achieve uniform transfer pressure. This establishes a clear design tradeoff which could be vital to achieving scalable nanomaterial-based printed devices.

(a)

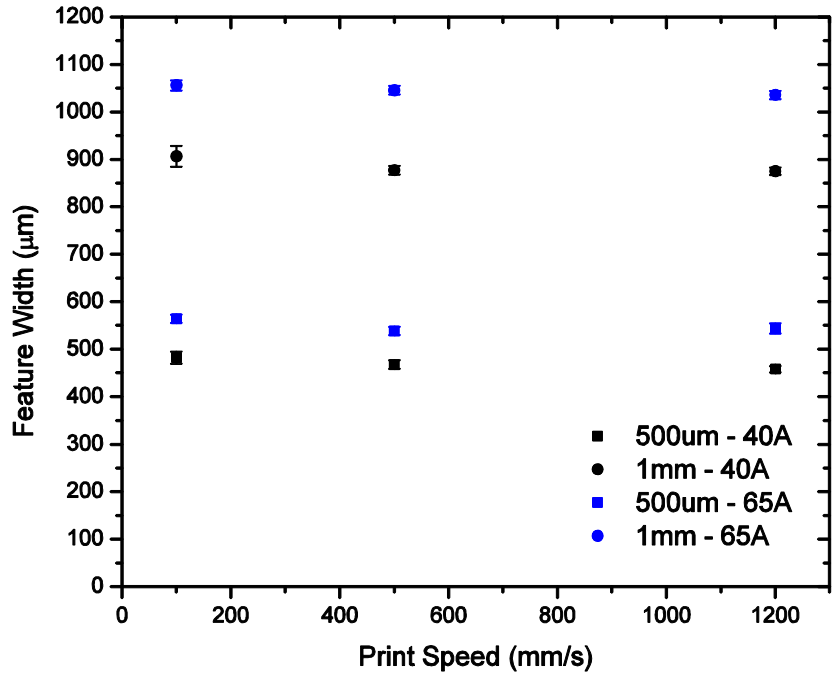


(b)

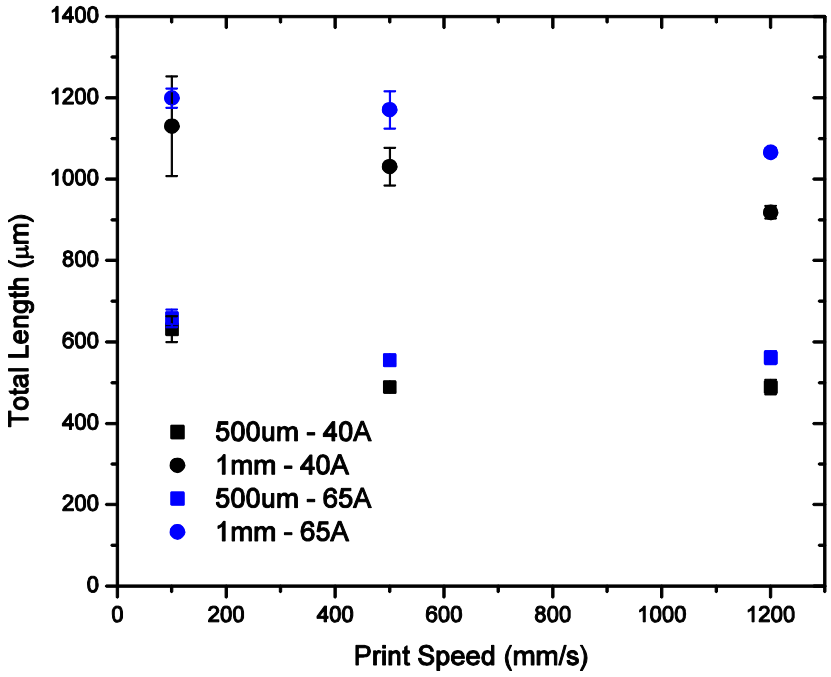


Figure 4.15 Absolute feature width (a) and feature length (b) vs print-speed for rubber substrate backings with varying hardness, doctored at 1000 mm/s.

Figure 4.16 Large area (120 mm x 300 mm) gravure-printed silver ink pattern printed utilizing soft (Shore A 40) rubber substrate backing.

## 4.6 Summary

This chapter presents a custom-designed tool for process-decoupled gravure printing using a sheet-fed design with pneumatically controlled doctoring and printing, and a rigid cantilevered bearing assembly. The feature set and capabilities of this machine were motivated by critical printing physics and engineering challenges identified through the work presented in Chapter 2 and Chapter 3. The mechanical features of the design allow the investigation of new printing physics via novel experimental controls. These techniques were applied to reveal the dependence of dragout tail formation in printed silver nanoparticle inks on the transfer contact mechanics between the roller and substrate. Engineering these contact mechanics with variable print pressure, speed, and substrate backing can allow controls by which to mitigate the artifacts and improve overall print fidelity. In the future, empirical models of the transfer induced squeezing flow based on these results could allow predictive modeling and design of optimal pixelated gravure cell layouts. Furthermore, the registration capabilities of this printer are expected to allow the fabrication of high-performance gravure-printed metal oxide transistors with short channel lengths and excellent registration accuracy.

## 4.7 References

[1] R. Kitsomboonloha, H. Kang, G. Grau, W. Scheideler, and V. Subramanian, “MHz-Range Fully Printed High-Performance Thin-Film Transistors by Using High-Resolution Gravure-Printed Lines,” *Adv. Electron. Mater*., vol. 1, no. 12, p. n/a-n/a, Dec. 2015.

[2] C. Kapnopoulos et al., “Fully gravure printed organic photovoltaic modules: A straightforward process with a high potential for large scale production,” *Sol. Energy Mater. Sol. Cells*, vol. 144, pp. 724–731, Jan. 2016.
[3] W. J. Scheideler, J. Jang, M. A. U. Karim, R. Kitsomboonloha, A. Zeumault, and V. Subramanian, “Gravure-Printed Sol–Gels on Flexible Glass: A Scalable Route to Additively Patterned Transparent Conductors,” *ACS Appl. Mater. Interfaces*, vol. 7, no. 23, pp. 12679–12687, Jun. 2015.
[4] Y. Khan, A. E. Ostfeld, C. M. Lochner, A. Pierre, and A. C. Arias, “Monitoring of Vital Signs with Flexible and Wearable Medical Devices,” *Adv. Mater.*, vol. 28, no. 22, pp. 4373–4395, Jun. 2016.
[5] V. Subramanian et al., “Progress Toward Development of All-Printed RFID Tags: Materials, Processes, and Devices,” *Proc. IEEE*, vol. 93, no. 7, pp. 1330–1338, Jul. 2005.
[6] G. Grau, J. Cen, H. Kang, R. Kitsomboonloha, W. J. Scheideler, and V. Subramanian, “Gravure-printed electronics: recent progress in tooling development, understanding of printing physics, and realization of printed devices,” *Flex. Print. Electron.*, vol. 1, no. 2, p. 023002, 2016.
[7] G. Grau and V. Subramanian, “Fully High-Speed Gravure Printed, Low-Variability, High-Performance Organic Polymer Transistors with Sub-5 V Operation,” *Adv. Electron. Mater.*, vol. 2, no. 4, p. n/a-n/a, Apr. 2016.
[8] K. Fukuda and T. Someya, “Recent Progress in the Development of Printed Thin-Film Transistors and Circuits with High-Resolution Printing Technology,” *Adv. Mater.*, p. n/a-n/a, Nov. 2016.
[9] R. Kitsomboonloha, S. J. S. Morris, X. Rong, and V. Subramanian, “Femtoliter-Scale Patterning by High-Speed, Highly Scaled Inverse Gravure Printing,” *Langmuir*, vol. 28, no. 48, pp. 16711–16723, Dec. 2012.
[10] R. D. W. Miller, “Variations of line pressure and rolling speed with indentation of covered rollers,” *Br. J. Appl. Phys.*, vol. 15, no. 11, pp. 1423–1435, Nov. 1964.
[11] G. Grau, W. J. Scheideler, and V. Subramanian, “High-resolution gravure printed lines: proximity effects and design rules,” *SPIE* 2015, vol. 9569, p. 95690B–95690B–8.

# Chapter 5: Aqueous Ink Design for Low-Temperature Printed Metal Oxide Transistors

## 5.1 Introduction

The preceding chapters established the use of high-resolution scalable printing technologies such as gravure as viable techniques for depositing metal oxide-based transparent conductors. Exploring the tradeoffs between metal oxide ink design, annealing, and printing performance revealed both the versatility and the limitations of sol-gel metal oxide inks. The extensibility of sol-gel ink design to various precursor materials and stoichiometries can be a powerful tool to develop a full material set for printed metal oxide devices such as thin film transistors, but the requirement that high-temperature processing (> 400 °C) be used limits the choice of substrates to flexible glass and other rigid materials. Lower cost flexible substrates such as polyethylene naphthalate (PEN) and polyimide (PI) can support thermal processing in the range of 200 - 350 °C and can therefore broaden the scope of potential applications for printed transparent electronics. However, new materials which reach high performance at low annealing temperatures must first be developed. This chapter presents aqueous ink chemistries which address the fluid and electronic limitations of conventional sol-gel inks. Although these chemistries are inkjet printed in this chapter, concentrated formulations similar to those used in Chapter 2 could extend these to gravure printing and other roll-based scalable patterning methods.

To date, there has been significant work towards lowering processing temperatures used for metal oxides by thin film combustion processing and alternative annealing methods like UV photoactivation, resulting in the achievement of high performance ($\mu_{eff}$ > 10 $cm^2$ $V^{-1}s^{-1}$) at annealing temperatures below 250 °C[1], [2], as well as some encouraging demonstrations of high-performance films fabricated on plastic substrates[3]. More recently, comparable device performance has been obtained with spincoated aqueous semiconductors based on metal nitrate salts which are easily synthesized and do not require the use of toxic volatile solvents.[3]–[7] Furthermore, these aqueous inks have been used to fabricate high-k metal oxide dielectric films which show low leakage in TFT structures.[8]–[12] However, these advancements have been applied predominately to spin-coated and spray-coated films. The use of additive patterning technologies to print these low-temperature compatible inks has not yet been addressed. This chapter will illustrate the principles of aqueous ink design for printing high-performance metal oxide transistors at low temperatures.

Although low-temperature processed semiconductors and dielectrics have received significant attention, there has been considerably less work on low-temperature metal oxide conductors suitable for use as source, drain and gate electrodes for solution-processed metal oxide transistors. The majority of work done developing low temperature and printed metal oxide transistors[13] has utilized opaque evaporated metal electrodes such as Al or Mo that sacrifice the transparency and process scalability offered by the solution-processed metal oxide semiconductors and dielectrics. Though graphene-based printed contacts were recently demonstrated at a processing temperature of 300 ºC [14], there remains a need to achieve lower processing temperatures, lower contact resistance ( < 2 kΩ-cm), and higher mass-loading (> 2.1 % w/v). The absence of high-quality low-temperature-processed ($T$ < 250 ºC) printable transparent conductors is therefore a significant shortcoming of the available material set for realization of low temperature transparent oxide thin film transistors.

Printed transparent metal oxide conductors could deliver both transparency and solution processability, leading to lower cost additive patterning and higher pixel aperture ratios[15] for display applications. Accomplishing this requires advances in ink formulation for printing, since high performance, low temperature processable solutions have primarily been used in spin coating formulations[16] that are not tailored for any high-throughput printing methods. Another barrier to replacing metallic electrodes in printed metal oxide TFTs has been the lack of solution-processed materials that can obtain good conductivity at low temperatures and form stable low-resistance contacts to metal oxide semiconductors during subsequent device processing. This property is essential, since good performance of semiconductors / dielectrics is achieved with oxidative air / $O_2$ anneals, while the conductivity of TCO films such as indium-tin oxide must typically be enhanced by reductive annealing in forming gas (95% $N_2$ / 5% $H_2$)[17], inert atmospheres (Ar, etc), or by reductive plasma treatments.[18] The manufacturing of high-performance printed metal oxide electronics, thus, calls for printed conductors which have high and stable conductivity, even after thermal treatments in various ambients.

Cadmium oxide is a highly conductive metal oxide that satisfies these material requirements for transparent TFT electrodes, but it has previously received comparatively little attention because of its toxicity and the associated cost of electronic materials recycling.[19]. Though the corresponding safety and environmental concerns of using cadmium are valid, CdO has exceptional electronic properties[20], [21] associated with its high electron affinity, high dielectric constant, and low conduction band edge. These include its extremely high number of intrinsic defects and the fact that it maintains record TCO mobility (up to 200 $cm^2/Vs$) even at free carrier concentrations approaching $10^{21}$ $cm^{-3}$. These properties make it an important archetypal TCO material system to investigate, and a useful TCO for selected optoelectronic applications. Both doped and undoped CdO show extremely high figure of merit in CVD[22]–[24] and sputtered systems, exceeding that of ubiquitous ITO films, in some cases. In this work, we demonstrate inkjet printed CdO-based conductors for applications in flexible transparent electronic systems. Using aqueous ink formulations to lower the required processing temperature and improve printed feature morphology, this chapter extends these materials to transparent printed transistors. Importantly, the additive manufacturing techniques developed here also offer a route to minimize material waste.

## 5.2 Aqueous Transparent Conductor Ink Design

Solution-processed transparent metal oxides present a complex material system in which ink design (precursor, solvent, etc.) and film conversion are strongly coupled. As discussed in Section 1.4, sol-gel films must undergo conversion from a precursor solution to a solid film through drying and annealing processes, which involve both precursor decomposition and volatilization. As a result, spin-coated formulations for metal oxides have evolved to include multiple solvents / stabilizers, and, even, multiple types of precursors. The problem this synthetic complexity poses is how to simultaneously optimize the printing, stability, and mass-loading of an ink while maintaining the performance advantages achieved with complex precursor and solvent combinations.

To address these issues, we present a simple printable ink design methodology consisting of aqueous solutions of metal nitrates, a class of low-cost sol-gel precursors that are readily available at high purity for use in scalable industrial processes. The use of aqueous solutions has significant

advantages for both the printing and the performance of the conductive features. The model system used herein for demonstrating the advantages of aqueous metal oxide inks is that of aluminum-doped cadmium oxide (ACO). ACO has demonstrated high performance ($\sigma$ > 1,000 S cm$^{-1}$) in sputtered films and spray-coated films processed at relatively high, glass-compatible temperatures ($T$ > 300 °C)[24]. The novel formulation of ACO inks for inkjet printing is used here to leverage this high performance in an additive process for scalable production of transparent electronics.

### 5.3 Inkjet Printing Aqueous Sol-Gel Metal Oxide Inks

Aqueous sol-gel metal oxide inks have several favorable properties for use in printed electronics. Firstly, metal nitrates such as $Al(NO_3)_3$ and $Cd(NO_3)_2$ are highly soluble in water (solubility > 5M at room temperature), allowing dissolution of above 60 % wt / vol of precursor compounds. This figure is particularly high compared to aqueous dispersions of carbon nanomaterials, which are typically below 3% wt / vol [25], [26].

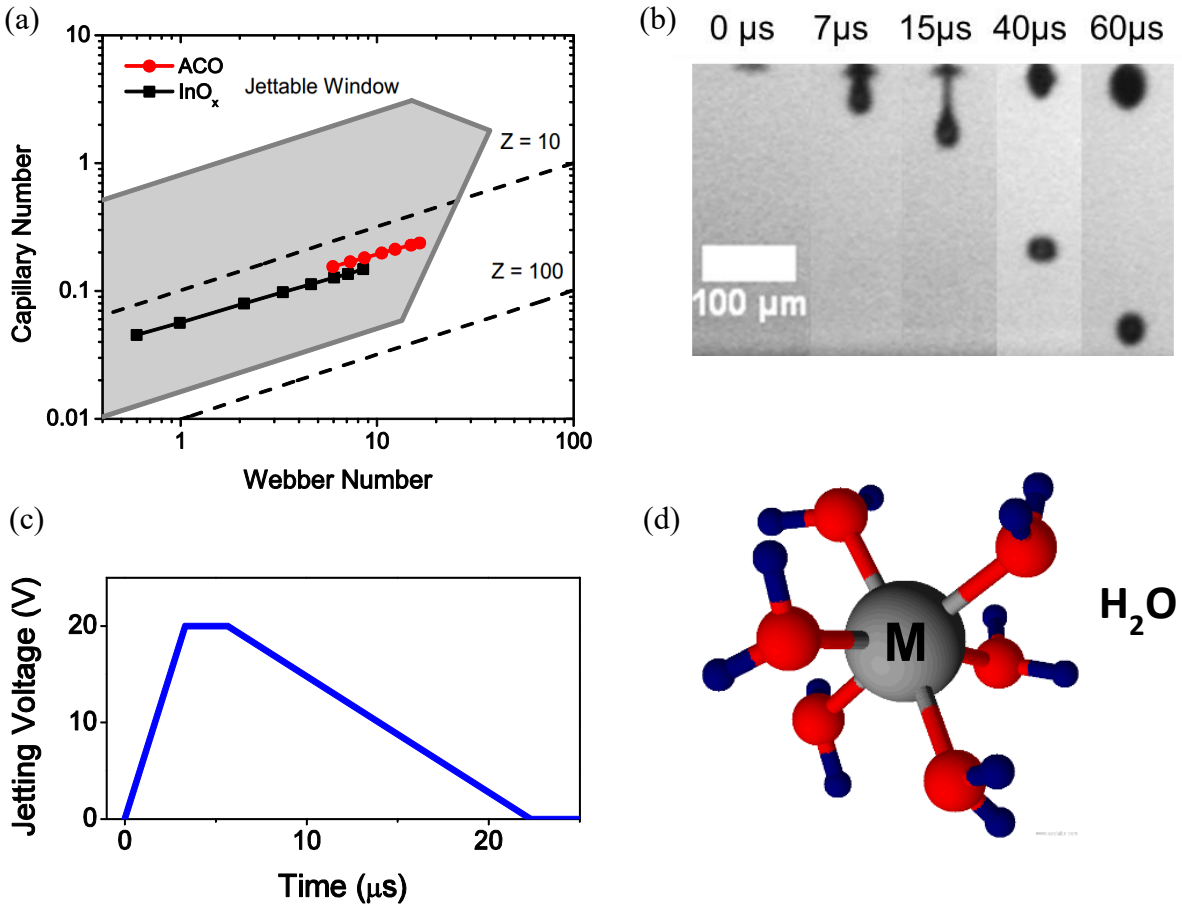


Figure 5.1 ACO inks plotted on a Capillary (*Ca*) number / Weber (*We*) number diagram with empirically determined jettable window shaded in green and Z numbers 10 and 100 indicated by dashed lines (a). Stroboscopic snapshots of ACO droplets (b) jetted from the piezoelectric print head by the corresponding jetting waveform (c). Solvated metal cations coordinated to shell of water molecules.

This has important implications for ink design, in that it is possible to print thicker films or, conversely, to scale down drop volumes and line widths while maintaining a suitable film thickness. As discussed earlier in this thesis, highly concentrated inks are a necessity for being able to print fine line and achieve control of spreading behavior and coffee-ring formation.

Additionally, the use of pure water as the solvent facilitates long-term ink stability. In this study, the inks showed stable jetting and high performance for more than six months after being loaded into plastic disposable printer cartridges (Dimatix DMP11010). In contrast to non-aqueous sol-gels, which can be extremely hygroscopic, these aqueous formulations are less prone to the absorption of moisture[27] and, therefore, less sensitive to storage conditions such as the ambient humidity. This is an essential feature for allowing scalable processing of these materials in air. The fluid properties of ACO transparent conductor inks are suitable for jet-based printing technologies. The viscosity (concentration 100 mM – 500 mM) is approximately 1.0 – 1.5 cP over a range of shear rates from 10 – 1000 $s^{-1}$. While this is near the lower range of acceptable viscosities for inkjet, the high surface tension of water enables stable jetting at frequencies from 200 Hz to 5 kHz.

Features were printed on a desktop Fujifilm Dimatix inkjet printer (DMP 2831) at a platen temperature of 32 °C and a cartridge temperature of 29 °C. Firing voltages of 18-28V were used to jet ACO inks at 2 kHz with drop spacing of 20 – 40 µm, in 1 – 5 layers. The *DI Water* waveform provided by Fujifilm Dimatix was used for aqueous inks, while Model Fluid 2 waveform was used to jet organic inks. Quantitative droplet analysis of drop volume and droplet velocity was performed on a Ceradrop X-Serie printer. Fluid viscosities were measured using a rotational cone / plate viscometer (Brookfield DV-III) at 22 °C and shear rates of 100 – 2000 $s^{-1}$. Surface tension was measured with a Wilhelmy plate (Pt) tensiometer (KSV Sigma 701).

To demonstrate this effect, we have plotted the ACO inks within an empirically determined Capillary number ( $Ca = \frac{\mu V}{\gamma}$ ) vs Weber number ( $We = \frac{\rho V^2 l}{\gamma}$ ) jetting window diagram[28]. As can be seen in Figure 5.1a, the aqueous inks fall within the jettable window over a range of jetting voltages, although they are located towards the regime of high inertial forces, similar to previously reported aqueous inkjet inks[29]. This is consistent with our observations that at the highest jetting voltages, which approach the limit of the empirically determined window, satellite droplet generation occurs and small stray droplets are jetted nearby printed features of interest. In this regime, drop velocities exceed 11 m $s^{-1}$ and droplet sizes increase beyond the nominal 10 pL drop volume of the Dimatix DMP 11010 cartridge. However, for intermediate jetting voltages, these issues are avoided and stable droplets may be consistently jetted (Figure 5.1b,c) to form high resolution features.

(a) (b)

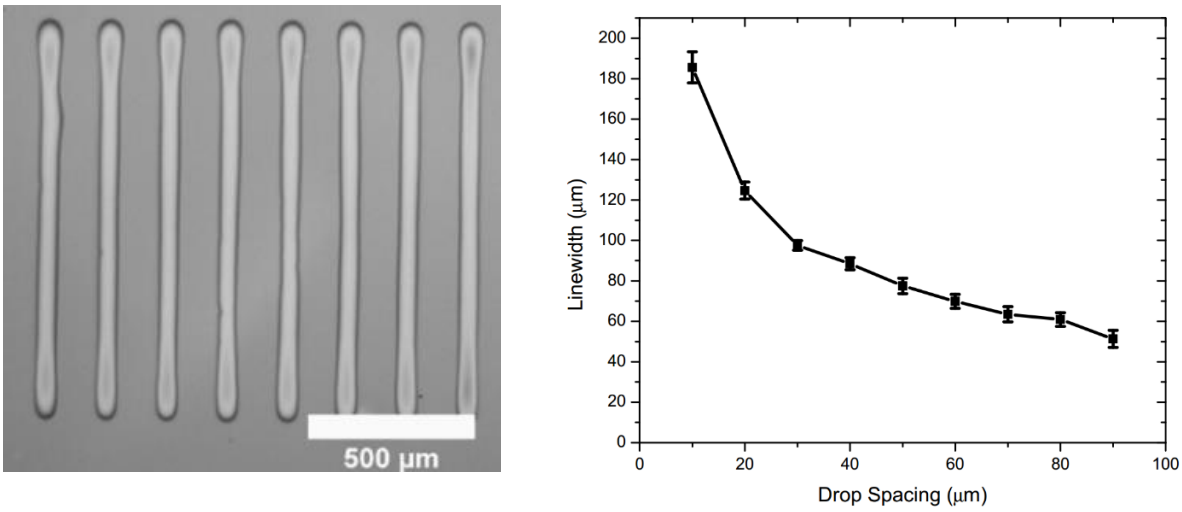


Figure 5.2 Array of inkjet printed transparent conductive lines (a). Linewidth of printed ACO lines (10 pL nozzle) on AlOx substrate with variable drop spacing (b).

By adjusting the drop spacing and substrate surface energy, reliable printed line morphologies with minimal line edge roughness were obtained, as shown in Figure 5.2. Stable lines were printed using drop spacing from 10 µm – 80 µm, allowing the patterning of linewidths as small as 60 µm with a 10pL cartridge (Figure 5.2b) and 25 µm with a 1 pL cartridge. In each case, features printed with aqueous inks showed no observable coffee-ring effect. For example, Figure 5.3 shows a micrograph and diagram of an inkjet printed indium oxide transistor with a highly uniform 25 nm $InO_x$ active layer and perfectly dome shaped ACO electrodes, as demonstrated by the height profile (1e). In fact, all line profiles of the aqueous inkjet printed inks are convex and lack edge deposits. This is particularly interesting if we consider that aqueous nanoparticle loaded inks typically show strong coffee-ring deposits[30], [31]. The lack of coffee-ring in these aqueous ink systems suggests an important interaction between the metal nitrate precursor and the aqueous solvent, which aids the formation of favorable line morphologies.

In most cases, high surface tension gradients are required to generate sufficiently strong Marangoni flows to overcome the outward flows responsible for the coffee-ring effect[32], [33]. These surface tension gradients have previously been generated by adding cosolvents, i.e. adding higher boiling point organic solvents such as ethylene glycol[32]. However, the addition of organic solvents in metal oxide sol-gel inks has been documented to yield carbon-based impurities in the annealed films, which can contribute to inferior performance, particularly in low-temperature annealed films[3]. The aqueous based inks shown herein avoid these issues with organic contamination, but still achieve domed morphologies. By avoiding complicated anti-coffee-ring schemes such as substrate cooling[34] and cosolvents[30], aqueous inks can facilitate scaling of these processes to high-throughput systems.

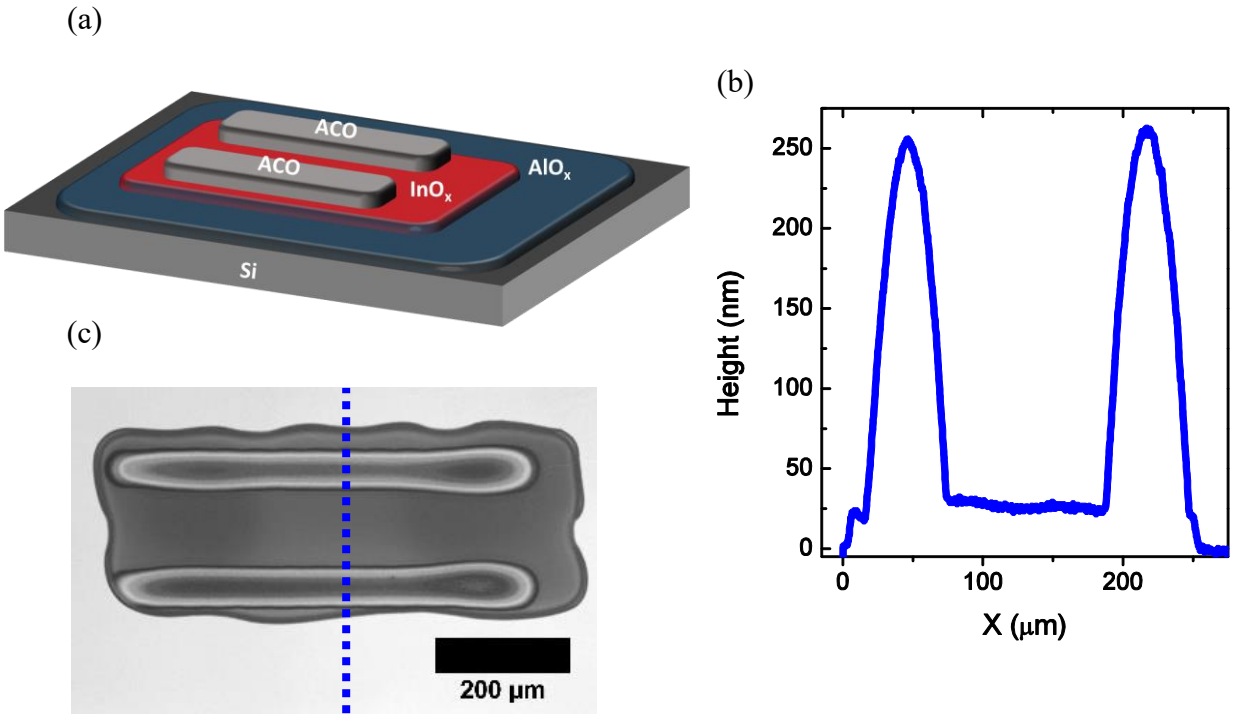


Figure 5.3 Isometric 3D illustration of printed Indium oxide transistor utilizing low-temperature aqueous processed semiconductor and conductor inks (a). Stylus profilometry obtained height profile (b) of printed transistor obtained by scanning from source to drain across channel region, as highlighted in the dashed blue line on the micrograph (c).

A mechanism consistent with these observations involves the high surface tension of water and the high solute concentration-induced surface tension gradient that exists for metal nitrates. As shown in Figure 5.4, aqueous solutions of the metal nitrates used here, such as $Al(NO_3)_3$ and $Cd(NO_3)_2$, have negative surface tension gradients with respect to their concentration. In the case of $Cd(NO_3)_2$ solutions, for example, the surface tension decreases by more than 15 mN $m^{-1}$ from neat solution to 500 mM. This compositional variation in surface tension is expected to result in evaporation-induced surface tension gradients that can drive inward flow from the contact line to the center of the feature. This effect has been observed in aqueous colloidal solutions loaded with small ionic surfactants[35], but has not previously been reported for sol-gels. Organic sol-gels by, have positive compositional surface tension gradients (Figure 5.5) which would tend to exacerbate coffee ring edge deposits.

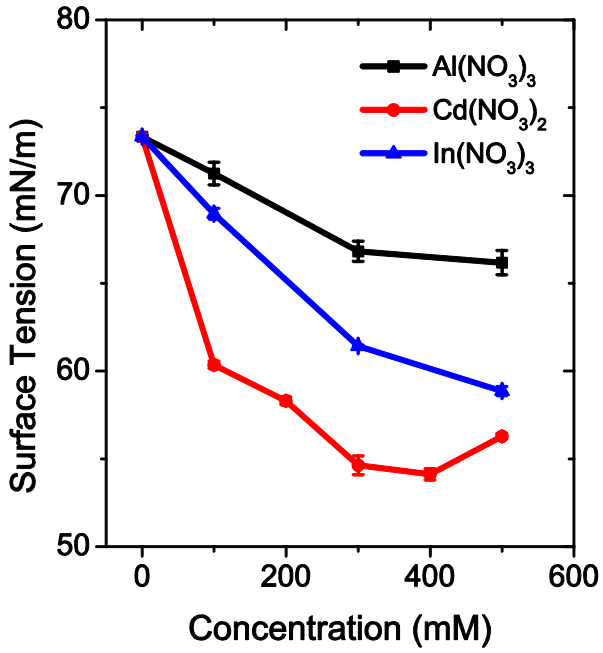


Figure 5.4 Surface tension of aqueous precursors vs organic $AlO_x$ precursor inks at varying concentrations.

Highlighting the benefit of water-based inks, inks consisting of equivalent metal salt concentrations dissolved in a commonly used organic solvent, 2-methoxyethanol (2-ME) were printed under similar conditions (substrate temperature and surface energy, etc). 2-ME is the primary solvent in many spin-coating formulations for low-temperature combustion-processed metal oxides. The ACO inks based on 2-ME showed worse printing performance in terms of linewidth and in the severity of the coffee-ring effect. At room temperature and elevated temperatures, printing the 2-ME inks also resulted in strong coffee-rings with edge thicknesses rising significantly higher than the middle (Figure 5.5b). This is an unfavorable morphology that may cause pinholes or non-uniform charge injection in devices such as thin film transistors. Inks based on 2-ME also showed significant spreading (linewidth > 300 µm) which could not be controlled by elevating the substrate temperature (>50 °C) to accelerate drying. The excess spreading of this organic ink suggests an alternative mechanism for coffee-ring relief in aqueous ink systems, which is the higher contact angle of aqueous inks (Table 5.1) and the lack of stable pinning at the contact line for organic inks. Previous studies of inkjet printed films found that an elevated contact angle reduced the severity of coffee-ring deposits[34]. This accentuates the unique advantages that aqueous inks have due to their intrinsic high surface tension.

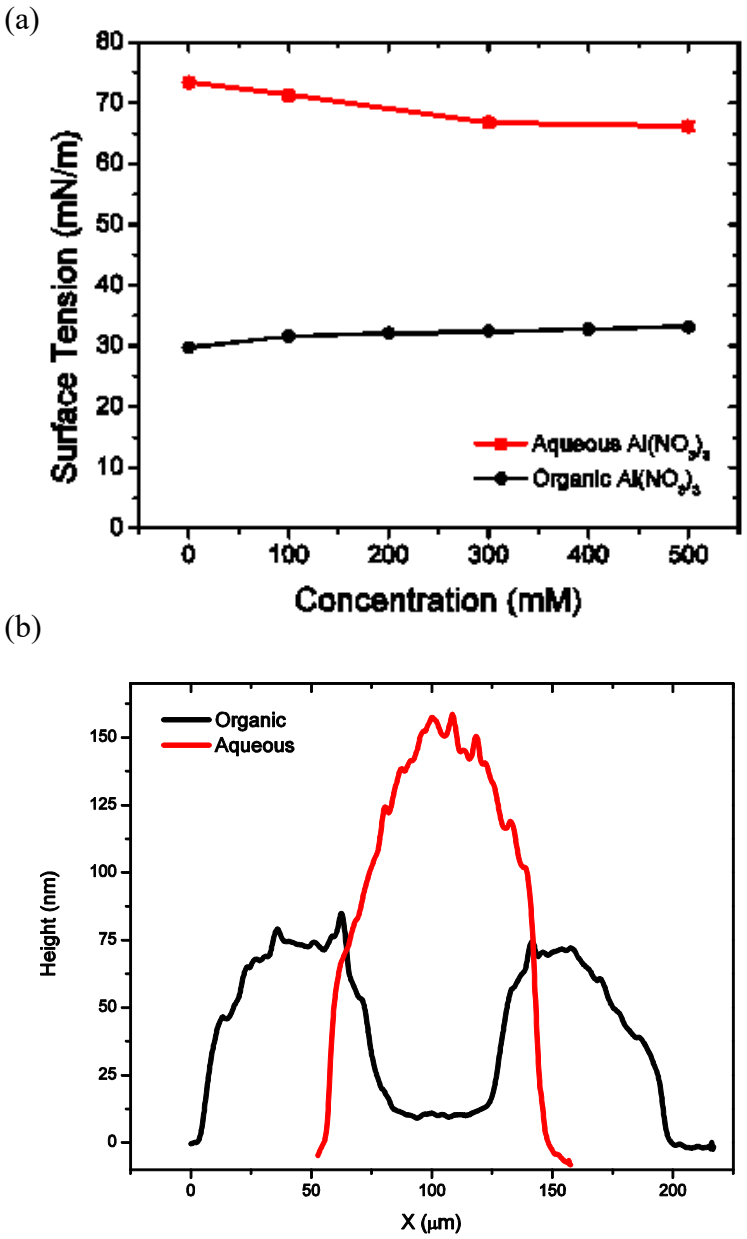


Figure 5.5 Surface tension of aqueous (red) $AlO_x$ precursors vs organic (black) AlOx precursor inks (2-methoxyethanol) at varying precursor concentrations (a). Printed line profiles for aqueous and organic low-temperature conductor inks.

$SiO_2$ wafers treated with a thin layer of $AlO_x$ were used as substrates in the study of the ACO conductivity and line morphology. $AlO_x$ was used to enhance wetting of the aqueous inks. The $AlO_x$ surface treatment was performed by treating the $SiO_2$ substrate with UV ozone (Jelight Model 42) for 10 min, followed by spinning a 100 mM aqueous solution of $Al(NO_3)_3$ at 6000 rpm for 30 s. After a 5 min dry (100 °C), the $AlO_x$ layer was transferred to a preheated aluminum top hot plate (250 °C) for 10 min. Following this process, the $AlO_x$ layer was treated with 2 min of UV Ozone (30 mW $cm^{-2}$). Following printing, ACO features were dried for 10 min (175 °C), and

then subsequently annealed at various temperatures (200 °C – 300 °C) for 20 min in air, on an aluminum top hot plate.

Table 5.1 Contact angle of solvents used in printing studies as a function of pretreatment by UV ozone.

| | **Sessile Drop Equilibrium Contact Angle** | |
|---|---|---|
| **Water on $AlO_x$:** | | |
| | Untreated | 39 ± 1˚ |
| | 30s UV Ozone | 36 ± 3˚ |
| | 60s UV Ozone | 31 ± 4˚ |
| | 120s UV Ozone | 24 ± 2 ˚ |
| | 240s UV Ozone | 14 ± 4 ˚ |
| **2-Methoxyethanol on $AlO_x$:** | | |
| | Untreated | < 5 ˚ |

## 5.4 Conductivity of Printed Source / Drain TFT Electrodes

Using the aqueous ACO inks, conductive lines were printed with varying numbers of layers. Multilayer printing was performed in consecutive passes of jetting, and the drying and annealing processes were performed only after all layers had been printed. Following the low temperature (250 °C) annealing process in air, conductive lines were fabricated with sheet resistances ($R_s$) of 600 Ω $\square^{-1}$ – 2 kΩ $\square^{-1}$ (Figure 5.6). As additional layers were added (total thickness > 300 nm), the specific conductivity remained relatively constant and the line profiles remained dome-shaped (Figure 5.6b) with minimal increases in linewidth due to a strongly pinned contact line.

The trend of conductivity stands in contrast to higher temperature (400 °C – 500 °C) processed printed conductors, which suffer from delamination and cracking which degrade conductivity for films of increasing thickness[36]. This attests to the benefit of the reduced volumetric compaction that occurs during drying of these water-based systems vis a vis conventional organic inks.

Similar to low temperature solution-processed semiconductors such as $InO_x$, and $InZnO_x$, the printed ACO undergoes conversion to solid functional films after annealing in the temperature range of 200 °C – 300 °C [37]. Conductive printed lines were formed at annealing temperatures as low as 220 °C, and significant conductivity ( > 43 S $cm^{-1}$) was achieved at 250 °C. As shown in Figure 5.7, performance improved monotonically up to 300 °C, reaching an optimal conductivity of more than 130 S $cm^{-1}$. The organic solvent based inks show a similar trend in conductivity with annealing temperature, but have lower performance relative to the aqueous processed ACO, particularly at lower temperatures (225 °C – 250 °C) which approach the viable temperature range for processing polymer substrates. This suggests that there is a considerable performance advantage to using aqueous inks for forming higher quality metal oxide conductors.

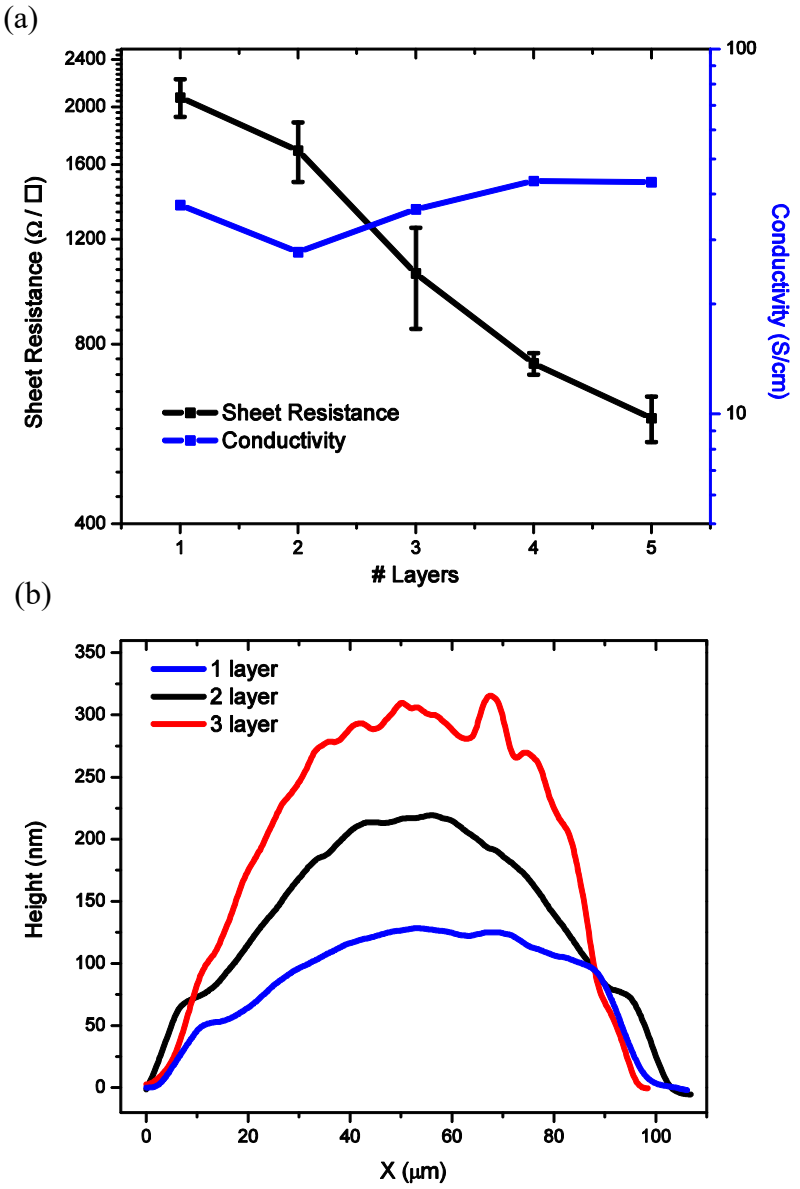


Figure 5.6 Conductivity and sheet resistance of printed ACO multilayer features (a). Line-profiles of multilayer printed ACO features (b).

### 5.5 ACO Conversion and Crystallization

To form metal oxides by a sol-gel route, films must undergo a conversion process during which solvent and precursor molecules are expelled and oxo bridges (M—O—M) are formed between metal cations. An important result of annealing is the densification and solidification of the film, which is often correlated with the onset and enhancement of functionality (mobility[1], dielectric constant[38], etc). To understand the effects of the thermal annealing on the low temperature conductors studied herein, both the volume contraction and mass-loss were measured. Stylus profilometry (Dektak Veeco 6M) performed on printed ACO lines after annealing at various temperatures (Figure 5.8) shows that, in total, there is approximately a 40% volume contraction

from 200 °C – 260 °C. This contraction is typically associated with densification and conversion of a sol-gel film. Above 260 °C there is minimal change in the cross-section of the printed features (Figure 5.8a).

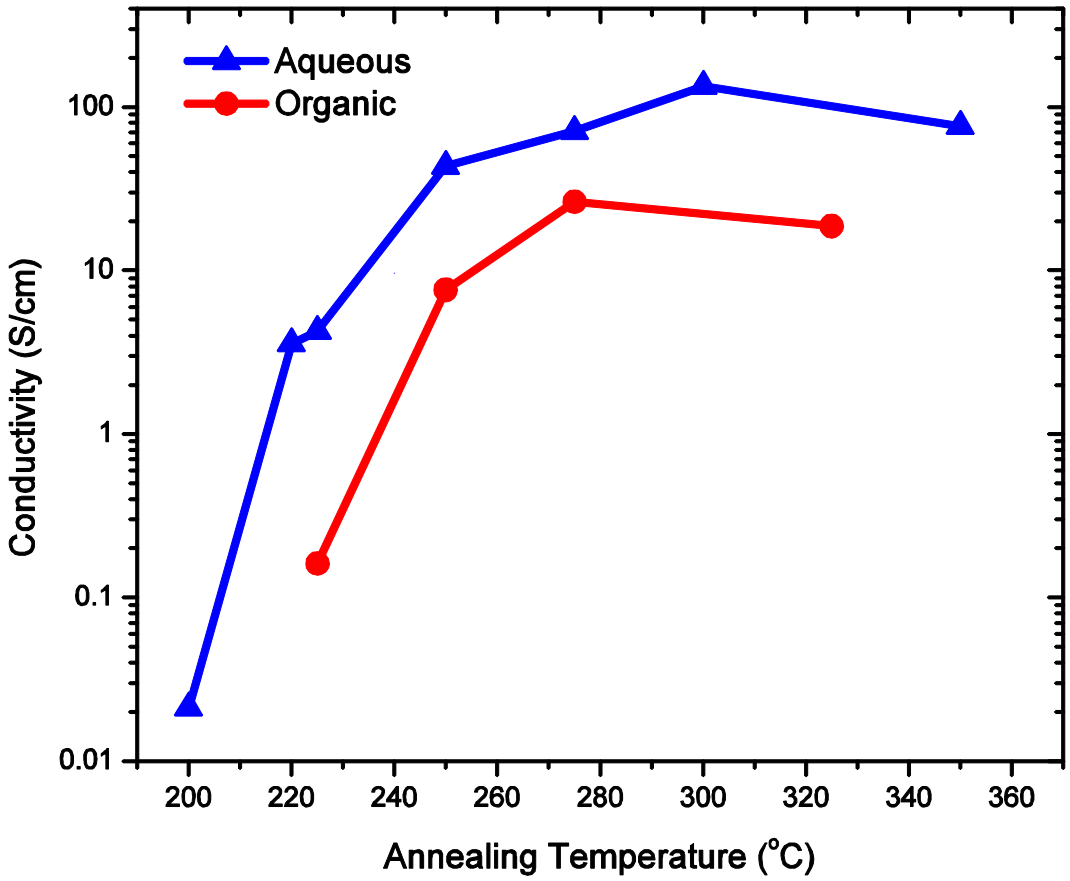


Figure 5.7 Conductivity of printed ACO conductors (3% Al doping) following low-temperature annealing at 200 – 350 °C.

The large volumetric reduction may be partially explained by thermal gravimetry (TGA) measurements of mass-loss that these inks undergo during heating. Thermogravimetric analyses of the precursor solutions were performed using a TGA analyzer (TA Instruments Q500). Samples (starting mass ~ 10 g) were loaded into aluminum crucibles and heated in dry air, with an initial 20 °C $min^{-1}$ ramp, followed by a 10 minute hold at 100 °C, followed by an additional 20 °C $min^{-1}$ ramp to 400 °C. TGA of the aqueous ACO ink shows initial mass-loss near 100 °C due to dehydration, followed by significant mass-loss (15%) in the range of 200 °C –250 °C, as illustrated in the differential mass-loss plotted in Figure 5.9. In comparison, the organic solvent-based ink consisting of 2-ME exhibits an abrupt mass-loss at 175 °C consistent with an auto-combustion reaction[18] before showing gradual additional mass-loss from 260 °C – 300 °C and a second decomposition peak around 350 °C – 400 °C. By comparison, the relatively complete decomposition of the aqueous ink at low temperatures may explain the enhanced conductivity achieved in the aqueous features compared to the organic solvent-based prints.

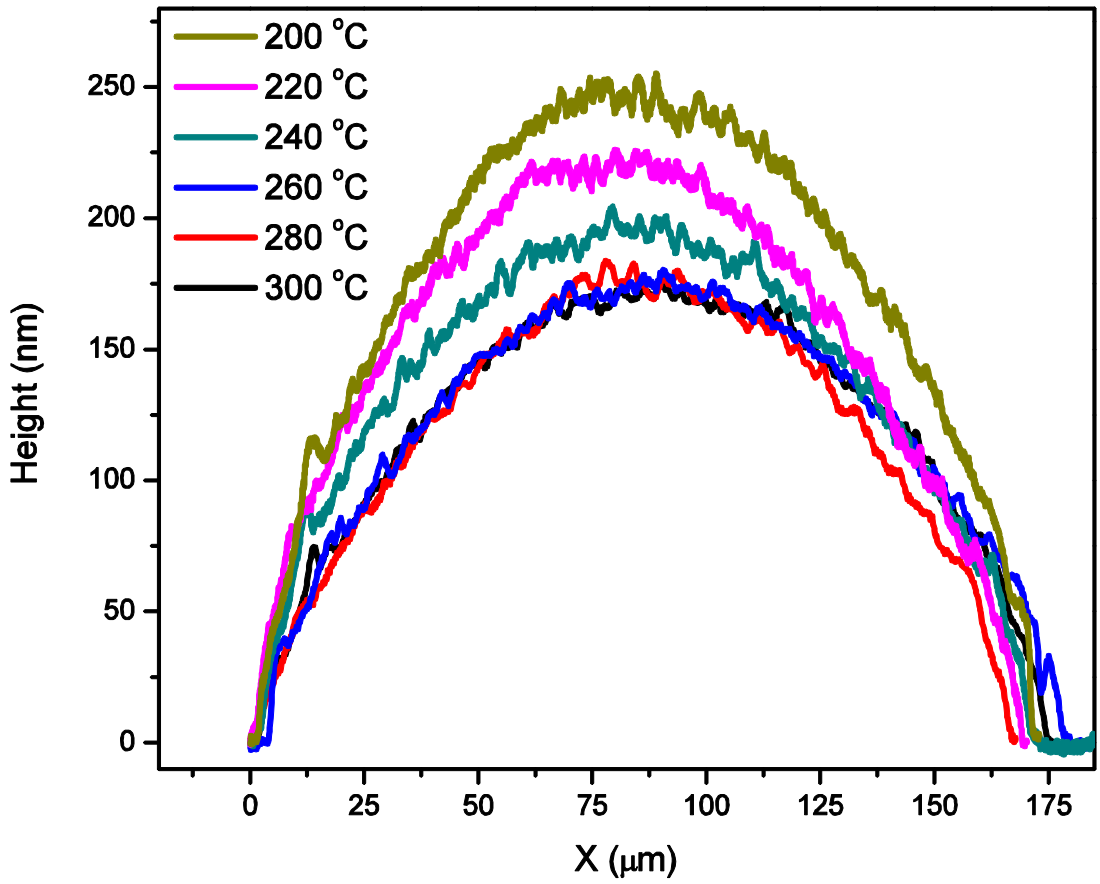


Figure 5.8 Line profiles of ACO printed lines following thermal annealing at various temperatures 200 °C – 300 °C for 10 minutes.

Another important factor determining TCO performance is the crystallinity of the film. In metal oxides, crystallization and grain growth are closely tied to decomposition and densification. Grazing incidence X-ray diffraction (GIXD) measurements were used to probe the crystallinity of spin coated CdO films annealed at temperatures from 200 °C – 300 °C. GIXD was performed on an X-Pert Analytical system with an angle of incidence of 0.43°. The GIXD spectra are shown in Figure 5.10. There is clear evidence that at annealing temperatures as low as 250 °C, the films have become nanocrystalline, showing the strong (111) and (200) peaks characteristic of CdO (reference peaks shown in black). At lower temperatures (200 °C – 225 °C), the spectra do not show strong (111) or (200) peaks of CdO, rather they show evidence for the existence of $Cd(NO_3)_2$ in the film (reference peaks shown in blue). In the sample annealed at 200 °C, multiple $Cd(NO_3)_2$ peaks are apparent, with the (200) $Cd(NO_3)_3$ peak appearing particularly strong. Indeed, by atomic force microscopy (Figure 5.11) it is possible to observe a coarser surface morphology consisting of micron scale aggregates in the 200 °C annealed sample, which is unique relative to the higher temperature cases. At 225 °C, the (111) $Cd(NO_3)_2$ peak can no longer be resolved, the (200) is significantly weaker, and the (220) appears to strengthen. Collectively, these observations are consistent with thermal gravimetry, suggesting that the primary mass-loss from 220 °C – 250 °C coincides with the decomposition of $Cd(NO_3)_2$ crystallites.

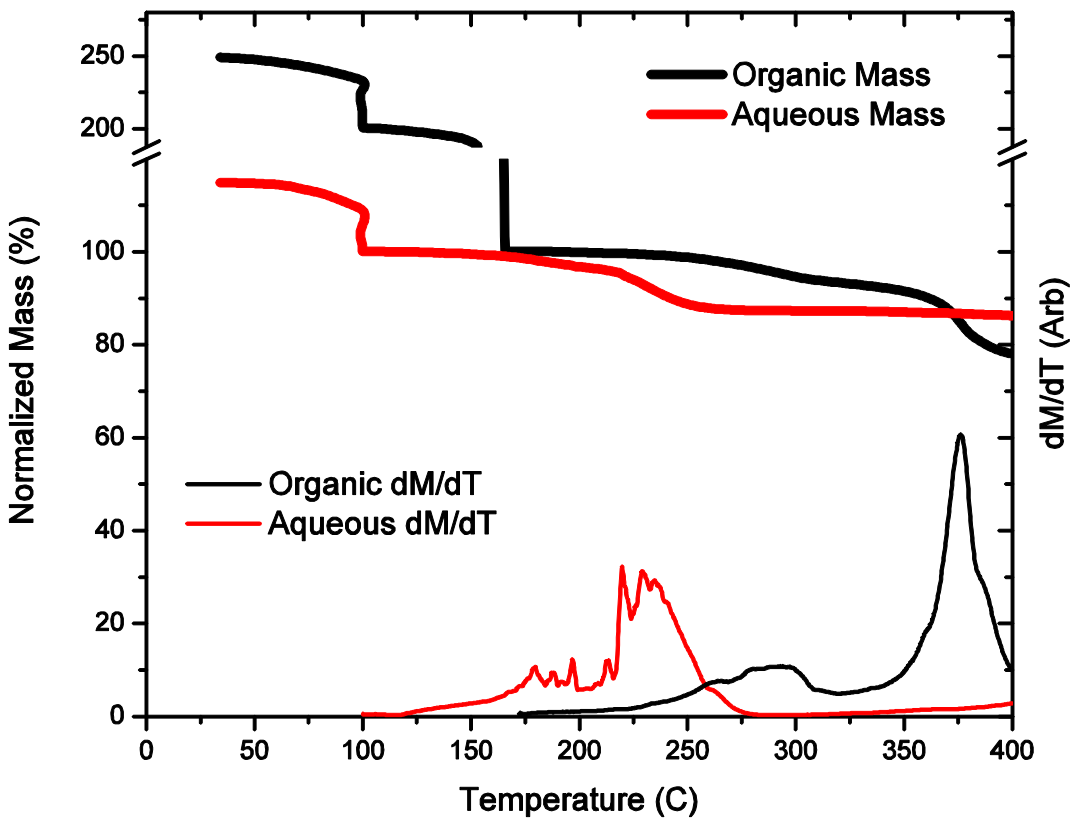


Figure 5.9 Thermal gravimetry measurements of precursor mass normalized to dry mass during heating to 400 °C. Organic and aqueous precursor masses are shown above, with the rate of change in mass shown below

A prominent feature of the low temperature samples is the presence of $Cd(OH)_2$ peaks. A peak at 29.5° appears at 225 °C, matching the primary (100) peak of the hexagonal phase of $Cd(OH)_2$[39], [40]. At elevated annealing temperatures of 275 °C and 300 °C, in fact, this same peak reappears and is complimented by the (102) peak of $Cd(OH)_2$ at ~ 49.5°. Interestingly, this trend of minimal OH peaks at 250 °C and increasing OH at 275 °C – 300 °C matches the trends observed in high quality aqueous $InO_x$ systems processed from nitrate precursors[41]. However, unlike these low temperature semiconductor systems, the ACO films' performance is not optimized at this intermediate condition with minimal hydroxide content. In fact, the electrical performance of the CdO films improves considerably at temperatures above 250 °C, suggesting that the conductivity is not dominated by the presence of hydroxide species as has been theorized for various low temperature oxide semiconductors[42]. A study of the surface of the printed ACO films by AFM (Figure 5.11) may provide an alternative explanation for the changes observed at higher temperatures (275 °C – 300 °C). From 250 °C to 300 °C, RMS surface roughness increases from 18 nm to 89 nm, as larger aggregates as well as microcracks and small voids appear in the films. These features could suggest that rapid mass-loss and decomposition during heating directly to 300 °C led to the development of a coarser microstructure with trapped hydroxide species that would have otherwise been expelled during slower decomposition at 250 °C.

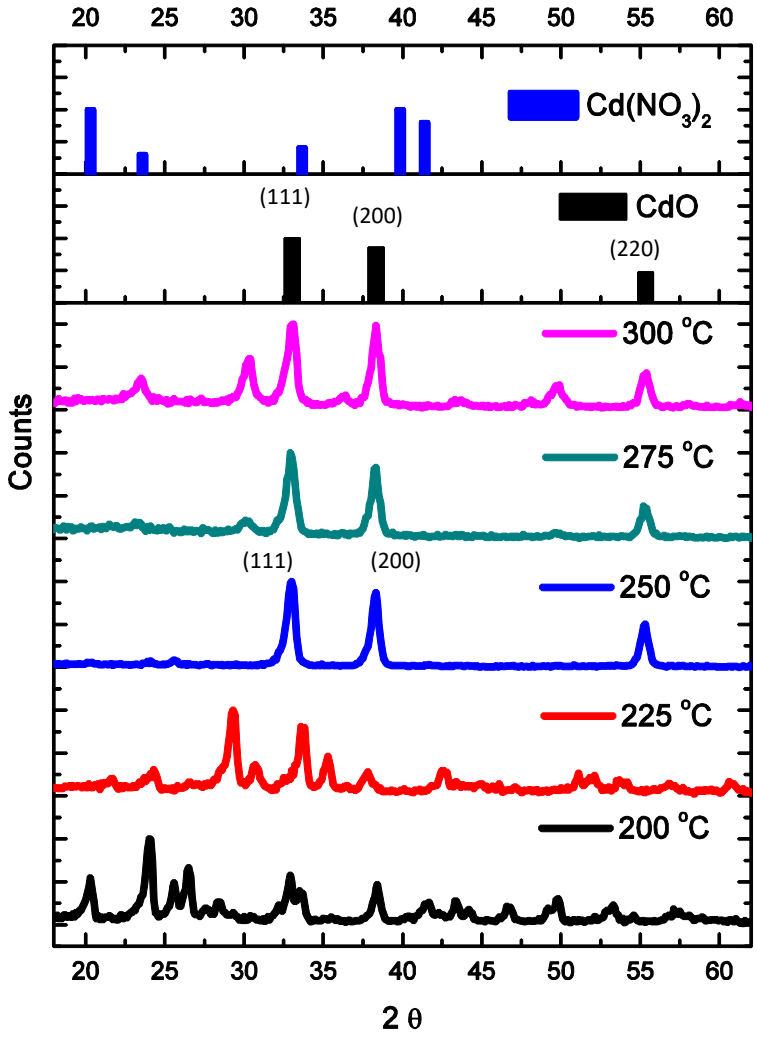


Figure 5.10 GIXD scans of CdO spin-coated films annealed at various temperatures from 200 °C – 300 °C. CdO and $Cd(NO_3)_2$ primary peaks are shown for reference (ICDD #04-016-6410 and #00-018-0265)

### 5.6 Impact of Aluminum Doping on Optical and Electrical Properties of ACO

Another important challenge in achieving high performing conductor systems at low processing temperatures is to effectively dope the material and reach a high carrier concentration. Undoped cadmium oxide has intrinsically high carrier concentrations (> $10^{20}$ $cm^{-3}$) which contribute to its exception conductivity, but its relatively low bandgap leads to considerable absorption in the visible range (400 nm – 800 nm). Doping with aliovalent cations such as In[20], Ga[22], Dy[43], and Al has been shown to enhance carrier concentrations and lead to noticeable Burstein-Moss shifts in the optical bandgap[24], which contribute to lower absorption and improved transparency.

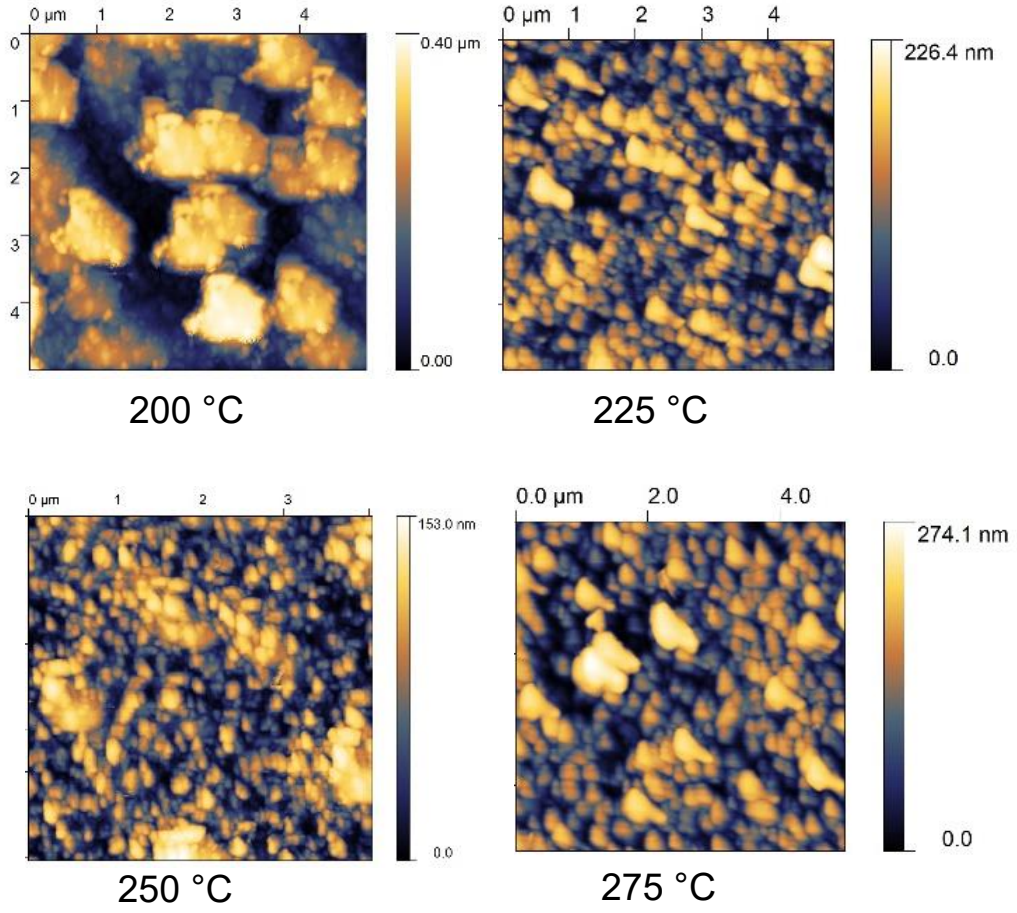


Figure 5.11 AFM scans of printed ACO electrode surfaces annealed at temperatures from 200 °C to 275 °C.

In this study, Al was chosen, since $Al(NO_3)_3$ exhibits extensive thermal decomposition below 200 °C, theoretically allowing for more effective conversion and dopant activation at low temperatures. Although $Al(NO_3)_3$ solutions had higher surface tension (65 – 70 mN/m) than $Cd(NO_3)_2$ and $In(NO_3)_3$ solutions, the concentration of Al (1 at. % - 8 at. %) did not significantly impact the surface tension or wetting of ACO inks, allowing accurate comparison between films fabricated with different doping levels.

Doping the cadmium oxide films with Al resulted in a shift in the optical absorption edge to lower wavelengths, consistent with a Burstein-Moss shift often observed in such degenerate TCO systems[24]. The Burstein-Moss effect occurs when films with films with exceptionally high carrier concentrations partially fill the conduction band, blocking the lowest energy states[44]. As a result of this effect, the transmittance of the Al doped films is considerably higher than that of undoped CdO, as illustrated in Figures 5.12a. Transmittance and absorption were measured with a Shimadzu UV-2600 spectrometer. By fitting the absorption spectra of the ACO films, the optical bandgap (Figure 5.12b) was extracted using an extrapolation of the linear fit of $(\alpha\ h\ \nu)^2$ at the absorption edge, showing a $\Delta E_G$ of up to 150 mV at 4 at. % Al doping. The important result of this shift is that the overall transmittance (averaged from 400nm – 1000nm) was improved from 71%

to 86%, reaching a level which is more suitable for transparent thin film electrodes in display applications or photovoltaics.

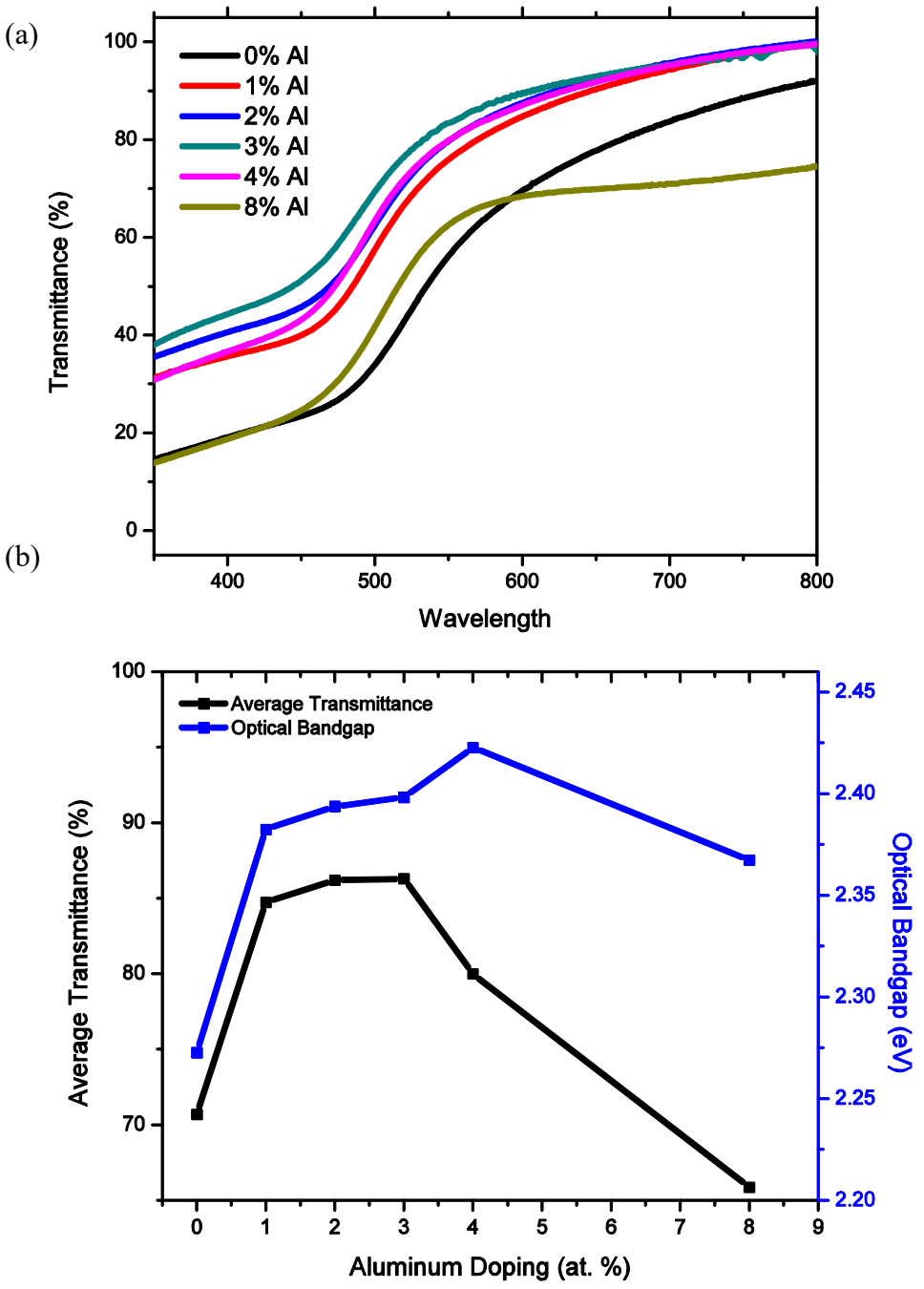


Figure 5.12 Transmittance spectra (a) and optical bandgap / average transmittance (b) of ACO films with varying Al doping (at. %) concentration in the precursor ink.

Doping CdO with Al critically influences the crystallinity of the film and the electrical performance. GIXD scans of ACO films with varying Al % indicate key differences in the structure

of films with heavier doping. For example, a significant amorphous halo emerges in the spectra for the 2%, 4%, and 8% Al doped films (Figure 5.13). This change is also reflected in the progressive broadening of the (111) and (200) CdO peaks. Scherrer-Debye estimated crystallite sizes decrease from approximately 20 nm for the intrinsic CdO and 1% Al doped case, to less than 13nm for the 4% Al doped case (Figure 5.14b). By 8% doping, the film appears entirely amorphous and peaks may not be resolved. The onset of the amorphous phase coincides with an abrupt decrease in conductivity for the 4% and 8% Al doped cases, compared to the optimal doping of approximately 2-3% Al (Figure 5.14a). It is interesting to note here that the amorphous 8% Al doped films remain functional TCOs, presenting an interesting amorphous conductor for fabricating printed oxide electronics on highly flexible substrates.

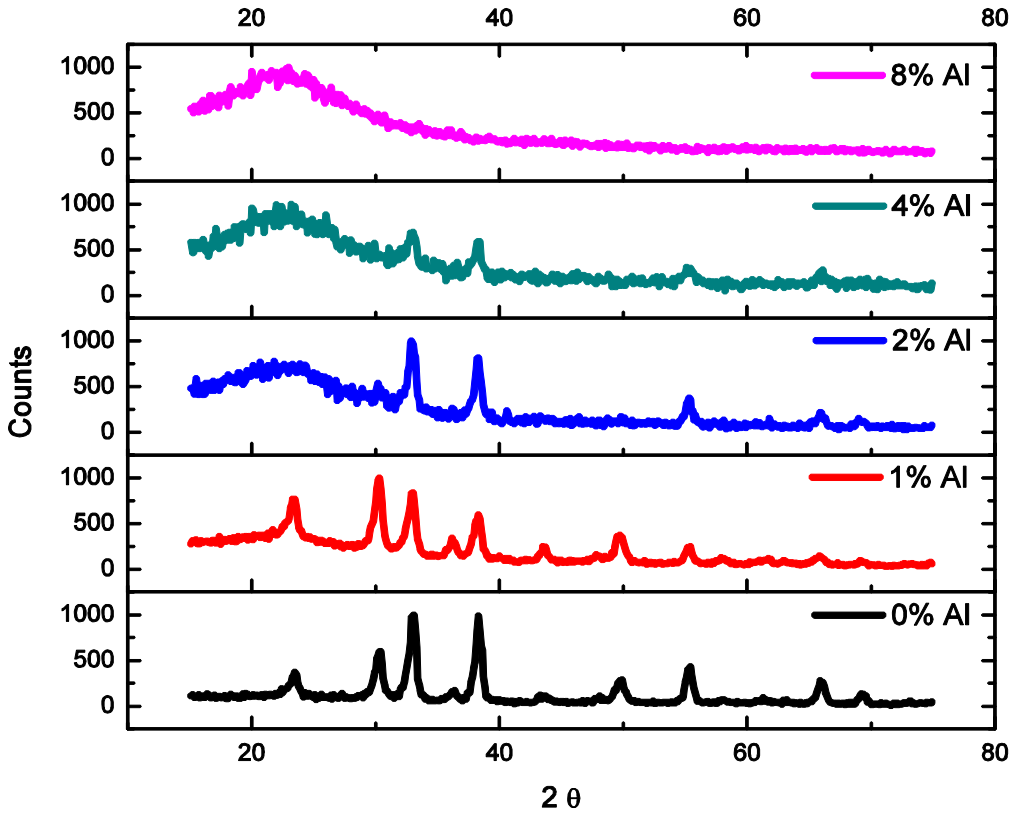


Figure 5.13 Grazing incidence x-ray diffraction spectra of ACO films with varying aluminum precursor doping.

(a)

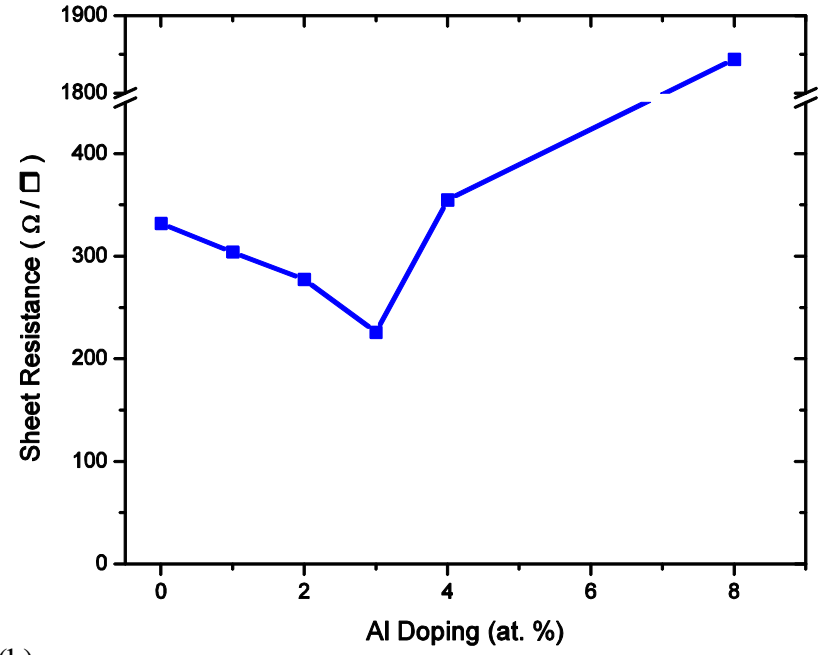


(b)

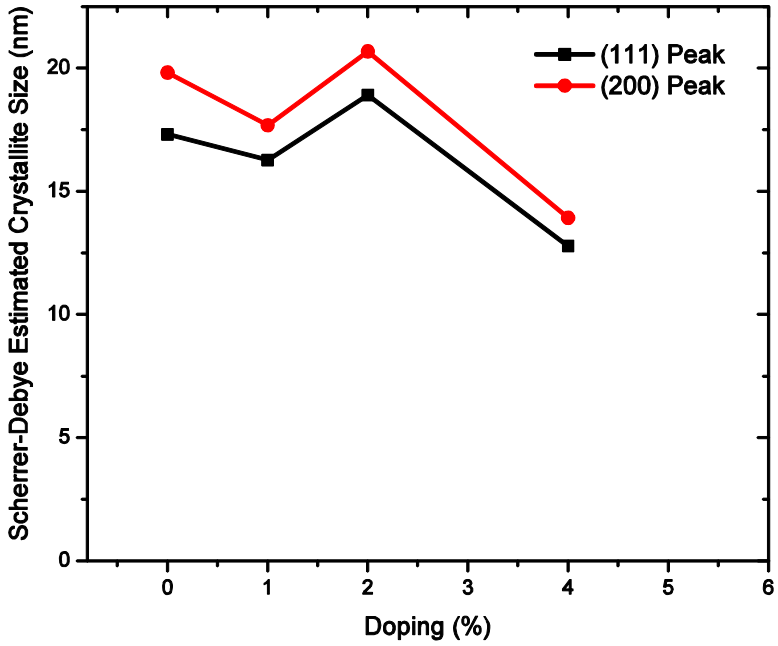


Figure 5.14 Sheet resistance of ACO films with varying Al precursor doping concentration (at. %) (a). Scherrer-Debye estimated crystallite size of ACO films with varying Al doping (at. %) (b).

## 5.7 Low-Temperature Aqueous Indium Oxide TFTs

To investigate the suitability of printed ACO electrodes as a contact for high-performance oxide electronics, fully aqueous processed transistors were fabricated at temperatures ≤ 250 °C, utilizing inkjet printed $InO_x$ semiconductor layers and 3% Al-doped ACO source-drains on spincoated $AlO_x$ dielectrics. Inkjet-printed top contact thin film $InO_x$ transistors were fabricated on Si substrates by spin coating a 200 mM aqueous solution of $Al(NO_3)_3$, drying for 5 min (100 °C), and annealing the dried films for 5 min (250 °C). The spin coating, drying, and annealing processes were completed sequentially for three layers of $AlO_x$, and the film then received a 1 hour anneal in air on a hot plate (250 °C). The substrate was then treated for 2 min with UV Ozone (30 mW $cm^{-2}$) and the $InO_x$ semiconductor was inkjet printed from a 100 mM aqueous solution of $In(NO_3)_3$ with a 40 μm drop spacing and a platen temperature of 30 °C. The $InO_x$ ink was printed with similar cartridge settings and the same waveform as the ACO inks. The $InO_x$ films were dried for 5 min (100 °C) and then annealed on a hot plate for 2 hours in air (250 °C). Finally, two layer ACO (3% Al) source / drain electrodes were inkjet printed using 35 μm drop spacing to form TFTs with an aspect ratio of W/L = 4-6, dried for 5 min (175 °C), and annealed for 160 minutes (250 °C). Inkjet-printed $InO_x$ transistors were also fabricated by similar methods on thermally grown $SiO_2$ (100nm thick) for use in contact resistance extraction ($L_c$ = 50 μm – 150 μm, $W_c$ = 450 μm) during post annealing studies. Before printing $InO_x$, $SiO_2$ surfaces were treated with 20 min of UV-Ozone (30 mW $cm^{-2}$).

As shown in the transfer characteristics displayed in Figure 5.15, the aqueous processed $InO_x$ TFTs exhibit strong performance (SS < 150 mV $dec^{-1}$ and $I_{on} / I_{off} \sim 10^7$) and have low hysteresis ($\Delta V_{th}$ < 100 mV). The devices also show excellent current saturation in their output characteristics (Figure 5.16a), with no evidence of a contact barrier between the ACO source / drains and the $InO_x$ semiconductor. As shown in Figure 5.16c, the devices typically have an average $V_{on}$ which is close to 0 V (-500 ± 250 mV) allowing for desirable enhancement mode operation at low voltages (± 6 V) afforded by the high-quality aqueous-based $AlO_x$ dielectric (Figure 5.16d). The distribution of linear and saturation mobility for these devices is included in Figure 5.16b, with a $\mu_{lin}$ of 11 ± 4 $cm^2V^{-1}s^{-1}$ and a $\mu_{sat}$ of 10 ± 4 $cm^2$ $V^{-1}s^{-1}$. The performance of these devices, with a $\mu_{lin}$ of up to 19 $cm^2$ $V^{-1}s^{-1}$, is competitive with $InO_x$ TFTs prepared at a similar thermal budget using photolithography and utilizing evaporated electrodes[3], but in this case no vacuum based equipment was necessary and additive patterning was achieved exclusively using low-cost inkjet printing methods. In particular, the performance of these aqueous processed devices is distinguished from other demonstrations of printed oxide transistors with printed electrodes [14], [45, p.] by an outstanding $I_{on}/I_{off}$ ratio, a minimal hysteresis window, and a limited overall thermal budget of only 250 °C, approaching the temperatures at which low cost transparent substrates such as PEN are viable. With advanced annealing methods, such as pulsed white light annealing, it may be possible to extend these high performing ink formulations to printing fully transparent transistors on flexible plastic substrates.

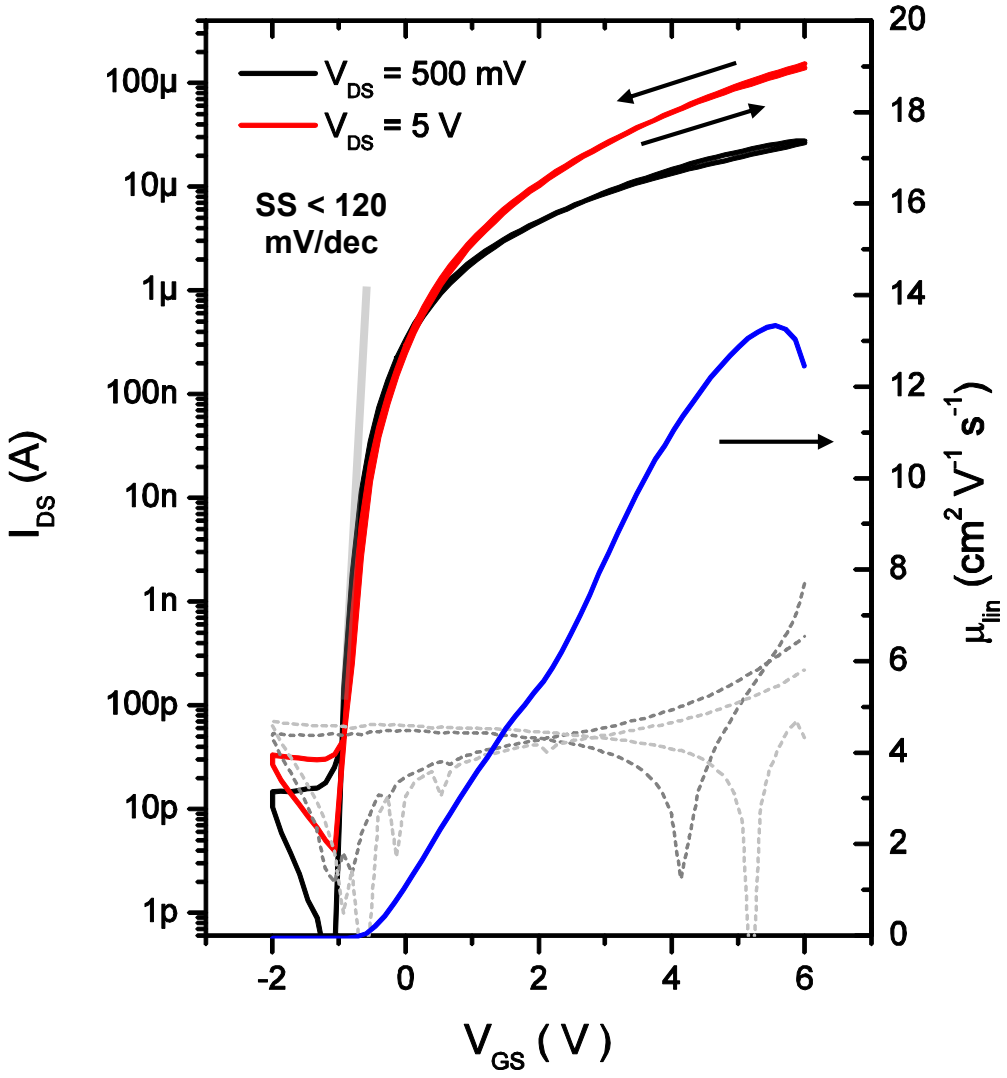


Figure 5.15 Transfer characteristics with linear mobility of aqueous $InO_x$ printed transistor with printed ACO contacts processed at ≤ 250 °C.

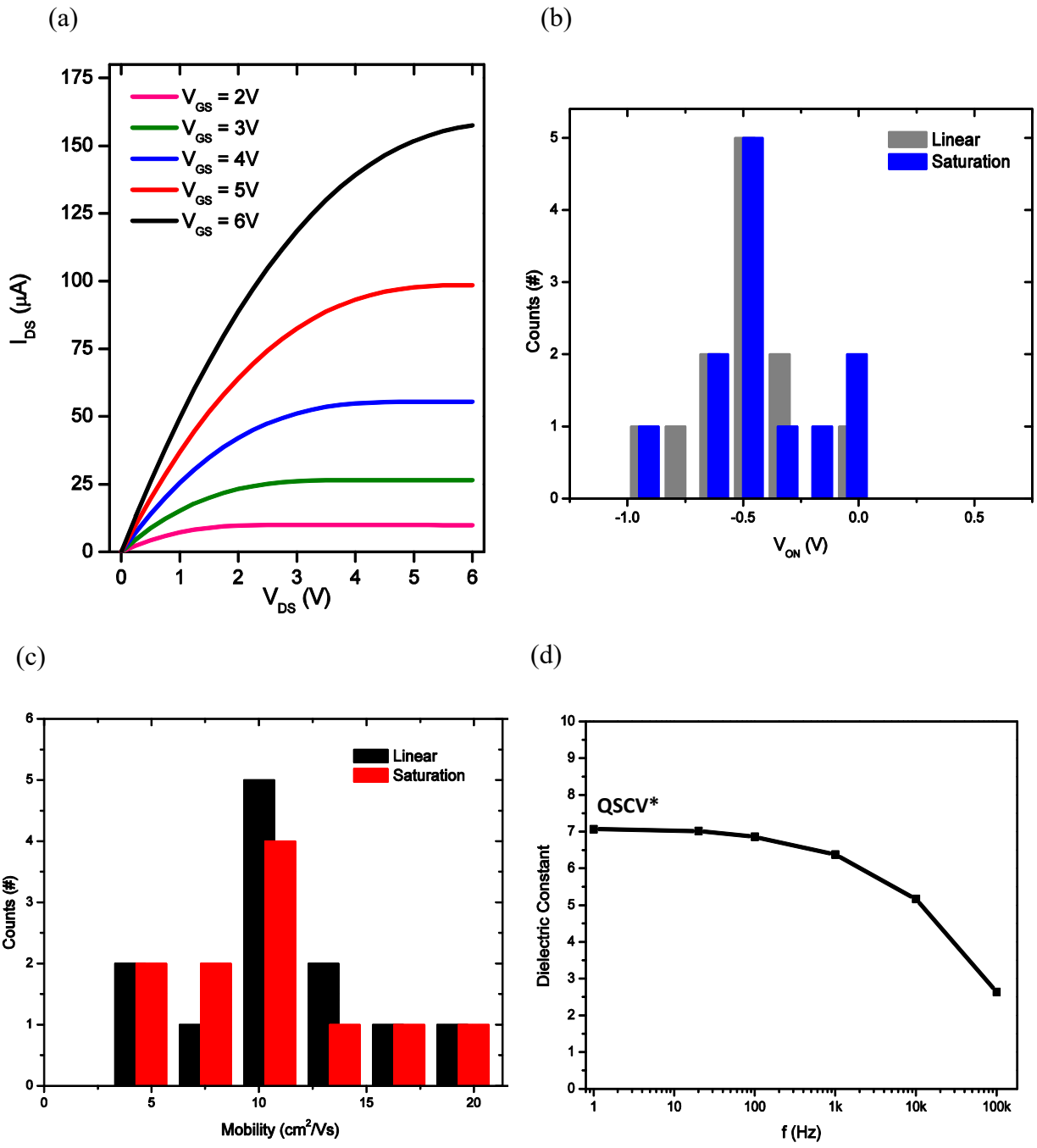


Figure 5.16 Output characteristics of aqueous $InO_x$ printed transistor with printed ACO contacts processed at ≤ 250 °C. Distribution of $V_{on}$ in linear and saturation operation (b). Distribution of linear and saturation mobility of printed InOx TFTs (c). Dielectric response of of $AlO_x$ aqueous dielectrics with printed ACO contacts and Si substrate back gate.

### 5.8 Contact Resistance of Printed ACO Electrodes in $InO_x$ TFTs

To benchmark the contact properties of this printed electrode system for oxide TFTs, the Transfer Length Method (TLM) was used to evaluate the contact resistance of the $InO_x$ / ACO devices for various durations of contact annealing at 250 °C. Devices with channel lengths ranging from approximately 50 µm – 220 µm were printed and the total source-drain resistance was extracted during operation at a low $V_{DS}$. The results of a linear fit of the total source-drain resistance are shown in Figure 5.19. Extended annealing of the ACO in air produced a low resistance contact to the $InO_x$ semiconductor ($R_c$ ~160 Ω-cm), comparable to vacuum deposited metal contacts such as Al[46], Ti[47], or Mo[48] and considerably lower than nanocarbon-based electrodes such as graphene[14]. This contact resistance showed a gate-voltage dependence similar to that of top contacted (Figure 5.17) systems such as post-annealed Al[46] or Ti[47] on IGZO. To understand the origin of this contact resistance, TLM extractions were performed for identical contact structures with varying $InO_x$ thickness from 15 nm to 75 nm. Thicker $InO_x$ films showed similar gate voltage dependence, but considerably higher $R_c$ ( > 1 kΩ-cm) relative to thin films. The strong increase in contact resistance with semiconductor thickness (Figure 5.18) indicates that this $R_c$ may be dominated by the bulk resistance of the $InO_x$ thin film. Interestingly, shorter contact anneals produced ohmic behavior with little gate voltage dependence in the extracted contact resistance. Contact anneals as short as 10 min resulted in a TLM intersection point at a positive channel length ($\Delta L_c$) of over 30 µm (Figure 5.19a), indicating an effectively shorter channel length. With additional annealing, $\Delta L_c$ was reduced to approximately 5 µm in the case of samples with a 40 minute contact anneal, and was eliminated entirely by the extended 160 min ACO contact anneal (Figure 5.19b).

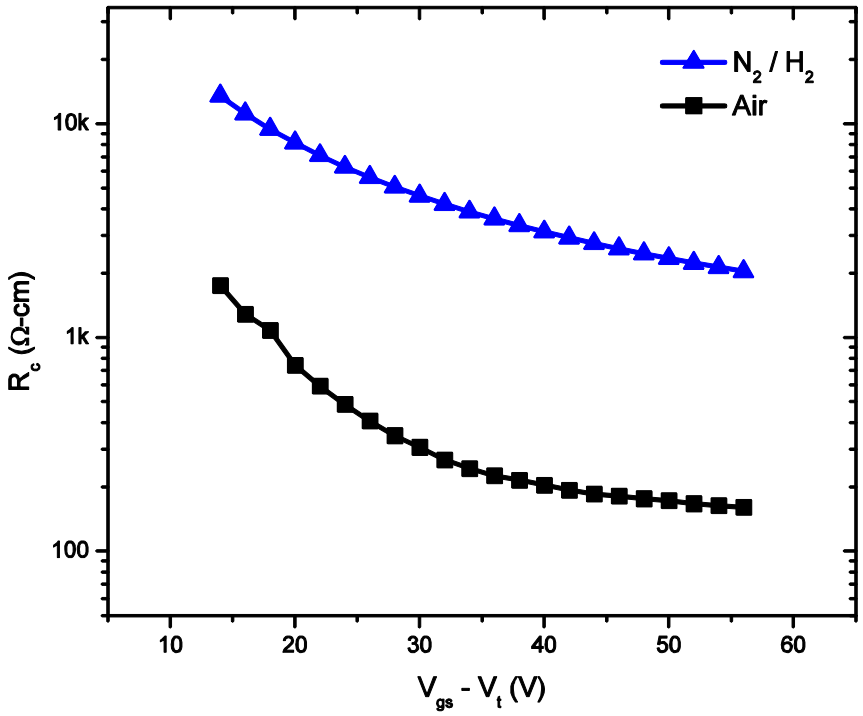


Figure 5.17 Contact resistance of ACO electrodes extracted by TLM analysis of $InO_x$ printed transistors as a function of gate bias and contact annealing conditions (oxidative vs reducing).

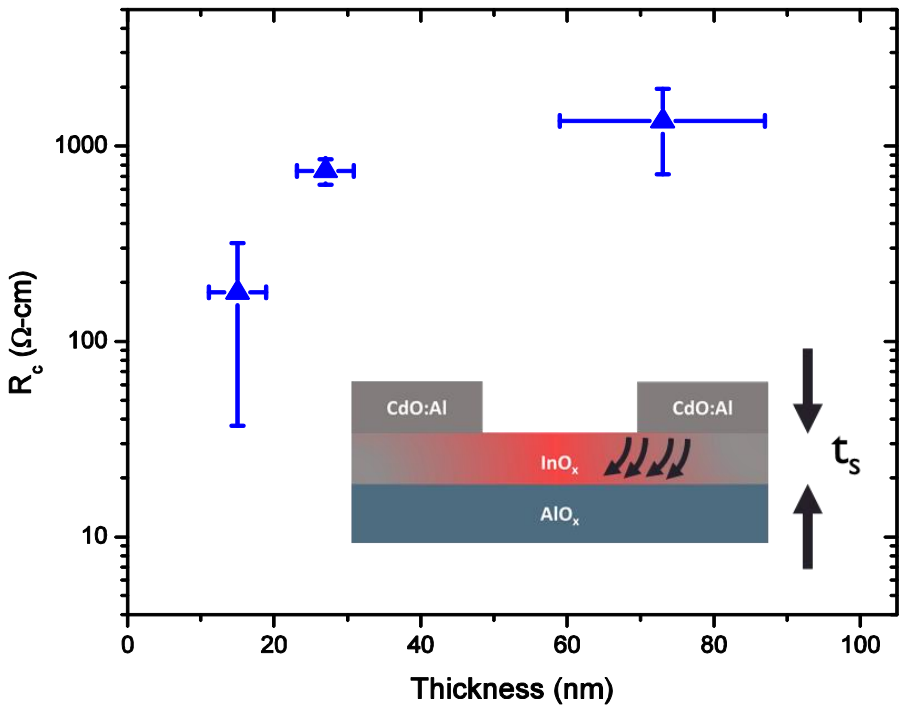


Figure 5.18 Contact resistance of ACO electrodes in top-contact configuration extracted by TLM analysis of $InO_x$ printed transistors as a function of $InO_x$ thickness at maximum $V_{gs}$.

(a) (b)

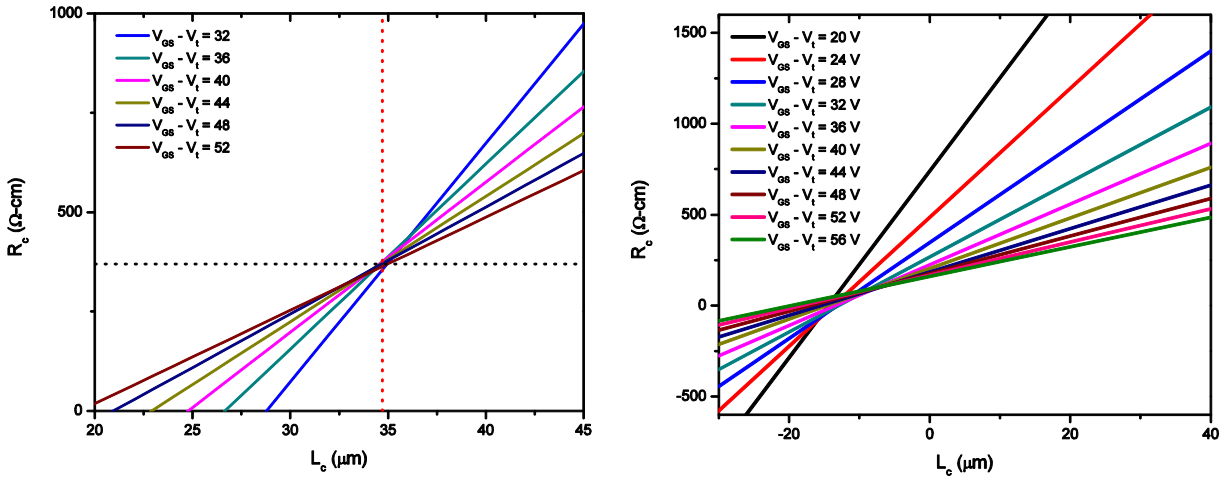


Figure 5.19 Transfer length method (TLM) contact resistance extractions (a,b) for post annealed ACO contacts (250 °C) of different durations (10 min, 160 min).

These observations may indicate that the printed ACO top contact formation process initially induced a high density of defects in the $InO_x$ films in the vicinity of the contacts, in a similar fashion to how sputtered metal contacts can create conductive oxygen deficient contact regions in IGZO TFTs[48] or metal rich contact regions in $InO_x$ thin films[49]. However, in the case of ACO contacted devices, the defective region can then be healed by extended annealing in air or forming gas (95% $N_2$ / 5% $H_2$), eliminating the positive $\Delta L_c$. As can be seen from Figure 5.17, there was a considerably lower contact resistance observed when using long oxidative post annealing in air relative to a long reducing post annealing in $N_2$ / $H_2$ gas. The long air anneals also resulted in overall improvements to device performance. These changes in contact behavior with extended annealing were reflected in considerable increases in the contact resistance corrected mobility of these devices, which improved from an average of 4.4 $cm^2$ $V^{-1}s^{-1}$ following a 10 min anneal to 10.7 $cm^2$ $V^{-1}s^{-1}$ after a longer 160 min anneal in air (Figure 5.20).

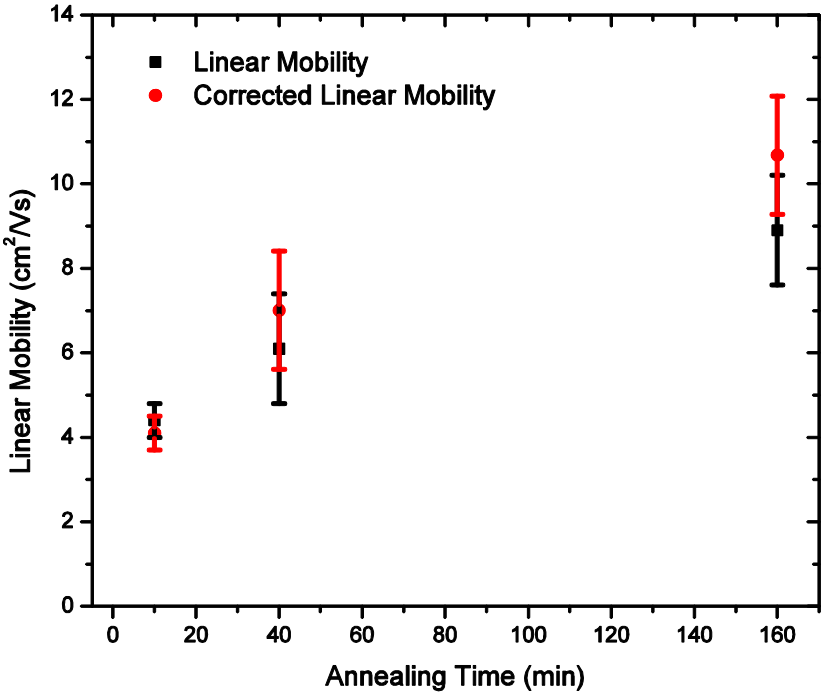


Figure 5.20 Contact resistance of ACO electrodes in top-contact configuration extracted by transfer length method (TLM) analysis of $InO_x$ printed transistors on $SiO_2$ dielectrics as a function of $InO_x$ thickness at maximum $V_{gs}$.

### 5.9 Summary

In summary, this chapter presents a strategy to address the high-temperature annealing requirements of conventional sol-gel metal oxides. Aqueous processing of transparent metal oxide transistors offers significant advantages both in terms of printing fidelity and material performance, relative to inks based on organic solvents. Aqueous ACO inks based on metal nitrate precursors were used to print single layer and multilayer fine source / drain lines with widths as

low as 25 – 50 μm and minimal line-edge roughness. The conductivity of these films (up to 130 S $cm^{-1}$) was evaluated as a function of the annealing temperature, showing an onset of conductivity at 220 °C. Thermal gravimetry and GIXD were performed to understand the onset of conductivity and crystallinity, respectively, at low temperatures. The role of Al doping in this material system was also examined, showing that moderate Al doping can improve visible range transmittance while enhancing conductivity. These low-temperature-processed electrodes were used to fabricate high-performance printed $InO_x$ TFTs at temperatures below 250 °C with subthreshold swing < 150 mV $dec^{-1}$and $\mu_{lin}$ up to 19 $cm^2$ $V^{-1}s^{-1}$. Further studies by the transfer length method (TLM) showed thermally stable contact properties and a low contact resistance of 160 Ω-cm, comparable to vacuum deposited Al metal contacts. These results illustrate the extensibility of printable aqueous ink formulations to a variety of metal oxide material systems and show a method for mitigating the tradeoff between the printability and performance of sol-gel processed electronic materials.

## 5.10 References


[1] X. Yu et al., "Spray-combustion synthesis: Efficient solution route to high-performance oxide transistors," *Proc. Natl. Acad. Sci.*, vol. 112, no. 11, pp. 3217–3222, Mar. 2015.

[2] Y.-H. Kim et al., "Flexible metal-oxide devices made by room-temperature photochemical activation of sol-gel films," *Nature*, vol. 489, no. 7414, pp. 128–132, Sep. 2012.

[3] Y. Hwan Hwang et al., "An 'aqueous route' for the fabrication of low-temperature-processable oxide flexible transparent thin-film transistors on plastic substrates," *NPG Asia Mater.*, vol. 5, no. 4, p. e45, Apr. 2013.

[4] Y. S. Rim, H. Chen, T.-B. Song, S.-H. Bae, and Y. Yang, "Hexaaqua Metal Complexes for Low-Temperature Formation of Fully Metal Oxide Thin-Film Transistors," *Chem. Mater.*, vol. 27, no. 16, pp. 5808–5812, Aug. 2015.

[5] Y.-H. Lin et al., "High-Performance ZnO Transistors Processed Via an Aqueous Carbon-Free Metal Oxide Precursor Route at Temperatures Between 80–180 °C," *Adv. Mater.*, vol. 25, no. 31, pp. 4340–4346, Aug. 2013.

[6] G. Liu et al., "Low-Temperature, Nontoxic Water-Induced Metal-Oxide Thin Films and Their Application in Thin-Film Transistors," *Adv. Funct. Mater.*, vol. 25, no. 17, pp. 2564–2572, May 2015.

[7] H. Chen, Y. S. Rim, C. Jiang, and Y. Yang, "Low-Impurity High-Performance Solution-Processed Metal Oxide Semiconductors via a Facile Redox Reaction," *Chem. Mater.*, vol. 27, no. 13, pp. 4713–4718, Jul. 2015.

[8] W. Xu, H. Cao, L. Liang, and J.-B. Xu, "Aqueous Solution-Deposited Gallium Oxide Dielectric for Low-Temperature, Low-Operating-Voltage Indium Oxide Thin-Film Transistors: A Facile Route to Green Oxide Electronics," *ACS Appl. Mater. Interfaces*, vol. 7, no. 27, pp. 14720–14725, Jul. 2015.

[9] W. Xu, H. Wang, F. Xie, J. Chen, H. Cao, and J.-B. Xu, "Facile and Environmentally Friendly Solution-Processed Aluminum Oxide Dielectric for Low-Temperature, High-Performance Oxide Thin-Film Transistors," *ACS Appl. Mater. Interfaces*, vol. 7, no. 10, pp. 5803–5810, Mar. 2015.

[10] P. N. Plassmeyer, K. Archila, J. F. Wager, and C. J. Page, "Lanthanum Aluminum Oxide Thin-Film Dielectrics from Aqueous Solution," *ACS Appl. Mater. Interfaces*, vol. 7, no. 3, pp. 1678–1684, Jan. 2015.

[11] A. Liu et al., “Water-Induced Scandium Oxide Dielectric for Low-Operating Voltage n- and p-Type Metal-Oxide Thin-Film Transistors,” *Adv. Funct. Mater.*, vol. 25, no. 46, pp. 7180–7188, Dec. 2015.
[12] A. Liu et al., “Solution-Processed Alkaline Lithium Oxide Dielectrics for Applications in n- and p-Type Thin-Film Transistors,” *Adv. Electron. Mater.*, vol. 2, no. 9, p. n/a-n/a, Sep. 2016.
[13] S. K. Garlapati et al., “Ink-Jet Printed CMOS Electronics from Oxide Semiconductors,” *Small*, vol. 11, no. 29, pp. 3591–3596, Aug. 2015.
[14] E. B. Secor, J. Smith, T. J. Marks, and M. C. Hersam, “High-Performance Inkjet-Printed Indium-Gallium-Zinc-Oxide Transistors Enabled by Embedded, Chemically Stable Graphene Electrodes,” *ACS Appl. Mater. Interfaces*, vol. 8, no. 27, pp. 17428–17434, Jul. 2016.
[15] S.-H. K. Park et al., “42.3: Transparent ZnO Thin Film Transistor for the Application of High Aperture Ratio Bottom Emission AM-OLED Display,” *SID Symp. Dig. Tech. Pap.*, vol. 39, no. 1, pp. 629–632, May 2008.
[16] K. K. Banger et al., “Low-temperature, high-performance solution-processed metal oxide thin-film transistors formed by a ‘sol–gel on chip’ process,” *Nat. Mater.*, vol. 10, no. 1, pp. 45–50, Jan. 2011.
[17] Z. Chen, W. Li, R. Li, Y. Zhang, G. Xu, and H. Cheng, “Fabrication of Highly Transparent and Conductive Indium–Tin Oxide Thin Films with a High Figure of Merit via Solution Processing,” *Langmuir*, vol. 29, no. 45, pp. 13836–13842, Nov. 2013.
[18] M.-G. Kim, J. W. Hennek, H. S. Kim, M. G. Kanatzidis, A. Facchetti, and T. J. Marks, “Delayed Ignition of Autocatalytic Combustion Precursors: Low-Temperature Nanomaterial Binder Approach to Electronically Functional Oxide Films,” *J. Am. Chem. Soc.*, vol. 134, no. 28, pp. 11583–11593, Jul. 2012.
[19] W. D. Cyrs, H. J. Avens, Z. A. Capshaw, R. A. Kingsbury, J. Sahmel, and B. E. Tvermoes, “Landfill waste and recycling: Use of a screening-level risk assessment tool for end-of-life cadmium telluride (CdTe) thin-film photovoltaic (PV) panels,” *Energy Policy*, vol. 68, pp. 524–533, May 2014.
[20] Y. Yang et al., “CdO as the Archetypical Transparent Conducting Oxide. Systematics of Dopant Ionic Radius and Electronic Structure Effects on Charge Transport and Band Structure,” *J. Am. Chem. Soc.*, vol. 127, no. 24, pp. 8796–8804, Jun. 2005.
[21] A. Wang et al., “Indium-cadmium-oxide films having exceptional electrical conductivity and optical transparency: Clues for optimizing transparent conductors,” *Proc. Natl. Acad. Sci.*, vol. 98, no. 13, pp. 7113–7116, Jun. 2001.
[22] S. Jin et al., “Tuning the Properties of Transparent Oxide Conductors. Dopant Ion Size and Electronic Structure Effects on CdO-Based Transparent Conducting Oxides. Ga- and In-Doped CdO Thin Films Grown by MOCVD,” *Chem. Mater.*, vol. 20, no. 1, pp. 220–230, Jan. 2008.
[23] A. W. Metz et al., “Transparent Conducting Oxides: Texture and Microstructure Effects on Charge Carrier Mobility in MOCVD-Derived CdO Thin Films Grown with A Thermally Stable, Low-Melting Precursor,” *J. Am. Chem. Soc.*, vol. 126, no. 27, pp. 8477–8492, Jul. 2004.
[24] K. M. Yu et al., “Defects and properties of cadmium oxide based transparent conductors,” *J. Appl. Phys.*, vol. 119, no. 18, p. 181501, May 2016.
[25] E. B. Secor, B. Y. Ahn, T. Z. Gao, J. A. Lewis, and M. C. Hersam, “Rapid and Versatile Photonic Annealing of Graphene Inks for Flexible Printed Electronics,” *Adv. Mater.*, vol. 27, no. 42, pp. 6683–6688, Nov. 2015.

[26] W. J. Hyun, E. B. Secor, M. C. Hersam, C. D. Frisbie, and L. F. Francis, “High-Resolution Patterning of Graphene by Screen Printing with a Silicon Stencil for Highly Flexible Printed Electronics,” *Adv. Mater.*, vol. 27, no. 1, pp. 109–115, Jan. 2015.
[27] R. J. P. Corriu and D. Leclercq, “Recent Developments of Molecular Chemistry for Sol–Gel Processes,” *Angew. Chem. Int. Ed. Engl.*, vol. 35, no. 13–14, pp. 1420–1436, Jul. 1996.
[28] H. C. Nallan, J. A. Sadie, R. Kitsomboonloha, S. K. Volkman, and V. Subramanian, “Systematic Design of Jettable Nanoparticle-Based Inkjet Inks: Rheology, Acoustics, and Jettability,” *Langmuir*, vol. 30, no. 44, pp. 13470–13477, Nov. 2014.
[29] J. Feys et al., “Ink-jet printing of YBa 2 Cu 3 O 7 superconducting coatings and patterns from aqueous solutions,” *J. Mater. Chem.*, vol. 22, no. 9, pp. 3717–3726, 2012.
[30] J. Park and J. Moon, “Control of Colloidal Particle Deposit Patterns within Picoliter Droplets Ejected by Ink-Jet Printing,” *Langmuir*, vol. 22, no. 8, pp. 3506–3513, Apr. 2006.
[31] N. D. Patil, P. G. Bange, R. Bhardwaj, and A. Sharma, “Effects of Substrate Heating and Wettability on Evaporation Dynamics and Deposition Patterns for a Sessile Water Droplet Containing Colloidal Particles,” *Langmuir*, vol. 32, no. 45, pp. 11958–11972, Nov. 2016.
[32] S. Jeong et al., “Stable Aqueous Based Cu Nanoparticle Ink for Printing Well-Defined Highly Conductive Features on a Plastic Substrate,” *Langmuir*, vol. 27, no. 6, pp. 3144–3149, Mar. 2011.
[33] B. Derby, “Additive Manufacture of Ceramics Components by Inkjet Printing,” *Engineering*, vol. 1, no. 1, pp. 113–123, Mar. 2015.
[34] D. Soltman and V. Subramanian, “Inkjet-Printed Line Morphologies and Temperature Control of the Coffee Ring Effect,” *Langmuir*, vol. 24, no. 5, pp. 2224–2231, Mar. 2008.
[35] T. Still, P. J. Yunker, and A. G. Yodh, “Surfactant-Induced Marangoni Eddies Alter the Coffee-Rings of Evaporating Colloidal Drops,” *Langmuir*, vol. 28, no. 11, pp. 4984–4988, Mar. 2012.
[36] W. J. Scheideler, J. Jang, M. A. U. Karim, R. Kitsomboonloha, A. Zeumault, and V. Subramanian, “Gravure-Printed Sol–Gels on Flexible Glass: A Scalable Route to Additively Patterned Transparent Conductors,” *ACS Appl. Mater. Interfaces*, vol. 7, no. 23, pp. 12679–12687, Jun. 2015.
[37] “Electronic Structure of Low-Temperature Solution-Processed Amorphous Metal Oxide Semiconductors for Thin-Film Transistor Applications - Socratous - 2015 - Advanced Functional Materials - Wiley Online Library.” [Online]. Available: http://onlinelibrary.wiley.com/doi/10.1002/adfm.201404375/full. [Accessed: 21-Mar-2016].
[38] J. H. Park et al., “Low-Temperature, High-Performance Solution-Processed Thin-Film Transistors with Peroxo-Zirconium Oxide Dielectric,” *ACS Appl. Mater. Interfaces*, vol. 5, no. 2, pp. 410–417, Jan. 2013.
[39] A. C. Nwanya, C. Chigbo, S. C. Ezugwu, R. U. Osuji, M. Malik, and F. I. Ezema, “Transformation of cadmium hydroxide to cadmium oxide thin films synthesized by SILAR deposition process: Role of varying deposition cycles,” *J. Assoc. Arab Univ. Basic Appl. Sci.*
[40] T. P. Gujar, V. R. Shinde, W.-Y. Kim, K.-D. Jung, C. D. Lokhande, and O.-S. Joo, “Formation of CdO films from chemically deposited Cd(OH)2 films as a precursor,” *Appl. Surf. Sci.*, vol. 254, no. 13, pp. 3813–3818, Apr. 2008.
[41] H. Faber et al., “Indium Oxide Thin-Film Transistors Processed at Low Temperature via Ultrasonic Spray Pyrolysis,” *ACS Appl. Mater. Interfaces*, vol. 7, no. 1, pp. 782–790, Jan. 2015.

[42] J. Socratous et al., “Electronic Structure of Low-Temperature Solution-Processed Amorphous Metal Oxide Semiconductors for Thin-Film Transistor Applications,” *Adv. Funct. Mater.*, vol. 25, no. 12, pp. 1873–1885, Mar. 2015.
[43] E. Sachet et al., “Dysprosium-doped cadmium oxide as a gateway material for mid-infrared plasmonics,” *Nat. Mater.*, vol. 14, no. 4, pp. 414–420, Apr. 2015.
[44] I. Hamberg, C. G. Granqvist, K.-F. Berggren, B. E. Sernelius, and L. Engström, “Band-gap widening in heavily Sn-doped $InO_x$$,” *Phys. Rev. B*, vol. 30, no. 6, pp. 3240–3249, Sep. 1984.
[45] Y. Li et al., “Coffee-Ring Defined Short Channels for Inkjet-Printed Metal Oxide Thin-Film Transistors,” *ACS Appl. Mater. Interfaces*, vol. 8, no. 30, pp. 19643–19648, Aug. 2016.
[46] Y. Xu et al., “Significant roles of low-temperature post-metallization annealing in solution-processed oxide thin-film transistors,” *Appl. Phys. Lett.*, vol. 105, no. 13, p. 133505, Sep. 2014.
[47] K.-H. Choi and H.-K. Kim, “Correlation between Ti source/drain contact and performance of InGaZnO-based thin film transistors,” *Appl. Phys. Lett.*, vol. 102, no. 5, p. 052103, Feb. 2013.
[48] S. H. Rha et al., “Performance Variation According to Device Structure and the Source/Drain Metal Electrode of a-IGZO TFTs,” *IEEE Trans. Electron Devices*, vol. 59, no. 12, pp. 3357–3363, Dec. 2012.
[49] O. Kryvchenkova et al., “Nondestructive Method for Mapping Metal Contact Diffusion in $In_2O_3$ Thin-Film Transistors,” *ACS Appl. Mater. Interfaces*, vol. 8, no. 38, pp. 25631–25636, Sep. 2016.

# Chapter 6: UV-Annealing Low-Temperature Printed Metal Oxide Transistors

## 6.1 Introduction

The previous chapter developed low-temperature processed aqueous inks for printing transparent metal oxide electrodes for oxide TFTs. The low-temperature conversion process was studied as a function of ink composition and thermal annealing temperature, showing that the critical transition to functional films occurs in the range of 225 – 250 °C. This exceeds the thermal capability of flexible plastic substrates such as polyethylene naphthalate, which exhibit irreversible dimensional changes after extended heat treatment above 200 °C. To target these lower annealing temperatures and develop R2R-compatible processing, this chapter develops UV-annealed printed metal oxide transistors. In Chapter 5, high-performance printed transistors integrating aqueous-based metal oxide conductors and semiconductors were fabricated. Here we address the challenge of integrating printed dielectric materials by developing high-performance, low-temperature processed (≤ 250 °C) printed $InO_x$ transistors utilizing ultraviolet (UV) annealed high-k $AlO_x$ dielectrics.

UV-annealing is an efficient R2R compatible curing method for thin film processing. UV lamps and other photonic curing systems are a vital fixture in the coating industry due to their high-speed and low curing temperatures for various thermally sensitive materials and substrates. In solution-processed sol-gel based metal oxides, UV irradiation during device fabrication has been shown to improve low-temperature conversion of metal oxide semiconductors to functional thin films[1]. The current understanding of the effects of UV radiation on metal oxide precursors is that high energy UV photons break the coordination complexes between metal cations and organic ligands that have been incorporated into the sol-gel films. The net effect of UV irradiation, as demonstrated by Park *et al.*[2] and Jo *et al.*[3], is a rapid densification of the metal oxide matrix and increased formation of M-O-M bonds as observed by surface sensitive techniques such as XPS[4].

These observations suggest that UV-annealing could address some of the primary technological barriers for printed metal oxide transistors by lowering process temperatures and allowing integration with R2R processing. This chapter leverages the integration of UV-processing and inkjet printing to develop low-temperature-processed printed metal oxide transistors with printed, UV-annealed high-k $AlO_x$ gate dielectrics. The design of these $AlO_x$ precursor inks as well as multi-nozzle printing methodologies are engineered to enhance film uniformity and allow R2R compatibility. The influence of UV-annealing on low-temperature-processed high-k dielectric properties and the characteristics of printed $InO_x$ TFTs is studied, as well as the significant role of UV-annealing in improving the long-term bias-stress stability of metal oxide transistors.

The performance and reliability of solution-processed metal oxide transistors is closely tied to the processing of the dielectric layers. Low-temperature processed transistors, in particular, can exhibit considerable enhancement in mobility and drive current when integrated with a low-temperature processed high-k dielectrics[23]. Leveraging these advantages in printed metal oxide transistors, however, requires greater development of precursor chemistries, printing techniques, and annealing methods of low-temperature printed dielectrics. To date, UV-annealing has been the predominant route to high performance, metal oxide semiconductors[16,24] and dielectrics[20] at low process temperatures below 300 °C. The majority of this work on UV-annealed metal oxide films

has focused on the impact of UV-annealing in inert atmospheres on ultrathin spincoated films (thickness < 20 nm). However, from a device integration and manufacturing perspective, the ultrathin dielectrics[21] and inert atmosphere annealing steps used in these studies present problems for integration into printed metal oxide TFTs. Printed devices have unique requirements due to their reliance on nanoparticle-based electrodes with higher surface roughness and the presence of printing and drying artifacts such as coffee-ring defects. Thicker dielectric films are needed to compensate for these printing-specific structural features and ensure reliable device operation. The results presented here will address these requirements and demonstrate successful printed transistor integration of UV-annealed high-k dielectric films.

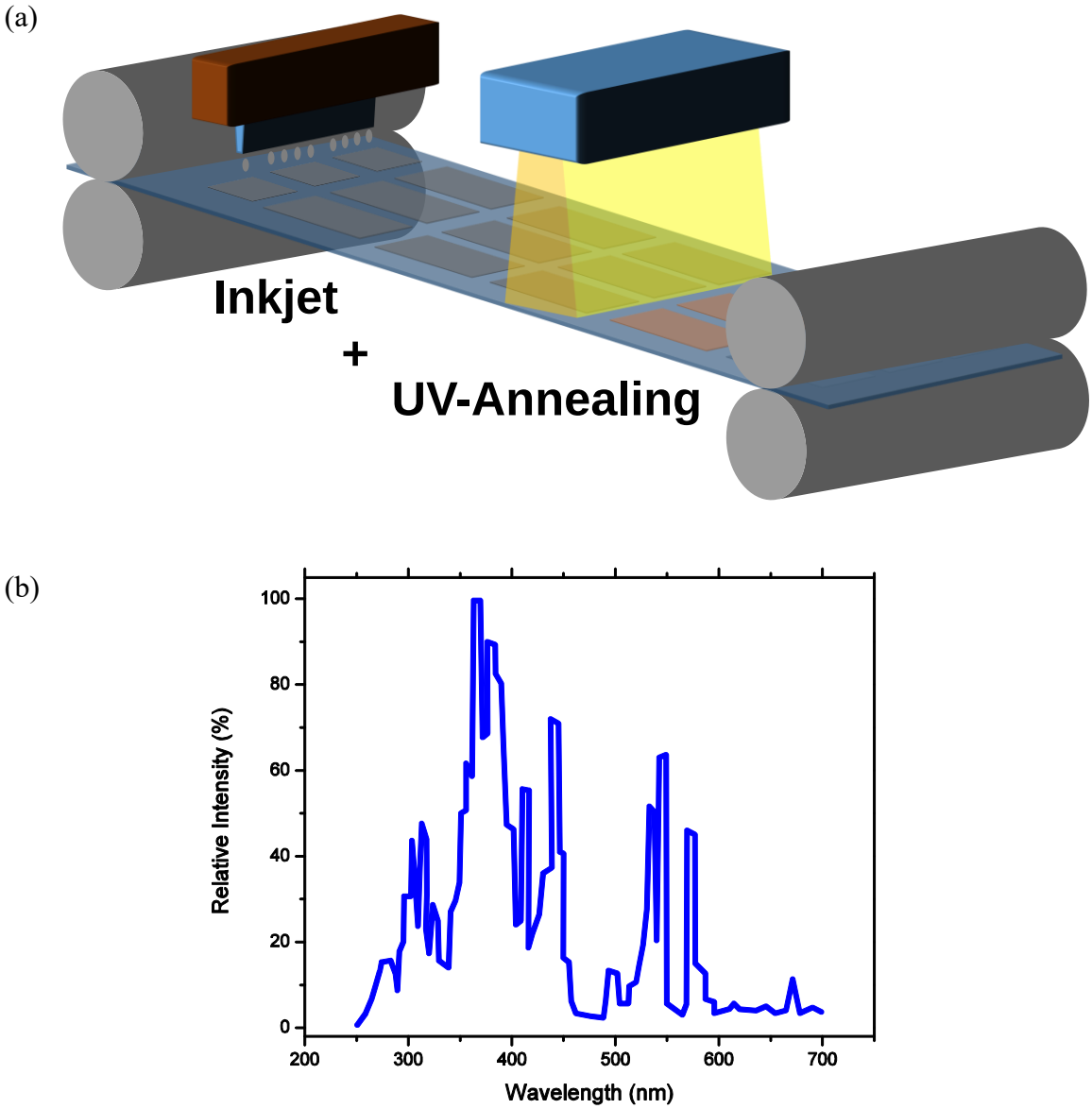


Figure 6.1 Illustration of R2R compatible integration of inkjet printing and UV annealing for printed transistor fabrication (a). Spectrum of UV lamp used in this study (b).

## 6.2 Inkjet Printed $AlO_x$ Dielectrics

Low-temperature-processed high-k $AlO_x$ dielectrics were fabricated by integrating inkjet printed sol-gel precursor inks consisting of $Al(NO_3)_3$ metal salts dissolved in 2-methoxyethanol with ambient UV-annealing. A scheme illustrating the potential inline R2R combination of these high-throughput printing and annealing methods is shown in Figure 6.1. To study the impact of film thickness and UV annealing on dielectric properties and TFT performance, multilayer printing and varying solute concentrations were used to deposit sol-gel films with a wide range of thicknesses from 15 nm up to 200 nm.

### 6.2.1 Ink Formulation

$AlO_x$ dielectric precursor inks were prepared from $Al(NO_3)_3$ (Sigma 229415, 99.997 %, 200mM-800mM) dissolved in 2-methoxyethanol. Dielectric inks were mixed fresh prior to printing, sonicated for 10 min, and filtered through a 0.45 µm PTFE filter before loading into a 1 pL Dimatix DMP (DMC-11601) cartridge. $InO_x$ semiconductor precursor inks were prepared from solutions of $In(NO_3)_3$ (Sigma 326127, 99.99 %, 200mM) in DI water and loaded into 1 pL Dimatix cartridges (DMC-11601). $InO_x$ aqueous inks remained stably dispersed indefinitely, and were used for device fabrication for more than three months. Finally, transparent conductive CdO:Al precursor inks were prepared from aqueous solutions of $Cd(NO_3)_2$ (Sigma 229520, 99.997 %, 200 mM) with a 3% molar ratio of $Al(NO_3)_3$ and filtered immediately before loading into 10 pL Dimatix cartridges (DMC-11610). All solvents were obtained from Sigma Aldrich and used as received.

### 6.2.2 Printed Film Deposition

Printed high-k $AlO_x$ dielectric pads of approximately 600 µm x 1200 µm were printed on n++ silicon substrates at 40 µm drop spacing and a platten temperature of 36 ºC using a Fujifilm Dimatix DMP-2850 desktop inkjet printer. Prior to printing, a 2 min UV ozone treatment (Jelight 42) was used to achieve favorable wetting of the inks. To jet the $AlO_x$ ink, the Dimatix *Model Fluid 2* waveform was used, with a jetting voltage of 11.0 V and a jetting frequency of 5 kHz. To build thicker wet films, multiple consecutive layers were deposited consecutively without an interlayer delay. $AlO_x$ films were then dried on a hot plate for 5 min at 150 ºC and subsequently exposed to UV irradiation in ambient atmosphere using a metal halide 400 W lamp (Loctite ZETA 7401) with a parabolic reflector and an incident intensity of approximately 1 W/cm$^2$ for 5 – 20 min. The spectral intensity of this UV source is included in Figure 6.1b. Following UV treatment, the $AlO_x$ dielectrics experienced a 2-hour thermal post anneal at 250 ºC on a hot plate in ambient conditions.

Highly uniform, insulating dielectric films were printed by utilizing multi-nozzle jetting and by tuning the concentration of the inks. This highlights an interesting feature of inkjet printing is that it easily allows the printing of multiple film thicknesses on the same substrate. As shown in Figure 6.2, a wide range of film thicknesses were printed with a single ink by varying the drop spacing and depositing multiple layers. This offers an interesting capability for printed circuit design to easily fabricate thin film capacitors of varying areal capacitance or to utilize transistors with high or low operating voltages on the same substrate.

The design of an inkjet printing process for high-k gate dielectrics is influenced by many factors such as ink viscosity, surface tension, wetting, jetting, and drying kinetics. Figure 6.3 summarizes the printing processes, highlighting the difference between single nozzle and multi-nozzle printing. In single nozzle printing of nanoscale films, the sequential drying of the film during print head raster cycles results in thickness non-uniformity (Figure 6.4). Even in cases when droplets merge to form a continuous film free of pinholes, the surface profile inherits a roughness with a wavelength equal to the drop-spacing of the pattern. Multi-nozzle printing, on the other hand, deposits an entire film in a single pass, eliminating intermittent drying and enhancing film uniformity. In Figure 6.4, parts (d) and (g) illustrate the results of using 16 nozzles at a time to print a single film. The thickness profiles lack the drop-spacing determined roughness, achieving a relatively flat surface (typical RMS variation < 5 % of thickness) as measured with a stylus profilometer.

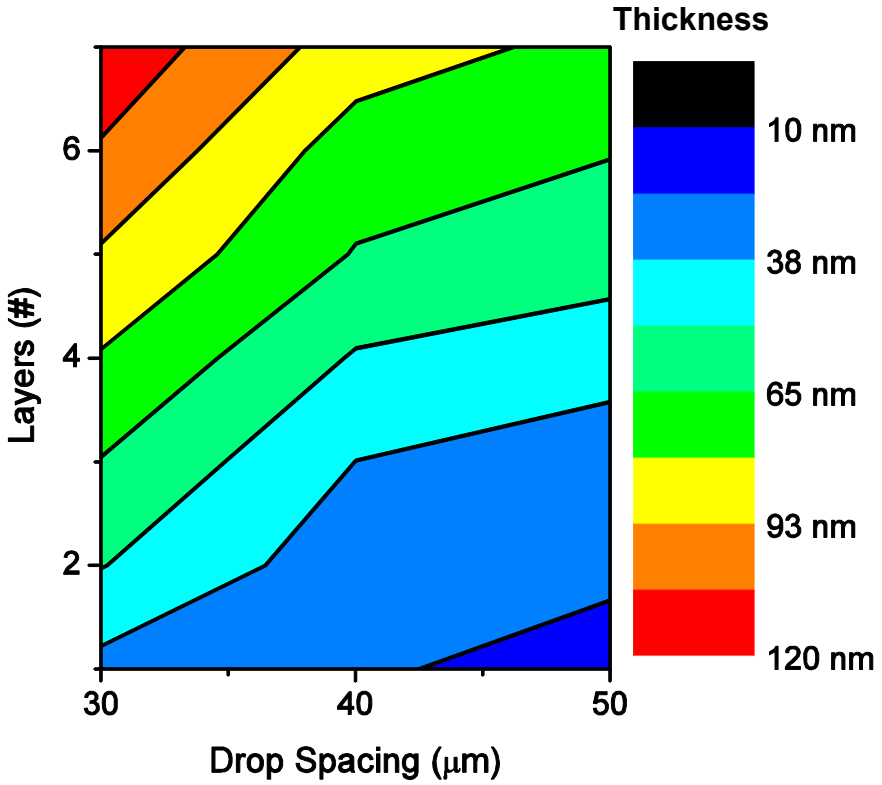


Figure 6.2 Contour map of printed thickness as a function of the number of layers printed and the drop-spacing used.

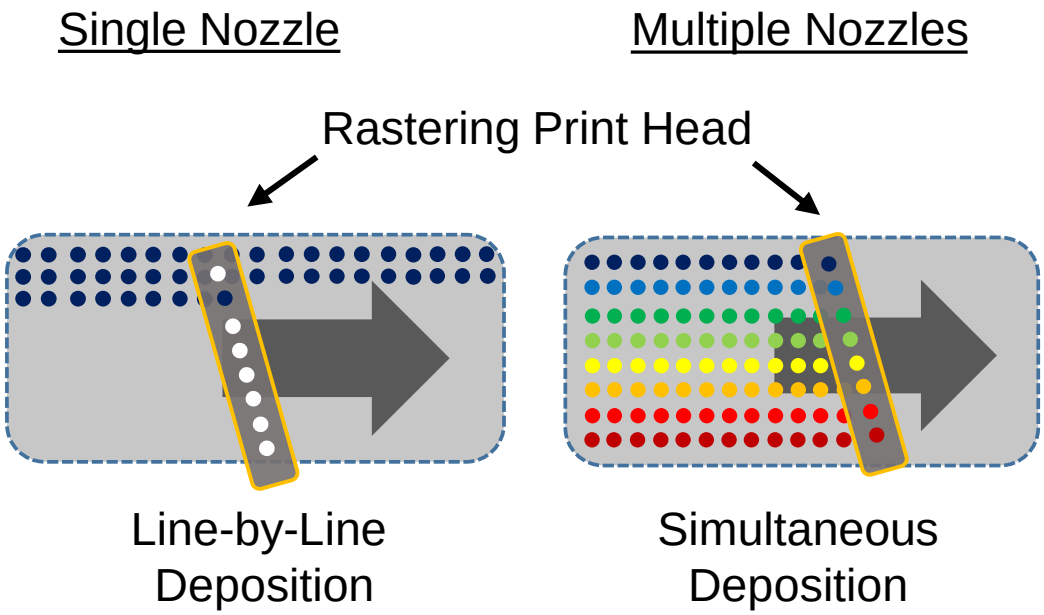


Figure 6.3 Comparison of the mechanisms of drying and film deposition for single and multi-nozzle printing.

An important characteristic of these profiles is that they lack the considerable coffee-ring edge deposits that are typically left by low-boiling point printed sol-gel inks[7]. Coffee-ring features typically result from an outward convective flow which deposits excess material near the contact line of a printed feature[8]. However, in this case, the coffee-ring effect was mitigated by using a thinner initial fluid film thickness and a higher ink concentration. Switching from the standard 10 pL nominal drop volume to a 1 pL nominal drop volume considerably reduced the coffee-ring edge deposits and improved overall uniformity. Similarly, higher concentration inks (400 mM – 1200 mM) resulted in elimination of the coffee-ring effect. These observations are consistent with an explanation that considers the reduced drying time of the thinner printed films. A reduced drying time allows less time for convective outward flows to occur, ensuring that the dried film will more closely resembled the initial profile of the deposited wet film. Similarly, the increased viscosity of a higher concentration ink, as shown in Figure 6.4e, retards the outward convective flow to the contact line. Therefore, we find that minimizing the drop volume and increasing the concentration of the ink are two key strategies in printing highly uniform dielectric films.

Dielectric thickness uniformity is an impactful parameter for printed device operation because it determines a tradeoff between capacitance, operating voltage, and reliability. Films with large thickness variations must sustain higher peak transverse electric fields in the thinnest regions, resulting in a lower intrinsic breakdown field for the same capacitance. Thus, for a device with a given dielectric thickness, a highly uniform film can sustain higher operating voltages without suffering from issues with dielectric reliability. Alternately, uniform gate dielectrics can allow

further dielectric thickness scaling to achieve higher gate capacitance for a given operating voltage. Thus, the printing processes shown here which enhance dielectric film uniformity have a direct impact on printed transistor performance and reliability.

Additionally, while these strategies are useful for attaining more uniform films, they are also essential for implementing a high-speed inkjet process suitable for R2R-compatible manufacturing. Because industrially scalable R2R inkjet technologies fully utilize large format print heads with over 1,000 nozzles[9], exploring the unique features of multi-nozzle printing is essential. This is also particularly relevant for this study of printing integration with photonic UV-annealing, which can also facilitate higher throughput processing by reducing the time for drying and annealing steps.

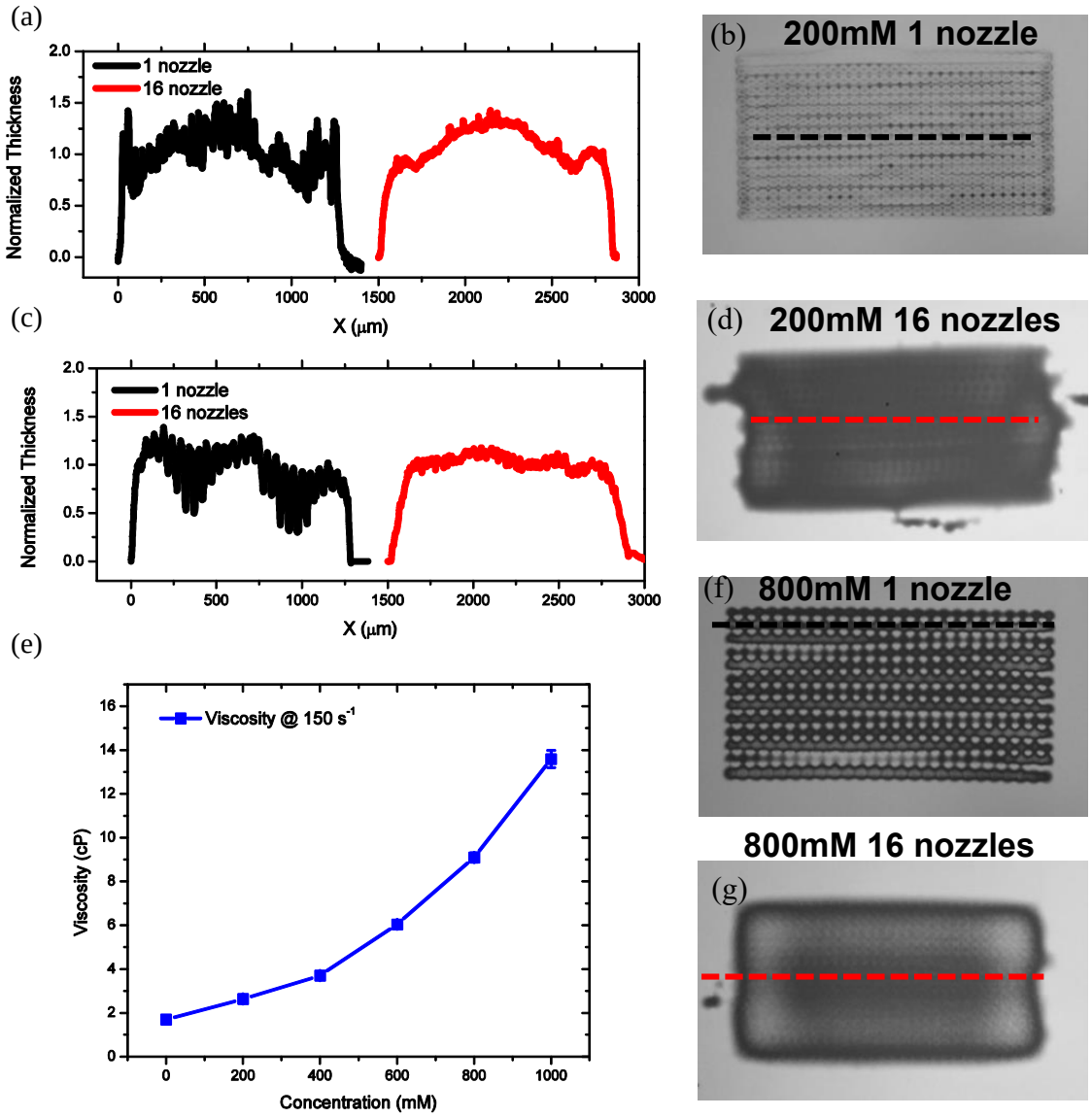


Figure 6.4 Comparison of the mechanisms of drying and film deposition for single and multi-nozzle printing.

## 6.3 UV-Annealing Printed Dielectrics

The dielectric response of the *thermal-only* annealed $AlO_x$ printed dielectrics showed significant differences between thinner films ($t_{ox}$ < 20 nm) and thicker films ($t_{ox}$ > 80 nm). Thicker films showed strong low-frequency dispersion, with dielectric constants of up to 30 measured at 20 Hz, whereas thinner films had a flatter dielectric response across a wide frequency range. This trend can be observed in Figure 6.6a for printed $AlO_x$ dielectrics of varying thickness. One reason for the poor characteristics of thicker films could be the presence of residual organic ligands left in the film following the low-temperature thermal annealing step at 250 ºC. Thermal gravimetric analysis (Figure 6.5c,d) of the aluminum nitrate ink indicates that decomposition is not completed until the sol-gel has been heated to beyond 300 ºC. Indeed, in other sol-gel systems, film quality and performance has tended to decrease above a critical film thickness[10], as precursor compounds are trapped in the bulk of the film rather than being volatilized and expelled.

UV-annealing offers a low thermal budget route to mitigate the tradeoff between film thickness and performance. In this study, UV-annealing was applied to the printed dielectric films prior to thermal annealing, yielding a significantly improved dielectric response. As shown in Figure 6.5a, increasing UV exposure results in printed films with a flatter frequency response and a dielectric constant of 5-7, similar to that of high-temperature processed $AlO_x$ sol-gel dielectrics[11]. This could suggest that residual organics are decomposed by the UV radiation[12] and are then volatilized by thermal annealing. Indeed, alternating UV exposure and short thermal anneals appeared to be more effective than singular long UV-anneals, indicating the synergy between these two methods.

Thickness measurements of the printed films (Figure 6.5b), show that UV-annealing for durations as short as 5 minutes rapidly causes significant thickness reduction, consistent with the decomposition and densification of the precursor film. The effect is particularly noticeable for the thicker precursor films, which exhibit a > 30% volume reduction following a 10 minute UV exposure. After longer exposures (20 minutes), the film thickness closely approaches the film thickness otherwise achieved following thermal annealing at 250 ºC for two hours. This suggests the role of UV-annealing in densifying the film and helping to convert it to a functional dielectric. Indeed, XPS measurements of the surface of the printed dielectric films (Figure 6.7) confirm that the extent of M-O-M bonding is enhanced by UV-annealing, even when compared to that of the samples which received only thermal annealing at 250 °C. Combined, these two factors, namely the densification and enhanced conversion, indicate that UV-annealing can play a vital role in low-temperature-processed, printed high-k metal oxide systems.

While UV-annealing has a large impact on the dielectric response and film thickness, the morphology, leakage current density, and breakdown fields of the printed metal-insulator-metal (MIM) capacitors were not observed to be sensitive to the amount of UV exposure. AFM scans of the printed $AlO_x$ films showed ideal low RMS roughness of approximately 0.4nm and 0.3nm for films with and without UV-annealing, respectively. Additionally, $AlO_x$ MIMs showed a consistently low leakage current density of approximately $10^{-7}$ A/cm$^2$ at an electric field of 1 MV/cm and a median breakdown field of 3.5 MV/cm (Figure 6.6b), appropriate for use in printed transistors. MIMs with varying $AlO_x$ thickness showed similar leakage and breakdown characteristics (Figure 6.6c).

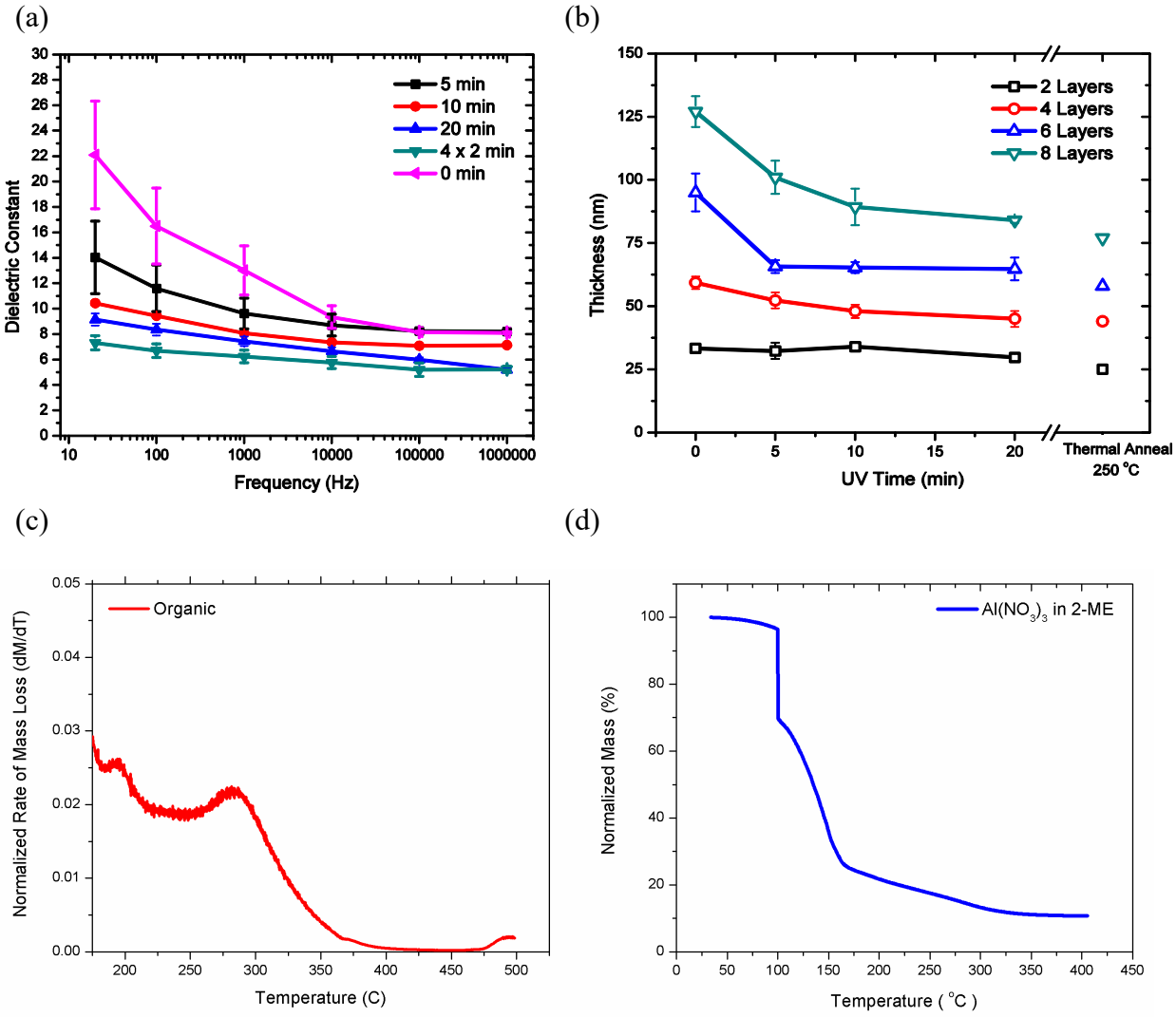


Figure 6.5 Dielectric response of UV-annealed $AlO_x$ printed dielectric films (a). Thickness of printed $AlO_x$ films following UV-annealing with varying durations (b). Differential mass-loss vs temperature for $AlO_x$ precursor ink (c). Normalized mass-loss of $AlO_x$ precursor ink during heating in air (d)

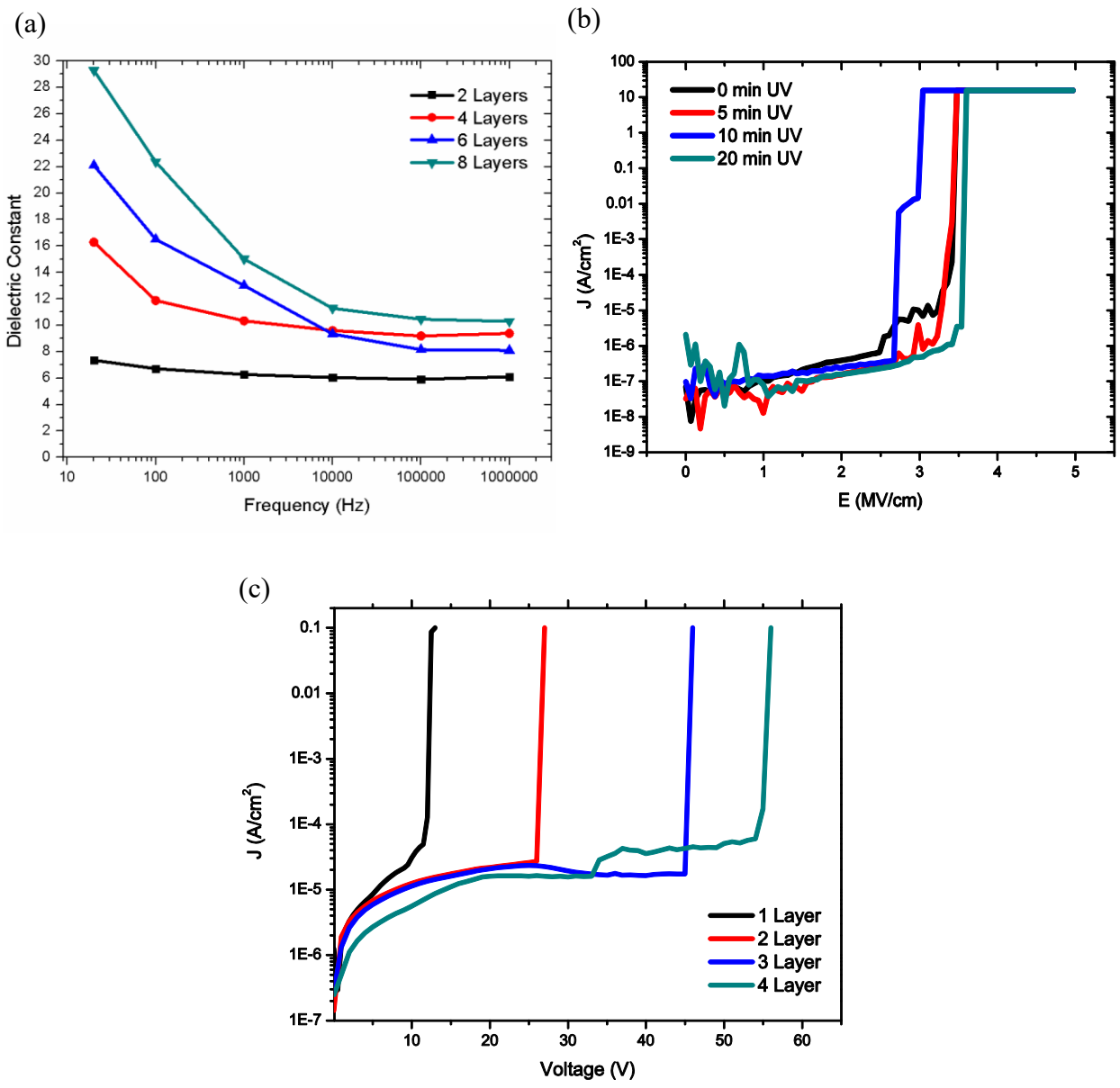


Figure 6.6 Dielectric constant vs frequency for printed, *thermal-only* annealed $AlO_x$ (a). Leakage current vs electric field for $AlO_x$ printed capacitors printed with 6 layers (b). Leakage current density for printed $AlO_x$ capacitors with varying thickness (c).

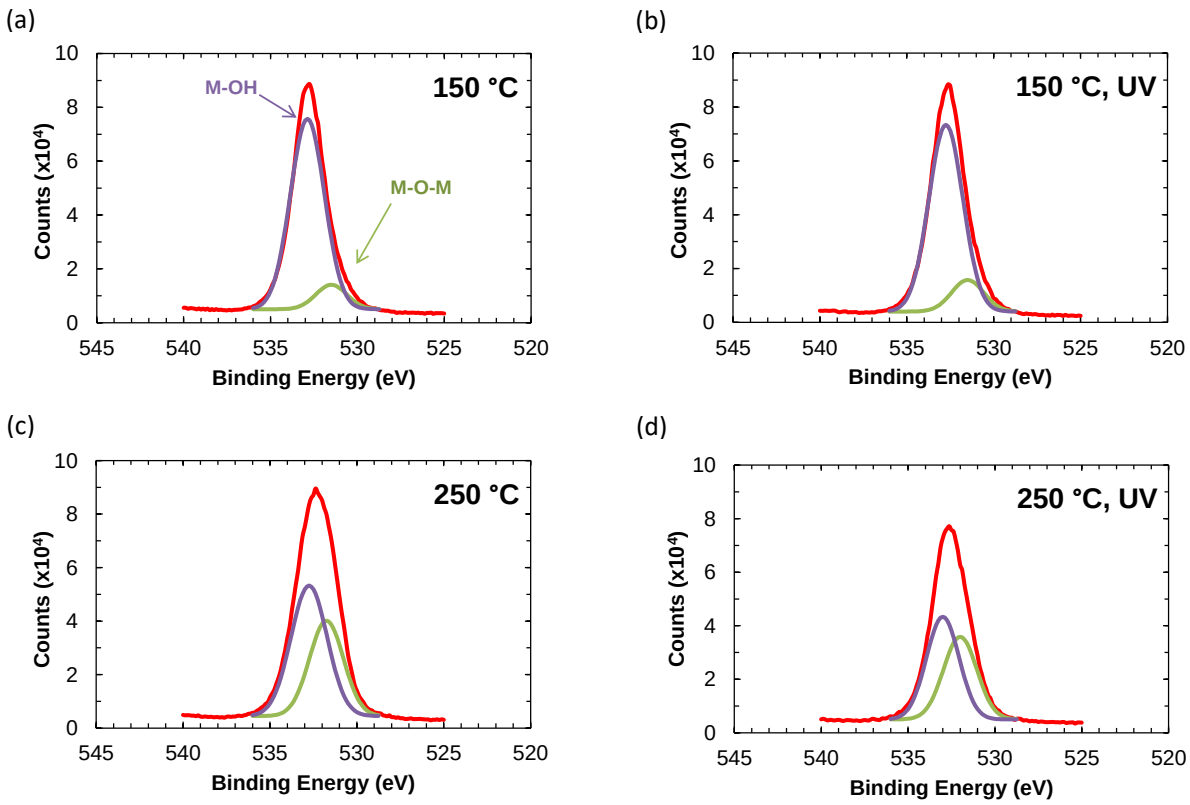


Figure 6.7 XPS spectra of the aluminum peaks for surface scans of four layer printed dielectrics after low-temperature drying (a), low-temperature drying with 10 min UV-annealing (b), only 250 °C thermal annealing (c), and UV-annealing followed by 250 °C thermal annealing (d).

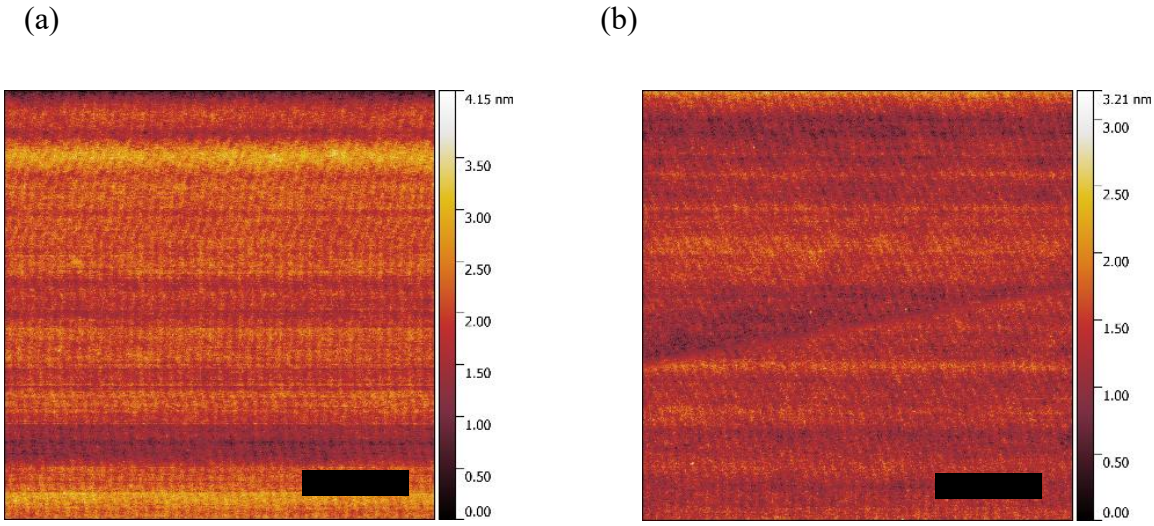


Figure 6.8 AFM scans of printed $AlO_x$ dielectrics with UV annealing (d) and without UV annealing (b) with 500 nm scale bar.

## 6.4 Printing Low-Temperature $InO_x$ Transistors

$InO_x$ semiconductors were deposited with a 1pL Dimatix cartridge at 40 µm drop spacing and a platten temperature of 32 ºC, using two printed layers. A two minute UV Ozone treatment was performed prior to semiconductor printing. Printed films were dried at 100 ºC for 5 min, and then annealed at 250 ºC on a hot plate in air for 2 hours. CdO:Al transparent source / drain electrodes were deposited by inkjet printing at 40 µm DS and 32 ºC platten temperature to form devices with a width of approximately 400 µm and a length of approximately 250 µm. Further details of the printed source / drain fabrication are listed in a previous work[13]. Films were dried at 200 ºC for 2 min and annealed at 250 ºC on a hot plate in air for 40 min. Printed MIM capacitors with Si / $AlO_x$ / CdO:Al structures were fabricated by equivalent dielectric printing procedures and electrode printing procedures for use in leakage, breakdown, and SILK measurements. MIMs with metallic Ag electrodes were printed (ANP DG-40LT-15C) at 20 µm drop spacing with a 1 pL cartridge for higher frequency (100 kHz – 1 MHz) capacitance evaluation due to the limited conductivity of CdO:Al electrodes. Control TFTs for bias-stress measurements were fabricated on Si wafers with 100 nm thermally grown $SiO_2$ using inkjet printed $InO_x$ semiconductor layers and CdO:Al electrodes by an equivalent process to the devices on printed $AlO_x$ dielectrics. A 20 min UV ozone treatment was performed before printing the $InO_x$ semiconductor.

## 6.5 Printed $InO_x$ Transistor Performance

The principal benefits of printing thicker $AlO_x$ dielectric films are improved device stability and control over TFT operating voltages. Without UV-annealing treatment, $AlO_x$ films above 100 nm in thickness become cracked following thermal annealing at 250 ºC, leading to non-functional transistor structures with high gate leakage. With UV-annealing induced densification, however, thicker high-quality printed dielectrics can be formed in a single deposition step without cracking. Using higher concentration $AlO_x$ precursor solution (400 mM), films anywhere from 15nm to 200nm in thickness were printed and UV annealed to form robust dielectrics.

$InO_x$ transistors fabricated with UV-annealing show excellent switching behavior for different thicknesses of $AlO_x$ dielectric, allowing reliable operation as low as ±2 V or up to ± 30 V, depending on the choice of the gate dielectric. As shown below in Figure 4a-c, the printed TFTs have steep turn on (subthreshold slope < 150 mV/dec in some cases) and show a minimal amount of counter-clockwise hysteresis (< 50 mV). These characteristics suggest that the integration of $InO_x$ with UV annealed $AlO_x$ is a favorable combination for producing a superior semiconductor / dielectric interface. Unlike many other solution-processed and printed metal oxide TFTs ($InO_x$[14], SnOx[15], etc), these devices operate with only a small negative turn-on voltage ($V_{on}$). As a result of the lower gate-field used to turn off these devices, the off current is relatively low (less than 10 pA) in nearly all cases, improving the $I_{on} / I_{off}$ ratio to greater than $10^7$, a key metric for applications such as power efficient high-resolution emissive displays.

The output characteristics of these printed devices (Figure 6.10) show efficient current injection at low drain bias and good current saturation at high drain bias for each $AlO_x$ thickness. The distribution of the peak linear mobility for devices built on 30 nm $AlO_x$ is shown below in Figure 6.11b, with an average $\mu_{lin}$ = 12 ±1.6 $cm^2$/Vs. The mobility extracted from these curves does not vary significantly for different $AlO_x$ thicknesses, and achieves a relatively constant peak mobility value at moderate operating voltages (Figure 6.9c).

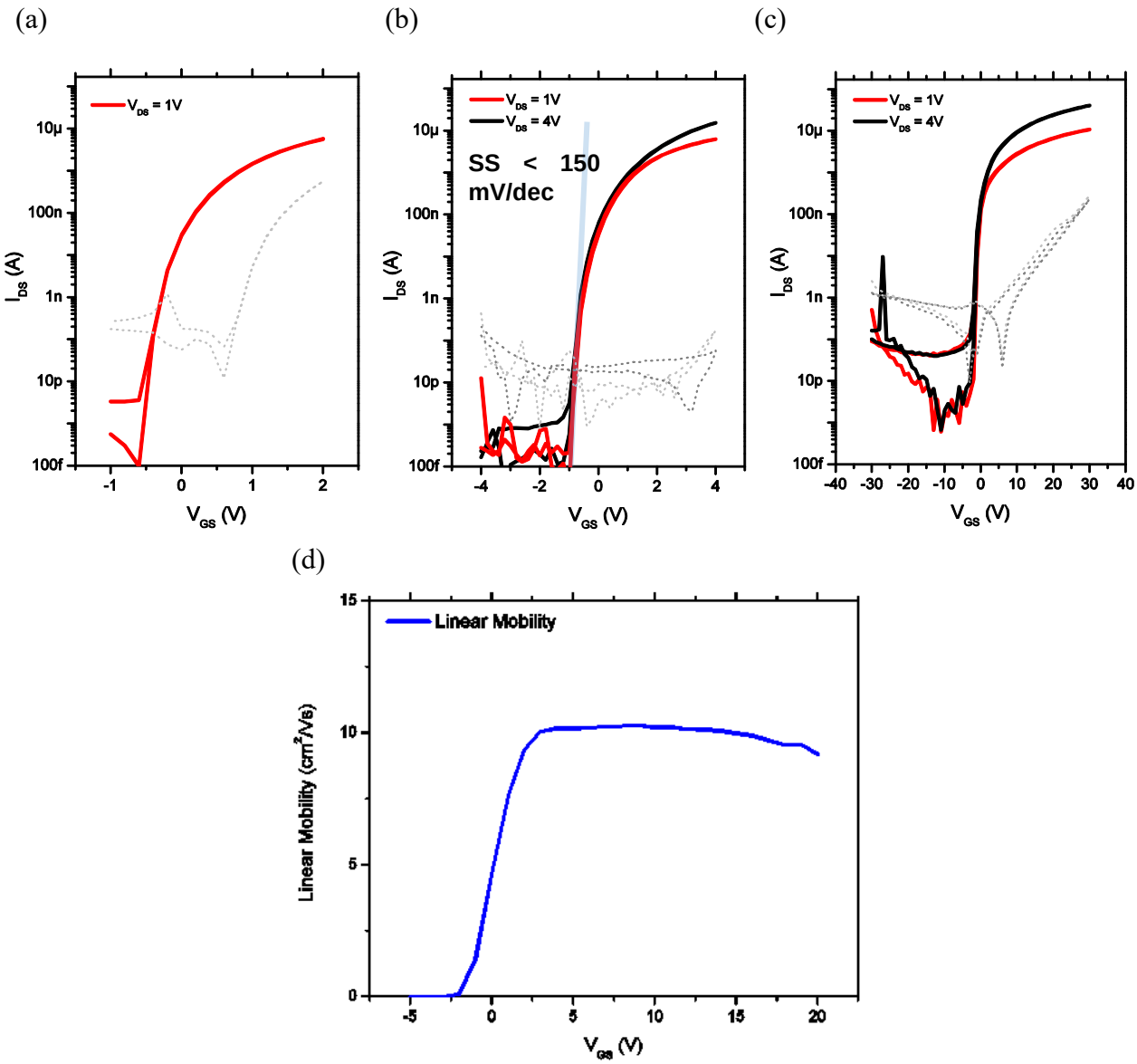


Figure 6.9 Transfer characteristics of $InO_x$ TFTs with AlOx dielectrics of $t_{ox}$ = 15 nm (a), 30 nm (b), and 200 nm (c). Incremental mobility during linear mode operation for $t_{ox}$ = 30 nm (d).

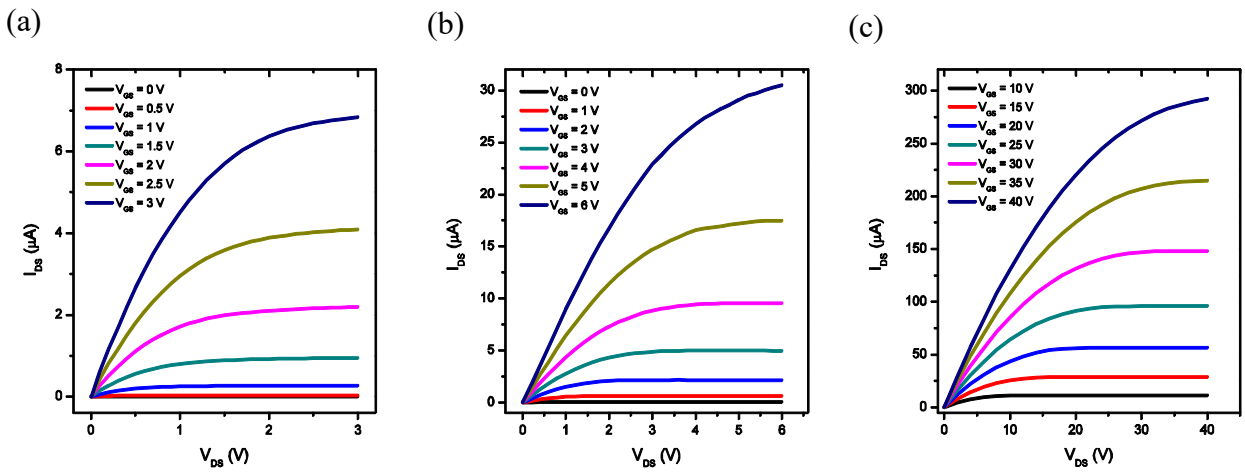


Figure 6.10 Transfer and output curves of $InO_x$ TFTs with $AlO_x$ dielectrics of $t_{ox}$ = 15nm (a), 30nm (b), and 200nm (c).

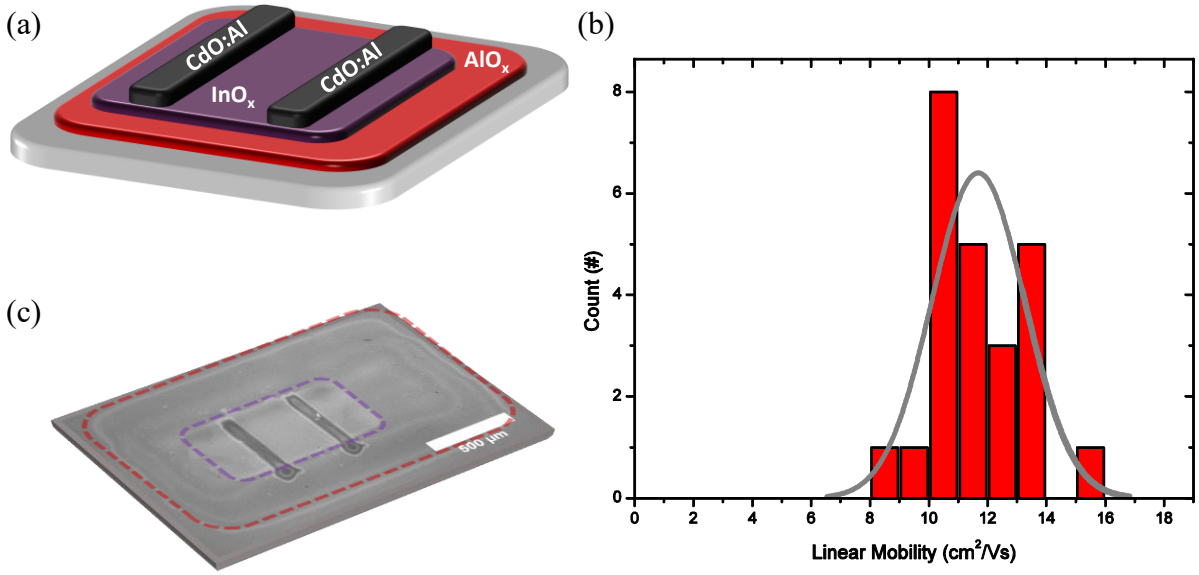


Figure 6.11 Printed transistor layer schematic (a). Distribution of peak linear mobility of printed $InO_x$ transistors (b). Isometric view of printed transistor (c).

### 6.6 Impact of UV-Annealing on Bias-Stress Stability

Bias-stress stability is an essential property of thin film transistors which can potentially limit their viability in various applications. Bias-stress describes the results of applying a gate bias in the on or off-state over an extended period of time, resulting in shifts in device properties such as the threshold-voltage ($V_t$)[16]. Transistors with high bias-stress stability retain their properties and maintain consistent drive current over time, a necessary feature for many circuit-level applications.

The bias-stress stability of the printed transistors was evaluated to investigate the influence of varying the $AlO_x$ dielectric. To distinguish the influence of bias-stress on the dielectric and the semiconductor layers, control devices utilizing a high-quality thermally grown $SiO_2$ (100nm) as a gate dielectric were fabricated by similar printing methods for the semiconductor layers and electrodes. These control devices were subjected to positive bias-stress (PBS) and negative bias-stress-under white light illumination (NBIS) at $V_G = \pm 50$ V for durations up to $10^3$ s. Figure 6.12a illustrates the results of (PBS) on these control devices. These devices showed moderate stability with $V_t$ shifts of approximately 10-15% of the operating voltage range. PBS induces positive $V_t$ shifts and NBIS induces negative $V_t$ shifts, consistent with electron trapping in the $InO_x$ semiconductor layers and at the $SiO_2$ / $InO_x$ interface[17]. In both cases of NBIS and PBS, the subthreshold swing is only slightly degraded in these control devices and the $V_{on}$ shifts by a similar amount to the threshold voltage.

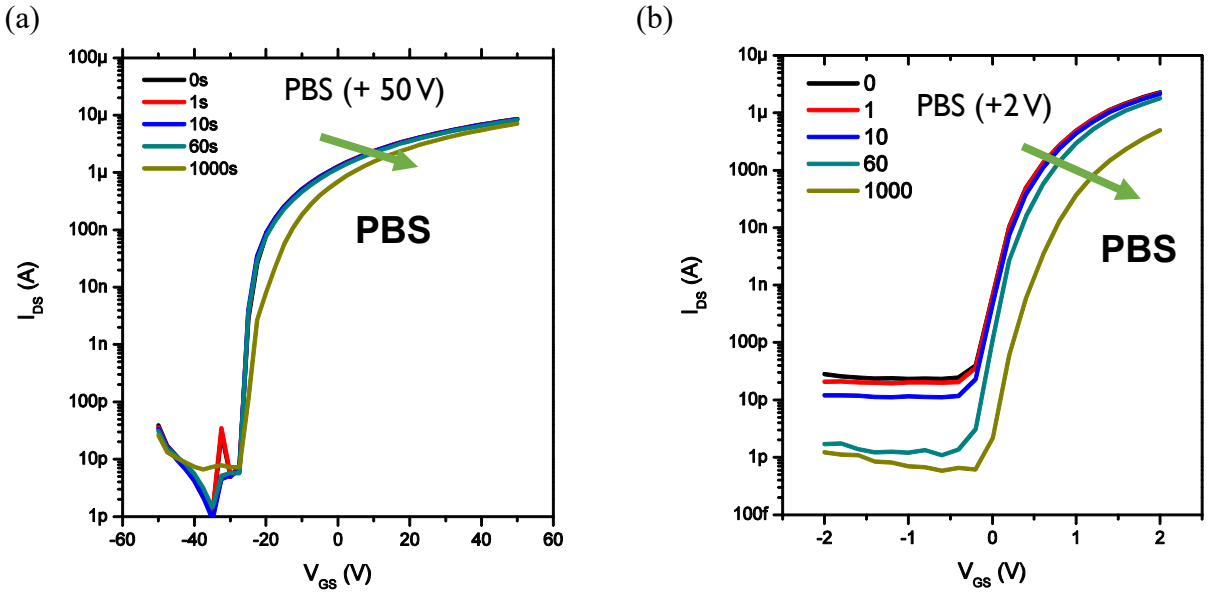


Figure 6.12 Inkjet printed $InO_x$ TFTs under PBS on 100 nm thermal $SiO_2$ (a) and 15nm $AlO_x$ (b) dielectrics.

The stressing characteristics of the TFTs with thin (15 – 30nm) printed $AlO_x$ dielectrics show similar general trends to the control devices on $SiO_2$, but have larger $V_t$ shifts relative to the operating voltage used, resulting in more significant degradation to on-current over the course of the stress measurements (Figure 6.12b). TFTs with thicker printed dielectrics, however, show superior stressing characteristics. The PBS and NBIS characteristics of $InO_x$ TFTs with 200nm thick $AlO_x$ dielectrics show somewhat degraded subthreshold swing after stressing, resulting in negative shifts to $V_{on}$ (Figure 6.13). However, in both cases the $V_t$ is relatively stable. Interestingly, the devices on thicker printed dielectrics also have inverted stressing characteristics with respect to $V_t$; these devices show negative $V_t$ shifts for positive stress (PBS) and slight positive $V_t$ shifts due to negative stress (NBIS). This change in polarity suggests that an alternative mechanism

drives the stressing characteristics of thicker printed dielectrics which partially compensates the typical shifts observed due to interface trapping in the $InO_x$ semiconductor layer. Indeed, a similar trend was recently observed by Carlos, et. al., for sputtered IGZO TFTs fabricated using UV-processed sol-gel $AlO_x$ dielectrics[18], suggesting that this compensation effect may be a more general feature of low-temperature spin-coated high-k dielectric films. One possible explanation for these observations is electron emission from donor traps in the bulk of the $AlO_x$ dielectric. The ionization of these donor traps would create positive charge in the dielectric, resulting in the negative $V_t$ shifts which are observed. The enhanced density of donor-like traps in solution-processed high-k dielectrics may, in fact, explain their tendency to compensate the electron trapping in the semiconductor bulk and interface states that normally drives the PBS behavior of these devices.

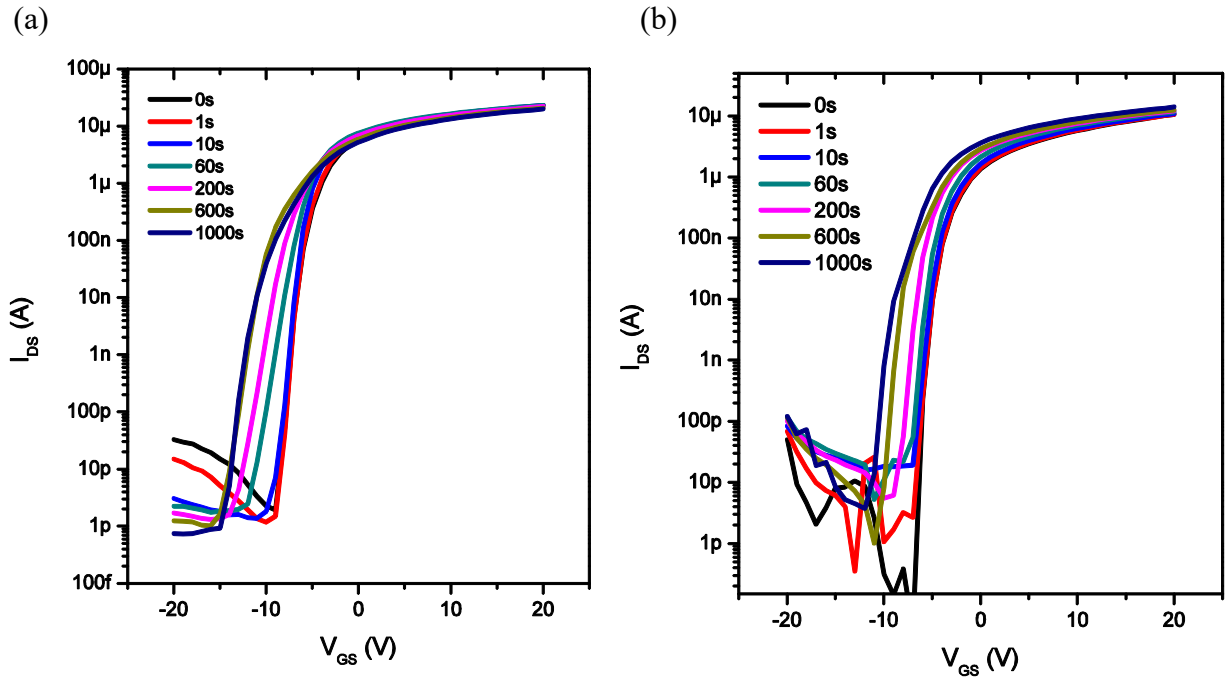


Figure 6.13 $InO_x$ TFTs on 200nm printed $AlO_x$ dielectrics under NBIS (a) and PBS (b).

A direct comparison of the magnitude of the $V_t$ shifts (normalized by the operating voltage, $V_{DD}$) vs stressing time is shown below in Figure 6.14a,b for $AlO_x$ dielectrics of varying thickness and $SiO_2$ control dielectrics. The operating ranges were selected to maintain an equivalent product of gate capacitance and operating voltage. Devices with the thinnest dielectrics have larger $V_t$ shifts relative to their operating voltage, amounting to greater than 25% of $V_{DD}$ over the course of a 1000 s period of stress.

(a)

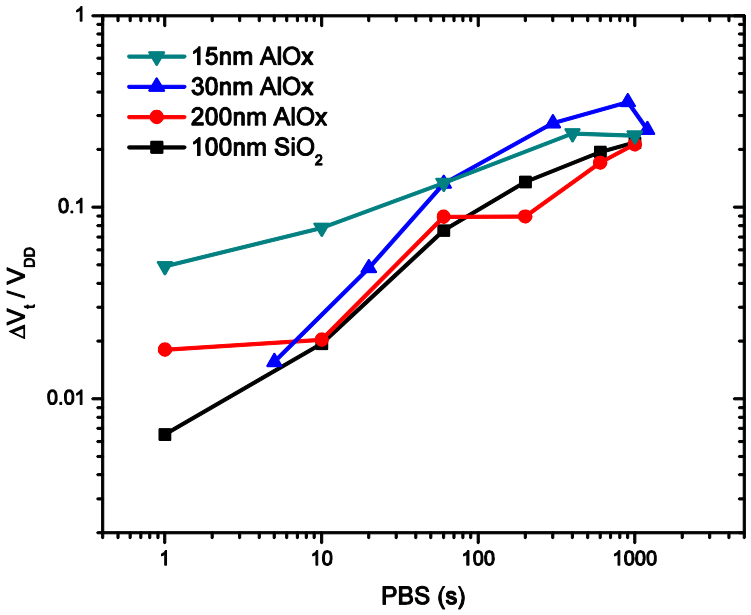


(b)

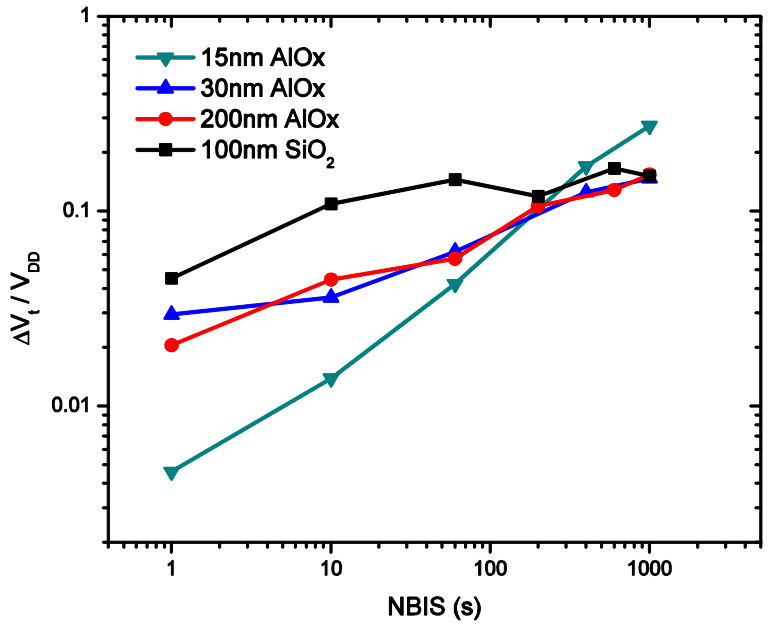


Figure 6.14 Normalized $V_t$ shifts for printed TFTs with various dielectrics under PBS (a) and NBIS (b).

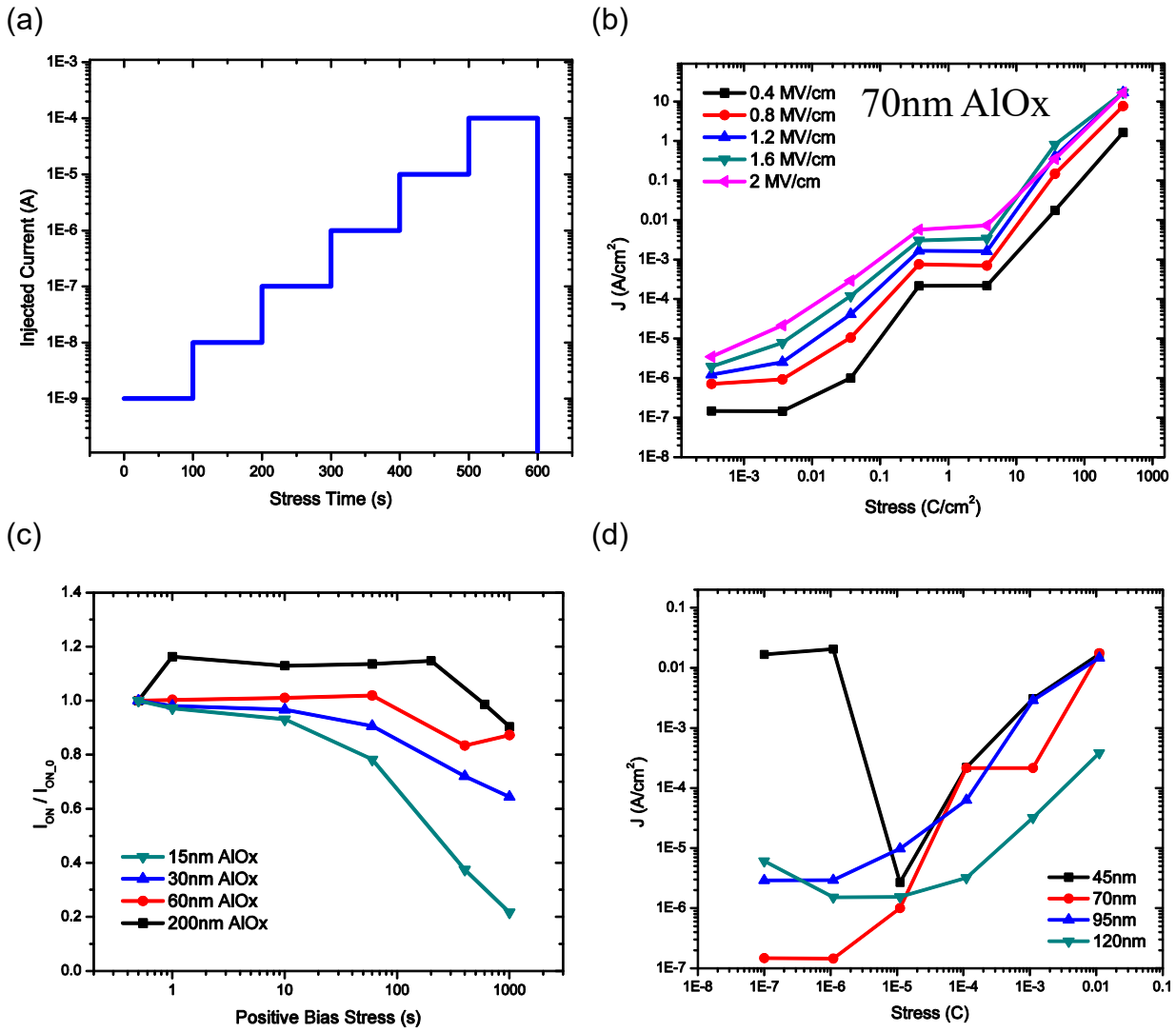


Figure 6.15 Stepped current injection for SILC measurements (a). Leakage current vs injected charge at varying fields for a 70nm $AlO_x$ printed capacitor (b). Normalized on current vs positive bias (c). Stress-induced leakage current for $AlO_x$ dielectrics of varying thickness (d).

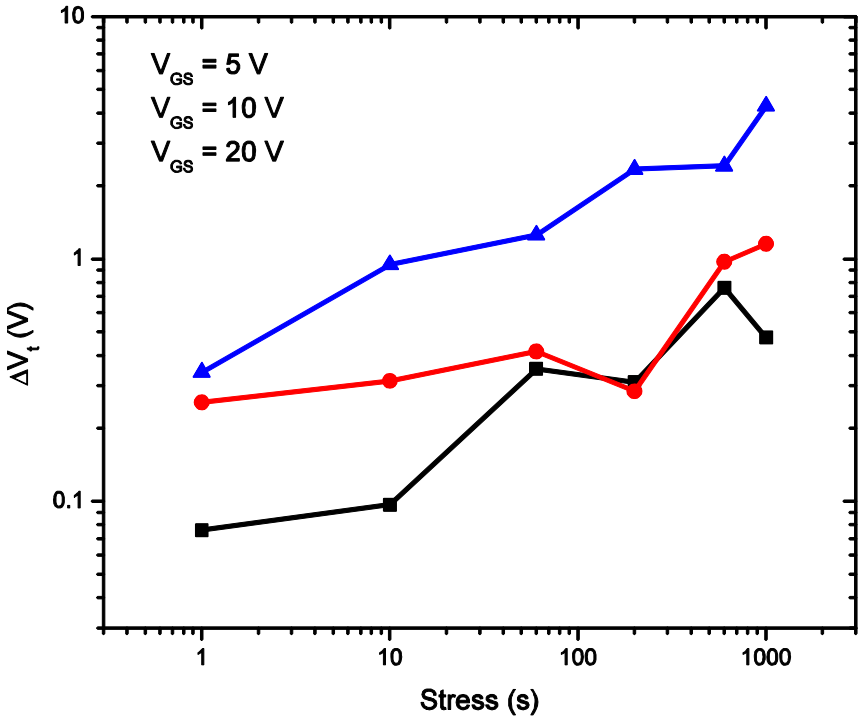


Figure 6.16 Threshold voltage shifts due to positive bias stress at various voltages for 200nm $AlO_x$ dielectric TFTs.

However, devices with thicker 200 nm $AlO_x$ show $V_t$ shifts roughly on par with the control devices built on highly stable thermally grown $SiO_2$, a dielectric which has been shown to lead to excellent bias-stress stability and low interface defect densities for IGZO TFTs[19], [20]. The result of this improved stability, as well as the inverted stressing characteristics of thicker $AlO_x$ dielectrics, is that the devices built on these printed dielectrics maintain a greater percentage of their original on current after lengthy positive bias-stress. As shown in Figure 6.15c, devices on 60 nm and 200 nm $AlO_x$ dielectrics maintain approximately 90% of their original $I_{on}$ over the course of the bias-stress measurement. In comparison, devices on thin $AlO_x$ dielectrics (15 nm, 30 nm), have severely degraded $I_{on}$ which drops by more than 50% of its original value as a result of the $V_t$ shift. Additionally, we add that that the steep subthreshold turn on of these printed TFTs can allow operation at a relatively lower gate bias, at which the threshold voltage shifts during bias-stress can be reduced by an order of magnitude to the ~ 100 mV range (Figure 6.16).

To understand the different stressing characteristics of thicker printed dielectrics, stress-induced leakage current (SILC) measurements were performed on MIM capacitors of varying thicknesses, using a stepped method of injecting charge (Figure 6.15a). After moderate to high amounts of injected charge (100 µC to 100 mC), the thicker dielectrics showed lower stress-induced leakage current than thinner dielectrics (Figure 6.15d). This result would be expected for thicker dielectrics, since larger areal defect concentrations are typically required to induce percolative leakage paths through the bulk of the dielectric film. In addition, there is a non-monotonic trend in the leakage current density specifically in thicker dielectrics. This observation of an initial decrease in leakage might suggest a complementary mechanism for how thicker dielectrics compensate stress-induced $V_t$ shifts in the $InO_x$ semiconductor. During PBS, for example, electron

trapping at the channel interface could initially be compensated by the emission of electrons from donor traps in the $AlO_x$ dielectric. Thinner dielectrics, on the other hand, showed higher, monotonically increasing leakage current with the application of constant-current stress, suggesting fast accumulation of a critical density of bulk defects in the $AlO_x$ layer. Collectively these observations indicate that the limits to these printed transistors' operational stability are primarily driven by the quality and physical thickness of the printed gate dielectric. Using UV-annealing methods we find that printed dielectrics can have a positive, compensating effect on the bias-stress stability of high-performance $InO_x$ transistors. As evidenced herein, it is possible to produce devices with excellent performance and substantial improvements in stability by using UV-annealing while maintaining low process temperatures.

## 6.7 Summary

This chapter explores the impact of integrating UV-annealing with low-temperature-processed printed transistors to achieve high performance and improved operational stability. UV-annealing offers a route to forming high-quality printed dielectrics with low leakage and suppressed dispersion that are not limited by a tradeoff between thickness and performance. These UV-annealed $AlO_x$ gate dielectrics are leveraged to fabricate printed $InO_x$ transistors with high mobility ($\mu_{lin}$ = 12 ± 1.6 $cm^2/Vs$), minimal hysteresis, and excellent subthreshold behavior at a low processing temperature of only 250 °C. The bias-stress characteristics of these devices are also analyzed to understand the critical relationship between printed dielectrics and threshold voltage stability. The improved bias-stress stability of $InO_x$ transistors with thicker printed $AlO_x$ dielectrics highlights the unique interactions between solution-processed high-k dielectrics and printed transparent metal oxide semiconductors such as $InO_x$. This work builds on previous chapters by completing the printed material set for printed metal oxide transistors and exploring a new annealing method which can lower processing temperatures to plastic compatible thermal budgets. These studies also investigated the important connections between printed materials integration and device stability, an essential parameter for ubiquitous applications in sensing and display technology.

## 6.8 References


[1] Y.-H. Kim et al., "Flexible metal-oxide devices made by room-temperature photochemical activation of sol-gel films," *Nature*, vol. 489, no. 7414, pp. 128–132, Sep. 2012.

[2] S. Park et al., "In-Depth Studies on Rapid Photochemical Activation of Various Sol–Gel Metal Oxide Films for Flexible Transparent Electronics," *Adv. Funct. Mater.*, vol. 25, no. 19, pp. 2807–2815, May 2015.

[3] J.-W. Jo et al., "Highly Stable and Imperceptible Electronics Utilizing Photoactivated Heterogeneous Sol-Gel Metal–Oxide Dielectrics and Semiconductors," *Adv. Mater.*, vol. 27, no. 7, pp. 1182–1188, Feb. 2015.

[4] R. A. John et al., "Low-Temperature Chemical Transformations for High-Performance Solution-Processed Oxide Transistors," *Chem. Mater.*, vol. 28, no. 22, pp. 8305–8313, Nov. 2016.

[5] M. Benwadih, R. Coppard, K. Bonrad, A. Klyszcz, and D. Vuillaume, "High Mobility Flexible Amorphous IGZO Thin-Film Transistors with a Low Thermal Budget Ultra-Violet Pulsed Light Process," *ACS Appl. Mater. Interfaces*, vol. 8, no. 50, pp. 34513–34519, Dec. 2016.

[6] J. Leppäniemi, K. Eiroma, H. Majumdar, and A. Alastalo, “Far-UV Annealed Inkjet-Printed In2O3 Semiconductor Layers for Thin-Film Transistors on a Flexible Polyethylene Naphthalate Substrate,” *ACS Appl. Mater. Interfaces*, vol. 9, no. 10, pp. 8774–8782, Mar. 2017.
[7] D. Kim, Y. Jeong, K. Song, S.-K. Park, G. Cao, and J. Moon, “Inkjet-Printed Zinc Tin Oxide Thin-Film Transistor,” *Langmuir*, vol. 25, no. 18, pp. 11149–11154, Sep. 2009.
[8] R. D. Deegan, O. Bakajin, T. F. Dupont, G. Huber, S. R. Nagel, and T. A. Witten, “Capillary flow as the cause of ring stains from dried liquid drops,” *Nature*, vol. 389, no. 6653, pp. 827–829, Oct. 1997.
[9] J. M. Allwood et al., “Manufacturing at double the speed,” *J. Mater. Process. Technol.*, vol. 229, pp. 729–757, Mar. 2016.
[10] W. J. Scheideler, J. Jang, M. A. U. Karim, R. Kitsomboonloha, A. Zeumault, and V. Subramanian, “Gravure-Printed Sol–Gels on Flexible Glass: A Scalable Route to Additively Patterned Transparent Conductors,” *ACS Appl. Mater. Interfaces*, vol. 7, no. 23, pp. 12679–12687, Jun. 2015.
[11] W. Xu, H. Wang, F. Xie, J. Chen, H. Cao, and J.-B. Xu, “Facile and Environmentally Friendly Solution-Processed Aluminum Oxide Dielectric for Low-Temperature, High-Performance Oxide Thin-Film Transistors,” *ACS Appl. Mater. Interfaces*, vol. 7, no. 10, pp. 5803–5810, Mar. 2015.
[12] P. C. With et al., “Low-Temperature Photochemical Conversion of Organometallic Precursor Layers to Titanium(IV) Oxide Thin Films,” *Chem. Mater.*, vol. 28, no. 21, pp. 7715–7724, Nov. 2016.
[13] W. J. Scheideler, R. Kumar, A. R. Zeumault, and V. Subramanian, “Low-Temperature-Processed Printed Metal Oxide Transistors Based on Pure Aqueous Inks,” *Adv. Funct. Mater.*, p. n/a-n/a, Mar. 2017.
[14] J. Smith et al., “Cation Size Effects on the Electronic and Structural Properties of Solution-Processed In–X–O Thin Films,” *Adv. Electron. Mater.*, vol. 1, no. 7, p. n/a-n/a, Jul. 2015.
[15] J. Jang, H. Kang, H. C. N. Chakravarthula, and V. Subramanian, “Fully Inkjet-Printed Transparent Oxide Thin Film Transistors Using a Fugitive Wettability Switch,” *Adv. Electron. Mater.*, vol. 1, no. 7, p. n/a-n/a, Jul. 2015.
[16] R. A. Street, “Thin-Film Transistors,” *Adv. Mater.*, vol. 21, no. 20, pp. 2007–2022, May 2009.
[17] K. Hoshino, D. Hong, H. Q. Chiang, and J. F. Wager, “Constant-Voltage-Bias Stress Testing of a-IGZO Thin-Film Transistors,” *IEEE Trans. Electron Devices*, vol. 56, no. 7, pp. 1365–1370, Jul. 2009.
[18] E. Carlos, R. Branquinho, A. Kiazadeh, P. Barquinha, R. Martins, and E. Fortunato, “UV-Mediated Photochemical Treatment for Low-Temperature Oxide-Based Thin-Film Transistors,” *ACS Appl. Mater. Interfaces*, vol. 8, no. 45, pp. 31100–31108, Nov. 2016.
[19] K. H. Ji et al., “Comparative Study on Light-Induced Bias Stress Instability of IGZO Transistors With and Gate Dielectrics,” *IEEE Electron Device Lett.*, vol. 31, no. 12, pp. 1404–1406, Dec. 2010.
[20] L. Y. Su, H. Y. Lin, H. K. Lin, S. L. Wang, L. H. Peng, and J. Huang, “Characterizations of Amorphous IGZO Thin-Film Transistors with Low Subthreshold Swing,” *IEEE Electron Device Lett.*, vol. 32, no. 9, pp. 1245–1247, Sep. 2011.

# Chapter 7: Conclusions and Future Work

## 7.1 Conclusions

The large-scale viability of transparent electronics depends on continued progress in the development of high-resolution and scalable printing methods such as gravure and inkjet, as well as the development of higher performance, versatile materials. This thesis explores the design of materials for printed metal oxide transistors and studies the physics of gravure printing to realize high-resolution printed devices. Methods and materials for printing transparent metal oxide conductors on glass are presented, showing the capabilities and limitations of high-temperature annealed sol-gel materials, as well as the physics of ink transfer on rigid substrates. To enhance the performance of low-temperature processed transparent conductors, hybrid gravure inks consisting of silver nanowires and sol-gel metal oxides were developed, showing increased performance and stability. To develop a greater understanding of ink transfer and feature formation during gravure printing, a sheet-fed high precision gravure printer was designed and constructed with the capability of decoupling the subprocesses of gravure for further study. Finally, in Chapter 5 and Chapter 6, low-temperature processable inks and UV-annealing methods for high-performance printed metal oxide transistors were developed, illustrating some of the critical tradeoffs between printability, annealing, and device performance. Based on this work, important topics for further study are now discussed, including existing challenges and potential solutions.

## 7.2 Advancing the Reliability and Scalability of Gravure Technology

### 7.2.1 Engineering Gravure Doctoring

Future work on gravure printing physics must address the entire process flow from roller inking to film formation. The physics of gravure printing depend critically on a number of fluid-solid and solid-solid interfaces with mechanical properties that can be carefully engineered. This is one of the next frontiers in developing reliable high speed and high-resolution printing tools. Because the doctoring process has an overwhelming contribution to large-scale haze and defect formation, particularly at high speeds and for high-viscosity inks, this area must remain a priority. Alternative materials for manufacturing the doctor blade could be one way to address its deficits. Bulk metallic glasses are interesting candidate materials for this job. The preparation and alloy composition of bulk metallic glasses results in their amorphous surface, a smooth interface which could theoretically provide ideal doctoring if matched with a smooth printing cliché or roll surface. Additionally, the durability and hardness of these blades remain unmatched by other materials, providing the two features essential to high precision doctoring and management of blade wear. Having these doctor blades as a control, an example of near perfect wiping, would present an interesting way to study wear and doctoring efficiency.

In addition to engineering the structural composition of the doctor blade, the surface's wettability could be adjusted to reduce printing artifacts such as dragout. Based on our group's recent work on understanding dragout-related artifact formation, we expect that robust hydrophobic coatings could be used to great advantage on the backside of the doctor blade. These coatings could help to prevent the capillary action of the meniscus on the backside of the blade and reduce the size of ink reservoirs which subsequently climb up the blade and redeposit tail features. The major challenge is finding robust coatings which adhere well to the relatively rough metallic finish of the doctor blade but also remain hydrophobic after printing with various inks.

An area which remains challenging for gravure printing is achieving high resolution printing over existing films and features. This requires greater understanding of the physics of film formation and the contact mechanics of ink transfer, as well as better methods for adjusting and homogenizing the surface energy of patterned surfaces. Additionally, gravure-printed multilayer devices need ink to first transfer efficiently from the roller, which, as discussed in Chapter 2 of this work, requires control over the dynamic contact angle and contact angle hysteresis. The question this surface engineering poses for printed transistors is how to engineer the surface energy without degrading electrical performance. Interfaces between the semiconductor and dielectric, for example, are critical for reliable operation and high-performance and can be quite sensitive to the exact processing conditions of each layer. Ideally, there would be multifunctional interlayer films which engineer the surface energy and are electrically functional. Self-assembled monolayers are interesting candidates to do this exact job, and have seen considerable use in spin-coated and printed organic transistors[1], [2] for a similar purpose.

### 7.2.2 Mechanically Induced Film Leveling

Uniform film leveling is an essential step in film formation for gravure-printed features. Because gravure printing utilizes pixelated representations of printed patterns, the droplets originating from individual cells must merge during and after ink transfer to form continuous films. However, the film transfer process can induce various non-uniformities either due to the cell-spacing induced non-uniformity or non-uniformities induced by hydrodynamic Saffman Taylor instabilities. Completely eliminating the Saffman Taylor instability is difficult given the practical constraints placed on print speed and ink viscosity for a particular application. While most inks have sufficient surface tension to level on their own, this process can be slow and requires that ink drying be performed slowly to allow time for leveling. Managing and mitigating these instabilities could perhaps be achieved with alternative methods. Ultrasonic vibration-induced film leveling has been explored for polymer layers in organic photovoltaics, showing improved film and device uniformity with lower defect concentrations and pinholes[3]. Utilizing these methods with gravure-printed films could provide a way to rapidly level the instabilities that result during ink transfer and allow for high-throughput processing. Ultrasonic leveling could be integrated inline in a roll-to-roll style configuration, following the printing station and preceding the drying or curing station. However, developing these methods may also require a deeper knowledge of the nature of the instabilities and their interactions with mechanical vibrations.

### 7.2.2 Sheared Patterned Deposition by Gravure Printing

Another method which could potentially direct gravure-printed formation is sheared deposition. The application of shear force during the blade-coating deposition of organic semiconductor has been shown to control and direct nucleation of large single-crystalline films for organic transistors [4] and in organic polymer photovoltaics[5]. Similarly, organic-inorganic metal-halide perovskite films have shown benefits from solution-shearing, which can aid in forming large, aligned single-crystalline grains[6]. Shearing during deposition could be accomplished using mismatched velocities of the roller and the substrate and by carefully controlling the contact mechanics. This would have advantages over the alternative methods for shearing solution-processed films, which are not amenable to additive two dimensional patterning.

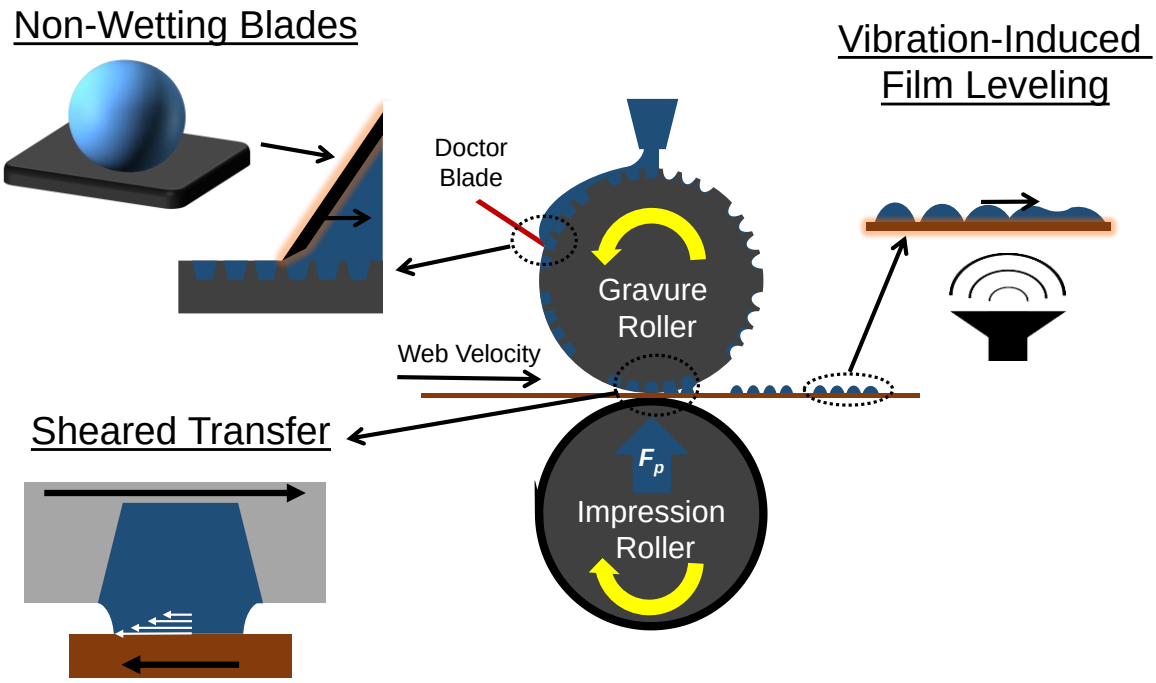


Figure 7.3 Concepts for future developments such as non-wetting blade materials, vibration induced leveling, and sheared transfer in gravure printing technology.

### 7.3 Next Generation Flexible Printed TFTs

Low-temperature processing of metal oxides still lags behind the performance and low-thermal budget required to make high performance flexible systems on plastic. Addressing this deficit will require new approaches which allow it to compete as a technology against carbon-nanotube systems and organic transistors. Although many alternative energy inputs such as ultraviolet annealing, pulsed white light annealing, and microwave annealing have been demonstrated, their integration with printing based manufacturing and with full transistor stacks has been slow. The use of multiple methods in parallel, for example, thermal annealing while performing UV treatment, could be essential to enhancing the performance of these devices to match the high-temperature processed systems.

Another approach to boosting the performance of metal oxide-based transparent electronics is the use of hybrid materials. As shown in Chp 3 of this thesis, there are considerable advantages to pairing the high intrinsic electrical performance of 1D nanomaterials with the mechanical and thermal stability of sol-gel based metal oxides. Perhaps these methods can be extended to semiconductor systems based on carbon nanotubes, for example, to allow high performance device at low temperatures which have the printability and mechanical robustness offered by sol-gel metal oxides. The use of hybrid electrodes as well could be an opportunity to boost low-temperature processing for printed transistors. The challenge of fabricating high conductivity inert electrodes is a formidable barrier to high performing transparent transistors on plastic, but with hybrid ink design techniques this may be overcome. The key is to choose suitable material systems which

complement each other and lend the thermomechanical and chemical stability to the highly conductive nanomaterial component. Developing a greater understanding of the chemistry of the precursor inks and of the detailed film formation process will be essential.

### 7.4 Improving Device Stability and Uniformity

To make printed metal oxide devices competitive with existing technologies, future work must be done to improve the yield, uniformity, and stability of printed devices. This is not a unique aspect of printed metal oxides, but it remains a critical area which could hamper the development of larger scale arrays and sensor systems based on these materials. The strength of metal oxide materials which has historically made them valuable as gas sensors is the modulation of carrier concentrations with exposure to different atmospheres. However, in some cases this sensitivity is a detriment to reliable device operation in applications such as display technology or photovoltaics. Understanding and mitigating these instabilities must therefore be a priority for further development of printed metal oxide devices.

Threshold voltage control and bias-stress stability have been primary challenges for printed metal oxides. Many circuit-level applications require high uniformity as well as long-term bias-stress stability. Metal oxides typically show positive $V_t$ shifts with the application of positive bias-stress and negative shifts with negative bias stress. Negative bias-stress $V_t$ shifts in particular, due to their dependence on electron emission from traps in the channel, also have a strong dependence on the incident light intensity. While these issues have largely been addressed for high-quality sputtered metal oxides, the bias-stress effects observed in solution-processed systems are typically more significant, perhaps due to their higher defect concentrations. Additionally, there has been relatively little study of bias-stress in printed metal oxide transistors[7] including the influence of varying ink chemistries and the effect of printed layer morphology. However, these issues will need to be addressed before printed oxide devices can be a viable technology. Encapsulation is an effective strategy to stabilize the back surface of metal oxide semiconductors and improve device stability. Printed electronic systems have potentially unique encapsulation requirements due to their applications in wearable systems or sensors for industrial and environmental monitoring. The use of additive processing for these encapsulation steps is also a must, since it minimizes additional process complexity for integrating various non-switching elements and for adding interconnects.

Many applications of metal oxide transistors demand high uniformity in device performance and high device-yield for fabrication of large scale arrays. Recent work in printed metal oxide TFTs has characterized the variability in TFT performance and has linked it to the geometrical and material device parameters. Ideal arrays of transistors will have minimal variation in threshold voltage and on-state current. Achieving this uniform switching behavior of printed transistors requires tight distributions of the critical geometrical parameters such as the channel length and the dielectric thickness. Methods such as self-alignment can result in low variation in channel length, even for short channel TFTs[8], but performance still varies as a function of the channel mobility. Indeed, most reports of the variability in printed device mobility show relatively large coefficients of variation in the range of 30-40%[8], [9]. Threshold voltage is also an important contributor to device-to-device variation. Circuit level applications requiring device-to-device matching in configurations such as differential pairs cannot tolerate the variability in threshold which has been reported[8], [9]. Diagnosing the source of this variability is essential to making printed devices viable for large scale applications. Finally, device-to-device printing variation

remains important even for small scale circuits because of its impact on reliability. Significant variation in dielectric thickness, for example, can lead to high off-state current and low device yield[10]. These topics must remain a priority as printing methods and printed materials mature in order to warrant printed metal oxide TFTs' technological relevance.

### 7.5 Printing Complementary Circuits

Integration of p-type channel materials is another important challenge for printed metal oxide transistors, since complementary logic can potentially yield printed circuits with lower power consumption and reduced complexity. However, metal oxides tend to be intrinsically n-type due to the high concentrations of deep donors states associated with oxygen vacancies and interstitial metal atoms[11]. Of the many candidate materials for p-type metal oxides, $NiO_x$ and CuO have shown the most promising performance for solution-processed systems, but still typically exhibit relatively low hole mobility in the range of 0.01 – 0.2 $cm^2/Vs$[12], [13] and poor on-off rations of $< 10^4$ [14], [15]. even after relatively high-temperature annealing and vacuum treatment. These properties remain inferior to alternative printed p-type material systems such as printed organic transistors (OTFTs) and ambipolar printed carbon nanotube (CNT) transistors. In vacuum-processed systems, there have been reports of higher performing ( $\mu_{lin} \sim 7$ $cm^2/Vs$) p-type devices based on materials such as SnO [16], but similar results have not been achieved by solution-processing to-date. Further control of film stoichiometry and precursor composition may be required before higher performance devices may be fabricated by printing.

However, it is also worth noting that additive printing technologies are well-suited to multimaterial integration. This could mean combining p-type printed CNT devices or high performance organic semiconductors with high-performance n-type metal oxides[17]. Some initial work has shown the possibility of successful integration of the same gate stack materials for both metal oxides and CNT devices on the same substrate, achieving higher inverter gain and good AC switching. These demonstrations also illustrate the advantages of the CNT / metal oxide combination for allowing low-voltage operation and compatibility with high-k gate dielectrics. Another viable approach is to engineer the threshold voltage of printed n-type devices to give devices with either depletion mode or enhancement mode operation. This strategy can accomplish similar results, giving inverter gains up to 45 [18]. This 'Dual-$V_t$' logic is attractive as it does not require separate material sets, just the ability to controllably shift the threshold voltage, for example, by adjusting the thickness of the channel material. Further development in this area, must weigh the application level benefits of using complementary logic against the increased manufacturing process complexity that is inherent to complementary device fabrication.

### 7.6 Printed Transistor Applications - Beyond Displays

Further innovation in printed metal oxide electronics must also be driven by a wider perspective on potential applications. Limiting the envisioned scope of solution-processed metal oxide transistors to flat panel displays can be problematic because it implies a direct comparison between printed devices and vacuum-processed incumbent technologies. These incumbent technologies have historical advantages due to the existing manufacturing infrastructure, proprietary intellectual property, and their proven marketability. But these challenges are avoided if printed devices target new system-level applications and markets that are out of reach of the incumbent technology.

Heterogeneous 3D integration of printed materials with traditional CMOS devices offers an interesting prospect for expanding the application space of printed systems and fully leveraging the advantages of additive manufacturing. The compatibility of low-temperature metal oxide processing with CMOS back end of line manufacturing (BEOL)[19] offers an interesting opportunity to integrate metal oxide TFTs directly into the interconnect layers of integrated circuits. This monolithic heterogeneous integration can be used, for example, to add high-voltage / low-voltage bridging input output (I/O) layers to a CMOS integrated circuit [20] or to add a vertically integrated gate drive circuit to a power management integrated circuit (PMIC). Although these demonstrations have exclusively used vacuum-processed layers and photolithographically defined patterns, the recent progress in printed metal oxide transistors suggests that additive manufacturing can be applied here as well. These examples highlight some of the primary benefits of using metal oxides, which have suitably high performance as well as robust enough thermal and chemical stability to be used in combination with higher power electronics[19]. These benefits are particularly relevant to 3D integrated systems which often struggle with thermal management, resulting in high operating temperatures.

Heterogeneous integration in 2.5 D is another powerful recent trend in electronics packaging which seeks to reduce system-level power and cost by integrating multiple integrated circuits (CPU, Memory, I/O, etc.) onto a single *interposer* substrate with dense interconnections provided by thin film metallization. The huge variety of application and cost requirements has driven interposer designs of various complexity, some of which now include thin film active components[21] and passives[22] which would have previously been discrete components. These trends emphasize the importance of multimaterial, multidevice integration and thin film processing, suggesting the imminent intersection of packaging and thin film technologies, a niche which could someday be addressed by printed metal oxide devices.

These capabilities of metal oxide electronics could also suggest their potential role as an interface to the physical world. The natural sensitivity of metal oxide TFTs to ambient gases[23], ions, and ultraviolet radiation[20] could make them useful sensor devices for the Internet of Things (IoT)[24] and the Industrial Internet. However, these new applications will require greater knowledge of the mechanisms that underlie device instabilities, to separate these artifacts from analyte sensing data and ensure long-term viability. Similarly, future printing studies of metal oxide materials and devices must address the causes of non-uniformity to allow reliable manufacturing within reasonable tolerances, a prerequisite for most all potential applications.

### 7.7 References

[1] J. Ha, S. Chung, M. Pei, K. Cho, H. Yang, and Y. Hong, “One-Step Interface Engineering for All-Inkjet-Printed, All-Organic Components in Transparent, Flexible Transistors and Inverters: Polymer Binding,” *ACS Appl. Mater. Interfaces*, vol. 9, no. 10, pp. 8819–8829, Mar. 2017.

[2] H. Klauk, U. Zschieschang, J. Pflaum, and M. Halik, “Ultralow-power organic complementary circuits,” *Nature*, vol. 445, no. 7129, pp. 745–748, Feb. 2007.

[3] Y. Xie, F. Zabihi, and M. Eslamian, “Fabrication of highly reproducible polymer solar cells using ultrasonic substrate vibration posttreatment,” *J. Photonics Energy*, vol. 6, no. 4, pp. 045502–045502, 2016.

[4] Y. Diao et al., “Solution coating of large-area organic semiconductor thin films with aligned single-crystalline domains,” *Nat. Mater.*, vol. 12, no. 7, pp. 665–671, Jul. 2013.

[5] Y. Diao et al., “Flow-enhanced solution printing of all-polymer solar cells,” *Nat. Commun.*, vol. 6, p. ncomms8955, Aug. 2015.
[6] J. Li et al., “Solution Coating of Superior Large-Area Flexible Perovskite Thin Films with Controlled Crystal Packing,” *Adv. Opt. Mater.*, vol. 5, no. 11, p. n/a-n/a, Jun. 2017.
[7] Y. Li et al., “All Inkjet-Printed Metal-Oxide Thin-Film Transistor Array with Good Stability and Uniformity Using Surface-Energy Patterns,” *ACS Appl. Mater. Interfaces*, vol. 9, no. 9, pp. 8194–8200, Mar. 2017.
[8] Y. Li et al., “Coffee-Ring Defined Short Channels for Inkjet-Printed Metal Oxide Thin-Film Transistors,” *ACS Appl. Mater. Interfaces*, vol. 8, no. 30, pp. 19643–19648, Aug. 2016.
[9] W. J. Scheideler, R. Kumar, A. R. Zeumault, and V. Subramanian, “Low-Temperature-Processed Printed Metal Oxide Transistors Based on Pure Aqueous Inks,” *Adv. Funct. Mater.*, p. n/a-n/a, Mar. 2017.
[10] A. Zeumault, S. Ma, and J. Holbery, “Fully inkjet-printed metal-oxide thin-film transistors on plastic,” *Phys. Status Solidi -Appl. Mater. Sci.*, vol. 213, no. 8, pp. 2189–2195, Aug. 2016.
[11] S. Lany and A. Zunger, “Dopability, Intrinsic Conductivity, and Nonstoichiometry of Transparent Conducting Oxides,” *Phys. Rev. Lett.*, vol. 98, no. 4, p. 045501, Jan. 2007.
[12] S. Y. Kim et al., “p-Channel Oxide Thin Film Transistors Using Solution-Processed Copper Oxide,” *ACS Appl. Mater. Interfaces*, vol. 5, no. 7, pp. 2417–2421, Apr. 2013.
[13] T. Lin, X. Li, and J. Jang, “P-channel oxide thin film transistors using sol-gel solution processed nickel oxide,” in 2015 *22nd International Workshop on Active-Matrix Flatpanel Displays and Devices* (*AM-FPD*), 2015, pp. 129–130.
[14] J. Jang, S. Chung, H. Kang, and V. Subramanian, “P-type CuO and Cu2O transistors derived from a sol–gel copper (II) acetate monohydrate precursor,” *Thin Solid Films*, vol. 600, pp. 157–161, Feb. 2016.
[15] J. Yu, G. Liu, A. Liu, Y. Meng, B. Shin, and F. Shan, “Solution-processed p-type copper oxide thin-film transistors fabricated by using a one-step vacuum annealing technique,” *J. Mater. Chem. C*, vol. 3, no. 37, pp. 9509–9513, 2015.
[16] J. A. Caraveo-Frescas, P. K. Nayak, H. A. Al-Jawhari, D. B. Granato, U. Schwingenschlögl, and H. N. Alshareef, “Record Mobility in Transparent p-Type Tin Monoxide Films and Devices by Phase Engineering,” *ACS Nano*, vol. 7, no. 6, pp. 5160–5167, Jun. 2013.
[17] B. Kim, S. Jang, M. L. Geier, P. L. Prabhumirashi, M. C. Hersam, and A. Dodabalapur, “High-Speed, Inkjet-Printed Carbon Nanotube/Zinc Tin Oxide Hybrid Complementary Ring Oscillators,” *Nano Lett.*, vol. 14, no. 6, pp. 3683–3687, Jun. 2014.
[18] J. Leppäniemi, K. Eiroma, H. S. Majumdar, and A. Alastalo, “In2O3 Thin-Film Transistors via Inkjet Printing for Depletion-Load nMOS Inverters,” *IEEE Electron Device Lett.*, vol. 37, no. 4, pp. 445–448, Apr. 2016.
[19] K. Kaneko, N. Inoue, S. Saito, N. Furutake, H. Sunamura, J. Kawahara, M. Hane, Y. Hayashi, in 2011 *Int. Electron Devices Meet.*, 2011, p. 7.4.1-7.4.4.
[20] W. Hyoung Lee, S. Jun Lee, J. Ah Lim, J. Ho Cho, *RSC Adv.* **2015**, *5*, 78655.
[21] J. A. Caraveo-Frescas, P. K. Nayak, H. A. Al-Jawhari, D. B. Granato, U. Schwingenschlögl, H. N. Alshareef, *ACS Nano* 2013, 7, 5160.
[22] B. Kim, S. Jang, M. L. Geier, P. L. Prabhumirashi, M. C. Hersam, A. Dodabalapur, *Nano Lett.* 2014, 14, 3683.
[23] J. Leppäniemi, K. Eiroma, H. S. Majumdar, A. Alastalo, *IEEE Electron Device Lett*. 2016, 37, 445.

[24] G. Hellings, M. Scholz, M. Detalle, D. Velenis, M. de P. de ten Broeck, C. R. Neve, Y. Li, S. V. Huylenbroek, S. H. Chen, E. J. Marinissen, A. L. Manna, G. V. der Plas, D. Linten, E. Beyne, A. Thean, in 2015 *Symp. VLSI Technol. VLSI Technol.*, 2015, pp. T222–T223.